Boost Through Reentry Trajectory Planning For Maneuvering Reentry Vehicles

by

Matthew James Abrahamson

S.B., Aerospace Engineering With Information Technology
Massachusetts Institute of Technology (2006)

Submitted to the Department of Aeronautics and Astronautics
in partial fulfillment of the requirements for the degree of

Master of Science in Aeronautics and Astronautics
at the
MASSACHUSETTS INSTITUTE OF TECHNOLOGY

May 2008

Author: _____
Department of Aeronautics and Astronautics
May 23, 2008

Certified by: _____
Ronald J. Proulx, Ph.D.
Principal Member of the Technical Staff
The Charles Stark Draper Laboratory, Inc.
Technical Supervisor

Certified by: _____
John Deyst, Ph.D.
Professor of Aeronautics and Astronautics
Thesis Advisor

Accepted by: _____
David L. Darmofal, Ph.D.
Associate Department Head
Chair, Committee on Graduate Students

[This page intentionally left blank.]

Boost Through Reentry Trajectory Planning For Maneuvering Reentry Vehicles

by

Matthew James Abrahamson

Submitted to the Department of Aeronautics and Astronautics
on May 23, 2008, in partial fulfillment of the
requirements for the degree of
Master of Science in Aeronautics and Astronautics

Abstract

New trajectory planning concepts are explored for rapidly planning a long range, boost-through-reentry mission, using a lightweight, highly maneuverable reentry vehicle. An Aimpoint Map, a set of all possible piercepoints through which a boost-through-reentry trajectory can be flown to a fixed target, contains valuable information about the joint capabilities of the booster and the reentry vehicle. At each piercepoint in the Aimpoint Map, a set of velocities and flight path angles exist that can be reached from launch as well as a set of velocities and flight path angles that allow the target to be reached from the piercepoint. The intersection of these velocity and flight path angle sets provides important information for the trajectory planner about the margins available at each piercepoint in the Aimpoint Map. Boost-through-reentry trajectory optimization is used with a six degrees-of-freedom (6DOF) vehicle model to provide a quantitative assessment of the limiting capabilities of the vehicle flight subject to complex terminal and path constraints. Particular constraints of interest include energy management, max g's, heating rate, final velocity and flight path angle, angle of attack, over-flight considerations, approach azimuth, and booster stage disposal.

Technical Supervisor: Ronald J. Proulx, Ph.D.
Title: Principal Member of the Technical Staff

Thesis Advisor: John Deyst, Ph.D.
Title: Professor of Aeronautics and Astronautics

[This page intentionally left blank.]

Acknowledgments

First and foremost, I would like to thank Draper Laboratory for the funding and opportunity to perform interesting research over the past two years. Also, I would like to thank my advisor, Ron Proulx, for his ideas and insights that have helped me through the thesis process. Many thanks to Stan Shepperd for providing lectures on everything from Kalman filtering to politics and also serving as a great mentor and friend. Many thanks also to Lee Norris for teaching me how to really put a good powerpoint presentation together. Also thanks to Professor John Deyst for his thoughtful comments on my thesis work as well as his guidance in 16.62x and 16.06.

As I recall the six years I have spent at MIT, there are two things that stand out in my mind as invaluable experiences: Phi Delta Theta Fraternity and The MIT Festival Jazz Ensemble. Some of my most rewarding experiences have come as a member of Phi Delta Theta. It was truly the one experience that made me feel "at home" at MIT. Learning to live and self-govern a house of 40 men is no easy task, and I believe that this experience builds great character and leadership qualities in a young man. I strongly believe in the values and vision of the Fraternity: friendship, sound learning, and moral rectitude. I also take the fraternity motto "One Man Is No Man" to hold true since my journey through MIT would not have been possible without the help and society of others. I only hope that more Fraternities around the country abandon the stereotypical "animal house" culture and return to the core values of Greek life. My experiences in the MIT Festival Jazz Ensemble (FJE) have also given me many rewarding experiences. I would like to thank my director, Dr. Fred Harris, for his creative and humorous instruction during Tuesday and Thursday night rehearsals. They provided a necessary "mind-relief" from the engineering number crunching performed during the day. I would also like to thank Fred for his dedicated effort to make each and every FJE concert a memorable one. I've played alongside jazz greats such as Kenny Werner, Steve Turre, Joe Lovano, Jeff Galindo, Greg Hopkins, and many more due to his hard work.

I would like to thank the AIMSense team for a great run through the Lunar Ventures Business Plan Competition and the MIT 1K Competition. I hope to collaborate with you

on more entrepreneurial activities in the future.

Finally, I'd like to thank my family and my girlfriend, Shannon, for their love and support over the past few months. I've had to make some sacrifices to complete this thesis and it wouldn't have been possible without their help and support.

This thesis was prepared at The Charles Stark Draper Laboratory, Inc., under Project 22203-004,, Trajectory Optimization, Contract CON01759-7.

Matthew J. Abrahamson

5/23/08
Date

[This page intentionally left blank.]

Contents

1 Introduction **21**

1.1 Maneuvering Reentry Vehicles 23

1.2 Skid-To-Turn Control 28

1.3 Mission Planning Considerations 33

1.4 Trajectory Optimization 35

1.5 Thesis Overview 39

2 Coordinate Frames **41**

2.1 Earth Centered Inertial (ECI) Coordinate Frame 41

2.2 Earth Centered Earth Fixed (ECEF) Coordinate Frame 43

2.3 Reference Plane (REF) Coordinate Frame 44

2.4 Up-Downrange-Crossrange (UDC) Coordinate Frame 47

2.5 Velocity (V) Coordinate Frame 49

2.6 Non-Rolling Body (B) Coordinate Frame 52

2.6.1 Aerodynamic Angles 54

2.7 Summary 59

3 Equations of Motion **61**

3.1 Translational Equations of Motion 61

3.1.1 Position Equations of Motion 64

3.1.2 Velocity Equations of Motion 67

3.2 Rotational Equations of Motion 76

3.3 Singularities 83

3.4 Summary 84

4 The Optimal Control Problem **89**

4.1 Optimal Control Fundamentals 90

4.1.1 Performance Index 90

4.1.2 Necessary Conditions and The Minimum Principle 91

4.1.3 Event Constraints 93

4.1.4 Path Constraints 94

4.1.5 Indirect Method Challenges 96

4.2 Nonlinear Programming Concepts 97

4.2.1 Optimality Conditions 98

4.3 Knotting Conditions 101

4.4 Parameter Scaling 104

4.4.1 Scaling Method 105

4.4.2 Segmented Scaling 110

4.5 Summary 111

5 The Boost Problem **113**

5.1 Launch Vehicle 113

5.1.1 Mass Sizing 114

5.1.2 Propellant Burn Rates 119

5.1.3 Thrust Force 120

5.1.4 Booster Length 121

5.1.5 Summary 123

5.2 Environment Models 123

5.2.1 Ellipsoidal-Earth Model 123

5.2.2 Atmosphere Model 125

5.3 Launch Vehicle Aerodynamics 127

5.4 Launch Vehicle Attitude Control 136

5.4.1 Thrust Vector Control 136

5.4.2 Attitude Control System 138

5.4.3 Aerodynamic Torques . . . 138
5.4.4 Launch Vehicle Control Summary . . . 140
5.5 Launch Optimal Control Problem Formulation . . . 140
5.5.1 Initial Conditions . . . 140
5.5.2 Knots . . . 141
5.5.3 State Bounds . . . 143
5.5.4 Control Bounds . . . 144
5.5.5 Event Constraints . . . 144
5.5.6 Path Constraints . . . 145
5.6 Launch Vehicle Capabilities . . . 147
5.6.1 Initial Guess . . . 147
5.6.2 Maximum Piercepoint Range Case . . . 153
5.7 Minimum Piercepoint Range Case . . . 158
5.8 Summary . . . 162

6 The Reentry Problem **163**
6.1 Reentry Vehicle Aerodynamics . . . 164
6.2 Reentry Vehicle Control . . . 167
6.3 Problem Formulation . . . 169
6.3.1 The Submunitions Deployment Mission . . . 169
6.3.2 Knots . . . 171
6.3.3 State Bounds . . . 172
6.3.4 Control Bounds . . . 173
6.3.5 Event Constraints . . . 173
6.3.6 Path Constraints . . . 174
6.4 Reentry Vehicle Capabilities . . . 176
6.4.1 Ballistic Reentry . . . 177
6.4.2 Maximum And Minimum Downrange . . . 180
6.4.3 Maximum Crossrange . . . 186
6.5 Summary . . . 188

7 The Aimpoint Map **191**

7.1 Aimpoint Boundaries 192

7.1.1 Corner Point Case 192

7.2 Aimpoint Minimum and Maximum Piercepoint Cases 204

7.3 Launch Footprint 211

7.3.1 Launch Footprint Trends 217

7.4 Reverse Reentry Footprint 220

7.4.1 Reverse Footprint Trends 222

7.5 Piercepoint V-Gamma Map 229

7.5.1 Minimum Point Case 230

7.5.2 Corner Point Case 231

7.5.3 Maximum Point Case 232

7.5.4 Interior Point Cases 233

7.6 Summary 236

8 Conclusions **237**

8.1 Future Work 239

List of Figures

1-1 Conceptual Vehicle Body With L/D $\approx$ 2 27

1-2 Relationship Between Attitude And Lift In The Lift Plane 29

1-3 Relationship Between Lift And Attitude As Observed By Looking Along The Velocity Vector Direction 30

1-4 Depiction Of A Bank-To-Turn Vehicle, As Seen From Behind The Vehicle Tail 32

1-5 Depiction Of Potential Trajectory Planning Concepts For The New Rapid, Long Range Mission 35

2-1 Earth Centered Inertial Coordinate Frame 42

2-2 Earth Centered Earth Fixed (ECEF) Frame 43

2-3 Reference (REF) Coordinate Frame 45

2-4 Up-Downrange-Crossrange Coordinate Frame 48

2-5 Velocity Frame 50

2-6 Representation of Velocity Vertical Frame and Local Horizontal Frame . . 51

2-7 Body Coordinate Frame 54

2-8 Relationship Between Sigma and Alpha 56

2-9 Illustration Of The Lift Plane 57

2-10 Relationship Between Sigma And The Lift Vector 58

3-1 Position And Velocity States Of The 6DOF System 62

3-2 Illustration Of Relationship Between Frame A And Frame B 64

4-1 Example of Knot Locations Along Vehicle Trajectory 102

4-2 Scaled States Using Scaling Method 108
4-3 Scaled Rates Using Scaling Method 109
4-4 Scaled States Using Segmented Scaling 111

5-1 Flight Segments Of The Boost Portion Of Flight 114
5-2 Illustration of Launch Vehicle Parameters 116
5-3 Isp Variation Over Altitude 121
5-4 Oblate Earth Model With Geodetic Altitude, h, and Geodetic Latitude, κ 124
5-5 Comparison Of Atmospheric Density Models Versus Altitude 126
5-6 Algorithm Sequence For Automatic Density Curve Fit 127
5-7 Axial Coefficient Of Force As A Function Of Mach Number And Angle Of Attack 130
5-8 Normal Coefficient Of Force As A Function Of Mach Number And Angle Of Attack 131
5-9 The Normalized Center Of Pressure As A Function Of Angle Of Attack And Mach Number 132
5-10 The Angle of Attack-Averaged Curve Fit To The Axial Coefficient Of Force Plotted Versus Mach Number 134
5-11 The Mach Number-Averaged Curve Fit For Normal Coefficient Of Force Plotted Versus Angle Of Attack 134
5-12 The Angle of Attack-Averaged Curve Fit For Center Of Pressure Plotted Versus Mach Number 135
5-13 In Plane and Out of Plane Thrust Vectoring Control 137
5-14 External Aerodynamic Torque 139
5-15 Knot Locations Along Launch Trajectory 142
5-16 Altitude Versus Relative Longitude For Guess Trajectory 148
5-17 Earth-Relative Velocity Versus Time For Guess Trajectory 149
5-18 Flight Path Angle Versus Time For The Guess Trajectory 149
5-19 Nose Pitch Angle Profile For Guess Trajectory 150
5-20 Dynamic Pressure As A Function Of Altitude For The Guess Trajectory . 151

5-21 Body Pitch Rate Versus Time For Guess Trajectory 152
5-22 Maximum Range Boost Trajectory 153
5-23 Flight Path Angle Profile For Maximum Range Launch Trajectory 155
5-24 Nose Pitch Angle Profile For Maximum Range Launch Trajectory 155
5-25 Body Pitch Rate Profile For Maximum Range Trajectory 156
5-26 Pitch Controls For Maximum Range Launch Trajectory 157
5-27 Minimum Range Launch Trajectory 159
5-28 Flight Path Angle Profile For Minimum Range Launch Trajectory 159
5-29 Nose Pitch Angle Profile For Minimum Range Launch Trajectory 160
5-30 Drag Profile For Minimum Range Launch Trajectory 161

6-1 Reentry Flight Profile 164
6-2 Reentry C_N as a Function of Angle of Attack 165
6-3 Reentry Vehicle C_X as a Function of Mach Number (M) 166
6-4 Reentry Vehicle Control Flaps 167
6-5 Submunitions Profile In Terms Of Relative Longitude And Relative Latitude 170
6-6 Knots Locations For The Reentry Problem 171
6-7 Ballistic Reentry Trajectory 177
6-8 Nose Pitch Angle Profile For Ballistic Reentry Trajectory 178
6-9 Velocity And Flight Path Angle Profiles For The Ballistic Reentry Trajectory 179
6-10 Comparison Of Maximum And Minimum Downrange Reentry Trajectories 181
6-11 Velocity And Flight Path Angle Profiles For Minimum Range Reentry Trajectory 182
6-12 Velocity And Flight Path Angle Profiles For Maximum Range Reentry Trajectory 183
6-13 Nose Pitch Angle Profile Versus Time For Minimum Range Reentry Trajectory 184
6-14 Nose Pitch Angle Profile For Maximum Range Reentry Trajectory 184
6-15 Optimal Pitch Flap Control For The Minimum Range Reentry Trajectory . 185
6-16 Optimal Pitch Flap Control For The Maximum Range Reentry Trajectory 185

6-17 Maximum Crossrange Reentry Trajectory 186
6-18 Pitch And Yaw Flap Controls For Maximum Crossrange Reentry Trajectory 187
6-19 Heading Angle Profile For Maximum Crossrange Trajectory 188

7-1 Illustration Of Geometry Used To Computed Corner Point Trajectory . . . 193
7-2 Corner Point Trajectory of Aimpoint Map 194
7-3 Top-View of Corner Point Trajectory 195
7-4 Side-View of Corner Point Trajectory 196
7-5 Velocity Profile Of Corner Point Trajectory 197
7-6 Flight Path Angle Profile For Corner Point Trajectory 198
7-7 Heading Angle Profile For Corner Point Trajectory 200
7-8 Nose Attitude Profile For Corner Point Trajectory 202
7-9 Pitch Control Profile For Corner Point Trajectory 203
7-10 Yaw Control Profile For Corner Point Trajectory 204
7-11 Concept For Sweeping Across The Aimpoint Map To Compute Minimum And Maximum Boundaries 205
7-12 The Aimpoint Map For The Submunitions Mission 206
7-13 Top-View Of Minimum Boundary Trajectories 207
7-14 Aimpoint Minimum Boundary Trajectories 208
7-15 Flight Path Angle Profile For Minimum Aimpoint Boundary Trajectories . 208
7-16 Top View Of Maximum Piercepoint Range Trajectories 210
7-17 Maximum Boundary Trajectories 211
7-18 Illustration of Skip Regions Along Aimpoint Boundaries 212
7-19 Flight Path Angle Profile For Minimum γ Trajectory With $\mu_{pierce} = 15$ deg, $\lambda_{pierce} = 4$ deg 213
7-20 Flight Path Angle For Shallowest Launch Trajectory For $\mu_{pierce} = 15$ deg, $\lambda_{pierce} = 4$ deg 214
7-21 Steepest And Shallowest Launch Trajectories For $\mu_{pierce} = 15$ deg, $\lambda_{pierce} = 4$ deg 215
7-22 Launch Foorprint For $\mu_{pierce} = 15$ deg, $\lambda_{pierce} = 4$ deg 216

7-23 Maximum And Minimum Velocity Trajectories For μ_{pierce} = 15 deg, λ_{pierce} = 4 deg, γ_{pierce} = -31.9 deg 218
7-24 Piercepoint Locations At Various Ranges For $\psi(t_0)$ = 4 deg 219
7-25 Launch Footprints For Various Piercepoints Within The Aimpoint Map . . 219
7-26 Piercepoint Located In The Aimpoint Map At μ = 15 deg, λ = 4 deg . . . 221
7-27 The Reverse Footprint For μ_{pierce} = 15 deg, λ_{pierce} = 4 deg 221
7-28 Interior Piercepoints Chosen For Comparison Of Reverse Footprints 223
7-29 Reverse Footprints For Interior Piercepoints 223
7-30 Shallow Reentry Trajectory From μ_{pierce} = 19 deg, λ_{pierce} = 0 deg 224
7-31 Piercepoints Located Along The Maximum Aimpoint Boundary 225
7-32 Reverse Footprints For Piercepoints Along The Maximum Aimpoint Boundary 226
7-33 Reverse Footprints For Trajectories With $\psi(t_0)$ = 4 deg 228
7-34 Piercepoint V-γ Map For Minimum Aimpoint Boundary Piercepoint Corresponding To $\psi(t_0)$ = 4 deg 230
7-35 The Piercepoint V-γ Map For The Corner Point Trajectory 231
7-36 Piercepoint V-γ Map For Maximum Aimpoint Boundary Corresponding To $\psi(t_0)$ = 26 deg 232
7-37 Piercepoint V-γ Map For μ_{pierce} = 15 deg, λ_{pierce} = 4 deg 234
7-38 Piercepoint V-γ Map For μ_{pierce} = 19 deg, λ_{pierce} = 0 deg 235

[This page intentionally left blank.]

List of Tables

5.1 *Launch Vehicle Properties* 123

5.2 *The Axial Force Coefficient C_X As A Function Of Angle Of Attack And Mach Number.* 130

5.3 *The Normal Force Coefficient C_N As A Function Of Angle Of Attack And Mach Number* 131

5.4 *The Center Of Pressure C_P As A Function Of Angle Of Attack And Mach Number Expressed As A Percentage Of Vehicle Length* 132

[This page intentionally left blank.]

Chapter 1

Introduction

In the years following the end of the Cold War, the United States has seen a dramatic shift in the character of its global adversaries. The state of the world today finds a proliferation of dangerous weapon technologies to small, decentralized extremist groups operating in some of the most remote locations of the world. As these threats continually evolve, so must our preparedness. While the U.S. nuclear arsenal has proved valuable in the past for satisfying the nation's deterrence policies against other superpower nations such as the USSR and China, it provides no such deterrence against emerging rogue threats. A rapid, long range, conventional weapon capability is desired to counter such emerging threats.

Current rapid, long range vehicle capabilities include Intercontinental Ballistic Missiles (ICBMs) and Submarine Launched Ballistic Missiles (SLBMs). These systems fly both endo- and exo-atmospherically, have ranges of well over 5,000 miles, are guided during boost, and can reach a target within 30 minutes [9]. However, these vehicles are typically designed for static, predetermined targets and exhibit little-to-no maneuvering capability (ballistic) during reentry. In addition, the use of nuclear-capable vehicles for conventional applications is undesirable since it could lead to a misinterpretation of U.S. intentions by other nations. Another vehicle option currently available for rapid, long range conventional missions is the Sea-Launched Cruise Missile (SLCM). However, many of these cruise missiles travel at subsonic speeds, requiring two or more hours to reach a maximum distance of 1,500 nautical miles [1]. Therefore, a new vehicle traveling at hypersonic speeds

[1] J. Buff, *Undersea Global Strike*, Military.com, March 13 2006

is needed to close the 0-to-60 minute response gap for conventional payloads [2]. This new vehicle will exhibit advanced maneuvering characteristics for range extension with a total mission completion time of under one hour. The need to plan for a rapid, long range mission using a lightweight, highly maneuverable vehicle requires the formulation of a completely new approach to mission design and planning.

The new time-sensitive mission requires both flexibility and continual readiness for U.S. forces. The mission planner must now be prepared to plan and execute a mission within a short time of target detection. Uncertainties in both the target location and U.S. ship/sub location, prior to target detection, will require a great deal of mission planning flexibility. For example, a ship patrolling the South China Sea must be able to respond to a threat in North Korea without flying over the People's Democratic Republic of China. Therefore, a maneuvering reentry vehicle with maximum coverage and high precision capabilities is desired.

The primary enabler to rapid mission planning is *boost-through-reentry trajectory optimization.* Such a capability can be used to maximize vehicle coverage while satisfying important fly-out, en route and terminal mission constraints (both technical and political), such as energy management, max g's, heating rate, final velocity and flight path angle, angle of attack, over-flight considerations, approach azimuth, and booster stage disposal. Trajectory optimization will provide the mission planner with a quantitative assessment of the vehicle capabilities and limitations with regard to its maximum and minimum maneuvering characteristics. Through careful examination of these capabilities, new mission possibilities may emerge, such as aiming the launch vehicle in a direction other than directly at the target or remaining in the atmosphere for a greater portion of flight.

In addition to defining the inherent capabilities of a proposed vehicle GN&C system, trajectory optimization also serves to define a multitude of mission options to the mission planner. The most pressing concern, with respect to planning a mission of this type, is choosing where to aim the launch vehicle such that the reentry vehicle can reach the target. Calculation of the launch vehicle "feasible aimpoints" involves tying together the capabilities of the launch system with the capabilities of the reentry system. The ultimate

[2]T. Benedict, *A New Role for the Trident Fleet*, Military.com, July 31 2006

goal is to demonstrate the properties of an *aimpoint map* that the mission planner can use for quickly and effectively aiming his launch vehicle.

The work presented here will analyze the boost-through-reentry optimization of a conceptual maneuvering reentry vehicle using a *skid-to-turn* control approach for the purpose of defining the characteristics of an aimpoint map. The conceptual maneuvering reentry vehicle for this mission is desired to be lightweight, travel at speeds up to Mach 16, and have a lift-to-drag ratio of approximately two.

1.1 Maneuvering Reentry Vehicles

A *maneuvering reentry vehicle* can be classified as a vehicle designed to enter a planetary atmosphere from orbital altitudes with the capability of performing preplanned flight maneuvers using either thrusters or flaps [9]. Reentry vehicles have been an active area of research since the dawn of the space age in the 1950s. The basic premise behind the reentry vehicle is to develop a body that can safely and accurately transport a payload from Earth orbit to a point on the Earth's surface. The development of reentry vehicle guidance systems has been a particularly active area of research due to the difficulty of maneuvering to a precise terminal location given the complex hypersonic aerodynamics encountered upon reentry. A variety of guidance schemes for maneuvering reentry vehicles have been conceptualized and studied over the past 40 years, leading to modern advances in both manned and unmanned vehicles.

Beginning with the development of the first ICBMs in the 1950s, unmanned reentry vehicles were developed and built to follow a ballistic (non-maneuvering) trajectory to a target on the Earth's surface [9]. With this design, all vehicle guidance maneuvers were performed during the launch portion of flight with the remainder of the flight flown ballistically [9]. In the 1960s, research in manned reentry vehicles became a national priority as the United States sought to establish a manned space presence with the Mercury, Gemini, and Apollo manned space programs. These vehicles used a high angle-of-attack trim condition along with a steering guidance law based on lift bank angle modulation to steer the capsule to the desired landing spot in the ocean [11]. By the 1970s and 1980s, inter-

est in higher precision targeting during reentry led to several research and development studies involving maneuverable reentry vehicles, including the Advanced Maneuverable Reentry Vehicle (AMaRV) [9], Precision Guided Reentry Vehicle (PGRV) [9], and U.S. Space Shuttle [15]. The AMaRV test flights in 1980-1981 were the first to demonstrate a high altitude maneuvering capability with new angles of attack, speed, acceleration, and guidance features [9]. The PGRV R&D program was an effort to build upon the AMaRV project by demonstrating a terminal guidance capability [9]. In contrast, the U.S. Space Shuttle was more limited in its design due to strict g-loading and heating limits enacted to ensure crew survivability and protection of its reusable thermal protection system. It was designed to fly at high angle of attack trim conditions for a majority of its reentry flight before energy management maneuvers were executed below 83,000 ft and final maneuvering to its runway below 10,000 feet [15].

Recent increases in computational power have provided a catalyst for research into higher fidelity reentry vehicle models exhibiting new flight characteristics with increased accuracy and maneuverability. Technologies developed for the AMaRV project in the 1980s have been revived recently for the development of a Common Aero Vehicle (CAV), a multi-mission capable reentry system for transportation of cargo, payload, or weapons through the atmosphere to the Earth's surface [13]. The CAV is designed to weigh 500 pounds and transport a nominal payload of 800 pounds to the Earth's surface. Additionally, it travels at speeds of up to Mach 30, has a cross range capability of 2,400 nautical miles from its reentry point, and can reach its destination on the Earth's surface in less than 90 minutes [13].

Clarke [12] investigated the maneuvering capabilities of the CAV using Legendre Pseudospectral Optimization, a direct collocation method. The mission profile used in Clarke's study examined the reentry portion of the vehicle trajectory with initial conditions of 40 kilometers (131,233 ft) altitude and a velocity of 7,000 m/s (22,965 ft/s). In particular, Clarke examined the effect of heat loads, dynamic pressure limits, and lift-to-drag ratio on the maximum control margin of the vehicle. The study used a 3 degrees-of-freedom (3DOF) model to govern the motion of the vehicle while assuming a time lag in the command of angle-of-attack and lift bank angle. The angle-of-attack and lift bank an-

gle rates were assumed to be instantaneously controlled. In addition, the vehicle model was assumed to have lift proportional to angle of attack, and a drag polar that increases quadratically with lift [12].

Other recent reentry vehicles studied include the Kistler K-1 Orbital Vehicle, the X-33, and the Crew Exploration Vehicle (CEV). Each of these vehicles are designed for a manned crew and, therefore, have much greater restrictions on maneuvering capability as compared to the CAV. Bibeau [16] generated optimal reentry trajectories for the Kistler K-1 vehicle using a direct collocation approach to discretize the optimal control problem, using as few as 10 node points. The Kistler K-1 is a reusable vehicle designed to place one or more payloads in low Earth orbit and return to a designated circular landing area 6,000 feet in diameter [17]. Bibeau modeled the K-1 vehicle motion using 4 degrees-of-freedom (4DOF) equations of motion, initialized at an entry interface (EI) altitude of 400,000 ft (121.9 km) and a velocity on the order of 26,000 feet per second (7,925 m/s) [17]. The model assumed fixed-trim angle-of-attack conditions during reentry with the vehicle bank angle used as the control variable for maneuvering. The optimization metric used was a weighted combination of control effort and target miss distance [16]. Similarly, Bairstow [11] examined the reentry characteristics of the Crew Exploration Vehicle (CEV) using similar initial conditions and a fixed-trim angle of attack. A guidance algorithm was designed to perform lift bank angle modulation upon reentry for extended range maneuvering to a land-based landing site.

The X-33 is an autonomous, reusable launch vehicle with aerodynamic control provided during reentry by a set of in-board and out-board elevons, split body flaps, and dual rudders [15]. Bollino [15] examined the reentry capabilities of the X-33 using a high-fidelity six degrees-of-freedom (6DOF) model with Legendre Pseudospectral Optimization. Unlike the other manned vehicle models mentioned above (i.e., K-1, CEV), the X-33 is not required to reenter at a fixed trim condition and thus has much greater maneuvering capability than the other vehicle models. In addition, Bollino concluded that optimal vehicle capabilities predicted by 6DOF models can be significantly more accurate than optimal capabilities predicted by a 3DOF model [15]. However, the X-33 is still a much larger, less agile vehicle than the vehicle to be considered in this study. Additionally,

the X-33 is an asymmetric vehicle which uses a bank-to-turn (BTT) control approach while the vehicle in this study is symmetric about the vehicle nose and uses a skid-to-turn (STT) control approach.

Undurti [1] examined the optimal reentry characteristics of a novel triconic-shaped maneuvering reentry vehicle designed by Textron Systems, Inc. The vehicle was modeled using four degrees-of-freedom (4DOF) equations of motion with a quadratic lag modeled for commanding the angle of attack and lift bank angle. Undurti investigated the variation of landing footprints due to limits on maximum G-loading, stagnation point heat rate, and lift-to-drag ratio (L/D) using a Legendre Pseudospectral Optimization Method. Complex phenomena were encountered in landing footprints with high L/D ratios due to the enhanced ability of the vehicle to skip. For this study, a vehicle with an L/D of approximately two will be used to explore more of this complex phenomena. Instead of computing landing footprints, however, this study will focus on computing the aimpoint map, or "footprint in the sky", along with associated characteristics that will enhance mission planning capabilities.

The vehicle in this study exhibits different characteristics from all of the aforementioned vehicles. Therefore, the vehicle model developed for this study will include several modeling choices that are different than those used in prior studies. First, the vehicle in this thesis will be modeled using a *six degrees-of-freedom* (6DOF) model so as to incorporate rotational motion. This will accurately model the ability of the vehicle to command both attitude and the proper lift magnitude and direction for maneuvering. Second, the vehicle will maneuver using a skid-to-turn control approach, as will be described in section 1.2. Third, the vehicle considered in this study will be much smaller, in volume and mass, and will reenter the atmosphere at suborbital speeds approaching Mach 16 rather than at orbital speeds. Fourth, and most importantly, the entire boost-through-reentry vehicle flight will be considered as a unified optimization problem. While many previous studies have performed optimization of the reentry flight with arbitrarily-chosen initial conditions, the reentry initial conditions in this study will be directly tied to the capability of the launch vehicle to target a reentry point. This represents a complex and challenging optimization problem.

A conceptual model of the reentry vehicle is depicted in Figure 1-1. This vehicle weighs 300 lbs, has a maximum diameter of 21 inches, a length of 1.43 meters, and has a lift-to-drag ratio of approximately two.

Figure 1-1: Conceptual Vehicle Body With L/D $\approx$ 2

1.2 Skid-To-Turn Control

The maneuvering reentry vehicle considered in this study will exhibit a *skid-to-turn (STT)* control approach, in which both the pitch and yaw plane responses have identical behavior due to body symmetry about the axis of roll [4]. Such a STT-controlled vehicle can maneuver in any preferred radial direction that is normal to the axis of roll ($\mathbf{x}_B$) with equal control response. In fact, the roll attitude of the vehicle is often stabilized to a fixed reference position for the STT control strategy, allowing the use of a non-rolling body frame [10]. The purpose of using such a model is that the cross coupling between pitch, roll, and yaw is eliminated, allowing a reduction in the number of necessary state variables.

The STT control approach dictates the motion of the vehicle body by orienting the nose of the body in a particular direction *relative to* the velocity vector. By orienting the body in this way, the vehicle is able to direct the aerodynamic forces in a desired direction. Unlike asymmetric vehicles, the roll attitude (about the nose) of this vehicle will have no effect on the direction or magnitude of the aerodynamic force since the relative wind pressure acting perpendicular to the nose axis exhibits the same force independent of which vehicle side is facing it. The lift force is directed in a plane spanned by the velocity vector and the nose pointing vector called the *lift plane*. The vehicle will turn by orienting the vehicle attitude (and, therefore, lift vector) in a particular direction relative to the velocity vector. The images in Figures 1-2 and 1-2 depict the necessary attitude of the vehicle for making a turn toward the left. Figure 1-2 shows the attitude of the vehicle within the lift plane while Figure 1-3 shows the range of allowable attitude pointing directions relative to the velocity vector. The resultant lift force is denoted as L, the angle of attack is denoted as α, and the lift bank angle is denoted as σ. Also, the displacement of the nose vector from the velocity vector in the vertical plane is defined as the *pitch channel* and the displacement in the horizontal plane is defined as the *yaw channel* [10]. The lift bank angle determines the radial direction relative to the velocity vector in which the attitude points, while the angle of attack determines how far along that direction the nose attitude is pointed. A particular attitude is shown within this

range that serves to turn the vehicle toward the left with the maximum angle of attack values, α_{max}.

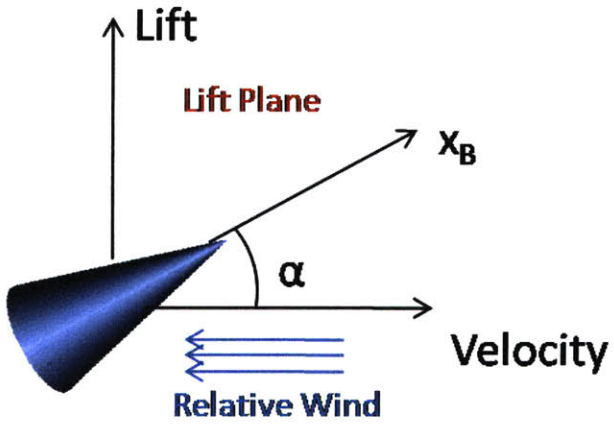

Figure 1-2: Relationship Between Attitude And Lift In The Lift Plane

Notice in Figure 1-2 and 1-3 that the lift can be resolved into a component in the vertical plane, $L\cos\sigma$, and a component in the horizontal plane, $L\sin\sigma$, dependent on the lift bank angle. While the vertical component affects the in-plane motion of the vehicle, it is the horizontal component that creates out of plane motion and turns the vehicle. The vehicle is essentially generating lateral force by allowing the relative wind to push it one way or another, so the vehicle can be thought of as slipping, or skidding, in a direction when it executes a turn. The goal of STT control is to direct the correct amount of horizontal lift using pitch and yaw control that obtains the desired turning while still satisfying the in-plane motion.

In contrast, the *bank-to-turn (BTT)* control approach directs the lift force using lifting surfaces (e.g. wings) that are fixed to the body in a particular orientation. For vehicles using this approach, there is a preferred *body vertical direction* that points perpendicular to the lifting surface and a *body side direction* that points along the lifting surface in a direction perpendicular to the body nose and body vertical. While the STT approach relied on relative wind exerted against the vehicle body to generate aerodynamic force, the BTT approach primarily relies on the lifting surface, which exhibits a much larger reference area and force coefficient than the body. Therefore, the majority of the lift force will be directed perpendicular to the lifting surface and the lift direction may be changed

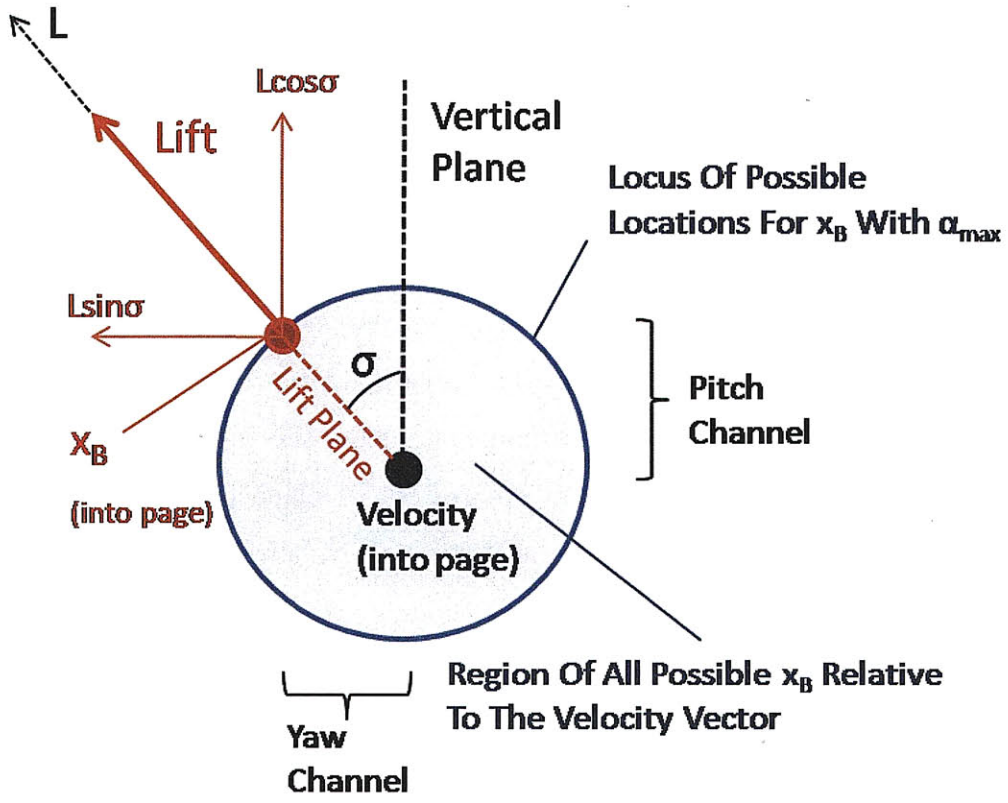

Figure 1-3: Relationship Between Lift And Attitude As Observed By Looking Along The Velocity Vector Direction

by changing the roll attitude of the vehicle. The remaining component of aerodynamic force due to pressure exerted on areas of the vehicle body other than the lifting surfaces is resolved as a sideslip force that acts in the side direction. Thus, the vehicle banks (or rolls) about the roll axis in order to divert the lift force in a desired turning direction.

It is important to note that the definitions of body vertical direction and body side direction are not applicable to the STT vehicle due to symmetry. For BTT vehicles, the *body roll angle*, v, is used to defined the orientation of the body vertical direction relative to the local vertical plane. While lift is often split up into a vertical lift component, $\mathbf{L_V}$, in the body vertical direction and a sideslip force component, $\mathbf{L_S}$, in the body side direction for BTT vehicles, it cannot defined as such for STT vehicles. The only analogous definitions for an STT vehicle are the pitch channel and yaw channel directions. Figure 1-4 illustrates a typical BTT vehicle, as observed from the aft, for comparison to the STT approach. In particular, the difference between the lift bank angle and the body roll angle should be noted. While the lift bank angle describes the direction of the lift vector relative to the vertical, the body roll angle describes the roll attitude of the vehicle body.

Notice that the STT and BTT control methods require different maneuvers to achieve the desired turning. The STT control method must pitch and yaw the nose vector to a desired position before the desired accelerations are obtained while BTT control can simply roll without changing the nose vector to obtain the desired acceleration. However, BTT control strategies suffer from increased complexity due to the coupling of the roll, pitch, and yaw channels [10]. Therefore, a STT control model is used for the symmetric reentry vehicle in this study.

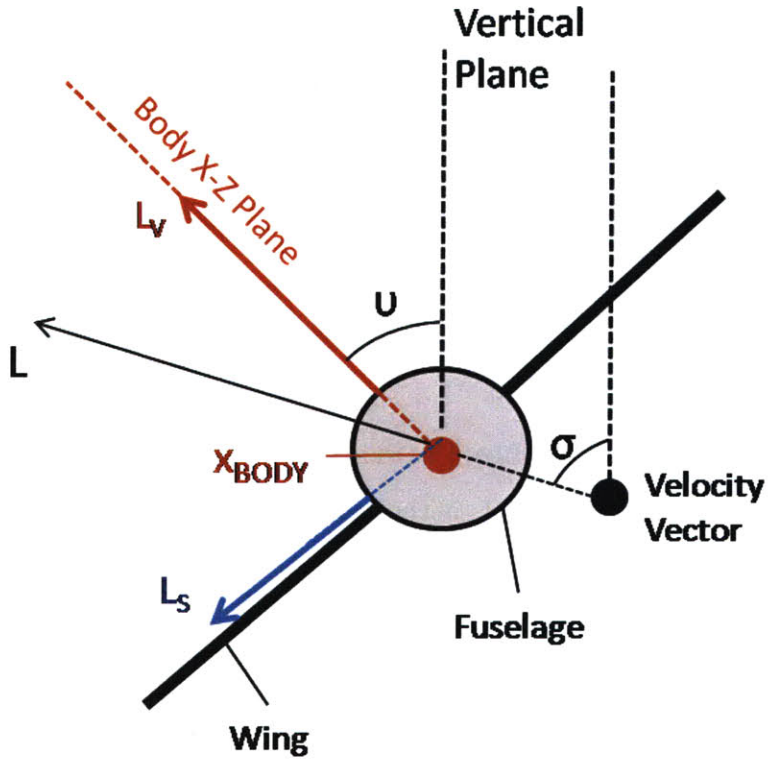

Figure 1-4: Depiction Of A Bank-To-Turn Vehicle, As Seen From Behind The Vehicle Tail

1.3 Mission Planning Considerations

Planning for the new rapid, long range mission requires a completely new set of tools and approaches. The fundamental question for the mission planner to consider is where to aim the launch vehicle such that the reentry vehicle can safely and accurately reach its target while satisfying all necessary flight constraints. The answer to this question is influenced by a variety of complex factors, including environmental perturbations, vehicle dynamics and control authority, mission constraints, flight path constraints, and navigational performance. A clear and concise method for depicting the vehicle capabilities associated with each choice of aimpoint is desired. This thesis will discuss the concept of an *Aimpoint Map*, which represents the locus of all points at the reentry interface that can be reached by the launch vehicle and from which the reentry vehicle can reach the target. The reentry interface is chosen in this problem to occur at an altitude of 400,000 feet, since the atmosphere first begins to have an effect on the vehicle motion below this altitude. The goal of this thesis is to understand the scope of the Aimpoint Map and investigate specific properties of the Aimpoint Map related to the vehicle maneuvering capabilities.

The Aimpoint Map is defined as the collection of latitude (λ) and longitude (μ) points at an altitude of 400,000 feet through which a boost-through-reentry trajectory can be flown that satisfies all terminal and path constraints for both the launch and reentry portions of flight. At each point (μ,λ) in the Aimpoint Map, there exists a collection of velocity magnitude and flight path angle pairs ($V - \gamma$) that can both be obtained from launch and used as valid reentry conditions for maneuvering to the target. Let the space of all such $V-\gamma$ pairs at a given piercepoint in the Aimpoint Map be defined as the *Piercepoint V-γ Map* for the given piercepoint. For all reentry points within the Aimpoint Map, at least one $V-\gamma$ pair must overlap between the launch $V-\gamma$ pairs and the reentry $V-\gamma$ pairs to ensure the validity of a boost-through-reentry trajectory that flied through a particular (μ,λ) point. Some points in the Aimpoint Map may have many more V-γ pairs than other points, suggesting that these points are more robust to uncertainties in the vehicle flight. Furthermore, given a chosen point in the Aimpoint Map and a chosen

$V - \gamma$ pair in the Piercepoint V-γ Map, a footprint of reachable landing locations exists which contains the target of interest. Undurti [1] demonstrated the computation of these footprints for a variety of reentry vehicles in his work. Therefore, the work presented here will focus on demonstration of the Aimpoint Map and the Piercepoint V-γ Map. These concepts are illustrated in Figure 1-5. This goal of this thesis is to demonstrate the properties of such mission planning maps for the new rapid, long range mission.

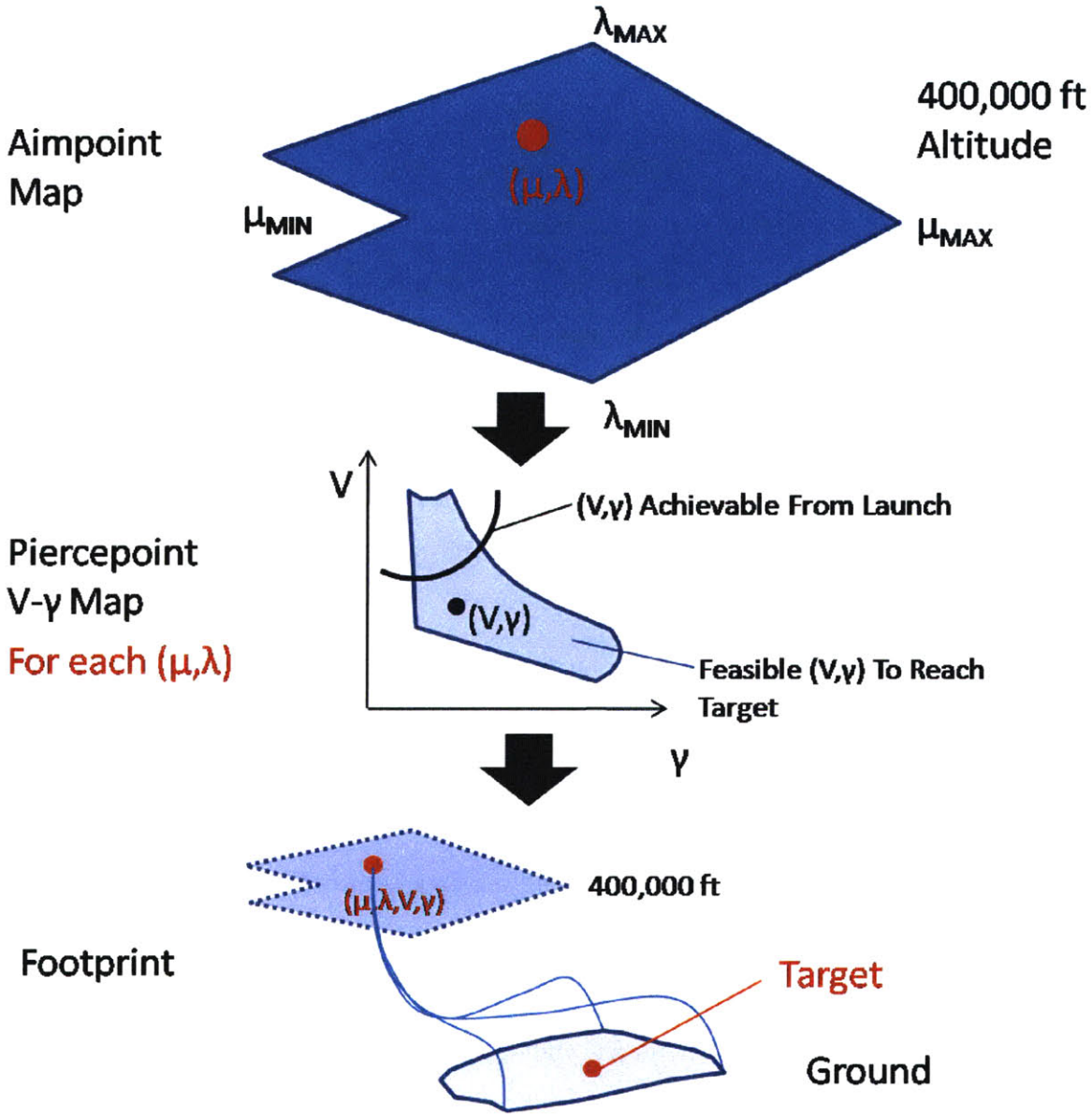

Figure 1-5: Depiction Of Potential Trajectory Planning Concepts For The New Rapid, Long Range Mission

1.4 Trajectory Optimization

Boost-through-reentry trajectory optimization is the primary method used to investigate the complex mission planning concepts described in the previous section. A variety of trajectory optimization tools exist today that exhibit different approaches to the opti-

mization problem. This section will briefly describe the fundamental differences between available approaches and explain which approach is best for solving this problem.

Trajectory optimization describes a variety of methods and approaches for determining a vehicle trajectory that optimizes a chosen performance index subject to a set of dynamic, path, and boundary constraints. It is founded upon the principles of optimal control, in which a set of controls is chosen to influence an evolving system state in some optimal manner. Optimal control problems are particularly challenging optimization problems because they almost always involve constraints in the form of differential equations. These constraints require that the system state evolves according to some fundamental law of motion over time. For the boost-through-reentry maneuvering mission described above, these constraints ensure that the vehicle motion is governed by Newton's Second Law over the entire flight.

The trajectory optimization problem can be approached in many ways. The desired solution is one that is both *optimal* and *feasible*. Optimality asserts that the performance index is at a minimum value while feasibility asserts that all constraints are satisfied. Many different approaches are available for verifying both the optimality and feasibility of an optimal control problem. Two main classifications of approaches to solving optimal control problems exist today: *direct methods* and *indirect methods* [7].

Most complex optimal control problems are solved numerically using nonlinear programming (NLP) principles. Both direct and indirect methods perform iterations of Newton's methods to solve for a finite set of unknowns [7]. The difference between them lies in the particular application of Newton's method. Indirect methods use Newton's method to solve a multipoint boundary value problem (BVP) that is formulated using Pontryagin's Minimum Principle and the Calculus of Variations. Any solution to the BVP will satisfy the first-order optimality conditions, which are the necessary conditions derived from the Calculus of Variations. In contrast, direct methods use Newton's method to iteratively conduct a search for the solution that reduces the performance index at each iteration until a minimum is converged upon [7]. At every Newton iteration, direct methods must compute gradients in an effort to move in a direction that moves closer to the minimum performance index. Thus, indirect methods seek to influence the perfor-

mance index indirectly through a set of derived necessary conditions while direct methods perform iterations that directly influence the performance index at each time step [7].

The fundamental drawback to using indirect methods, as compared to direct methods, is that a new set of necessary conditions must be analytically derived for each new optimization application. This can be difficult and time consuming for complicated dynamical systems, such as the vehicle investigated in this study. In addition, indirect methods typically require better initial guesses than direct methods and have difficulty solving problems with path inequality constraints [7]. However, as mentioned before, solutions to indirect methods are guaranteed to satisfy first-order optimality conditions and do not require any additional check on feasibility and optimality [7], whereas direct methods typically do not provide a method for checking the optimality conditions. Direct methods can also suffer from high computation costs and inaccuracies when analytic gradients are not available. For very complicated optimization problems, such as the problem considered in this study, gradients must be computed numerically using finite difference approximations, representing a source of potential inaccuracies and increased computation time.

Among direct and indirect methods, *shooting methods* and *collocation methods* are the most popular. Direct and indirect variants exist for both shooting and collocation methods. Shooting methods approach the problem by solving an initial value problem within each Newton iteration. Direct shooting propagates the trajectory to an end condition, evaluates the constraints and performance index, and returns these values to the Newton iterator for a search towards the minimum performance index that satisfies all flight constraints. Similarly, indirect shooting propagates the necessary conditions to the end state, evaluates the constraint residuals, and iterates until the BVP is solved. Shooting methods suffer from high sensitivity to small perturbations early in the trajectory. Since these methods iterate over values evaluated at the end of a propagation, small changes early in the propagation can have very large, nonlinear effects at the terminal boundary. Additionally, these methods are only reasonable for problems containing a small number of variables since the finite difference approximations for the gradient are obtained through a numerical integration of the trajectory [7]. If many gradients must be computed and

checked for each Newton iteration, the problem can become very time consuming. Many commercial optimizers, such as POST, utilize the direct shooting approach for a variety of problems while indirect shooting has primarily been used to solve very specialized cases due to sensitivity issues [7].

Collocation methods solve the trajectory optimization problem by discretizing the trajectory into a set of grid points, or nodes [7]. By discretizing the trajectory, collocation methods transform the original trajectory optimization problem into a discrete NLP problem where the variables are the states and controls at each node point. At each node, the trajectory states must be chosen such that they satisfy the differential equations governing the motion of the state, as well as other boundary and path constraints. This approach differs significantly from the shooting method, which numerically integrates an entire trajectory during each Newton iteration. The NLP approach requires no numerical integration. Rather, a series of iterations are performed to choose the trajectory states at the nodes that minimize the performance index. Indirect collocation seeks to satisfy the dynamics of the BVP at each node while direct collocation seeks to satisfy the trajectory dynamics at each node while iterating over the performance index. Both approaches have the disadvantage of solving a NLP problem with a very large number of variables. However, many direct collocation methods are able to increase computational efficiency by exploiting the sparsity of the gradient matrices [7]. Unlike all of the other methods mentioned, direct collocation methods have the distinct advantage of being able to solve problems with path inequalities without needing to define portions of the trajectory where each path constraint is active and inactive a priori [7].

The exact spacing of the nodes has been an active area of research in optimization theory. It is advantageous to choose a spacing for the nodes that allows for the best polynomial approximation of the trajectory states by values evaluated at the node points [12]. Pseudospectral (PS) methods are direct collocation methods that choose the nodes to be located at the Legendre-Gauss-Lobatto (LGL) points, which provide the optimal node spacing for constructing Legendre polynomial approximations [6] [12]. Pseudospectral methods are increasingly popular for numerically solving optimal control problems because they offer an exponential convergence rate for the approximation of analytic functions [19].

For the optimal control problems addressed in this thesis, a direct collocation method using Pseudospectral discretization will be used. This approach is chosen because the problems in this thesis involve a variety of complex path and terminal constraints that cannot be solved easily with other approaches. In addition, a variety of different metrics will be optimized in these problems, which are readily achieved with direct methods using a single formulation, but require many different formulations for indirect methods. Furthermore, the LGL node spacing provides superior convergence properties [19]. DIDO, a MATLAB application for solving smooth and nonsmooth hybrid optimal control problems using Pseudospectral methods, will be used to solve the optimization problems in this thesis [6]. DIDO will numerically solve an optimal control problem involving a dynamic model of the vehicle and a formulation of the flight constraints. These models will be developed in the coming chapters for application to DIDO.

1.5 Thesis Overview

The goal of this thesis is to investigate properties of potential mission planning concepts for the new long-range, high-precision boost-through-reentry mission. Chapter 2 will develop a set of relevant coordinate frames and parameters for describing the complex boost and reentry motion of the vehicle relative to a rotating, spherical Earth. In chapter 3, a six degrees-of-freedom (6DOF) vehicle model will be derived for governing the translational and rotational motion of the vehicle in flight. Chapter 4 will discuss the formulation of the optimal control problem, while chapter 5 and chapter 6 will discuss vehicle models for boost and reentry. Finally, chapter 7 ties together the boost and reentry portions of flight with the computation of a representative Aimpoint Map.

[This page intentionally left blank.]

Chapter 2

Coordinate Frames

This chapter will develop the framework for describing the motion of a manuevering reentry vehicle moving at hypersonic speeds in the Earth's atmosphere. A variety of coordinate frames will be developed to adequately describe the translational and rotational motion of the vehicle including:

- Earth Centered Inertial Coordinate Frame (ECI)
- Earth Centered Earth Fixed Coordinate Frame (ECEF)
- Reference Plane Coordinate Frame (REF)
- Up-Downrange-Crossrange Coordinate Frame (UDC)
- Velocity Coordinate Frame (V)
- Non-Rolling Body Coordinate Frame (B)

The goal of this chapter is to develop a series of coordinate systems that define relevant parameters for position, velocity, and attitude determination and exhibit uniform validity for both endo-atmospheric and exo-atmospheric flight regimes.

2.1 Earth Centered Inertial (ECI) Coordinate Frame

The Earth Centered Inertial Coordinate Frame is an inertial reference frame fixed at the center of the Earth. An Earth centered inertial frame can have many different orientations,

provided that it is fixed to the center of the Earth and non-rotating. A commonly used inertial frame is the J2000 frame, a geocentric inertial coordinate frame that is defined with reference to the Julian Epoch of January 1, 2000. The z-axis, $\hat{\mathbf{z}}_\mathbf{I}$, points along the Earth's rotation axis through the Geographic North Pole, defined as 90 degrees North Latitude. The x-axis, $\hat{\mathbf{x}}_\mathbf{I}$, points in the direction of the Vernal Point, defined as the unit vector pointing from the center of the Earth to the Sun location during the Vernal Equinox (referenced to the Julian Epoch). The third axis, $\hat{\mathbf{y}}_\mathbf{I} = \hat{\mathbf{z}}_\mathbf{I} \times \hat{\mathbf{x}}_\mathbf{I}$, completes the right-handed coordinate system. By definition, the $\hat{\mathbf{x}}_\mathbf{I} - \hat{\mathbf{y}}_\mathbf{I}$ plane is aligned with the Earth's equator, defined as 0 degrees latitude.

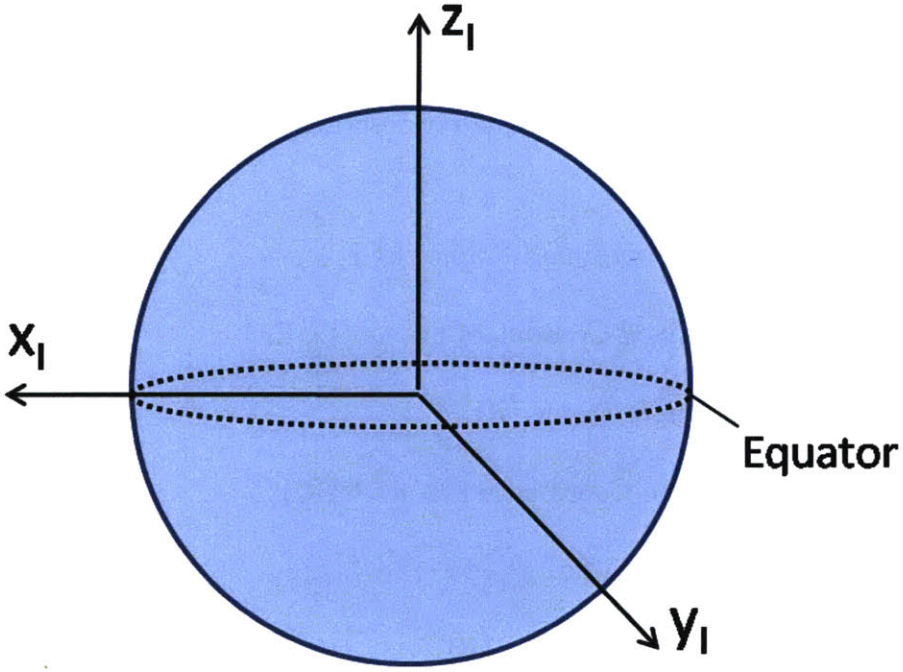

Figure 2-1: Earth Centered Inertial Coordinate Frame

The ECI frame translates with the Earth as it revolves around the Sun, but does not rotate with the Earth. The position and velocity of the vehicle in this frame, therefore, are inertial and are defined relative to a fixed orientation in space. Since the work in this study is concerned with motion relative to the Earth's surface, additional reference frames are required to adequately define Earth-relative motion with continually changing local vertical and local horizontal planes.

2.2 Earth Centered Earth Fixed (ECEF) Coordinate Frame

The Earth Centered Earth Fixed Coordinate Frame is an Earth-fixed rotating frame that is positioned at the center of the Earth and rotates about the Earth's rotation axis. The Earth's rotation axis is assumed to rotate with a constant rotation rate, Ω_E, of 7.292115×10^{-5} radians per second, neglecting precession and nutation effects. The x-axis, $\hat{\mathbf{x}}_\mathbf{E}$, points to 0 degrees latitude, 0 degrees longitude at all times. The z-axis, $\hat{\mathbf{z}}_\mathbf{E}$, is aligned with the Earth's rotation axis and the y-axis, $\hat{\mathbf{y}}_\mathbf{E} = \hat{\mathbf{z}}_\mathbf{E} \times \hat{\mathbf{x}}_\mathbf{E}$, completes the right-handed coordinate system. The $\hat{\mathbf{x}}_\mathbf{E}$ - $\hat{\mathbf{y}}_\mathbf{E}$ plane defines the Earth Equatorial Plane with $\hat{\mathbf{z}}_\mathbf{E}$ pointing perpendicular to the Equator and through the Geographic North Pole.

At any time t, the transformation from the ECI frame to the ECEF frame involves a rotation of $\Omega_E(t - t_I)$, where $\mathbf{t_I}$ is the reference time when the $\hat{\mathbf{x}}_\mathbf{I}$ and $\hat{\mathbf{x}}_\mathbf{E}$ axes were last aligned.

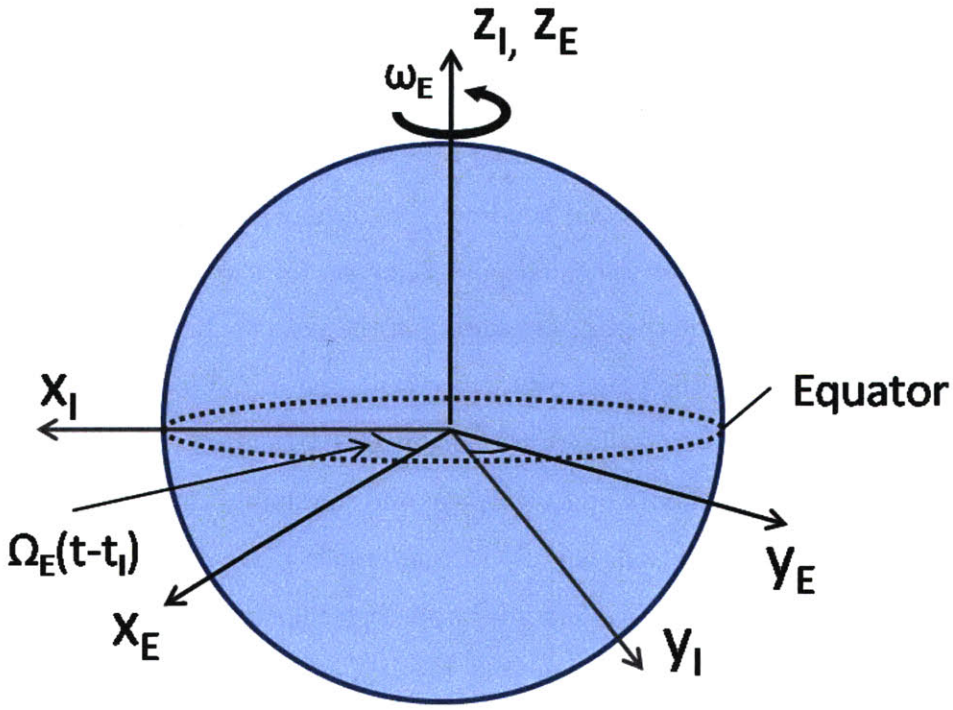

Figure 2-2: Earth Centered Earth Fixed (ECEF) Frame

The transformation matrix from ECI to ECEF is as follows:

$$\mathbf{T}_{\mathbf{I}}^{\mathbf{E}} = \begin{bmatrix} \cos\Omega_E(t-t_I) & \sin\Omega_E(t-t_I) & 0 \\ -\sin\Omega_E(t-t_I) & \cos\Omega_E(t-t_I) & 0 \\ 0 & 0 & 1 \end{bmatrix}$$

The angular velocity vector of the ECEF frame with respect to the ECI frame is

$$\omega_{\mathbf{E-I}} = \Omega_E \hat{\mathbf{z}}_{\mathbf{I}} = \Omega_E \hat{\mathbf{z}}_{\mathbf{E}}$$

2.3 Reference Plane (REF) Coordinate Frame

The Reference Plane Coordinate Frame is an Earth-fixed, rotating frame positioned at the center of the Earth with axes positioned along a chosen plane of reference passing through the center of the Earth. It rotates with the same rotation rate as the ECEF frame, and therefore is observed to be fixed relative to the ECEF frame. The purpose of the Reference Plane Coordinate Frame is to provide a frame that measures vehicle motion relative to a chosen plane of reference. In this frame, the Equator, used as a plane of reference in the ECEF frame, is replaced by a new plane of reference. This plane of reference can be defined by an initial vehicle position and heading or by a plane containing a launch point and a landing point. Ikawa [2] derives equations of motion for a vehicle traveling relative to a plane of reference defined by the initial heading of the vehicle. In this study, the plane of reference will be defined as the plane containing both the initial location and the final destination. The use of such a coordinate frame can be particularly advantageous when when attempting to measure maximum downrange and maximum crossrange capabilities from a plane of interest. In addition, the use of a reference plane can avoid singularities that occur when angular values (e.g. latitude) approach 90 degrees. The new variables defining the vehicle position in this frame will be defined as *relative longitude*, μ, and *relative latitude*, λ, as measured relative to the plane of reference and the initial vehicle location.

The axes are transformed from the ECEF frame such that the x and y axes lie in a

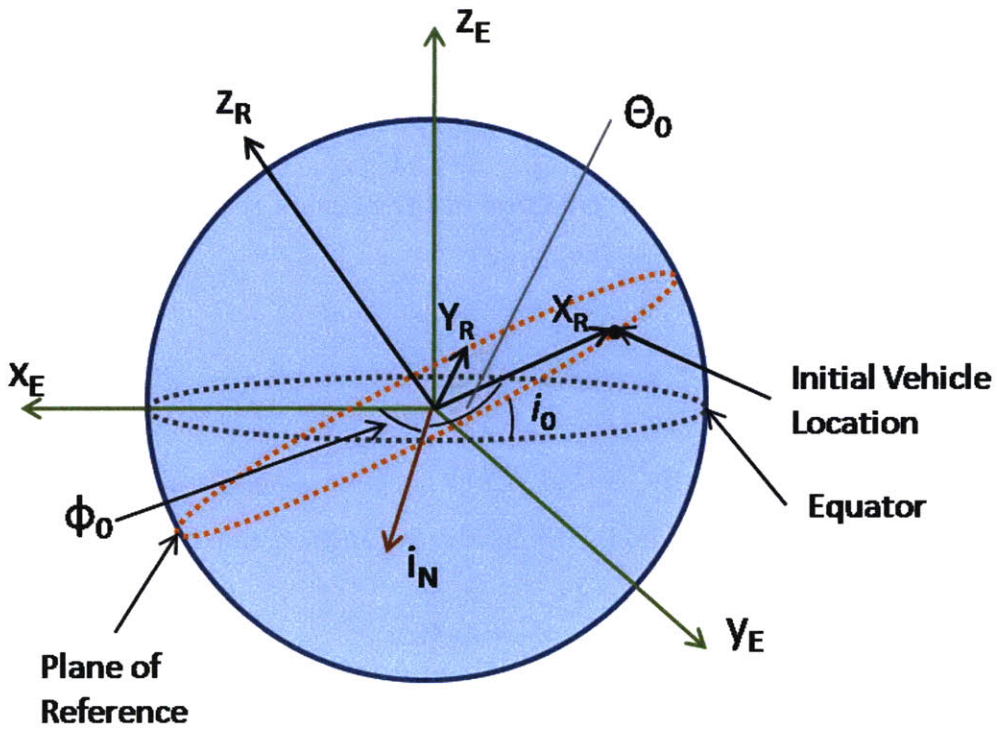

Figure 2-3: Reference (REF) Coordinate Frame

chosen plane of reference and the z axis points perpendicular to this plane. The x-axis, $\hat{\mathbf{x}}_\mathbf{R}$, points towards the initial vehicle position, while the z-axis, $\hat{\mathbf{z}}_\mathbf{R}$, is directed normal to the plane of reference and the y-axis, $\hat{\mathbf{y}}_\mathbf{R} = \hat{\mathbf{z}}_\mathbf{R} \times \hat{\mathbf{x}}_\mathbf{R}$, completes the right-handed coordinate system.

The initial vehicle position and plane of reference can be described in terms of the three angles Φ_0, i_0, and θ_0. The first angle, Φ_0, describes the *nodal point shift* of the plane of reference, defined as the positive angle measured counter-clockwise along the Equator from the $\hat{\mathbf{x}}_\mathbf{E}$ axis to the nodal point of the reference plane, $\hat{\mathbf{i}}_\mathbf{N}$. The unit direction of nodal point is defined as

$$\hat{\mathbf{i}}_\mathbf{N} = \frac{\hat{\mathbf{z}}_\mathbf{E} \times \hat{\mathbf{z}}_\mathbf{R}}{|\hat{\mathbf{z}}_\mathbf{E} \times \hat{\mathbf{z}}_\mathbf{R}|}$$

Φ_0 can then be computed as the angle between $\hat{\mathbf{x}}_\mathbf{E}$ and $\hat{\mathbf{i}}_\mathbf{N}$:

$$\Phi_0 = \cos^{-1} \frac{\hat{\mathbf{i}}_\mathbf{N} \cdot \hat{\mathbf{x}}_\mathbf{E}}{|\hat{\mathbf{i}}_\mathbf{N}||\hat{\mathbf{x}}_\mathbf{E}|}$$

The second angle, i_0, defines the *inclination* of the plane of reference with respect to the Equator. This is defined mathematically as

$$i_0 = \cos^{-1} \frac{\hat{\mathbf{z}}_\mathbf{R} \cdot \hat{\mathbf{z}}_\mathbf{E}}{|\hat{\mathbf{z}}_\mathbf{R}||\hat{\mathbf{z}}_\mathbf{E}|}$$

The third angle, θ_0, defines the *initial vehicle angular position* along the plane of reference as measured from the node, $\hat{\mathbf{i}}_\mathbf{N}$. Similarly, θ_0 can be defined mathematically as:

$$\theta_0 = \cos^{-1} \frac{\hat{\mathbf{i}}_\mathbf{N} \cdot \hat{\mathbf{x}}_\mathbf{R}}{|\hat{\mathbf{i}}_\mathbf{N}||\hat{\mathbf{x}}_\mathbf{R}|}$$

When i_0, θ_0, and Φ_0 are equal to zero, the plane of reference becomes the Equator and μ and λ represent the longitude and latitude location of a point on the Earth. With the use of the REF coordinate frame, the Earth-relative vehicle position can now be expressed relative to any arbitrary reference point and reference plane.

The REF frame can be obtained from the ECEF coordinate frame through a series of three rotations as follows:

1. Rotation about the $\hat{\mathbf{z}}_\mathbf{E}$ axis by Φ_0.

2. Rotation about the $\hat{\mathbf{i}}_\mathbf{N}$ vector by i_0.

3. Rotation about the $\hat{\mathbf{z}}_\mathbf{R}$ axis by θ_0.

Thus, the transformation matrix from ECEF coordinates to REF coordinates is defined as

$$\mathbf{T}_\mathbf{E}^\mathbf{R} = \begin{bmatrix} \cos\theta_0 & \sin\theta_0 & 0 \\ -\sin\theta_0 & \cos\theta_0 & 0 \\ 0 & 0 & 1 \end{bmatrix} \begin{bmatrix} 1 & 0 & 0 \\ 0 & \cos i_0 & \sin i_0 \\ 0 & -\sin i_0 & \cos i_0 \end{bmatrix} \begin{bmatrix} \cos\Omega_0 & \sin\Omega_0 & 0 \\ -\sin\Omega_0 & \cos\Omega_0 & 0 \\ 0 & 0 & 1 \end{bmatrix}$$

$$\mathbf{T}_{\mathbf{E}}^{\mathbf{R}} = \begin{bmatrix} \cos\theta_0 \cos\Omega_0 - \sin\theta_0 \cos i_0 \sin\omega_0 & \cos\theta_0 \sin\omega_0 + \sin\theta_0 \cos i_0 \cos\omega_0 & \sin\theta_0 \sin i_0 \\ -\sin\theta_0 \cos\omega_0 - \cos\theta_0 \cos i_0 \sin\omega_0 & -\sin\theta_0 \sin\omega_0 + \cos\theta_0 \cos i_0 \cos\omega_0 & \cos\theta_0 \sin i_0 \\ \sin i_0 \sin\omega_0 & -\sin i_0 \cos\omega_0 & \cos i_0 \end{bmatrix}$$

The REF frame and the ECEF frame remain fixed relative to one another as the Earth rotates. Thus, the reference frame must rotate in such a way that the relative shift angles between the ECEF and REF frame (Φ_0, i_0, θ_0) remain constant over all time. This requirement will ensure that the plane of reference rotates with the surface of the Earth. Relative to the ECI frame, the REF frame must rotate about all three axes to keep pace with the Earth's rotation. The angular velocity vector of the REF frame relative to the ECI frame is given below in REF coordinates.

$$\omega_{R-I} = \Omega_E \hat{\mathbf{z}}_{\mathbf{E}} = \Omega_E \sin i_0 \sin\theta_0 \hat{\mathbf{x}}_{\mathbf{R}} + \Omega_E \sin i_0 \cos\theta_0 \hat{\mathbf{y}}_{\mathbf{R}} + \Omega_E \cos i_0 \hat{\mathbf{z}}_{\mathbf{R}} \qquad (2.1)$$

2.4 Up-Downrange-Crossrange (UDC) Coordinate Frame

The Up-Downrange-Crossrange Coordinate Frame is used to describe the vehicle's motion relative to a local horizontal and local vertical plane. Since the equations of motion are defined in spherical coordinates, the local horizontal plane will be tangent to a unit sphere at every instant in time and the local vertical plane will be perpendicular to this horizontal plane along a given heading direction. Although an ellipsoidal-Earth model will be introduced in chapter 5 to compute accurate altitude and latitude information relative to an oblate Earth, the coordinate frames and equations of motion will remain defined in spherical coordinates for the entirety of this study.

The UDC frame is positioned at the center of mass of the vehicle with the x-axis, $\hat{\mathbf{x}}_{\mathbf{U}}$, pointing radially outward away from the center of the Earth. The y-axis, $\hat{\mathbf{y}}_{\mathbf{U}}$, and the z-axis, $\hat{\mathbf{z}}_{\mathbf{U}}$, define a local horizontal plane that is normal to the radial direction at each point in time. Within the horizontal plane, $\hat{\mathbf{y}}_{\mathbf{U}}$ defines the downrange direction and $\hat{\mathbf{z}}_{\mathbf{U}}$ defines the crossrange direction with respect to the plane of reference defined in the

previous section.

$$\begin{aligned} \hat{\mathbf{x}}_{\mathbf{U}} &= \frac{\mathbf{r}}{|\mathbf{r}|} \\ \hat{\mathbf{y}}_{\mathbf{U}} &= \frac{\hat{\mathbf{z}}_{\mathbf{R}} \times \hat{\mathbf{x}}_{\mathbf{U}}}{|\hat{\mathbf{z}}_{\mathbf{R}} \times \hat{\mathbf{x}}_{\mathbf{U}}|} \\ \hat{\mathbf{z}}_{\mathbf{U}} &= \hat{\mathbf{x}}_{\mathbf{U}} \times \hat{\mathbf{y}}_{\mathbf{U}} \end{aligned}$$

$\hat{\mathbf{y}}_{\mathbf{U}}$ can be interpreted as the *Reference East* direction and $\hat{\mathbf{z}}_{\mathbf{U}}$ can be interpreted as the *Reference North* direction, as determined by the chosen plane of reference. When i_0 and Φ_0 are equal to zero, the chosen plane of reference is the Equator and the UDC frame reduces to the Up-East-North (UEN) frame in which $\hat{\mathbf{y}}_{\mathbf{U}}$ points East and $\hat{\mathbf{z}}_{\mathbf{U}}$ points North at each moment in time.

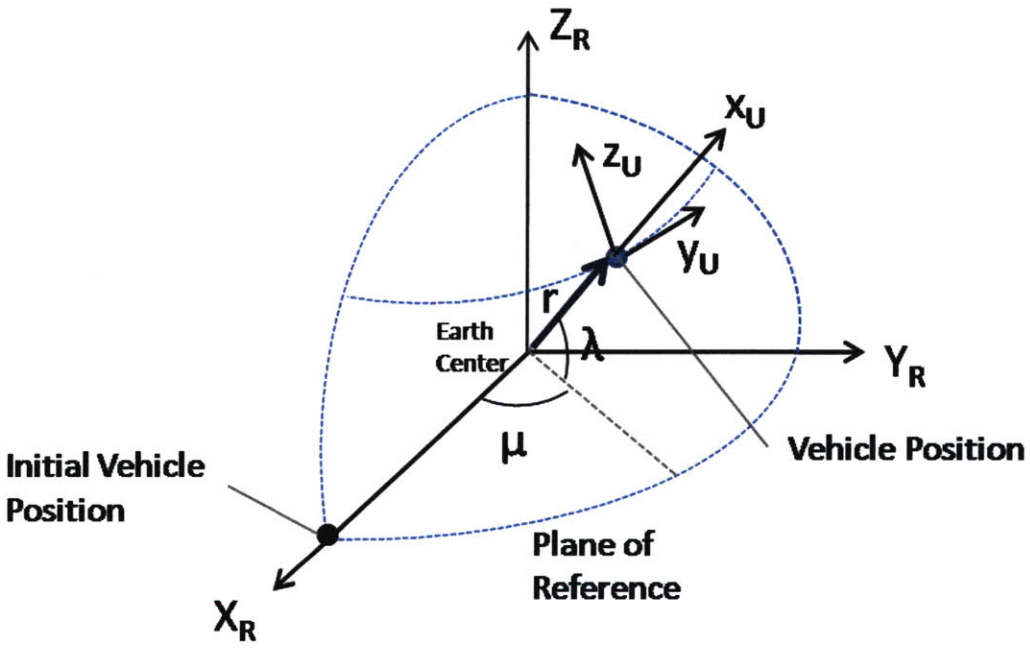

Figure 2-4: Up-Downrange-Crossrange Coordinate Frame

The UDC coordinate frame can be obtained from the REF coordinate frame by two rotations.

1. A rotation about the $\hat{\mathbf{z}}_{\mathbf{R}}$ axis by an angle μ

2. A rotation about the $\hat{\mathbf{y}}_{\mathbf{U}}$ axis by an angle -λ

The angles μ and λ, along with the radial distance r, represent the polar coordinates of the vehicle position in the REF frame. The angle μ represents the *downrange* angular position (relative longitude) of the vehicle along the plane of reference and the angle λ represents the *crossrange* angular position (relative latitude) from the plane of reference. The corresponding rotation matrix for a transformation from REF coordinates to UDC coordinates is given by

$$\mathbf{T}_{\mathbf{R}}^{\mathbf{U}} = \begin{bmatrix} \cos\lambda & 0 & \sin\lambda \\ 0 & 1 & 0 \\ -\sin\lambda & 0 & \cos\lambda \end{bmatrix} \begin{bmatrix} \cos\mu & \sin\mu & 0 \\ -\sin\mu & \cos\mu & 0 \\ 0 & 0 & 1 \end{bmatrix}$$

$$\mathbf{T}_{\mathbf{R}}^{\mathbf{U}} = \begin{bmatrix} \cos\lambda\cos\mu & \cos\lambda\sin\mu & \sin\lambda \\ -\sin\mu & \cos\mu & 0 \\ -\sin\lambda\cos\mu & -\sin\lambda\sin\mu & \cos\lambda \end{bmatrix}$$

The UDC frame must rotate as μ and λ vary in order to keep the $\hat{\mathbf{y}}_{\mathbf{U}}$ and $\hat{\mathbf{z}}_{\mathbf{U}}$ axes in the instantaneous local horizontal frame and $\hat{\mathbf{x}}_{\mathbf{U}}$ in the instantaneous vertical direction at each instant in time. The angular velocity vector of the UDC frame relative to the REF frame can be expressed as

$$\omega_{U-R} = \dot{\mu}\hat{\mathbf{z}}_{\mathbf{R}} - \dot{\lambda}\hat{\mathbf{y}}_{\mathbf{U}} = \dot{\lambda}\sin\mu\hat{\mathbf{x}}_{\mathbf{R}} - \dot{\lambda}\cos\mu\hat{\mathbf{y}}_{\mathbf{R}} + \dot{\mu}\hat{\mathbf{z}}_{\mathbf{R}} \tag{2.2}$$

2.5 Velocity (V) Coordinate Frame

The Velocity Coordinate Frame is a non-inertial frame positioned at the center of mass of the vehicle that follows the motion of the Earth-relative velocity vector, $\overrightarrow{\mathbf{V}_{\mathbf{E}}}$, over time. The x-axis, $\hat{\mathbf{x}}_{\mathbf{V}}$, is directed along the velocity vector while the y-axis, $\hat{\mathbf{y}}_{\mathbf{V}}$, points in the direction perpendicular to both the $\overrightarrow{\mathbf{r}}$ and $\overrightarrow{\mathbf{V}_{\mathbf{E}}}$ vectors. The z-axis, $\hat{\mathbf{z}}_{\mathbf{V}}$, completes the right-handed coordinate system and lies in a vertical plane, along with $\hat{\mathbf{x}}_{\mathbf{V}}$, that passes through the center of the Earth.

$$
\begin{aligned}
\mathbf{x_V} &= \frac{\mathbf{V_E}}{|V_E|} \\
\mathbf{y_V} &= \frac{\mathbf{x_U} \times \mathbf{x_V}}{|\mathbf{x_U} \times \mathbf{x_V}|} \\
\mathbf{z_V} &= \mathbf{x_V} \times \mathbf{y_V}
\end{aligned}
$$

Figure 2-5 depicts the orientation of the V frame axes relative to the UDC frame axes. Notice that the $\hat{\mathbf{y}}_\mathbf{V}$ axis lies in the local horizontal plane, an angle ψ away from the $\hat{\mathbf{z}}_\mathbf{U}$ axis, while the $\hat{\mathbf{z}}_\mathbf{V}$ axis lies in a local vertical plane, an angle γ away from $\hat{\mathbf{x}}_\mathbf{U}$ and 90 degrees away from $\hat{\mathbf{x}}_\mathbf{V}$. The local vertical and horizontal planes are illustrated in Figure 2-6.

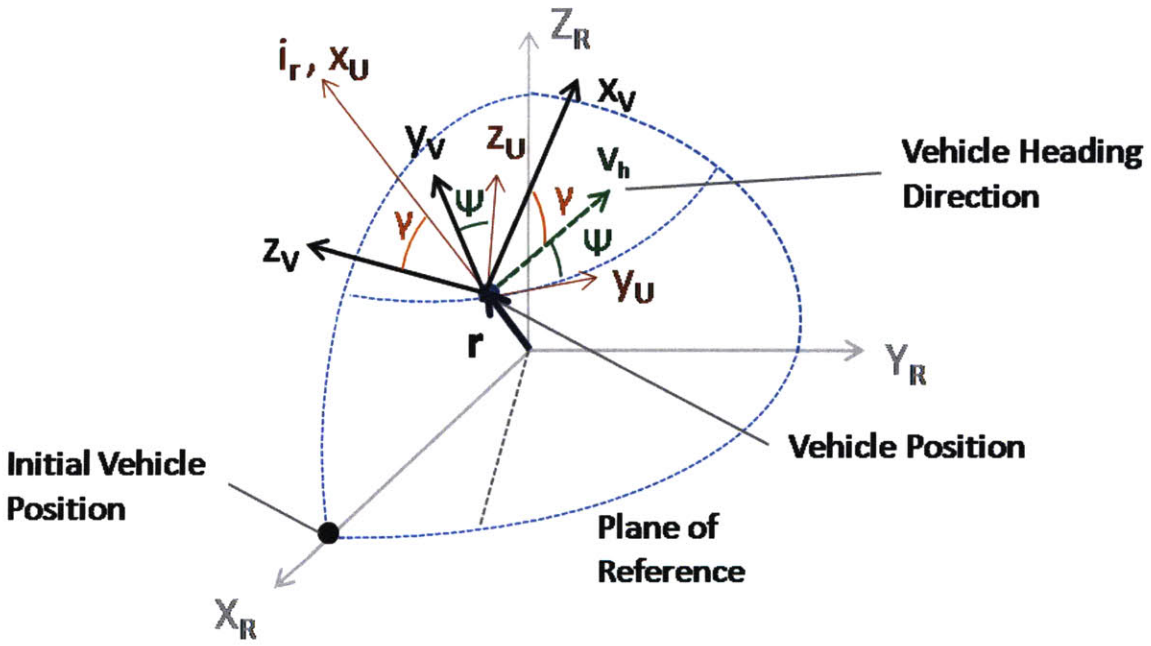

Figure 2-5: Velocity Frame

The velocity frame is obtained from the UDC frame by a series of four rotations.

1. A rotation about the $\hat{\mathbf{y}}_\mathbf{U}$ axis by $\frac{\pi}{2}$

2. A rotation about the radial direction, $\hat{\mathbf{i}}_\mathbf{r}$, by $\frac{\pi}{2}$

3. A rotation about the radial direction, $\hat{\mathbf{i}}_\mathbf{r}$, by angle ψ

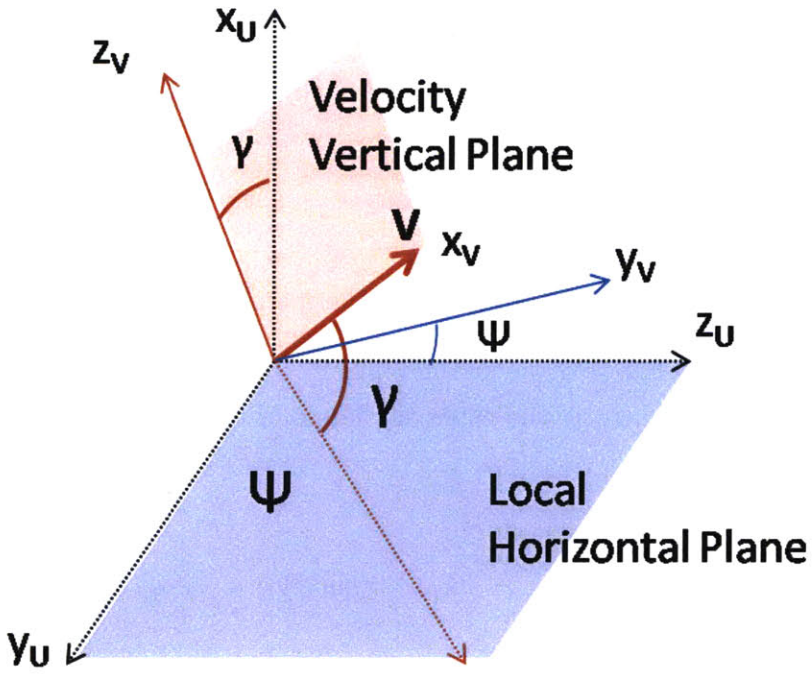

Figure 2-6: Representation of Velocity Vertical Frame and Local Horizontal Frame

4. A rotation about the $\hat{\mathbf{y}}_\mathbf{V}$ axis by angle -γ

The first two rotations serve to simply switch the axes so that the z-axis points up, the x-axis points downrange, and the y-axis points crossrange. The first angle of rotation, ψ, is the *velocity heading angle* that defines the horizontal velocity direction, V_h, measured positive counter-clockwise from the Relative East, $\hat{\mathbf{y}}_\mathbf{U}$. This angle lies in the $\hat{\mathbf{y}}_\mathbf{U}$ - $\hat{\mathbf{z}}_\mathbf{U}$ plane and defines the vehicle heading direction at each instant in time. The second angle of rotation, γ, is the *flight path angle* that defines the $\overrightarrow{\mathbf{V_E}}$ inclination with respect to the local horizontal plane. This angle is measured as a positive rotation about the -$\hat{\mathbf{y}}_\mathbf{V}$ axis. With this definition, γ is measured positive when $\overrightarrow{\mathbf{V_E}}$ is above the local horizontal plane and negative when it is below the local horizontal plane.

The transformation matrix from the UDC frame to the V frame can be expressed as

$$\mathbf{T}_\mathbf{U}^\mathbf{V} = \begin{bmatrix} \cos\gamma & 0 & \sin\gamma \\ 0 & 1 & 0 \\ -\sin\gamma & 0 & \cos\gamma \end{bmatrix} \begin{bmatrix} \cos\psi & \sin\psi & 0 \\ -\sin\psi & \cos\psi & 0 \\ 0 & 0 & 1 \end{bmatrix} \begin{bmatrix} \cos\frac{\pi}{2} & \sin\frac{\pi}{2} & 0 \\ -\sin\frac{\pi}{2} & \cos\frac{\pi}{2} & 0 \\ 0 & 0 & 1 \end{bmatrix} \begin{bmatrix} \cos\frac{\pi}{2} & 0 & -\sin\frac{\pi}{2} \\ 0 & 1 & 0 \\ \sin\frac{\pi}{2} & 0 & \cos\frac{\pi}{2} \end{bmatrix}$$

$$\mathbf{T}^{\mathbf{V}}_{\mathbf{UDC}} = \begin{bmatrix} \sin\gamma & \cos\gamma\cos\psi & \cos\gamma\sin\psi \\ 0 & -\sin\psi & \cos\psi \\ \cos\gamma & -\sin\gamma\cos\psi & -\sin\gamma\sin\psi \end{bmatrix}$$

The rotation of the velocity frame must align the instantaneous $\hat{\mathbf{x}}_{\mathbf{V}}$ axis with the $\overrightarrow{\mathbf{V_E}}$ vector at each instant in time. Thus, the rotation of the velocity frame with respect to the UDC frame will be governed by the rates of change of the velocity unit vector, $\dot{\gamma}$ and $\dot{\psi}$.

$$\omega_{V-U} = \dot{\psi}\hat{\mathbf{x}}_{\mathbf{U}} - \dot{\gamma}\hat{\mathbf{y}}_{\mathbf{V}} = \dot{\psi}\hat{\mathbf{x}}_{\mathbf{U}} + \dot{\gamma}\sin\psi\hat{\mathbf{y}}_{\mathbf{U}} - \dot{\gamma}\cos\psi\hat{\mathbf{z}}_{\mathbf{U}}$$

2.6 Non-Rolling Body (B) Coordinate Frame

The Non-Rolling Body Coordinate Frame is a non-inertial frame that is positioned at the center of mass of the vehicle with the x-axis, $\hat{\mathbf{x}}_{\mathbf{B}}$, fixed to the body nose. The purpose of the body frame is to define the nose attitude of the vehicle at each point in time. The x-axis, $\hat{\mathbf{x}}_{\mathbf{B}}$, points along the nose of the vehicle, while the y-axis, $\hat{\mathbf{y}}_{\mathbf{B}}$, and the z-axis, $\hat{\mathbf{z}}_{\mathbf{B}}$, lie perpendicular to $\hat{\mathbf{x}}_{\mathbf{B}}$. Figure 2-7 illustrates the orientation of these axes relative to the V frame axes.

Typically in reentry analysis, a body-fixed coordinate frame is used in which all three axes are fixed to the vehicle body. As mentioned in Section 1.2, the vehicle considered in this study uses a skid-to-turn (STT) control approach in which the roll orientation of the vehicle has negligible effect on its manuevering capabilities [10]. Therefore, the particular orientation of the $\hat{\mathbf{y}}_{\mathbf{B}}$ and $\hat{\mathbf{z}}_{\mathbf{B}}$ axes at any instant in time is inconsequential to the determination of the vehicle trajectory. The axes $\hat{\mathbf{y}}_{\mathbf{B}}$ and $\hat{\mathbf{z}}_{\mathbf{B}}$ can be aligned in any direction such that they are both perpendicular to $\hat{\mathbf{x}}_{\mathbf{B}}$ and to each other. In contrast, for bank-to-turn (BTT) vehicles, the $\hat{\mathbf{y}}_{\mathbf{B}}$ and $\hat{\mathbf{z}}_{\mathbf{B}}$ axes define the body side and body vertical directions, respectively, and must rotate about the $\hat{\mathbf{x}}_{\mathbf{B}}$ axis as the vehicle rolls. For the formulation presented here, $\hat{\mathbf{y}}_{\mathbf{B}}$ and $\hat{\mathbf{z}}_{\mathbf{B}}$ axes are not required to roll with the vehicle body.

The $\hat{\mathbf{y}}_\mathbf{B}$ and $\hat{\mathbf{z}}_\mathbf{B}$ axes are defined such that the transformation between the V frame and the B frame can be expressed as a yaw about the $\hat{\mathbf{z}}_\mathbf{V}$ axis followed by a pitch about the $\hat{\mathbf{y}}'_\mathbf{V} = \hat{\mathbf{y}}_\mathbf{B}$ axis.

Thus, the vehicle body attitude, $\hat{\mathbf{x}}_\mathbf{B}$, can be defined relative to the V frame by

1. A yaw about the $\hat{\mathbf{z}}_\mathbf{V}$ axis by angle ϕ

2. A pitch about the $\hat{\mathbf{y}}_\mathbf{B}$ axis by angle -θ

The ϕ and θ angles mentioned above represent the position of the $\hat{\mathbf{x}}_\mathbf{B}$ axis relative to $\overrightarrow{\mathbf{V}_\mathbf{E}}$. Let ϕ be defined as the *nose yaw angle* and θ as the *nose pitch angle* defined *relative to* the velocity vector.

The transformation matrix from V frame coordinates and B frame coordinates is defined as

$$\mathbf{T}_\mathbf{V}^\mathbf{B} = \begin{bmatrix} \cos\theta & 0 & \sin\theta \\ 0 & 1 & 0 \\ -\sin\theta & 0 & \cos\theta \end{bmatrix} \begin{bmatrix} \cos\phi & \sin\phi & 0 \\ -\sin\phi & \cos\phi & 0 \\ 0 & 0 & 1 \end{bmatrix}$$

$$\mathbf{T}_\mathbf{V}^\mathbf{B} = \begin{bmatrix} \cos\theta\cos\phi & \cos\theta\sin\phi & \sin\theta \\ -\sin\phi & \cos\phi & 0 \\ -\sin\theta\cos\phi & -\sin\theta\sin\phi & \cos\theta \end{bmatrix}$$

The $\hat{\mathbf{y}}_\mathbf{B}$ axis will lie in the $\hat{\mathbf{x}}_\mathbf{V}$ - $\hat{\mathbf{y}}_\mathbf{V}$ plane, directed at an angle ϕ counter-clockwise from $\hat{\mathbf{y}}_\mathbf{V}$. Likewise, the $\hat{\mathbf{z}}_\mathbf{B}$ axis will lie in the $\hat{\mathbf{x}}_\mathbf{B}$ - $\hat{\mathbf{z}}_\mathbf{V}$ plane, directed at an angle θ counter-clockwise from $\hat{\mathbf{z}}_\mathbf{V}$.

The rotation of the B frame relative to the V frame will depend on the attitude dynamics of the vehicle. Since the relative attitude is defined here in terms of ϕ and θ, the relative rotation will depend on $\dot{\phi}$ and $\dot{\theta}$.

$$\omega_{B-V} = \dot{\phi}\hat{\mathbf{z}}_\mathbf{V} - \dot{\theta}\hat{\mathbf{y}}_\mathbf{B} = \dot{\theta}\sin\phi\hat{\mathbf{x}}_\mathbf{V} - \dot{\theta}\cos\phi\hat{\mathbf{y}}_\mathbf{V} + \dot{\phi}\hat{\mathbf{z}}_\mathbf{V} \tag{2.3}$$

2.6.1 Aerodynamic Angles

In addition to defining attitude angles, ϕ and θ, it is important to define the aerodynamic angles α and σ. α is defined as the *angle of attack* and represents the angle between the vehicle nose attitude, $\hat{\mathbf{x}}_\mathbf{B}$, and the vehicle velocity, $\hat{\mathbf{x}}_\mathbf{V}$. This can be respresented mathematically as

$$\cos\alpha = \hat{\mathbf{x}}_\mathbf{B} \cdot \hat{\mathbf{x}}_\mathbf{V} \tag{2.4}$$

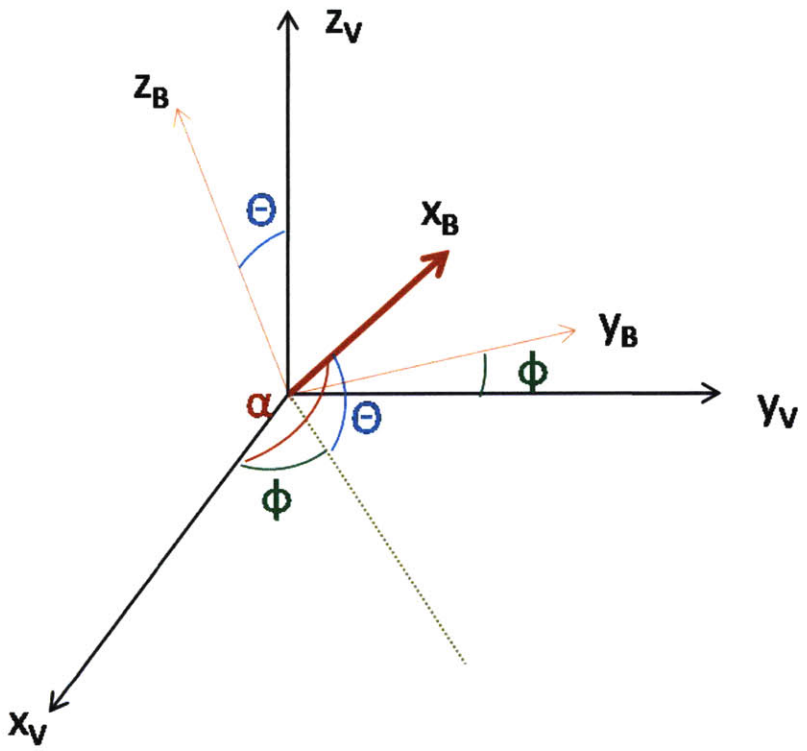

Figure 2-7: Body Coordinate Frame

Figure 2-7 illustrates the relationships between the angles ϕ, θ, and α. The angles θ and ϕ are intermediate angles measured along perpendicular planes that define the body attitude relative to the velocity vector, while the angle α is a direct angle between $\hat{\mathbf{x}}_\mathbf{V}$ and $\hat{\mathbf{x}}_\mathbf{B}$ measured in the plane defined by $\hat{\mathbf{x}}_\mathbf{V}$ and $\hat{\mathbf{x}}_\mathbf{B}$.

The expression for $\hat{\mathbf{x}}_\mathbf{B}$ in the velocity coordinate system, $(\hat{\mathbf{x}}_\mathbf{B})_V$, can be computed using the transformation matrix, $\mathbf{T}_\mathbf{V}^\mathbf{B}$.

$$(\hat{\mathbf{x}}_\mathbf{B})_V = \mathbf{T}_\mathbf{B}^\mathbf{V}\hat{\mathbf{x}}_\mathbf{B} = \mathbf{T}_\mathbf{V}^{\mathbf{B^T}}\hat{\mathbf{x}}_\mathbf{B} = \cos\theta\cos\phi\hat{\mathbf{x}}_\mathbf{V} + \cos\theta\sin\phi\hat{\mathbf{y}}_\mathbf{V} + \sin\theta\hat{\mathbf{z}}_\mathbf{V} \tag{2.5}$$

Therefore, by substituting 2.5 into 2.4, an expression for the angle of attack in terms of the nose yaw and nose pitch angles can be obtained.

$$\cos\alpha = \cos\theta\cos\phi \tag{2.6}$$

By using a trigonometric identity, the sine of α can also be expressed.

$$\sin\alpha = \sqrt{1-\cos^2\alpha} = \sqrt{1-\cos^2\theta\cos^2\phi} \tag{2.7}$$

σ is defined as the *lift bank angle*, which describes the direction of the lift vector relative to the velocity vertical plane, illustrated in Figure 2-8. Since the vehicle considered in this study uses a skid-to-steer control approach, the lift vector will always lie in the $\hat{\mathbf{x}}_\mathbf{V}$ - $\hat{\mathbf{x}}_\mathbf{B}$ plane, the plane that the vehicle attitude makes with the velocity vector. The angle between this plane and the velocity vertical plane is defined as σ. Thus, the orientation of the vehicle relative to the velocity vector defines σ.

The *velocity vertical plane* is defined by the normal vector

$$\hat{\mathbf{n}}_\mathbf{V} = \frac{\hat{\mathbf{x}}_\mathbf{V}\times\hat{\mathbf{z}}_\mathbf{V}}{|\hat{\mathbf{x}}_\mathbf{V}\times\hat{\mathbf{z}}_\mathbf{V}|} = -\hat{\mathbf{y}}_\mathbf{V}$$

Likewise, the *lift plane* is defined as the plane which contains both $\hat{\mathbf{x}}_\mathbf{V}$ and $\hat{\mathbf{x}}_\mathbf{B}$ with normal vector

$$\hat{\mathbf{n}}_\mathbf{L} = \frac{\hat{\mathbf{x}}_\mathbf{V}\times\hat{\mathbf{x}}_\mathbf{B}}{|\hat{\mathbf{x}}_\mathbf{V}\times\hat{\mathbf{x}}_\mathbf{B}|} \tag{2.8}$$

Therefore, using 2.5 with 2.8, the normal vector to the lift plane can be expressed in the velocity coordinate frame.

$$\hat{\mathbf{n}}_\mathbf{L} = \frac{-\sin\theta\hat{\mathbf{y}}_\mathbf{V} + \cos\theta\sin\phi\hat{\mathbf{z}}_\mathbf{V}}{\sqrt{\sin^2\theta+\cos^2\theta\sin^2\phi}} \tag{2.9}$$

σ is then defined as the angle between the lift plane normal vector, $\hat{\mathbf{n}}_\mathbf{L}$ and the vertical

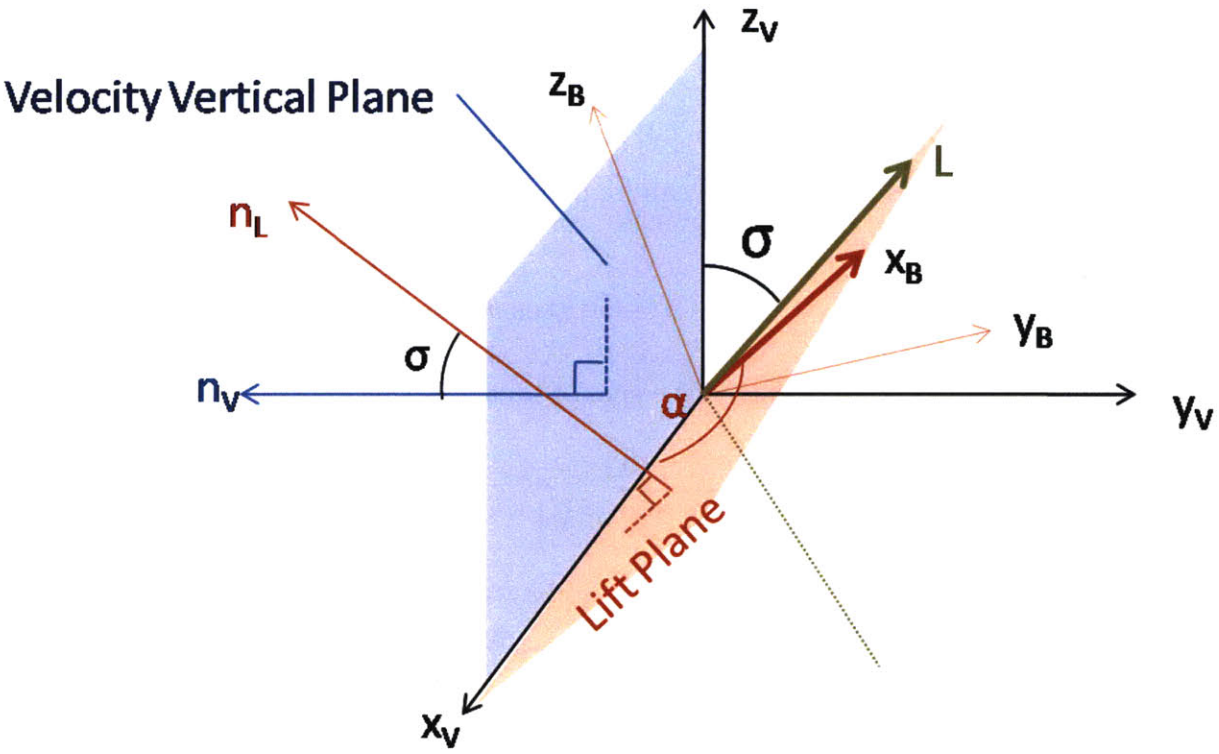

Figure 2-8: Relationship Between Sigma and Alpha

velocity plane normal vector, $\hat{\mathbf{n}}_\mathbf{V}$.

$$\cos\sigma = \hat{\mathbf{n}}_\mathbf{L} \cdot \hat{\mathbf{n}}_\mathbf{V} = \hat{\mathbf{n}}_\mathbf{L} \cdot -\hat{\mathbf{y}}_\mathbf{V} = \frac{\sin\theta}{\sqrt{\sin^2\theta + \cos^2\theta \sin^2\phi}} \tag{2.10}$$

Furthermore, Equation 2.7 can be related to 2.10 through a series of trigonometric substitutions. First, $\cos^2\phi$ can be replaced by the identity $1 - \sin^2\phi$.

$$\sin\alpha = \sqrt{1 - \cos^2\theta\left(1 - \sin^2\phi\right)} = \sqrt{1 - \cos^2\theta + \cos^2\theta\sin^2\phi} \tag{2.11}$$

Next, the $1 - \cos^2\theta$ term can be replaced by $\sin^2\theta$.

$$\sin\alpha = \sqrt{\sin^2\theta + \cos^2\theta\sin^2\phi} \tag{2.12}$$

By comparing 2.12 with 2.10, it can be seen that $\sin\alpha$ is equivalent to the denominator of $\cos\sigma$.

$$\cos\sigma = \frac{\sin\theta}{\sin\alpha} \tag{2.13}$$

Furthermore, by examining Equation 2.5, it can be observed that $\sin\alpha$ is equivalent to the component of $\hat{\mathbf{x}}_\mathbf{B}$ projected onto the $\hat{\mathbf{y}}_\mathbf{V}$ - $\hat{\mathbf{z}}_\mathbf{V}$ plane. This component of the $\hat{\mathbf{x}}_\mathbf{B}$ unit vector lies along the line where the lift plane intersects the $\hat{\mathbf{y}}_\mathbf{V}$ - $\hat{\mathbf{z}}_\mathbf{V}$ plane, equivalent to the lift vector direction. Similarly, $\cos\alpha$ is the component of $\hat{\mathbf{x}}_\mathbf{B}$ projected along the $\hat{\mathbf{x}}_\mathbf{V}$ axis, equivalent to the velocity vector direction. This relationship is illustrated in Figure 2-9.

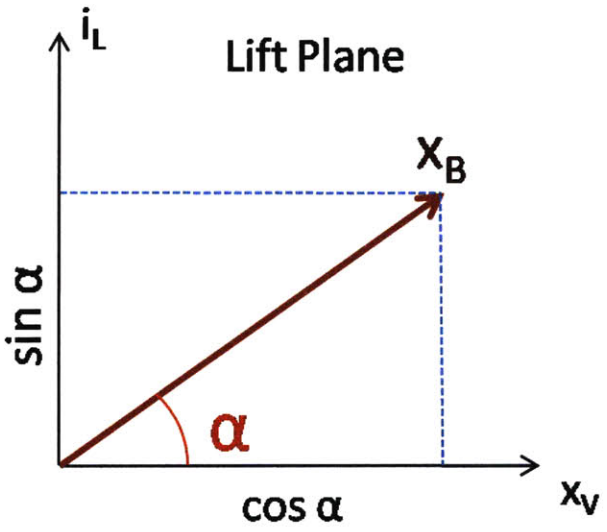

Figure 2-9: Illustration Of The Lift Plane

Thus, the lift unit vector, $\hat{\mathbf{i}}_\mathbf{L}$, can be described as the normalized component of $\hat{\mathbf{x}}_\mathbf{B}$ in the $\hat{\mathbf{y}}_\mathbf{V}$ - $\hat{\mathbf{z}}_\mathbf{V}$ plane.

$$\hat{\mathbf{i}}_\mathbf{L} = \frac{\cos\theta\sin\phi\hat{\mathbf{y}}_\mathbf{V} + \sin\theta\hat{\mathbf{z}}_\mathbf{V}}{\sin\alpha} \tag{2.14}$$

The relationship between $\hat{\mathbf{i}}_\mathbf{L}$ and σ is shown in Figure 2-10. Notice that since the lift vector is defined as perpendicular to the velocity vector, it will always lie in the $\hat{\mathbf{y}}_\mathbf{V}$ - $\hat{\mathbf{z}}_\mathbf{V}$ plane and σ will be the angle between $\hat{\mathbf{z}}_\mathbf{V}$ and $\hat{\mathbf{i}}_\mathbf{L}$.

Thus, from Equation 2.14 additional trigonometric properties of σ can be derived.

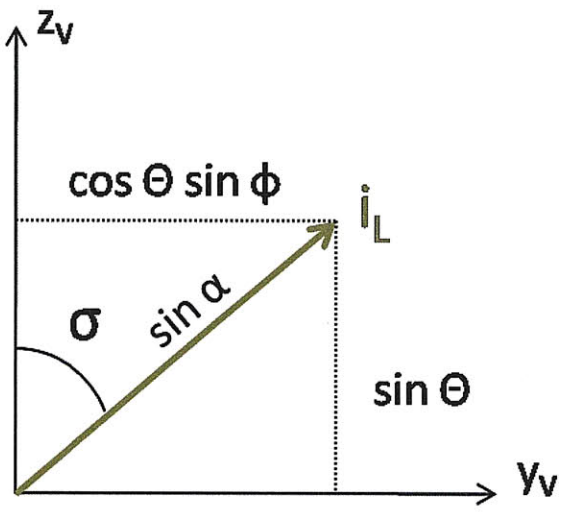

Figure 2-10: Relationship Between Sigma And The Lift Vector

$$\sin\sigma = \frac{\cos\theta\sin\phi}{\sin\alpha} \tag{2.15}$$

$$\tan\sigma = \frac{\cos\theta\sin\phi}{\sin\theta} \tag{2.16}$$

Finally, the rotation rate of the body frame with respect to the velocity frame can be expressed in terms of the aerodynamic angles. The rotation of the body frame is affected by the rate of change of α as well as the rate of change of σ. $\dot{\alpha}$ changes the orientation of $\hat{\mathbf{x}}_\mathbf{B}$ within the lift plane, while $\dot{\sigma}$ changes the orientation of the lift plane with respect to the velocity vertical plane.

$$\omega_{B-V} = \dot{\alpha}\hat{\mathbf{n}}_\mathbf{L} - \dot{\sigma}\hat{\mathbf{x}}_\mathbf{V} \tag{2.17}$$

By substituting Equation 2.12 into Equation 2.9, $\hat{\mathbf{n}}_\mathbf{L}$ can be expressed as

$$\hat{\mathbf{n}}_\mathbf{L} = \frac{-\sin\theta\hat{\mathbf{y}}_\mathbf{V} + \cos\theta\sin\phi\hat{\mathbf{z}}_\mathbf{V}}{\sin\alpha} \tag{2.18}$$

Futhermore, from Equation 2.10 and Equation 2.15, the following relationships can be substituted into Equation 2.18.

$$\begin{aligned} \sin\theta &= \cos\sigma\sin\alpha \\ \cos\theta\sin\phi &= \sin\sigma\sin\alpha \end{aligned}$$

Thus, by substituting the above identities into Equation 2.18, $\hat{\mathbf{n}}_{\mathbf{L}}$ can be expressed entirely in terms of the aerodynamic angles, α and σ.

$$\hat{\mathbf{n}}_{\mathbf{L}} = \frac{-\cos\sigma\sin\alpha\hat{\mathbf{y}}_{\mathbf{V}} + \sin\sigma\sin\alpha\hat{\mathbf{z}}_{\mathbf{V}}}{\sin\alpha} \tag{2.19}$$

This can then be substituted into Equation 2.17 to obtain the angular velocity vector of the body frame with respect to the velocity frame in terms of the aerodynamic angles. This is equivalent to Equation 2.3, now expressed in terms of the aerodynamic angles and their rates.

$$\omega_{\mathbf{B-V}} = -\dot{\sigma}\hat{\mathbf{x}}_{\mathbf{V}} - \dot{\alpha}\cos\sigma\hat{\mathbf{y}}_{\mathbf{V}} + \dot{\alpha}\sin\sigma\hat{\mathbf{z}}_{\mathbf{V}}$$

2.7 Summary

In this chapter, a set of coordinate frames have been defined for position, velocity, and attitude. The ECEF coordinate frame provides a convenient reference for determining the vehicle position relative to the rotating Earth. Furthermore, the REF coordinate frame provides the capability for position determination relative to a plane of reference other than the Equator. This formulation will allow simple determination of downrange, crossrange, and radial movement relative to the chosen reference frame. The position vector of the vehicle over time can be expressed in the REF frame in terms of the angles defined above and the *radial distance* from the center of the Earth, r.

$$(\overrightarrow{\mathbf{r}})_R = r\hat{\mathbf{x}}_{\mathbf{U}} = r\cos\lambda\cos\mu\hat{\mathbf{x}}_{\mathbf{R}} + r\cos\lambda\sin\mu\hat{\mathbf{y}}_{\mathbf{R}} + r\sin\lambda\hat{\mathbf{z}}_{\mathbf{R}} \tag{2.20}$$

The UDC coordinate frame provides convenient local vertical and local horizontal reference planes that can readily define the Earth-relative velocity vector, $\overrightarrow{\mathbf{V_E}}$, through

use of a heading angle, ψ, and a flight path angle, γ.

$$\left(\overrightarrow{\mathbf{V_E}}\right)_U = V_E\hat{\mathbf{x}}_\mathbf{V} = V_E \sin\gamma\hat{\mathbf{x}}_\mathbf{U} + V_E \cos\gamma\cos\psi\hat{\mathbf{y}}_\mathbf{U} + V_E \cos\gamma\sin\psi\hat{\mathbf{z}}_\mathbf{U} \tag{2.21}$$

Finally, the Velocity Coordinate Frame provides a reference for determination of the vehicle attitude either in terms of the nose pitch and yaw angles, θ and ϕ, or the aerodynamic angles, α and σ, all defined relative to $\overrightarrow{\mathbf{V_E}}$.

$$\begin{aligned}(\hat{\mathbf{x}}_\mathbf{B})_V &= \cos\theta\cos\phi\hat{\mathbf{x}}_\mathbf{V} + \cos\theta\sin\phi\hat{\mathbf{y}}_\mathbf{V} + \sin\theta\hat{\mathbf{z}}_\mathbf{V} \\ (\hat{\mathbf{x}}_\mathbf{B})_V &= \cos\alpha\hat{\mathbf{x}}_\mathbf{V} + \sin\sigma\sin\alpha\hat{\mathbf{y}}_\mathbf{V} + \cos\sigma\sin\alpha\hat{\mathbf{z}}_\mathbf{V}\end{aligned}$$

The body nose axis is defined using a Non-Rolling Body Coordinate Frame, which has an x-axis, $\hat{\mathbf{x}}_\mathbf{B}$, fixed to the vehicle axis of symmetry and perpendicular $\hat{\mathbf{y}}_\mathbf{B}$ and $\hat{\mathbf{z}}_\mathbf{B}$ axes that do not roll with the vehicle body for simplicity. A non-rolling body frame is valid for vehicles using the skid-to-turn control approach due to symmetry about the $\hat{\mathbf{x}}_\mathbf{B}$ axis.

The expressions shown here for position, velocity, and attitude determination can be transformed to any of the other coordinate frames using the transformation matrices defined in the preceding sections.

Chapter 3

Equations of Motion

In this chapter, a single set of 6DOF equations of motion will be defined to describe both the endo-atmospheric and exo-atmospheric motion of a flight vehicle over a rotating, spherical Earth. The motion of the vehicle will be described by a set of 10 states in total, with 6 states defining the translational motion of the vehicle and 4 states defining the rotational motion of the vehicle about its center of gravity.

3.1 Translational Equations of Motion

The translational motion of the vehicle will be described by 6 states:

$$\mathbf{x} = \begin{bmatrix} r \\ \mu \\ \lambda \\ V_E \\ \gamma \\ \psi \end{bmatrix} \tag{3.1}$$

As defined in chapter 2, the vehicle position is determined by the *radial distance*, r, *relative longitude*, μ, and *relative latitude*, λ. Likewise, the vehicle velocity is determined by the *Earth-relative velocity magnitude*, V_E, *flight path angle*, γ, and *heading angle*, ψ.

The translational dynamics of the vehicle will be governed by nonlinear expressions

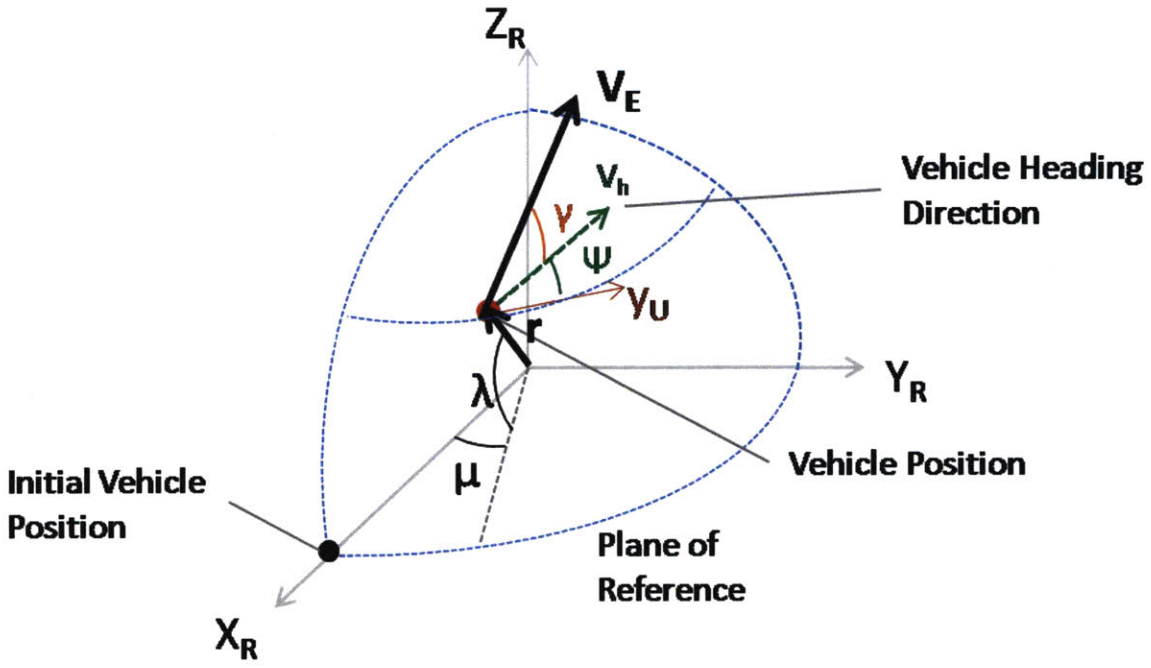

Figure 3-1: Position And Velocity States Of The 6DOF System

for the rates of change of the six states in terms of the states, $\mathbf{x}$, controls, $\mathbf{u}$, and time t. These expressions will be derived in full in this section.

$$\dot{\mathbf{x}} = \begin{bmatrix} \dot{r} \\ \dot{\mu} \\ \dot{\lambda} \\ \dot{V}_E \\ \dot{\gamma} \\ \dot{\psi} \end{bmatrix} = \mathbf{f}(\mathbf{x}, \mathbf{u}, t) \tag{3.2}$$

A careful discussion of the relationships between the states, state dynamics (rates), and the coordinate frames is warranted here. At every instant in time, the states are defined by the instantaneous $\overrightarrow{\mathbf{r}}$ and $\overrightarrow{\mathbf{V_E}}$ vectors as well as the instantaneous orientations of the coordinate frames in which they are defined. For example, the value of $\psi(t)$ at any arbitrary time t can be obtained by examining the instantaneous orientation of $\overrightarrow{\mathbf{V_E}}$ relative to the instantaneous UDC frame at time t. However, the state dynamics are dependent on not only the observed rates of change of $\overrightarrow{\mathbf{r}}$ and $\overrightarrow{\mathbf{V_E}}$, but also on the rotation rates of

the coordinate frames in which they are observed to be changing. Continuing the example above, $\dot{\psi}(t)$ not only depends on the rate of change of ψ as seen by an observer in the UDC frame, but also on the rotation rate of the UDC frame over time. In other words, since ψ is defined as the velocity heading angle relative to the UDC frame, its time derivative must account for both the $\overrightarrow{\mathbf{V_E}}$ motion within the UDC frame as well as the UDC frame rotation over time relative to the inertial frame. It is important to clearly define the frame in which a vector is *observed* to be changing. Therefore, the time derivative of a vector, $\overrightarrow{\mathbf{x}}$, as observed in a frame A will be notated as follows.

$$\frac{d\overrightarrow{\mathbf{x}}}{dt}|_A = \dot{\overrightarrow{\mathbf{x}}}|_A$$

It should be noted that the time derivative of a vector as observed in one frame is not equivalent to the time derivative of a vector as observed in a second frame. For example, $\dot{\overrightarrow{\mathbf{V}}}_E|_U$ as seen by an observer in the UDC frame is not equivalent to $\dot{\overrightarrow{\mathbf{V}}}_E|_R$ as seen by an observer in the REF frame since the UDC frame is rotating relative to the REF frame. While the instantaneous position and velocity vectors may be freely expressed in any of the defined coordinate frames and still represent the same vectors, the vector rates over time will have different representations by observers in different frames. Therefore, the effect of coordinate frame rotation rates on the state dynamics will be explored in the derivation of the state rates.

The time derivative of the position vector, $\dot{\overrightarrow{\mathbf{r}}}$, as well as the time derivative of the Earth-relative velocity vector, $\dot{\overrightarrow{\mathbf{V}}}_E$, as observed in various frames, can be used to extract expressions for the rates of the state variables. For notational purposes, $\overrightarrow{\mathbf{V_I}}$ will be defined as the derivative of the position vector as seen by an observer in the ECI (inertial) frame, while $\overrightarrow{\mathbf{V_E}}$, the Earth-relative velocity vector, is equivalent to the derivative of the position vector as seen by an observer in the REF frame (Earth rotating).

$$\begin{aligned}\overrightarrow{\mathbf{V_I}} &= \dot{\overrightarrow{\mathbf{r}}}|_I \\ \overrightarrow{\mathbf{V_E}} &= \dot{\overrightarrow{\mathbf{r}}}|_R\end{aligned}$$

3.1.1 Position Equations of Motion

In order to obtain the rates of the position variables (r, μ, λ), the time derivative of the position vector is taken. Suppose that the position vector is expressed in an arbitrary rotating frame, *frame A*, that rotates relative to an inertial frame, *frame B*, with rotation rate ω_{A-B}. Let frame A have axes $\hat{i}$, $\hat{j}$, and $\hat{k}$ and frame B have axes $\hat{I}$, $\hat{J}$, and $\hat{K}$.

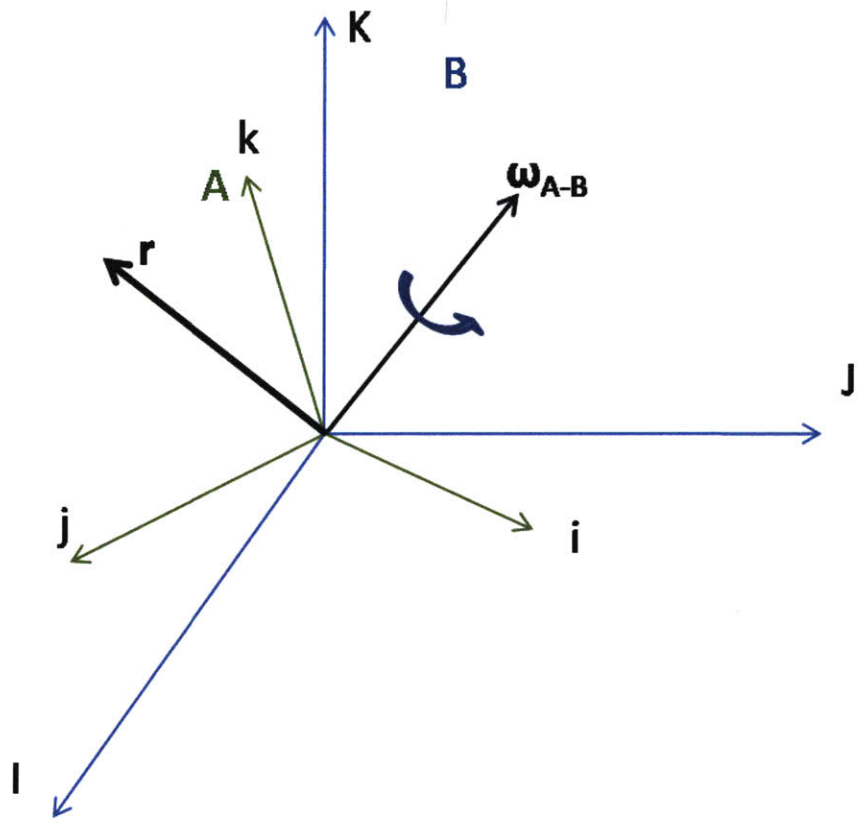

Figure 3-2: Illustration Of Relationship Between Frame A And Frame B

The rate of change of the position vector *as observed by frame B* is obtained by differentiating **r**, as shown in Equation 3.4.

$$\mathbf{r} = r_x\,\hat{\mathbf{i}} + r_y\,\hat{\mathbf{j}} + r_z\,\hat{\mathbf{k}} \tag{3.3}$$

$$\begin{aligned} \dot{\mathbf{r}}|_B &= \dot{r}_x\,\hat{\mathbf{i}} + \dot{r}_y\,\hat{\mathbf{j}} + \dot{r}_z\,\hat{\mathbf{k}} + r_x\dot{\hat{\mathbf{i}}} + r_y\dot{\hat{\mathbf{j}}} + r_z\dot{\hat{\mathbf{k}}} \\ &= \dot{\mathbf{r}}|_A + r_x\,\dot{\hat{\mathbf{i}}} + r_y\,\dot{\hat{\mathbf{j}}} + r_z\,\dot{\hat{\mathbf{k}}} \end{aligned} \tag{3.4}$$

In Equation 3.4, the first three terms on the right hand side represent the motion of the $\mathbf{r}$ vector observed from within the rotating frame A, assuming all axes are fixed, while the latter three terms represent the motion of the coordinate frame axes due to the rotation of frame A relative to frame B. As shown in Vinh [5], the rates of change of a rotating frame's axes are given by Poisson's formulas.

$$\dot{\hat{\mathbf{i}}} = \frac{d\hat{\mathbf{i}}}{dt} = \omega_{\mathbf{A-B}} \times \hat{\mathbf{i}} \tag{3.5}$$

$$\dot{\hat{\mathbf{j}}} = \frac{d\hat{\mathbf{j}}}{dt} = \omega_{\mathbf{A-B}} \times \hat{\mathbf{j}} \tag{3.6}$$

$$\dot{\hat{\mathbf{k}}} = \frac{d\hat{\mathbf{k}}}{dt} = \omega_{\mathbf{A-B}} \times \hat{\mathbf{k}} \tag{3.7}$$

By substituting these expressions into Equation 3.4, the following expression is obtained for transforming the time derivative of a vector from frame A, which is rotating with relative rate ω_{A-B}, to frame B.

$$\dot{\mathbf{r}}|_B = \dot{\mathbf{r}}|_A + \omega_{\mathbf{A-B}} \times \mathbf{r} \tag{3.8}$$

In the expression above, the $\dot{\mathbf{r}}|_A$ term represents the rate of change of vector $\mathbf{r}$ as observed within frame A, assuming all axes are fixed, and is equivalent to the first three terms on the right hand side of Equation 3.4. The remainder of the expression accounts for the additional motion due to the frame rotation that will be seen by an observer in frame B. In the case at hand, frame A will be chosen as the UDC frame and frame B will be chosen as the REF frame in order to express the position vector rate of change relative to the REF coordinate frame, since this expression will contain $\dot{\mu}$ and $\dot{\lambda}$. The expressions below show the relationships between the rates of change as observed in the two frames.

$$(\mathbf{r})_U = r\hat{\mathbf{x}}_{\mathbf{U}} \tag{3.9}$$

$$\dot{\mathbf{r}}|_U = \dot{r}\hat{\mathbf{x}}_{\mathbf{U}} \tag{3.10}$$

$$\dot{\mathbf{r}}|_R = \dot{r}\hat{\mathbf{x}}_\mathbf{U} + r\dot{\hat{\mathbf{x}}}_\mathbf{U} \tag{3.11}$$

$$= \dot{r}\mathbf{x}_\mathbf{U} + r\left(\omega_{U-R} \times \mathbf{x}_\mathbf{U}\right) \tag{3.12}$$

$$= \dot{\mathbf{r}}|_U + \omega_{U-R} \times \mathbf{r} \tag{3.13}$$

Some discussion is helpful for differentiating the physical meaning of $\dot{\mathbf{r}}|_R$ and $\dot{\mathbf{r}}|_U$. As mentioned above, $\dot{\mathbf{r}}|_R$ describes the motion of the position vector relative to a reference frame that is rotating with the Earth's surface (REF frame) while $\dot{\mathbf{r}}|_U$ provides the motion of the position vector relative to the rotating UDC frame, which is rotating with the local horizontal. Thus, $\dot{\mathbf{r}}|_U$ only expresses the position change that occurs relative to the changing local vertical and local horizontal planes. Since the position vector is always defined to point along the x-axis in the UDC frame, $\dot{\mathbf{r}}_U$ only expresses the position motion along the $\mathbf{x}_\mathbf{U}$ axis, while the remainder of the position motion is assumed by the rotation of the UDC frame. The observed position rate in the REF frame, $\dot{\mathbf{r}}|_R$, contains both contributions to the position motion and is equivalent to the Earth-relative velocity vector. Similarly, if the observed position rate in the ECI frame were desired, it would consist of a contribution from $\dot{\mathbf{r}}|_R$ and a contribution from the rotation rate of the REF frame relative to ECI.

As shown in Equation 2.2, the rotation of the UDC frame relative to the REF frame can be expressed in UDC coordinates as

$$\omega_{U-R} = \dot{\mu}\,\hat{\mathbf{z}}_\mathbf{R} - \dot{\lambda}\,\hat{\mathbf{y}}_\mathbf{U} = \dot{\mu}\sin\lambda\,\hat{\mathbf{x}}_\mathbf{U} - \dot{\lambda}\,\hat{\mathbf{y}}_\mathbf{U} + \dot{\mu}\cos\lambda\,\hat{\mathbf{z}}_\mathbf{U}$$

Thus, by taking the cross product given in Equation 3.13, the rate of change of $\vec{\mathbf{r}}$ due to the rotation of the UDC axes is given by

$$\omega_{U-R} \times \mathbf{r} = r\dot{\mu}\cos\lambda\,\hat{\mathbf{y}}_\mathbf{U} + r\dot{\lambda}\,\hat{\mathbf{z}}_\mathbf{U} \tag{3.14}$$

By substituting Equation 3.14 into Equation 3.13, an expression for the position vector

rate of change can be obtained.

$$\dot{\mathbf{r}}|_R = \mathbf{V_E} = \dot{r}\hat{\mathbf{x}}_\mathbf{U} + r\dot{\mu}\cos\lambda\,\hat{\mathbf{y}}_\mathbf{U} + r\dot{\lambda}\,\hat{\mathbf{z}}_\mathbf{U} \tag{3.15}$$

By comparing Equation 3.15 to the expression derived in Equation 2.21 for $\overrightarrow{\mathbf{V_E}}$, the equations of motion for the vehicle position are obtained.

$$\dot{r} = V_E \sin\gamma \tag{3.16}$$

$$\dot{\mu} = \frac{V_E \cos\gamma\cos\psi}{r\cos\lambda} \tag{3.17}$$

$$\dot{\lambda} = \frac{V_E \cos\gamma\sin\psi}{r} \tag{3.18}$$

In the above equations, V_E represents the Earth-relative velocity magnitude, γ and ψ represent the flight path angle and heading angle as defined in section 2.5, μ and λ are the relative longitude and latitude as defined in section 2.4, and r represents the distance from the center of the Earth to the vehicle. These equations define the motion of the vehicle in terms of position altitude, downrange position and crossrange position from the defined plane of reference.

3.1.2 Velocity Equations of Motion

Next, the equations of motion for the velocity vector will be defined. Fundamentally, the motion of the vehicle must obey Newton's Second Law. Recall that the position vector rate of change *as observed in the ECI frame* is denoted as $\overrightarrow{\mathbf{V_I}}$. This is equivalent to the velocity vector in the inertial frame. Thus, Newton's Second Law is given below.

$$m\ddot{\mathbf{r}}|_I = m\dot{\mathbf{V}}_\mathbf{I}|_I = \sum \mathbf{F} \tag{3.19}$$

The right-hand side of Equation 3.19 represents all of the external forces acting inertially on the vehicle, including gravitational, propulsive, and aerodynamic forces. The goal is to extract expressions for the velocity parameter rates of change ($\dot{V}$,$\dot{\gamma}$,$\dot{\psi}$) from the governing dynamics of the vehicle. The first step is to differentiate Equation 3.8 with

respect to time to obtain an expression for the inertial acceleration of the vehicle in terms of the frame rotation rates.

$$\ddot{\mathbf{r}}|_B = \frac{d}{dt}\left(\dot{\mathbf{r}}|_A + \omega_{A-B} \times \mathbf{r}\right)\Big\|_A + \omega_{A-B} \times \left(\dot{\mathbf{r}}|_A + \omega_{A-B} \times \mathbf{r}\right)$$

$$= \left(\ddot{\mathbf{r}}|_A + \dot{\omega}_{A-B} \times \mathbf{r} + \omega_{A-B} \times \dot{\mathbf{r}}|_A\right) + \left(\omega_{A-B} \times \dot{\mathbf{r}}|_A + \omega_{A-B} \times \omega_{A-B} \times \mathbf{r}\right)$$

$$= \ddot{\mathbf{r}}|_A + \dot{\omega}_{A-B} \times \mathbf{r} + 2\omega_{A-B} \times \dot{\mathbf{r}}|_A + \omega_{A-B} \times \left(\omega_{A-B} \times \mathbf{r}\right) \tag{3.20}$$

In this study, Equation 3.20 will only be applied to frames that are rotating with the Earth's rotation rate, Ω_E. Since the rotation rate of the Earth is assumed to be constant in this study, $\dot{\omega}_{A-B} = 0$ and the second term in Equation 3.20 can be neglected. In addition, $\dot{\mathbf{r}}|_A$ represents the velocity of the vehicle, $\mathbf{V_A}$, as observed in the rotating frame, A. Thus, the expression for the inertial acceleration, $\ddot{\mathbf{r}}|_B$, is given in terms of the observed rates of change in a rotating frame and the frame rotation rate.

$$\ddot{\mathbf{r}}|_B = \ddot{\mathbf{r}}|_A + 2\omega_{A-B} \times \mathbf{V_A} + \omega_{A-B} \times \omega_{A-B} \times \mathbf{r} \tag{3.21}$$

The second term on the right hand side in Equation 3.21 is defined as the *Coriolis acceleration* due to the vehicle moving with a velocity $\mathbf{V_A}$ within the rotating A frame. Likewise, the third term on the right hand side represents the *centrifugal accleration* which results from the position vector being offset from the axis of rotation of the A frame.

For the development of the velocity equations of motion, the inertial acceleration must be related to the velocity flight angles, so the B frame will represent the ECI frame and the A frame will represent the REF frame. Therefore, the expression given in Equation 3.19 for inertial acceleration, $\ddot{\mathbf{r}}_\mathbf{B} = \frac{\sum \mathbf{F}}{m}$, can be substituted into Equation 3.21. Thus, a dynamical expression governed by Newton's 2nd Law is created to represent the velocity vector motion within the REF rotating frame.

$$\ddot{\mathbf{r}}|_R = \dot{\mathbf{V}}_\mathbf{E}|_R = \frac{\sum \mathbf{F}}{m} - 2\omega_{R-I} \times \mathbf{V}_\mathbf{E} - \omega_{R-I} \times \left(\omega_{R-I} \times \mathbf{r}\right) \tag{3.22}$$

Examining Equation 3.22, it should be noted that the velocity and position vectors, as well as their derivatives, are all expressed relative to the rotating frame, while the forces acting on the vehicle are expressed inertially. The forces can also be resolved at each instant in time along the instantaneous axes of any of the coordinate frames derived in chapter 2.

Returning to the pursuit of the velocity rates, it is possible to incorporate a third rotating frame into Equation 3.22. The reason for this is that the velocity angles (γ, ψ) are expressed relative to the UDC frame, and it would be convenient to relate the velocity rate in the UDC frame directly with the inertial acceleration to avoid extra computation later. Therefore, using the expression for transferring derivatives between rotating frames in Equation 3.8, the left hand side of Equation 3.22 can be expressed as follows.

$$\dot{\mathbf{V}}_\mathbf{E}|_R = \dot{\mathbf{V}}_\mathbf{E}|_U + \omega_{U-R} \times \mathbf{V}_\mathbf{E} \tag{3.23}$$

Thus, by substituting in the expression above and moving the proper terms to the right side, Equation 3.22 becomes

$$\dot{\mathbf{V}}_\mathbf{E}|_U = \frac{\sum \mathbf{F}}{m} - \left(2\omega_{R-I} + \omega_{U-R}\right) \times \mathbf{V}_\mathbf{E} - \omega_{R-I} \times \omega_{R-I} \times \mathbf{r} \tag{3.24}$$

The objective is to derive equations of motion for V, γ, and ψ, so the first step will be to derive an expression for the left side of Equation 3.24 in terms of $\dot{V}$, $\dot{\gamma}$, and $\dot{\psi}$. Using the expression for transferring derivatives between rotating frames in Equation 3.8, the velocity rate observed in the UDC frame can be expressed in terms of the velocity rate observed in the V frame and the rotation rate of the V frame relative to the UDC frame.

$$\dot{\mathbf{V}}_\mathbf{E}|_U = \dot{\mathbf{V}}_\mathbf{E}|_V + \omega_{V-U} \times \mathbf{V}_\mathbf{E} \tag{3.25}$$

The velocity rate observed in the V frame is simple since the x-axis points in the velocity vector direction. An observer in this frame would observe the velocity changing

with rate $\dot{r}$ along this axis. The rotation rate of the V frame relative to the UDC frame is given by Equation 2.5. By using $\mathbf{T}_{\mathbf{U}}^{\mathbf{V}}$, it can be expressed in V frame coordinates.

$$\left(\omega_{V-U}\right)_V = \dot{\psi}\sin\gamma\hat{\mathbf{x}}_{\mathbf{V}} - \dot{\gamma}\hat{\mathbf{y}}_{\mathbf{V}} + \dot{\psi}\cos\gamma\hat{\mathbf{z}}_{\mathbf{V}} \tag{3.26}$$

By substituting into Equation 3.25 and performing the cross product, an expression is obtained for the left side of Equation 3.24.

$$\dot{\mathbf{V}}_{\mathbf{E}}|_U = \begin{bmatrix} \dot{V}_E \\ 0 \\ 0 \end{bmatrix} + \begin{bmatrix} 0 \\ V_E\dot{\psi}\cos\gamma \\ V_E\dot{\gamma} \end{bmatrix} = \dot{V}_E\,\hat{\mathbf{x}}_{\mathbf{V}} + V_E\dot{\psi}\cos\gamma\,\hat{\mathbf{y}}_{\mathbf{V}} + V_E\dot{\gamma}\,\hat{\mathbf{z}}_{\mathbf{V}} \tag{3.27}$$

The rotation rate of the UDC frame with respect to the REF frame is given by Equation 2.2 in REF coordinates. Using $\mathbf{T}_{\mathbf{R}}^{\mathbf{U}}$, the rotation rate can be transformed to UDC coordinates, as shown below.

$$\left(\omega_{U-R}\right)_U = \dot{\mu}\sin\lambda\,\hat{\mathbf{x}}_{\mathbf{U}} - \dot{\lambda}\,\hat{\mathbf{y}}_{\mathbf{U}} + \dot{\mu}\cos\lambda\,\hat{\mathbf{z}}_{\mathbf{U}} \tag{3.28}$$

In the expression above, $\dot{\mu}$ and $\dot{\lambda}$ are given by the position equations of motion in Equations 3.17 and 3.18.

Similarly, Equation 2.1 gives the rotation rate of the REF frame with respect to the ECI frame, which can also be transformed to UDC coordinates using $\mathbf{T}_{\mathbf{R}}^{\mathbf{U}}$.

$$\begin{aligned}\left(\omega_{R-I}\right)_U = {} & \Omega_E\left(\cos\mu\cos\lambda\sin\theta_0\sin i_0 + \sin\mu\cos\lambda\cos\theta_0\sin i_0 + \sin\lambda\cos i_0\right)\hat{\mathbf{x}}_{\mathbf{U}} \\ & + \Omega_E\left(-\sin\mu\sin\theta_0\sin i_0 + \cos\mu\cos\theta_0\sin i_0\right)\hat{\mathbf{y}}_{\mathbf{U}} \\ & + \Omega_E\left(-\cos\mu\sin\lambda\sin\theta_0\sin i_0 - \sin\mu\sin\lambda\cos\theta_0\sin i_0 + \cos\lambda\cos i_0\right)\hat{\mathbf{z}}_{\mathbf{U}}\end{aligned} \tag{3.29}$$

Let the $\hat{\mathbf{x}}_{\mathbf{U}}$, $\hat{\mathbf{y}}_{\mathbf{U}}$, and $\hat{\mathbf{z}}_{\mathbf{U}}$ components of ω_{R-I} given in Equation 3.29 be denoted as ω_1, ω_2, and ω_3, respectively.

$$
\begin{aligned}
\omega_1 = &\ \Omega_E \left(\cos\mu\cos\lambda\sin\theta_0\sin i_0 + \sin\mu\cos\lambda\cos\theta_0\sin i_0 + \sin\lambda\cos i_0\right) \\
\omega_2 = &\ \Omega_E \left(-\sin\mu\sin\theta_0\sin i_0 + \cos\mu\cos\theta_0\sin i_0\right) \\
\omega_3 = &\ \Omega_E \left(-\cos\mu\sin\lambda\sin\theta_0\sin i_0 - \sin\mu\sin\lambda\cos\theta_0\sin i_0 + \cos\lambda\cos i_0\right)
\end{aligned}
$$

The rotation rates in the Coriolis acceleration term of Equation 3.24 can now be combined and transformed to V frame coordinates.

$$
\begin{aligned}
2\omega_{R-I} + \omega_{U-R} &= \mathbf{T}_{\mathbf{U}}^{\mathbf{V}} \left(\omega_1 + \dot{\mu}\sin\lambda\,\hat{\mathbf{x}}_{\mathbf{U}} + \omega_2 - \dot{\lambda}\,\hat{\mathbf{y}}_{\mathbf{U}} + \omega_3 + \dot{\mu}\cos\lambda\,\hat{\mathbf{z}}_{\mathbf{U}}\right) \\
&= \left(2\omega_1 + \dot{\mu}\sin\lambda\right)\sin\gamma + \left(2\omega_2 - \dot{\lambda}\right)\cos\gamma\cos\psi + \left(2\omega_3 + \dot{\mu}\cos\lambda\right)\cos\gamma\sin\psi\hat{\mathbf{x}}_{\mathbf{V}} \\
&\quad - \left(2\omega_2 - \dot{\lambda}\right)\sin\psi + \left(2\omega_3 + \dot{\mu}\cos\lambda\right)\cos\psi\hat{\mathbf{y}}_{\mathbf{V}} \\
&\quad + \left(2\omega_1 + \dot{\mu}\sin\lambda\right)\cos\gamma - \left(2\omega_2 - \dot{\lambda}\right)\sin\gamma\cos\psi - \left(2\omega_3 + \dot{\mu}\cos\lambda\right)\sin\gamma\sin\psi\hat{\mathbf{z}}_{\mathbf{V}}
\end{aligned}
\tag{3.30}
$$

Thus, the Coriolis term in Equation 3.24 can be obtained in V frame coordinates by taking the cross product of the rotation rates shown above with the velocity vector.

$$
\begin{aligned}
&\left(2\omega_{R-I} + \omega_{U-R}\right)_V \times V_E\hat{\mathbf{x}}_{\mathbf{V}} = \\
&\quad V_E\left(\left(2\omega_1 + \dot{\mu}\sin\lambda\right)\cos\gamma - \left(2\omega_2 - \dot{\lambda}\right)\sin\gamma\cos\psi - \left(2\omega_3 + \dot{\mu}\cos\lambda\right)\sin\gamma\sin\psi\right)\hat{\mathbf{y}}_{\mathbf{V}} \\
&\qquad + V_E\left(\left(2\omega_2 - \dot{\lambda}\right)\sin\psi - \left(2\omega_3 + \dot{\mu}\cos\lambda\right)\cos\psi\right)\hat{\mathbf{z}}_{\mathbf{V}}
\end{aligned}
\tag{3.31}
$$

As observed above, the Coriolis accleration acts only in directions perpendicular to the velocity vector. This confirms the fact that the Coriolis acceleration generated by the rotating frames applies corrections to the direction of the velocity vector but does

not affect the magnitude of the velocity. This acceleration has contributions from two sources: the rotation of the REF frame relative to ECI and the rotation of the UDC frame relative to the REF frame. The contributions from the first source are in terms of ω_1, ω_2, and ω_3 while the contributions from the second source are in terms of miu and $\dot{\lambda}$. The contributions from the second source can be simplified by substituting the position rates (Equations 3.16-3.18) into the expressions shown in 3.31.

First, the position rate terms in the $\hat{\mathbf{y}}_\mathbf{V}$ component can be simplified by replacing $\dot{\mu}$ and $\dot{\lambda}$ and manipulating the new expression.

$$\dot{\mu}\left(\sin\lambda\cos\gamma - \cos\lambda\sin\gamma\sin\psi\right) + \dot{\lambda}\sin\gamma\cos\psi = \frac{V_E\cos^2\gamma\cos\psi\tan\lambda}{r}$$

Similarly, the same operation can be performed for the position rate terms in the $\mathbf{z}_\mathbf{V}$ component.

$$-\dot{\lambda}\sin\psi - \dot{\mu}\cos\lambda\cos\psi = -\frac{V_E\cos^2\gamma}{r}$$

Next, the third term on the right side of Equation 3.24 can be expressed in V frame coordinates by taking the cross products then transforming from UDC coordinates to V coordinates using $\mathbf{T}^\mathbf{V}_\mathbf{U}$.

$$\begin{aligned}\mathbf{T}^\mathbf{V}_\mathbf{U}\left(\omega_{R-I}\times\left(\omega_{R-I}\times\mathbf{r}\right)\right) = {} & r\left(-\omega_2^2-\omega_3^2\right)\sin\gamma + r\omega_1\omega_2\cos\gamma\cos\psi + r\omega_1\omega_3\cos\gamma\sin\psi\hat{\mathbf{x}}_\mathbf{V} \\ & -r\omega_1\omega_2\sin\psi + r\omega_1\omega_3\cos\psi\hat{\mathbf{y}}_\mathbf{V} \\ & +r\left(-\omega_2^2-\omega_3^2\right)\cos\gamma - r\omega_1\omega_2\sin\gamma\cos\psi - r\omega_1\omega_3\sin\gamma\sin\psi\hat{\mathbf{z}}_\mathbf{V}\end{aligned} \tag{3.32}$$

The next step is to incorporate the external forces acting on the vehicle into Equation 3.24. It is most convenient to sum the external forces along the velocity frame axes since many of the aerodynamic forces act along these axes. External forces acting on

the vehicle include *lift* (L) and *drag* (D) aerodynamic forces, *gravity* force, and *thrust* (T) force provided by the launch vehicle. Using common convention, the drag force acts opposite the velocity vector ($-D\hat{\mathbf{x}}_{\mathbf{V}}$), the gravity force acts radially inward towards the center of the Earth ($-g(r)\hat{\mathbf{x}}_{\mathbf{U}}$), and the lift force acts perpendicular to the velocity vector in the lift plane ($L\hat{\mathbf{i}}_{\mathbf{L}}$). Furthermore, the gravity force will be expressed according to the inverse square law, $\mathbf{g}(\mathbf{r}) = m\frac{\mu_G}{r^2}$, where $\mu_G = 3.9860064 \times 10^{14} m^3/s^2$ is the gravitational constant of the Earth and m is the vehicle mass. Since the thrust force acts from the back of the vehicle, only the component of thrust acting along the vehicle nose axis will accelerate the vehicle center of gravity, while the other components will induce torques. The axial thrust force will be denoted as $\mathbf{T_A}$, with T_{A_x}, T_{A_y}, and T_{A_z} components exerted along the $\hat{\mathbf{x}}_{\mathbf{V}}$, $\hat{\mathbf{y}}_{\mathbf{V}}$, and $\hat{\mathbf{z}}_{\mathbf{V}}$ axes, respectively. Since the axial force acts along the x_B axis, the aerodynamic angles can be used to identify the components along the velocity axes.

$$T_{A_x} = T_A \cos\alpha \tag{3.33}$$

$$T_{A_y} = T_A \sin\alpha \sin\sigma \tag{3.34}$$

$$T_{A_z} = T_A \sin\alpha \cos\sigma \tag{3.35}$$

By expressing each of these forces in the velocity coordinate frame, the following force components can be obtained.

$$\sum F_{x_V} = T_A \cos\alpha - D - m\frac{\mu_G}{r^2}\sin\gamma \tag{3.36}$$

$$\sum F_{y_V} = T_A \sin\alpha \sin\sigma + L\sin\sigma \tag{3.37}$$

$$\sum F_{z_V} = T_A \sin\alpha \cos\sigma + L\cos\sigma - m\frac{\mu_G}{r^2}\cos\gamma \tag{3.38}$$

Models of these forces based upon the vehicle model will be discussed in detail in Chapters 5 and 6. By substituting into Equation 3.24, the equations of motion for the velocity parameters are obtained.

$$
\begin{pmatrix} \dot{V}_E \\ V_E\dot{\psi}\cos\gamma \\ V_E\dot{\gamma} \end{pmatrix} = \begin{pmatrix} \frac{T_A\cos\alpha}{m} - \frac{D}{m} - \frac{\mu_G}{r^2}\sin\gamma \\ \frac{T_A\sin\alpha\sin\sigma}{m} + \frac{L\sin\sigma}{m} \\ \frac{T_A\sin\alpha\cos\sigma}{m} + \frac{L\cos\sigma}{m} - \frac{\mu_G}{r^2}\cos\gamma \end{pmatrix} \quad \textit{Inertial Acceleration}
$$

$$
- \begin{pmatrix} 0 \\ V_E\left(2\omega_1\cos\gamma - 2\omega_2\sin\gamma\cos\psi - 2\omega_3\sin\gamma\sin\psi\right) \\ +V_E\left(2\omega_2\sin\psi - 2\omega_3\cos\psi\right) \end{pmatrix} \quad \begin{matrix} \textit{Coriolis Acceleration} \\ \textit{Due To Earth Rotation} \end{matrix}
$$

$$
- \begin{pmatrix} 0 \\ \frac{V_E^2\cos^2\gamma\cos\psi\tan\lambda}{r} \\ -\frac{V_E^2\cos^2\gamma}{r} \end{pmatrix} \quad \textit{Coriolis Acceleration Due To UDC Frame Rotation}
$$

$$
- \begin{pmatrix} r\left(-\omega_2^2 - \omega_3^2\right)\sin\gamma + r\omega_1\omega_2\cos\gamma\cos\psi + r\omega_1\omega_3\cos\gamma\sin\psi \\ -r\omega_1\omega_2\sin\psi + r\omega_1\omega_3\cos\psi \\ +r\left(-\omega_2^2 - \omega_3^2\right)\cos\gamma - r\omega_1\omega_2\sin\gamma\cos\psi - r\omega_1\omega_3\sin\gamma\sin\psi \end{pmatrix} \quad \begin{matrix} \textit{Centrifugal} \\ \textit{Acceleration} \end{matrix}
$$

(3.39)

The equations of motion given above can be cleaned up by extracting the rotation of the Earth, Ω_E, from the ω_1, ω_2, and ω_3 terms and dividing by the necessary terms to leave $\dot{V}_E$, $\dot{\gamma}$, and $\dot{\psi}$ on the left side. Thus, we have the equations of motion governing the Earth-relative velocity of the vehicle.

$$
\dot{V}_E = \frac{T_A\cos\alpha}{m} - \frac{D}{m} - \frac{\mu_G}{r^2}\sin\gamma - \Omega_E^2 r F_1 \tag{3.40}
$$

$$
\dot{\gamma} = \frac{T_A\sin\alpha\cos\sigma}{m} + \frac{L\cos\sigma}{mV_E} + \left(\frac{V_E}{r} - \frac{\mu_G}{r^2V_E}\right)\cos\gamma - 2\Omega_E C_2 - \frac{r\Omega_E^2 F_2}{V_E} \tag{3.41}
$$

$$
\dot{\psi} = \frac{T_A\sin\alpha\sin\sigma}{m} + \frac{L\sin\sigma}{mV_E\cos\gamma} - \frac{V_E}{r}\cos\gamma\cos\psi\tan\lambda - \frac{2\Omega_E C_3}{\cos\gamma} - \frac{r\Omega_E^2 F_3}{V_E\cos\gamma} \tag{3.42}
$$

The terms defined as C_2, C_3, F_1, F_2, and F_3 represent coefficients for the Coriolis and centrifugal acceleration terms from the Earth's rotation contributing to $\dot{V}$, $\dot{\gamma}$, and $\dot{\psi}$,

respectfully. As can be seen by examining Equation 3.39, these terms are entirely due to the Earth's rotation rate, Ω_E. A non-Earth rotating model can be obtained by simply setting Ω_E to zero and neglecting these term. They are defined as

$$C_2 = \frac{\omega_1 \cos\gamma - \omega_2 \sin\gamma \cos\psi - \omega_3 \sin\gamma \sin\psi}{\Omega_E} \tag{3.43}$$

$$C_3 = \frac{\omega_2 \sin\psi - \omega_3 \cos\psi}{\Omega_E} \tag{3.44}$$

$$F_1 = \frac{(-\omega_2^2 - \omega_3^2)\sin\gamma + \omega_1\omega_2 \cos\gamma \cos\psi + \omega_1\omega_3 \cos\gamma \sin\psi}{\Omega_E^2} \tag{3.45}$$

$$F_2 = \frac{-\omega_1\omega_2 \sin\psi + \omega_1\omega_3 \cos\psi}{\Omega_E^2} \tag{3.46}$$

$$F_3 = \frac{(-\omega_2^2 - \omega_3^2)\cos\gamma - \omega_1\omega_2 \sin\gamma \cos\psi - \omega_1\omega_3 \sin\gamma \sin\psi}{\Omega_E^2} \tag{3.47}$$

For perspective, the maximum value of the centrifugal acceleration, $\Omega_E^2 r$, is on the order of $10^{-3}\, g_0$ for the Earth rotation, while the maximum value of the Coriolis acceleration, $2\Omega_E V_E$, is on the order of $10^{-1}\, g_0$ for vehicles traveling at orbital speeds, where $g_0 = 9.81 m/s^2$ is the gravity acceleration at sea level [5]. After dividing both terms by V_E, which is on the order of 10^3, the maximum Coriolis contribution to the $\dot{\gamma}$ and $\dot{\psi}$ rates is on order $10^{-4}\, g_0$, while the maximum contribution from centrifugal acceleration is on order $10^{-6}\, g_0$. While these terms have little effect on the high dynamics of $\dot{\gamma}$ and $\dot{\psi}$, they have a drifting effect on the low dynamics of $\dot{\mu}$ and $\dot{\lambda}$, which can lead the vehicle slightly off-course when targeting a terminal destination. These terms can often be ignored for short range, low speed flight, but they are important for accurate modeling of high speed, long range flight, especially when targeting a terminal destination.

Similarly, the third set of terms on the right hand side of Equation 3.39 are corrections to the velocity direction due to the spherical coordinates used to define the UDC frame. As the vehicle travels downrange and crossrange from its initial position, the local horizontal plane (UDC frame) will rotate to remain tangent to the unit sphere, affecting the velocity direction. A flat Earth model can be obtained by allowing r to approach ∞ and neglecting these terms.

3.2 Rotational Equations of Motion

The remaining four states will describe the attitude motion of the vehicle body. As described in the introduction, the vehicle considered in this study exhibits *skid-to-turn* control due to an axially symmetric body with a pointed nose. Therefore, the entire control of the vehicle amounts to directing the body attitude in a chosen direction relative to the velocity vector. In essence, by choosing the body attitude relative to the velocity vector, the vehicle is choosing the *lift plane*, defined by the $\mathbf{x_B}$ and $\mathbf{x_V}$ axes. The formulation given in this section will introduce a 6DOF model with skid-to-turn control that describes the motion of the body attitude relative to the velocity vector.

It is first important to define new parameters related to the attitude motion of the body. The rotation of the non-rolling body frame relative to the ECI (inertial) frame is given by

$$\omega_{B-I} = q_{body}\hat{\mathbf{y}}_\mathbf{B} + r_{body}\hat{\mathbf{z}}_\mathbf{B} \tag{3.48}$$

The parameters q_{body}, and r_{body} represent *body pitch rate*, and *bodyyaw rate*, respectively, about the $\mathbf{y_B}$ and $\mathbf{z_B}$ axes. The resultant rate from these two components represents the total angular motion of the body nose relative to inertial space. For an asymmetric bank-to-turn vehicle, the roll rate about the $\mathbf{x_B}$ axis, p_{body}, would also be included in this analysis. However, since the roll rate has negligible effect on the control authority of a skid-to-turn vehicle and is often stabilized to zero, it is ignored in this analysis [10].

It is important to note that the $\mathbf{y_B}$ and $\mathbf{z_B}$ axes are not fixed to the vehicle and therefore do not rotate with the vehicle's roll motion. The yaw and pitch motion should be thought of as components of the total body angular motion composed along pre-defined axes perpendicular to the vehicle nose direction, $\hat{\mathbf{x}}_\mathbf{B}$. As mentioned earlier, when defining the non-rolling body frame in section 2.6, these axes can be oriented in any way such that they are perpendicular to $\mathbf{x_B}$ and perpendicular to one another. The end goal is to define the total body angular motion along some defined axes and use that definition to describe the vehicle attitude motion relative to the velocity vector. Whether the defined pitch and yaw axes are always pointing out of the "top" or "side" of the vehicle is irrelevant due to

the vehicle symmetry.

Equations describing the change in these body rates over time can be derived using Newton's Second Law. Newton's Second Law states that the sum of torques acting about a body's center of mass is equal to the body's change in angular momentum.

$$\sum \tau = \dot{H}|_I = \left(\mathbf{I}\dot{\omega}_{B-I}\right)_I$$

Let the symbol $\mathbf{I}$ be defined as the inertia matrix, given as

$$\mathbf{I} = \begin{bmatrix} I_{xx} & I_{xy} & I_{xz} \\ I_{yx} & I_{yy} & I_{yz} \\ I_{zx} & I_{zy} & I_{zz} \end{bmatrix}$$

The derivative of angular momentum in the inertial frame can be computed in terms of the angular momentum derivative in the body frame and the rotation rate of the body frame. The inertia matrix does not change over time in the body frame since the $\mathbf{x_B}$ axis is fixed to the roll principle axis and the y_B and z_B axes continually point in directions with identical inertia properties ($I_{yy} = I_{zz}$). Since the inertia matrix does not change in the body frame, the derivative of the angular momentum in the body frame is the product of the inertia matrix and the derivative of ω_{B-I} observed in the body frame.

$$\sum \tau = \dot{H}|_I = I\dot{\omega}_{B-I}|_B + \omega_{B-I} \times I\omega_{B-I} \tag{3.49}$$

$$= \begin{bmatrix} I_{xx} & I_{xy} & I_{xz} \\ I_{yx} & I_{yy} & I_{yz} \\ I_{zx} & I_{zy} & I_{zz} \end{bmatrix} \begin{bmatrix} 0 \\ \dot{q}_{body} \\ \dot{r}_{body} \end{bmatrix} + \begin{bmatrix} 0 \\ q_{body} \\ r_{body} \end{bmatrix} \times \begin{bmatrix} I_{xx} & I_{xy} & I_{xz} \\ I_{yx} & I_{yy} & I_{yz} \\ I_{zx} & I_{zy} & I_{zz} \end{bmatrix} \begin{bmatrix} 0 \\ q_{body} \\ r_{body} \end{bmatrix} \tag{3.50}$$

Since the vehicle considered in this study is symmetric about the x-axis, all cross terms in the inertia matrix are equal to zero and $I_{yy} = I_{zz}$. By multiplying the matrices above with the proper terms set to zero and taking the cross product, expressions for the body angular accelerations in terms of external torques acting on the body are obtained.

$$\dot{q}_{body} = \frac{\sum \tau_{y_B}}{I_{yy}} \tag{3.51}$$

$$\dot{r}_{body} = \frac{\sum \tau_{z_B}}{I_{zz}} \tag{3.52}$$

As seen above, the pitch and yaw motion of the vehicle is completely decoupled due to the vehicle symmetry as well as the roll attitude stabilization. For a bank-to-turn vehicle, in contrast, the terms above would include cross-coupling terms in terms of the roll axis inertia, I_{xx}, and the roll rate, p_{body}.

The body rates given in Equation 3.48 express the angular rate of the body relative to inertial space but the purpose of this model is to define the body attitude motion relative to the velocity vector. In Section 2.6, the nose yaw angle, ϕ, and nose pitch angle, θ, were introduced to relate the body frame to the velocity frame. The objective of this exercise is to derive equations for the rates of change of those angles in terms of the body rates q_{body} and r_{body}.

The first step is to express the body axis of symmetry, $\mathbf{x_B}$, in V frame coordinates.

$$(\hat{\mathbf{x}}_\mathbf{B})_V = \mathbf{T_V^{B^T}} \begin{bmatrix} 1 \\ 0 \\ 0 \end{bmatrix} = \cos\theta\cos\phi\hat{\mathbf{x}}_\mathbf{V} + \cos\theta\sin\phi\hat{\mathbf{y}}_\mathbf{V} + \sin\theta\hat{\mathbf{z}}_\mathbf{V}$$

Next, the time derivative of $\hat{\mathbf{x}}_\mathbf{B}$, as observed in the ECI (inertial) frame, will be taken to find expressions for $\dot{\theta}$ and $\dot{\phi}$. Using Equation 3.8, the change of the $\mathbf{x_B}$ axis in inertial space can be defined in terms of the change of $\mathbf{x_B}$ observed in the V frame and the rotation rate of the V frame relative to inertial space.

$$\dot{\hat{\mathbf{x}}}_\mathbf{B}|_I = \dot{\hat{\mathbf{x}}}_\mathbf{B}|_V + \omega_{V-I} \times \hat{\mathbf{x}}_\mathbf{B} \tag{3.53}$$

The left hand side of Equation 3.53 represents the derivative of the body x-axis with respect to inertial frame, which can be expressed using Equation 3.5.

$$\begin{aligned}\dot{\hat{\mathbf{x}}}_{\mathbf{B}}|_I &= \omega_{B-I} \times \hat{\mathbf{x}}_{\mathbf{B}} \\ &= [0 \quad q_{body} \quad r_{body}]_B^T \times \hat{\mathbf{x}}_{\mathbf{B}} \\ &= r_{body}\hat{\mathbf{y}}_{\mathbf{B}} - q_{body}\hat{\mathbf{z}}_{\mathbf{B}}\end{aligned} \tag{3.54}$$

The first term on the right side of Equation 3.53, the derivative of $\hat{\mathbf{x}}_{\mathbf{B}}$ as observed in the V frame, can be expressed using the expression for a time derivative in a rotating frame as defined in Equation 3.8.

$$\dot{\hat{\mathbf{x}}}_{\mathbf{B}}|_V = \dot{\hat{\mathbf{x}}}_{\mathbf{B}}|_B + \omega_{B-V} \times \hat{\mathbf{x}}_{\mathbf{B}} \tag{3.55}$$

The first term on the right side, $\dot{\hat{\mathbf{x}}}_{\mathbf{B}}|_B$, is a vector of zeros since the B frame is fixed to the body attitude and the attitude will not appear to change when observed in the B frame. The rotation rate of the B frame relative to the V frame is given by Equation 2.3 can be expressed in B frame coordinates as

$$\left(\dot{\omega}_{B-V}\right)_B = \dot{\phi}\sin\theta\hat{\mathbf{x}}_{\mathbf{B}} - \dot{\theta}\hat{\mathbf{y}}_{\mathbf{B}} + \dot{\phi}\cos\theta\hat{\mathbf{z}}_{\mathbf{B}}$$

Now, performing the cross product with $\hat{\mathbf{x}}_{\mathbf{B}}$, an expression is obtained for $\dot{\hat{\mathbf{x}}}_{\mathbf{B}}|_V$ in B frame coordinates.

$$\dot{\hat{\mathbf{x}}}_{\mathbf{B}}|_V = \dot{\phi}\cos\theta\hat{\mathbf{y}}_{\mathbf{B}} + \dot{\theta}\hat{\mathbf{z}}_{\mathbf{B}} \tag{3.56}$$

Next, the rotational component of Equation 3.53 requires an expression for the rotation rate of the V frame relative to inertial space, ω_{V-I}. An expression for ω_{V-I} is composed of three terms describing the Earth rotation, the local level frame rotation, and the velocity rotation.

$$\omega_{V-I} = \omega_{V-U} + \omega_{U-R} + \omega_{R-I}$$

An expression for $\left(\omega_{R-I}\right)_U$ in UDC coordinates is given by Equation 3.29. As in section 3.1, let ω_1, ω_2, and ω_3 represent the components of the Earth's rotation along the $\mathbf{x_U}$, $\mathbf{y_U}$, and $\mathbf{z_U}$ axes, respectfully. Similarly, $\left(\omega_{U-R}\right)_U$ was expressed in UDC coordinates in Equation 3.28. Lastly, $\left(\omega_{V-U}\right)_V$ is expressed in V frame coordinates by Equation 3.26.

First, the rotation rates discussed above must be transformed to a common frame before they are combined to form ω_{V-I}. Therefore, $\left(\omega_{R-I}\right)_U$ and $\left(\omega_{U-R}\right)_U$ will be transformed from the UDC frame to the V frame.

$$\begin{aligned}\left(\omega_{R-I}\right)_V = \quad & \omega_1 \sin\gamma + \omega_2 \cos\gamma \cos\psi + \omega_3 \cos\gamma \sin\psi \hat{\mathbf{x}}_\mathbf{V} \\ & -\omega_2 \sin\psi + \omega_3 \cos\psi \hat{\mathbf{y}}_\mathbf{V} \\ & +\omega_1 \cos\gamma - \omega_2 \sin\gamma \cos\psi - \omega_3 \sin\gamma \sin\psi \hat{\mathbf{z}}_\mathbf{V}\end{aligned}$$

$$\begin{aligned}\left(\omega_{U-R}\right)_V = \; & \dot{\mu}\left(\sin\gamma \sin\lambda + \cos\gamma \sin\psi \cos\lambda\right) - \dot{\lambda} \cos\gamma \cos\psi \hat{\mathbf{x}}_\mathbf{V} \\ & +\dot{\mu} \cos\psi \cos\lambda + \dot{\lambda} \sin\psi \hat{\mathbf{y}}_\mathbf{V} \\ & +\dot{\mu}\left(\cos\gamma \sin\lambda - \sin\gamma \sin\psi \cos\lambda\right) + \dot{\lambda} \sin\gamma \cos\psi \hat{\mathbf{z}}_\mathbf{V}\end{aligned}$$

In the second equation above, expressions for $\dot{\mu}$ and $\dot{\lambda}$ can be replaced by Equations (3.17-3.18), as was done in section 3.1 to obtain simpler expressions in terms of V.

$$\left(\omega_{U-R}\right)_V = \frac{V_E \cos\psi \cos\gamma \sin\gamma \tan\lambda}{r} \hat{\mathbf{x}}_\mathbf{V} + \frac{V_E \cos^2\gamma}{r} \hat{\mathbf{y}}_\mathbf{V} + \frac{V_E \cos^2\gamma \cos\psi \tan\lambda}{r} \hat{\mathbf{z}}_\mathbf{V}$$

Therefore, the rotation rate of the velocity frame as observed in the inertial frame (ECI) can be expressed in V frame coordinates by summing the components described above.

$$\left(\omega_{V-I}\right)_V = \begin{bmatrix} \dot{\psi} \sin\gamma + \frac{V_E \cos\psi \cos\gamma \sin\gamma \tan\lambda}{r} + \omega_1 \sin\gamma + \omega_2 \cos\gamma \cos\psi + \omega_3 \cos\gamma \sin\psi \\ -\dot{\gamma} + \frac{V_E \cos^2\gamma}{r} - \Omega_E C_3 \\ \dot{\psi} \cos\gamma + \frac{V_E \cos^2\gamma \cos\psi \tan\lambda}{r} + \Omega_E C_2 \end{bmatrix}_V \tag{3.57}$$

By comparing the equation above with the Coriolis coefficients defined in Equations

(3.43-3.44), it should be noticed that the contributions from the Earth's rotation in Equation 3.57 can be expressed in terms of these coefficients. However, since only two Coriolis coefficients are defined in section 3.1, a third coefficient, C_1, will be defined to represent the contributions from the REF frame rotation in the $\hat{\mathbf{x}}_\mathbf{V}$ direction. Therefore, C_1 will be defined as

$$C_1 = \frac{\omega_1 \sin\gamma + \omega_2 \cos\gamma \cos\psi + \omega_3 \cos\gamma \sin\psi}{\Omega_E}$$

Similarly, terms can be defined to represent the contributions to the V frame rotation from the UDC frame motion relative to the Earth. Let U_1, U_2, and U_3 represents the contributions along the $\hat{\mathbf{x}}_\mathbf{V}$, $\hat{\mathbf{y}}_\mathbf{V}$, and $\hat{\mathbf{z}}_\mathbf{V}$ axes, respectively.

$$U_1 = \frac{V_E \cos\psi \cos\gamma \sin\gamma \tan\lambda}{r}$$
$$U_2 = \frac{V_E \cos^2\gamma}{r}$$
$$U_3 = \frac{V_E \cos^2\gamma \cos\psi \tan\lambda}{r}$$

Using these newly defined terms along with the previous definitions for C_2 and C_3, ω_{V-I} can be expressed more cleanly as

$$\left(\omega_{V-I}\right)_V = \begin{bmatrix} \dot{\psi}\sin\gamma + U_1 + \Omega_E C_1 \\ -\dot{\gamma} + U_2 - \Omega_E C_3 \\ \dot{\psi}\cos\gamma + U_3 + \Omega_E C_2 \end{bmatrix}_V \tag{3.58}$$

Now, transforming to the body frame using $\mathbf{T}_\mathbf{V}^\mathbf{B}$, performing the cross product with $\hat{\mathbf{x}}_\mathbf{B}$ as shown in Equation 3.53, and adding the terms previously defined for Equation 3.53, the body rates q_{body} and r_{body} can be expressed in terms of $\dot{\theta}$ and $\dot{\phi}$.

$$\begin{bmatrix} 0 \\ r_{body} \\ -q_{body} \end{bmatrix} = \begin{bmatrix} 0 \\ \dot{\phi}\cos\theta \\ \dot{\theta} \end{bmatrix}_B + \begin{bmatrix} 0 \\ \dot{\gamma}\sin\theta\sin\phi + \dot{\psi}\left(\cos\gamma\cos\theta - \sin\gamma\sin\theta\cos\phi\right) \\ -\left(U_1 + \Omega_E C_1\right)\sin\theta\cos\phi - \left(U_2 - \Omega_E C_3\right)\sin\theta\sin\phi + \left(U_3 + \Omega_E C_2\right)\cos\theta \\ \dot{\gamma}\cos\phi + \dot{\psi}\sin\gamma\sin\phi + \\ \left(U_1 + \Omega_E C_1\right)\sin\phi + \left(U_2 - \Omega_E C_3\right)\cos\phi \end{bmatrix}_B \tag{3.59}$$

The equation above can now be solved for $\dot{\theta}$ and $\dot{\phi}$ to obtain expressions for the body attitude dynamics relative to the velocity vector in terms of the pitch and yaw body rates, q_{body} and r_{body}.

$$\begin{aligned} \dot{\phi} = {} & r_{body}\sec\theta - \dot{\gamma}\tan\theta\sin\phi + \dot{\psi}\left(\sin\gamma\tan\theta\cos\phi - \cos\gamma\right) \\ & + \left(U_1 + \Omega_E C_1\right)\tan\theta\cos\phi + \left(U_2 - \Omega_E C_3\right)\tan\theta\sin\phi - U_3 - \Omega_E C_2 \end{aligned} \tag{3.60}$$

$$\begin{aligned} \dot{\theta} = {} & -q_{body} - \dot{\gamma}\cos\phi - \dot{\psi}\sin\gamma\sin\phi \\ & - \left(U_1 + \Omega_E C_1\right)\sin\phi - \left(U_2 - \Omega_E C_3\right)\cos\phi \end{aligned} \tag{3.61}$$

The equations here describe the motion of the vehicle nose relative to the velocity vector. The state angles, θ and ϕ, can be used to compute the aerodynamic angles, α and σ, as shown in chapter 2. The lift and drag forces present in the translational equations of motion are explicit functions of α and σ.

Notice that the equations above each have contributions from the rotations of the V frame, UDC frame, and REF frame, as well as the body rates. The terms containing $\dot{\psi}$ and $\dot{\gamma}$ represent the effects of the velocity frame rotation, the U_i terms represent the effects of the rotating UDC frame, and the C_i terms represent the effects of the rotating REF frame. The effects from the rotation of the Earth involve Ω_E, which is on the order of $10^{-5}\,rad/s$, multiplied by the sum of at most eight different sinusoidal terms. Therefore,

these terms will be on the order of $10^{-4} - 10^{-5}\, rad/s$. The contributions from the UDC frame rotation, U_i, are bounded by a maximum of $\frac{V}{r}$. Since the vehicle in this study reaches a maximum velocity of approximately 16,000 feet per second (4877 m/s) and flies primarily at suborbital altitudes (r $\approx$ 6380 km), these terms are on the order of $10^{-4}\, rad/s$. In contrast, the body rates (q_{body}, r_{body}) and the velocity rates ($\dot{\gamma}$, $\dot{\psi}$) are commanded by large lift and thrust forces and control torques and, therefore, will be more on the order of 10^{-1} radians per seconds. Therefore, in the analysis presented in this thesis, effects on the rotational dynamics due to the Earth's rotation, C_i, and the local horizontal rotation, U_i, will be neglected.

3.3 Singularities

The 6DOF equations derived in the previous two sections have the advantage of providing a uniform description of vehicle motion about a rotating, spherical Earth for both endo-atmospheric and exo-atmospheric flight. However, the equations contain singularities that must be carefully avoided in order to allow computation of an optimal trajectory.

The most problematic singularity is the presence of $\cos\gamma$ in the denominator of terms determining $\dot{\psi}$. The reason for this is that the vehicle heading direction is undefined when γ is 90 degrees, i.e. the velocity vector points straight up, along the radial vector. To avoid this singularity, the flight path angle is bounded by ± 89 degrees. Similarly, a singularity occurs when the Earth-relative velocity magnitude, V_E, is equal to zero. Therefore, velocity will be bounded to be greater than zero. The only difficulty that arises from these bounds is choosing initial conditions for the launch vehicle. As suggested by Ashley [3], the initial conditions can be chosen a few moments after launch when the vehicle has a finite velocity magnitude and a finite heading angle (i.e. $|\gamma| < 89$).

Another singularity occurs in the $\dot{\mu}$ equations when λ is equal to 90 degrees (i.e. the position vector is perpendicular to the plane of reference). This singularity is particularly troublesome for formulations using the Equator as the plane of reference because trajectories are not allowed to fly over the poles. However, the formulation described in chapter 2 takes care of this problem by allowing an arbitrary choice for the plane of reference.

Lastly, a singularity occurs in the computation of the lift bank angle, σ, from the angles θ and ϕ, given in chapter 2.

$$\begin{aligned} \sin\alpha &= \sqrt{1-\cos\theta^2\cos\phi^2} \\ \cos\sigma &= \frac{\sin\theta}{\sin\alpha} \\ \sin\sigma &= \frac{\cos\theta\sin\phi}{\sin\alpha} \end{aligned}$$

When θ and ϕ are both exactly zero, the angle of attack, α, equals zero and the body nose is oriented directly along the velocity vector. Since the lift direction is defined by the orientation of the $\mathbf{x_B}$ axis relative to the $\mathbf{x_V}$ axis, the lift direction, and therefore σ, are undefined when α equals zero. The singularity can be avoided by fixing σ to equal zero when α is exactly zero. Fixing this value will not affect the results because the lift force is also equal to zero when α equals zero, and the only place where σ is used in the equations of motion is to calculate lift.

Other singularities are possible if r or m are equal to zero, or if θ is equal to 90 degrees, but these singularities are never encountered due to the definition of the problem.

3.4 Summary

In this chapter, a six-degrees of freedom (6DOF) vehicle dynamic model was formulated to govern the translational and rotational motion of the vehicle in both exo-atmospheric and endo-atmospheric flight. The states of the system are chosen to be the radial distance from the Earth's center, r, relative longitude, μ, relative latitude, λ, Earth-relative velocity magnitude, V_E, flight path angle, γ, heading angle, ψ, body pitch rate, q_{body}, body yaw rate, r_{body}, nose pitch angle, θ, and nose yaw angle, ϕ.

$$\mathbf{x} = \begin{bmatrix} r \\ \mu \\ \lambda \\ V_E \\ \gamma \\ \psi \\ q_{body} \\ r_{body} \\ \theta \\ \phi \end{bmatrix} \tag{3.62}$$

For the long range, high speed flights desired for this vehicle, it is important to include Coriolis and centrifugal effects on the translational motion of the vehicle from the Earth's rotation. These accelerations will cause the vehicle to drift to a different final destination (r, μ, λ) since the ground position of the target will be rotating over time.

The contributions to the rotational dynamics from the Earth's rotation and the UDC frame rotation can be neglected in the computational analysis due to their small magnitudes relative to the high rotational dynamics of $\dot{\theta}$ and $\dot{\phi}$. These neglected terms include the following terms from the $\dot{\theta}$ and $\dot{\phi}$ equations:

$$-(U_1 + \Omega_E C_1)\sin\phi - (U_2 - \Omega_E C_3)\cos\phi$$
$$(U_1 + \Omega_E C_1)\tan\theta\cos\phi + (U_2 - \Omega_E C_3)\tan\theta\sin\phi - U_3 - \Omega_E C_2$$

The full 6DOF equations of motion, including the neglected terms, are presented below.

$$\dot{r} = V_E \sin\gamma \tag{3.63}$$

$$\dot{\mu} = \frac{V_E \cos\gamma \cos\psi}{r \cos\lambda} \tag{3.64}$$

$$\dot{\lambda} = \frac{V_E \cos\gamma \sin\psi}{r} \tag{3.65}$$

$$\dot{V}_E = \frac{T_A \cos\alpha}{m} - \frac{D}{m} - \frac{\mu_G}{r^2}\sin\gamma - \Omega_E^2 r F_1 \tag{3.66}$$

$$\dot{\gamma} = \frac{T_A \sin\alpha \cos\sigma}{m} + \frac{L\cos\sigma}{mV} + \left(\frac{V_E}{r} - \frac{\mu_G}{r^2 V_E}\right)\cos\gamma - 2\Omega_E C_2 - \frac{r\Omega_E^2 F_2}{V_E} \tag{3.67}$$

$$\dot{\psi} = \frac{T_A \sin\alpha \sin\sigma}{m} + \frac{L\sin\sigma}{mV\cos\gamma} - \frac{V_E}{r}\cos\gamma\cos\psi\tan\lambda - \frac{2\Omega_E C_3}{\cos\gamma} - \frac{r\Omega_E^2 F_3}{V_E\cos\gamma} \tag{3.68}$$

$$\dot{q}_{body} = \frac{\sum \tau_{y_B}}{I_{yy}} \tag{3.69}$$

$$\dot{r}_{body} = \frac{\sum \tau_{z_B}}{I_{zz}} \tag{3.70}$$

$$\begin{aligned}\dot{\theta} = &-q_{body} - \dot{\gamma}\cos\phi - \dot{\psi}\sin\gamma\sin\phi \\ &- (U_1 + \Omega_E C_1)\sin\phi - (U_2 - \Omega_E C_3)\cos\phi\end{aligned} \tag{3.71}$$

$$\begin{aligned}\dot{\phi} = &\, r_{body}\sec\theta - \dot{\gamma}\tan\theta\sin\phi + \dot{\psi}(\sin\gamma\tan\theta\cos\phi - \cos\gamma) \\ &+ (U_1 + \Omega_E C_1)\tan\theta\cos\phi + (U_2 - \Omega_E C_3)\tan\theta\sin\phi - U_3 - \Omega_E C_2\end{aligned} \tag{3.72}$$

where

$$C_1 = \frac{\omega_1 \sin\gamma + \omega_2 \cos\gamma\cos\psi + \omega_3\cos\gamma\sin\psi}{\Omega_E} \tag{3.73}$$

$$C_2 = \frac{\omega_1\cos\gamma - \omega_2\sin\gamma\cos\psi - \omega_3\sin\gamma\sin\psi}{\Omega_E} \tag{3.74}$$

$$C_3 = \frac{\omega_2\sin\psi - \omega_3\cos\psi}{\Omega_E} \tag{3.75}$$

$$F_1 = \frac{(-\omega_2^2 - \omega_3^2)\sin\gamma + \omega_1\omega_2\cos\gamma\cos\psi + \omega_1\omega_3\cos\gamma\sin\psi}{\Omega_E^2} \tag{3.76}$$

$$F_2 = \frac{-\omega_1\omega_2\sin\psi + \omega_1\omega_3\cos\psi}{\Omega_E^2} \tag{3.77}$$

$$F_3 = \frac{(-\omega_2^2 - \omega_3^2)\cos\gamma - \omega_1\omega_2 \sin\gamma\cos\psi - \omega_1\omega_3 \sin\gamma\sin\psi}{\Omega_E^2} \tag{3.78}$$

$$U_1 = \frac{V_E \cos\psi\cos\gamma\sin\gamma\tan\lambda}{r} \tag{3.79}$$

$$U_2 = \frac{V_E \cos^2\gamma}{r} \tag{3.80}$$

$$U_3 = \frac{V_E \cos^2\gamma\cos\psi\tan\lambda}{r} \tag{3.81}$$

$$\omega_1 = \Omega_E\left(\cos\mu\cos\lambda\sin\theta_0\sin i_0 + \sin\mu\cos\lambda\cos\theta_0\sin i_0 + \sin\lambda\cos i_0\right) \tag{3.82}$$

$$\omega_2 = \Omega_E\left(-\sin\mu\sin\theta_0\sin i_0 + \cos\mu\cos\theta_0\sin i_0\right) \tag{3.83}$$

$$\omega_3 = \Omega_E\left(-\cos\mu\sin\lambda\sin\theta_0\sin i_0 - \sin\mu\sin\lambda\cos\theta_0\sin i_0 + \cos\lambda\cos i_0\right) \tag{3.84}$$

$$\sin\alpha = \sqrt{1 - \cos\theta^2\cos\phi^2} \tag{3.85}$$

$$\cos\sigma = \frac{\sin\theta}{\sin\alpha} \tag{3.86}$$

$$\sin\sigma = \frac{\cos\theta\sin\phi}{\sin\alpha} \tag{3.87}$$

Notice that if i_0 and θ_0 are set to zero in the above expressions, the familiar 6DOF equations of motion used by Bollino [14] are obtained.

Now that the dynamical model of the vehicle has been formulated, the flight profile will be elaborated upon in detail in the next chapter.

[This page intentionally left blank.]

Chapter 4

The Optimal Control Problem

In the previous chapters, a 6DOF dynamics model was developed to describe the motion of a skid-to-turn maneuvering vehicle. In this chapter, a nonlinear optimal control problem will be formulated that applies the vehicle dynamics model as a set of constraints on the optimal control solution. The optimal control problem will seek to minimize a performance index

$$J\left(\mathbf{x}\left(t\right),\mathbf{u}\left(t\right),t_0,t_f\right)=E\left(\mathbf{x}\left(t_0\right),\mathbf{x}\left(t_f\right),t_0,t_f\right)+\int_{t_0}^{t_f}F\left(\mathbf{x}\left(t\right),\mathbf{u}\left(t\right),t\right)\,dt$$

subject to the *dynamic constraints*,

$$\dot{\mathbf{x}}=\mathbf{f}\left(\mathbf{x}\left(t\right),\mathbf{u}\left(t\right),t\right)$$

event constraints,

$$\mathbf{e}^L\leq\mathbf{e}\left(\mathbf{x}\left(t_0\right),\mathbf{x}\left(t_f\right),t_0,t_f\right)\leq\mathbf{e}^U$$

path constraints,

$$\mathbf{h}^L\leq\mathbf{h}\left(\mathbf{x}\left(t\right),\mathbf{u}\left(t\right),t\right)\leq\mathbf{h}^U$$

and the *state and control bounds*

$$\mathbf{x}^L \leq \mathbf{x}(t) \leq \mathbf{x}^U$$
$$\mathbf{u}^L \leq \mathbf{u}(t) \leq \mathbf{u}^U$$

As mentioned in chapter 1, a direct optimization method will be used to solve the optimal control problem presented in this thesis. In order to enhance understanding of the results, fundamental concepts from optimal control and nonlinear programming theory will be discussed here. In particular, the necessary conditions for indirect methods will be formulated and it will be shown why solving the problem in this manner presents several difficulties for the problem in this thesis. Additional considerations for proper problem formulation, such as the use of knots and parameter scaling, will also be discussed.

4.1 Optimal Control Fundamentals

The optimal control problem involves a state, $\mathbf{x}(t)$, that is governed by a set of nonlinear differential equations:

$$\dot{\mathbf{x}} = \mathbf{f}(\mathbf{x}(t), \mathbf{u}(t), t) \tag{4.1}$$

As can be seen in the Equation 4.1, the rate of change of the state, $\mathbf{x}(t)$, is dependent on the control $\mathbf{u}(t)$. The optimal control problem attempts to solve for the control solution $\mathbf{u}(t)$ that controls the state $\mathbf{x}(t)$ in some optimal way. In essence, by choosing the optimal control, the solution to the problem will determine a *feasible* and *optimal* state-control function-pair, $(\mathbf{x}(t), \mathbf{u}(t))$ [6].

4.1.1 Performance Index

The desired optimal control is dependent on the specification of a *performance index*, or *objective function*, $J(\mathbf{x}(t), \mathbf{u}(t), t_0, t_f)$. This is the parameter that algorithm will attempt to minimize subject to the constraints. The optimal control, $\mathbf{u}(t)$, is chosen in a way to minimize the performance index:

$$J\left(\mathbf{x}\left(t\right),\mathbf{u}\left(t\right),t_0,t_f\right)=E\left(\mathbf{x}\left(t_0\right),\mathbf{x}\left(t_f\right),t_0,t_f\right)+\int_{t_0}^{t_f}F\left(\mathbf{x}\left(t\right),\mathbf{u}\left(t\right),t\right)\,dt \tag{4.2}$$

The objective function given above is expressed in Bolza form, J, which contains a Mayer term, E, and a Lagrange term, F. The Mayer term, $E\left(\mathbf{x}\left(t_0\right),\mathbf{x}\left(t_f\right),t_0,t_f\right)$, represents the *terminal cost*, as determined by state and control values at the terminal points of a trajectory, and the Lagrange term, $F\left(\mathbf{x}\left(t\right),\mathbf{u}\left(t\right),t\right)$, represents the cost that accumulates over the time interval of a trajectory segment. The vehicle state and control pair $\left(\mathbf{x}\left(t\right),\mathbf{u}\left(t\right)\right)$ that minimizes $J\left(\mathbf{x}\left(t\right),\mathbf{u}\left(t\right),t_0,t_f\right)$ while also satisfying all dynamic, path, and event constraints is a solution to the optimal control problem.

4.1.2 Necessary Conditions and The Minimum Principle

A set of necessary conditions for indirect methods are derived here using Calculus of Variations and Pontryagin's Minimum Principle. The necessary conditions define first-order optimality subject to a set of constraints on the states and controls. As with any constrained optimization problem, constraints can be incorporated into the problem using Lagrange multipliers. Since the control chosen must satisfy the vehicle state dynamics over the entire trajectory, the dynamics equation (4.1) becomes a differential constraint in this problem. It can be adjoined to the objective function with a set of Lagrange multipliers, $\mathbf{p}$:

$$\begin{aligned}J_a\left(\mathbf{x}\left(t\right),\mathbf{u}\left(t\right),\mathbf{p}\left(t\right),t_0,t_f\right)=&E\left(\mathbf{x}\left(t_0\right),\mathbf{x}\left(t_f\right),t_0,t_f\right)\\&+\int_{t_0}^{t_f}\left[F\left(\mathbf{x}\left(t\right),\mathbf{u}\left(t\right),t\right)+\mathbf{p}^T\left(t\right)\left[\mathbf{f}\left(\mathbf{x}\left(t\right),\mathbf{u}\left(t\right),t\right)-\dot{\mathbf{x}}\right]\right]\,dt\end{aligned} \tag{4.3}$$

The value of the objective function remains the same because the additional term added to the right side of the equation is defined to be zero at all times. The Lagrange multipliers adjoining the dynamics to the performance index, $\mathbf{p}$, are referred to as the

dual variables or *co-states*. The necessary conditions for optimality in this problem can be solved by the Calculus of Variations by setting the variation of the objective function, δJ_a, equal to zero. The initial state, $\mathbf{x}(t_0)$, and time, t_0, are assumed here to be fixed, but the final state, $\mathbf{x}(t_f)$ and time, t_f, may either be fixed or free to vary. In order to simplify the notation, the following expression is defined as the *control Hamiltonian*, H:

$$H(\mathbf{x}(t), \mathbf{u}(t), \mathbf{p}(t), t) = F(\mathbf{x}(t), \mathbf{u}(t), t) + \mathbf{p}^T(t)[\mathbf{f}(\mathbf{x}(t), \mathbf{u}(t), t) - \dot{\mathbf{x}}] \tag{4.4}$$

By solving the equation $\delta J_a = 0$, using partial differentiation with respect to the varying parameters and integration by parts, the following necessary conditions for optimality and feasibility are found to satisfy $\delta J_a = 0$ in terms of the Hamiltonian:

Necessary Conditions

$$\dot{\mathbf{p}} = -\left(\frac{\partial H}{\partial \mathbf{x}}\right)^T \tag{4.5}$$

$$\frac{\partial H}{\partial \mathbf{u}} = 0 \tag{4.6}$$

$$\dot{\mathbf{x}} = \mathbf{f}(\mathbf{x}(t), \mathbf{u}(t), t) \tag{4.7}$$

Boundary Conditions

$$\frac{\partial E}{\partial t_f} + H(\mathbf{x}(t_f), \mathbf{u}(t_f), \mathbf{p}(t_f), t_f) = 0 \quad \text{if } t_f \text{ free} \tag{4.8}$$

$$p_i(t_f) = \left(\frac{\partial E}{\partial x_i}\right)^T \quad \text{for each } x_i(t_f) \text{ free} \tag{4.9}$$

The necessary conditions above define a two-point boundary value problem. The first three conditions are conditions that must hold over the entire time interval, while the final two expressions are terminal boundary conditions. The first necessary condition provides a set of differential equations for the co-states, $\mathbf{p}(t)$, while the second necessary condition expresses the control, $\mathbf{u}(t)$, in terms of the states and co-states. The third necessary condition ensures that the vehicle dynamics are satisfied throughout the trajectory. The first boundary condition, called the *transversality condition*, is only active if the final time

t_f is free to vary in the problem. The second boundary condition will impose boundary values for the co-states associated with any terminal states that are not fixed. Solving the boundary value problem formulated above guarantees first-order optimality and feasibility of an optimal control solution.

For problems with a constrained set of allowable controls, $\mathbf{u} \in U$, *Pontryagin's Minimum Principle* dictates that the optimal control solution will be the choice of controls that minimizes the Hamiltonian.

$$\mathbf{u}^* = \arg\min_{\mathbf{u}\in U} H\left(\mathbf{x}\left(t\right), \mathbf{u}\left(t\right), \mathbf{p}\left(t\right), t\right)$$

In addition to the dynamic constraints considered in this section, terminal constraints and path constraints can also be incorporated into the problem, as will be shown in the next few sections.

4.1.3 Event Constraints

Event constraints, $\mathbf{e}$, specify a set of terminal constraints imposed at the end points of a trajectory in terms of either inequality or equality constraints. They can be incorporated into the optimal control problem just as the dynamic constraints were incorporated into the problem in the previous section using a set of Lagrange multipliers.

$$\mathbf{e}^L \leq \mathbf{e}\left(\mathbf{x}\left(t_0\right), \mathbf{x}\left(t_f\right), t_0, t_f\right) \leq \mathbf{e}^U \tag{4.10}$$

The expression above is equivalent to an equality constraint when $\mathbf{e}^L = \mathbf{e}^U$ [6]. The inequality constraints can also be expressed in the following general form:

$$\mathbf{e}\left(\mathbf{x}\left(t_0\right), \mathbf{x}\left(t_f\right), t_0, t_f\right) \leq \mathbf{0}$$

Since the event constraints act at the terminal points of a trajectory segment, they are adjoined to the Mayer term, E, in the objective function using the Lagrange multipliers, ν.

$$J_a(\mathbf{x}(t),\mathbf{u}(t),\mathbf{p}(t),t_0,t_f) = E(\mathbf{x}(t_0),\mathbf{x}(t_f),t_0,t_f) + \nu(\mathbf{t})^T\mathbf{e}(\mathbf{x}(t_0),\mathbf{x}(t_f),t_0,t_f) + \int_{t_0}^{t_f}\left[F(\mathbf{x}(t),\mathbf{u}(t),t) + \mathbf{p}(t)^T\left[\mathbf{f}(\mathbf{x}(t),\mathbf{u}(t),t) - \dot{\mathbf{x}}\right]\right]dt$$

Since the adjoined term must be equal to zero at all times, it is important to identify whether each event constraint is active ($e_i = 0$) or inactive ($e_i < 0$). The values of the Lagrange multipliers, ν, will be constrained to different values depending on how the event constraints are met.

$$\nu_i \begin{cases} \geq 0 & \text{if } e_i = 0 \quad \text{active} \\ = 0 & \text{if } e_i < 0 \quad \text{inactive} \end{cases}$$

By setting the variation $\delta J_a = 0$, the event constraints then become incorporated into the boundary conditions of the two-point boundary value problem in the previous section. While the first three necessary conditions remain identical to the conditions given in Equations 4.5 - 4.7, the modified boundary conditions are given by the following expressions.

$$\begin{aligned} \frac{\partial \overline{E}}{\partial t_f} + H(\mathbf{x}(t_f),\mathbf{u}(t_f),\mathbf{p}(t_f),t_f) &= 0 && \text{if } t_f \text{ free} \\ p_i(t_f) &= \left(\frac{\partial \overline{E}}{\partial x_i}\right)^T && \text{for each } x_i(t_f) \text{ free} \end{aligned}$$

where

$$\overline{E} = E(\mathbf{x}(t_0),\mathbf{x}(t_f),t_0,t_f) + \nu^T\mathbf{e}(\mathbf{x}(t_0),\mathbf{x}(t_f),t_0,t_f)$$

4.1.4 Path Constraints

The path constraints, in contrast, specify constraints that must be met at every point along the trajectory. In the problems examined in this thesis, path constraints will be examined that are functions of both the time-varying states and controls.

$$\mathbf{h}^L \leq \mathbf{h}(\mathbf{x}(t),\mathbf{u}(t),t) \leq \mathbf{h}^U \tag{4.11}$$

In similar fashion to the manipulation of the event constraints, the path constraints

can be expressed in the following general form.

$$\mathbf{h}\left(\mathbf{x}\left(t\right),\mathbf{u}\left(t\right),t\right)\leq\mathbf{0}$$

They can be incorporated into the optimal control problem by adjoining them to the Lagrange term, F, using a set of Lagrange multipliers, μ.

$$\begin{aligned}J_a\left(\mathbf{x}\left(t\right),\mathbf{u}\left(t\right),\mathbf{p}\left(t\right),t_0,t_f\right)= & \ E\left(\mathbf{x}\left(t_0\right),\mathbf{x}\left(t_f\right),t_0,t_f\right)+\nu\left(\mathbf{t}\right)^T\mathbf{e}\left(\mathbf{x}\left(t_0\right),\mathbf{x}\left(t_f\right),t_0,t_f\right)\\ & +\int_{t_0}^{t_f}\left[F\left(\mathbf{x}\left(t\right),\mathbf{u}\left(t\right),t\right)+\mathbf{p}\left(\mathbf{t}\right)^T\left(t\right)\left[\mathbf{f}\left(\mathbf{x}\left(t\right),\mathbf{u}\left(t\right),t\right)-\dot{\mathbf{x}}\right]\right.\\ & \left.+\mu^T\left(t\right)\mathbf{h}\left(\mathbf{x}\left(t\right),\mathbf{u}\left(t\right),t\right)\right]dt\end{aligned}$$

As with the event constraints, the Lagrange multipliers associated with the path constraints will have different values depending on whether the path constraints are active or inactive. Unlike the event constraints, path constraints act over all portions of the trajectory. The portions of the trajectory during which a path constraint is active and the portions of the trajectory during which the path constraints are inactive must be identified in order to apply the proper constraints on the Lagrange multipliers, given below.

$$\mu_i\left\{\begin{array}{lll}\geq 0 & \text{if}\, h_i=0 & \text{active}\\ =0 & \text{if}\, h_i<0 & \text{inactive}\end{array}\right\}$$

The Hamiltonian can be augmented with the path constraints using the set of Lagrange multipliers, μ, as shown below.

$$H_a\left(\mathbf{x}\left(t\right),\mathbf{u}\left(t\right),\mathbf{p}\left(t\right),t\right)=F\left(\mathbf{x}\left(t\right),\mathbf{u}\left(t\right),t\right)+\mathbf{p}^T\left(t\right)\left[\mathbf{f}\left(\mathbf{x}\left(t\right),\mathbf{u}\left(t\right),t\right)-\dot{\mathbf{x}}\right]+\mu^T\left(t\right)\mathbf{h}\left(\mathbf{x}\left(t\right),\mathbf{u}\left(t\right),t\right)$$

The necessary conditions for an optimal control problem with dynamic, path, and event constraints are now derived in terms of the augmented Hamiltonian.

$$
\begin{aligned}
\dot{\mathbf{p}} &= -\left(\frac{\partial H_a}{\partial \mathbf{x}}\right)^T \\
\frac{\partial H_a}{\partial \mathbf{u}} &= 0 \\
\dot{\mathbf{x}} &= \mathbf{f}\left(\mathbf{x}\left(t\right), \mathbf{u}\left(t\right), t\right) \\
\frac{\partial \overline{E}}{\partial t_f} &+ H_a\left(\mathbf{x}\left(t_f\right), \mathbf{u}\left(t_f\right), \mathbf{p}\left(t_f\right), t_f\right) = 0 \qquad \text{if } t_f \text{ free} \\
p_i\left(t_f\right) &= \left(\frac{\partial \overline{E}}{\partial x_i}\right)^T \qquad \text{for each } x_i\left(t_f\right) \text{ free}
\end{aligned}
$$

The path constraints add additional complications to the optimal control problem because they act over all parts of the trajectory while the event constraints only act at the trajectory end points. Therefore, the portions of the trajectory in which the path constraints are active must be identified prior to solving an optimal control problem with indirect methods. For example, an optimal control problem with the heating constraint, $q \leq q_{max}$, can only be solved by specifying a priori which portions of the trajectory meet the constraint $q = q_{max}$ and which portions of the trajectory have an inactive heating constraint $q < q_{max}$. This amounts to specifying a sequence of constrained and unconstrained trajectory arcs prior to solving the problem [7]. This presents a challenging obstacle to indirect solution methods since path constraints, such as heating constraints and g-loading constraints, are important limitations to the problem considered in this study.

4.1.5 Indirect Method Challenges

Indirect solution methods take the approach of solving the two-point boundary value problem, requiring a separate analytic derivation of the necessary conditions in Equations (4.5 - 4.9) for each case. For problems with complex dynamics, such as the problem considered in this thesis, this can become challenging and time consuming. This derivation process must be repeated for each new optimization problem, presenting a difficulty for analyzing the maximum and minimum capabilities of several different parameters.

As mentioned in the preceding section, indirect methods have a difficulty incorporating important path inequality constraints into the optimal control problem. In particular, the

trajectory must be segmented into portions which contain active equality constraints and portions which contain inequality constraints that are defined prior to solving the problem.

In order to avoid these potential challenges, a direct collocation method is used to solve the optimal control problem that allows the use of dynamic, path, and event constraints without the need to derive necessary conditions or specify path-constrained trajectory arcs a priori.

4.2 Nonlinear Programming Concepts

The direct collocation method used in this study approaches the problem by solving a discretized nonlinear programming problem (NLP) rather than the two-point boundary value problem. Direct collocation transforms the optimal control problem, via discretization, into an NLP with a much larger number of variables. The NLP is then solved using an iterative algorithm which seeks to improve the performance index at each step until a minimum value is reached. The nonlinear programming problem for determining an optimal choice for the variables, $\mathbf{x}$, that minimizes the nonlinear function, $\mathbf{f}(\mathbf{x})$ is formulated as follows:

$$\begin{aligned} & \min_{\mathbf{x}} \mathbf{f}(\mathbf{x}) \\ \text{subject to} \quad & g_i(\mathbf{x}) \leq 0 \quad \forall i = 1, \ldots, l \\ & h_j(\mathbf{x}) = 0 \quad \forall j = 1, \ldots, m \\ & \mathbf{x} \in X \end{aligned}$$

The standard nonlinear programming problem solves static problems, not dynamic problems with states that vary over time. The key to solving dynamic optimal control problems with nonlinear programming is the use of proper discretization techniques. The time history of the states and controls can be discretized into a set of discrete variables (x_{ij}, u_{ij}) at nodal points corresponding to the discrete times t_i. The total number of variables in the nonlinear programming problem will be

$$N = N_t (N_x + N_u)$$

where N_t is the number of nodes, N_x is the number of states, and N_u is the number of controls. The continuous functions approximated by the discrete nodal points are more accurately represented with a higher number of nodes, but an increase in the number of nodes significantly increases the number of variables in the problem, and, thus, the computation time.

The DIDO solver used in this analysis uses Legendre polynomials to approximate the continuous functions in the optimal control problem. The pseudospectral method implemented in the DIDO solver places the nodal points at Legendre-Gauss-Lobatto (LGL) points to provide an exponential convergence rate for the approximation of analytic functions [19]. Detailed discussion of the pseudospectral discretization is available in [12] and [15].

The underlying nonlinear programming solver that solves the discretized optimal control problem in the DIDO software used for this project is SNOPT. SNOPT is a general purpose optimization software package that solves optimization problems with the use of Sequential Quadratic Programming (SQP) [12]. The solver performs a series of iterations using quadratic approximations to the problem to determine a direction and a distance along that direction to search for the minimum performance index [15]. The optimizer returns when the first-order optimality conditions are met. These conditions are discussed in the next section.

4.2.1 Optimality Conditions

Similar to optimal control formulations, nonlinear programming problems return with an optimal solution if and only if both feasibility and optimality are achieved to some tolerance. Feasibility is often dictated by the *primal problem*, while optimality is dictated by the *dual problem*. An illustration of this can be shown with a simple linear programming problem, containing a linear performance index, $\mathbf{c}^T\mathbf{x}$ subject to a set of linear constraints, $A\mathbf{x} \leq \mathbf{b}$. The primal problem with optimal solution $\mathbf{x}^*$ is given as

$$\min \mathbf{c}^T\mathbf{x}$$
$$s.t.\ A\mathbf{x} \geq \mathbf{b}$$

The optimization of trajectory parameters subject to dynamic, path, and event constraints is also a primal problem. The objective of the primal problem is to find a minimum value of the performance index within a *feasible space* bounded by the constraints ($\mathbf{b} - A\mathbf{x} \leq 0$). Notice that the primal problem has strict bounds on the feasible space bounded by the constraints. The primal problem can be *relaxed* by removing the constraints and adjoining them to the performance index with a set of Lagrange multipliers, $\mathbf{p}$. $\mathbf{p}$ can be thought of as a price, or penalty, that is imposed with every incremental violation of the constraints. Since the adjoined constraint should incur a positive penalty when violated, $\mathbf{p}$ is constrained to be nonnegative ($\mathbf{p} \geq \mathbf{0}$). Notice that this is the same approach taken when deriving the Necessary Conditions in section 4.1.2.

$$\begin{aligned} & \min_{\mathbf{x}} \mathbf{c}^T\mathbf{x} + p^T(\mathbf{b} - A\mathbf{x}) \\ s.t. \quad & \mathbf{x} \text{ free} \end{aligned}$$

Since the new problem is now more relaxed than the initial problem (i.e. fewer constraints), its minimum performance index must be less than or equal to the minimum performance index of the initial problem, $\mathbf{c}^T\mathbf{x}^*$ [20].

$$\min_{\mathbf{x}} \mathbf{c}^T\mathbf{x} + \mathbf{p}^T(\mathbf{b} - A\mathbf{x}) \;=\; \mathbf{p}^T\mathbf{b} + \min_{\mathbf{x}} \left(\mathbf{c}^T - \mathbf{p}^T A\right)\mathbf{x} \leq \mathbf{c}^T\mathbf{x}^*$$

Therefore, the maximum value of the performance index in the relaxed problem provides a *lower bound* on the performance index of the primal problem [20]. In other words, by finding the maximum value of the relaxed problem, the minimum value of the primal problem is also found.

$$\max_{\mathbf{p}} \left[\mathbf{p}^T\mathbf{b} + \min_{\mathbf{x}} \left(\mathbf{c}^T - \mathbf{p}^T A\right)\mathbf{x}\right] = \mathbf{c}^T\mathbf{x}^*$$

Notice that the performance index for the relaxed problem contains a minimization of $\left(\mathbf{c}^T - \mathbf{p}^T A\right)\mathbf{x}$ over all values of $\mathbf{x}$. The maximum value that this minimization term can be is zero when the coefficient $\mathbf{c}^T - \mathbf{p}^T A$ is equal than zero. If this coefficient is any value other than zero, the minimization will pick a value for $\mathbf{x}$ that makes the term

approach $-\infty$. In addition, the Lagrange multipliers are constrained to be nonnegative, as mentioned earlier. Therefore, the *dual problem* is given as the following maximization problem.

$$\begin{aligned} &\max_{\mathbf{p}} \mathbf{p}^T \mathbf{b} \\ &s.t. \, \mathbf{p}^T A = \mathbf{c}^T \\ &\mathbf{p} \geq \mathbf{0} \end{aligned}$$

At the optimal solution, the maximum value of the dual problem will be equal to the minimum value of the primal problem ($\mathbf{c}^T \mathbf{x}^* = \mathbf{p}^{T^*} \mathbf{b}$). Furthermore, satisfaction of the dual constraints ($\mathbf{p}^T A = \mathbf{c}^T$, $\mathbf{p} \geq \mathbf{0}$) ensures optimality while satisfaction of the primal constraints ($A\mathbf{x} \geq \mathbf{b}$) ensures feasibility of the solution. An important relation between primal and dual optimal solutions is given by the *complementary slackness* conditions.

$$\begin{aligned} \mathbf{p}^T (A\mathbf{x} - \mathbf{b}) &= \mathbf{0} \\ \left(\mathbf{c}^T - \mathbf{p}^T A\right) \mathbf{x} &= \mathbf{0} \end{aligned}$$

Notice that this is equivalent to ensuring that the terms adjoined by Lagrange multipliers to the objective functions of the primal and dual problems must always be equal to zero. In other words, either the primal and dual constraints are met or the Lagrange multipliers adjoining them must equal zero. More about this subject can be found in [20].

The same concepts of primal feasibility, dual feasibility, and complementary slackness are used in nonlinear optimization to define the optimization conditions, known as the Karush-Kuhn-Tucker (KKT) Conditions [15]. For the general nonlinear optimization problem (Equation 4.2) with p_i and q_i representing the dual variables associated with the inequality and equality constraints, respectively, the KKT are given as

$$\nabla f(\mathbf{x}^*) = \sum_{i=1}^{l} p_i^* \nabla g_i(\mathbf{x}^*) + \sum_{j=1}^{m} q_j^* \nabla h_j(\mathbf{x}^*) \tag{4.12}$$

$$p_i^* \geq 0 \quad \forall i = 1, \ldots, l \tag{4.13}$$

$$g_i(\mathbf{x}^*) \leq 0 \quad \forall i = 1, \ldots, l \tag{4.14}$$

$$h_j(\mathbf{x}^*) = 0 \quad \forall j = 1, \ldots, m \tag{4.15}$$

$$p_i^* g_i(\mathbf{x}^*) = 0 \quad \forall i = 1, \ldots, l \tag{4.16}$$

The first two KKT conditions specify dual feasbility ($\mathbf{c}^T = \mathbf{p}^T A, \mathbf{p} \geq \mathbf{0}$ in linear case), while the third and fourth conditions specify primal feasibility and the last condition specifies the complementary slackness condition. Notice that a complementary slackness condition is not necessary for the q_j dual variables since the corresponding h_j equality constraints are already constrained to be zero by primal feasibility.

The equality and inequality constraints in the optimal control problem consist of the event constraints, path constraints, and the discretized dynamic constraints with the corresponding dual variables, $\mathbf{p}$, ν, and μ. The algorithm within SNOPT will conduct a search that attempts to move closer to satisfaction of the KKT conditions with each iteration step. DIDO will return a solution to the optimal control problem when all KKT conditions are met.

4.3 Knotting Conditions

The analysis presented in the preceding sections examined the problem of solving for an optimal trajectory subject to a single set of dynamic, event, and path constraints. In reality, many trajectories pass through portions of flight that are governed by different dynamics and which are constrained differently with respect to point and path constraints. Therefore, trajectories are often split up into separate segments, each of which has a unique set of dynamics, event constraints, and path constraints. The boundaries between the separate segments occur at points called *knots*. DIDO allows a user to place knots at fixed times along a trajectory or to specify event conditions at the knots that determine

the knot time location.

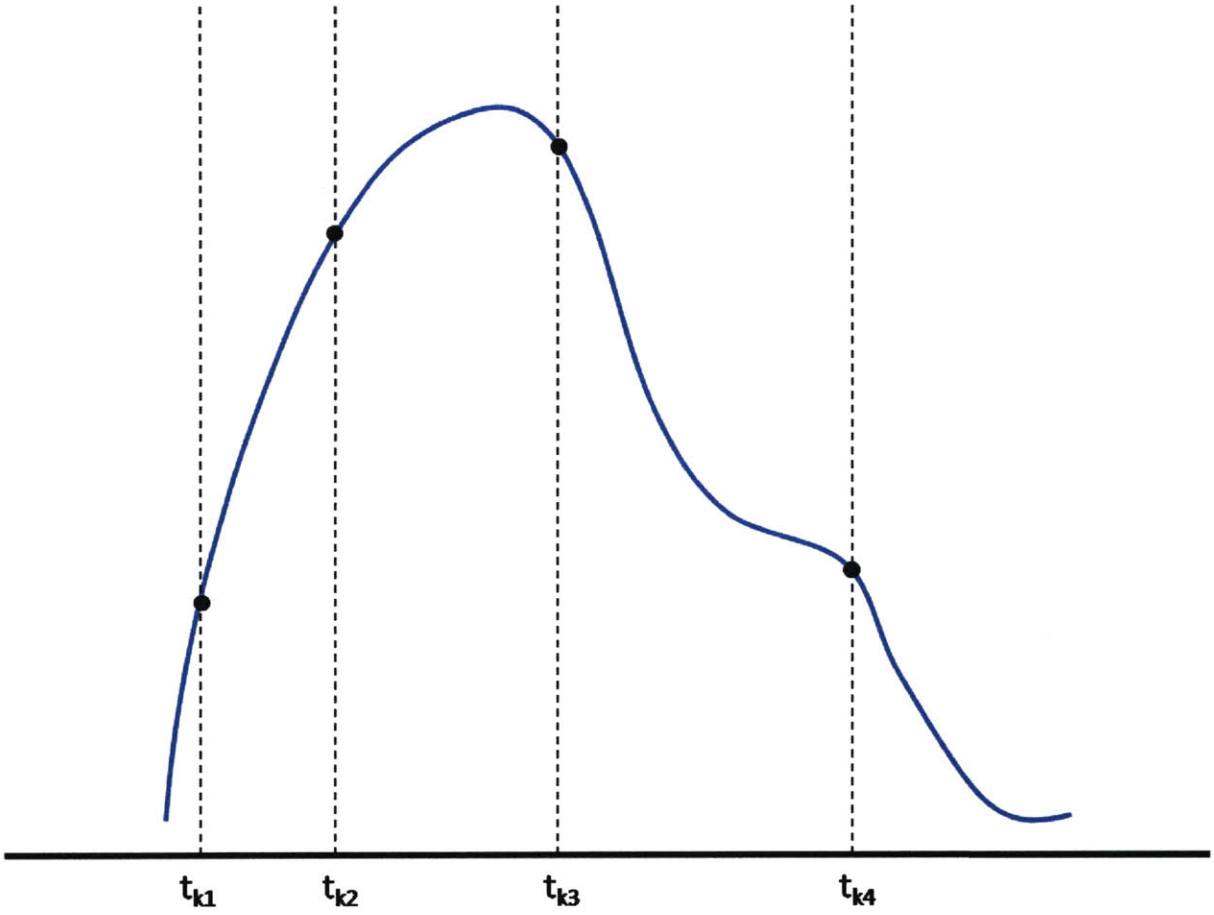

Figure 4-1: Example of Knot Locations Along Vehicle Trajectory

A set of *connection constraints* at the knot locations must connect the variables on the left side of the knot appropriately with the variables on the right side of the knot. Typical connection constraints include enforcing continuity of a particular state, such as altitude, across the knot or enforcing an instantaneous mass drop of a certain size at the knot location. Let t_{k_i} be the time of the i^{th} knot and K be the total number of interior knots (excluding knots at terminal conditions). Then the following connection constraints must be ensured for the problem studied here.

$$\begin{aligned}
r\left(t_{k_i}^+\right) - r\left(t_{k_i}^-\right) &= 0 \\
\mu\left(t_{k_i}^+\right) - \mu\left(t_{k_i}^-\right) &= 0 \\
\lambda\left(t_{k_i}^+\right) - \lambda\left(t_{k_i}^-\right) &= 0 \\
V_E\left(t_{k_i}^+\right) - V_E\left(t_{k_i}^-\right) &= 0 \\
\gamma\left(t_{k_i}^+\right) - \gamma\left(t_{k_i}^-\right) &= 0 \\
\psi\left(t_{k_i}^+\right) - \psi\left(t_{k_i}^-\right) &= 0 \qquad \forall i = 1, \ldots, K \\
q_{body}\left(t_{k_i}^+\right) - q_{body}\left(t_{k_i}^-\right) &= 0 \\
r_{body}\left(t_{k_i}^+\right) - r_{body}\left(t_{k_i}^-\right) &= 0 \\
\theta\left(t_{k_i}^+\right) - \theta\left(t_{k_i}^-\right) &= 0 \\
\phi\left(t_{k_i}^+\right) - \phi\left(t_{k_i}^-\right) &= 0
\end{aligned} \tag{4.17}$$

The event constraints located at each knot provide an opportunity for specifying interior point constraints at specific points within the trajectory. This capability will be important later when specifying certain conditions at the piercepoint reentry interface. In addition, the capability of using knots to segment the path constraints will allow for the modeling of different control approaches over different segments of the trajectory. This will become important when modeling the boost, coasting, and reentry phases of flight.

4.4 Parameter Scaling

Scaling of the problem variables is one of the most important aspects of successfully solving a complex optimal control problem. Poor scaling of the parameters in the problem can lead to a long and misdirected optimization search which increases the computation time significantly. Trajectory optimization, in particular, is aided greatly by scaling since the trajectory states exhibit significantly different magnitudes (e.g. velocity $\approx 10^3$, attitude angles $\approx 10^{-1}$).

Scaling each of the states, controls, and time essentially involves expressing the optimal control problem in a new set of units. Each of the states, controls, and time variables (y_i) are divided by a *scaling factor* (k_{y_i}), converting the SI units to scaled units.

$$\overline{y}_i = \frac{y_i}{k_{y_i}}$$

A *scaling matrix* can be established for the states and controls to allow easy and convenient transformations from SI units to scaled units. Expressions for the scaled time, τ, states, $\overline{\mathbf{x}}$, and controls, $\overline{\mathbf{u}}$ are given below.

$$\tau = \frac{t}{k_t}$$

$$\begin{bmatrix} \overline{x}_1 \\ \overline{x}_2 \\ \overline{x}_3 \\ \vdots \\ \overline{x}_N \end{bmatrix} = \begin{bmatrix} \frac{1}{k_{x_1}} & 0 & 0 & \dots & 0 \\ 0 & \frac{1}{k_{x_2}} & 0 & \dots & 0 \\ 0 & 0 & \frac{1}{k_{x_3}} & \dots & 0 \\ \vdots & & & \ddots & \\ 0 & 0 & 0 & \dots & \frac{1}{k_{x_N}} \end{bmatrix} \begin{bmatrix} x_1 \\ x_2 \\ x_3 \\ \vdots \\ x_N \end{bmatrix} = K_x \mathbf{x}$$

$$\begin{bmatrix} \overline{u}_1 \\ \overline{u}_2 \\ \overline{u}_3 \\ \vdots \\ \overline{u}_N \end{bmatrix} = \begin{bmatrix} \frac{1}{k_{u_1}} & 0 & 0 & \dots & 0 \\ 0 & \frac{1}{k_{u_2}} & 0 & \dots & 0 \\ 0 & 0 & \frac{1}{k_{u_3}} & \dots & 0 \\ \vdots & & & \ddots & \\ 0 & 0 & 0 & \dots & \frac{1}{k_{u_N}} \end{bmatrix} \begin{bmatrix} u_1 \\ u_2 \\ u_3 \\ \vdots \\ u_N \end{bmatrix} = K_u \mathbf{u}$$

Scaling of the time variable has implications for the time derivatives in the optimal control problem. The vehicle dynamics are now defined as the *scaled states*, $\overline{\mathbf{x}}$, varying with respect to the *scaled time*, τ, rather than time, t.

$$\frac{d\overline{\mathbf{x}}}{d\tau} = \frac{d\left(K_x \mathbf{x}\right)}{d\left(\frac{1}{k_t}\right)t} = K_x \, k_t \frac{d\mathbf{x}}{dt} = K_x \, k_t \, \mathbf{f}\left(\mathbf{x}\left(t\right), \mathbf{u}\left(t\right), t\right)$$

Therefore, in order to specify the rates of the scaled NLP variables with respect to the scaled time, the dynamics of the vehicle, as computed with the unscaled states, controls, and time, must be multiplied by a time scaling factor, k_t, and a state scaling matrix, K_x. These two factors can be packaged together into another scaling matrix, called the *rate scaling matrix*, $K_r = k_t \, K_x$.

$$\frac{d\overline{\mathbf{x}}}{d\tau} = \begin{bmatrix} \frac{k_t}{k_{x_1}} & 0 & 0 & \dots & 0 \\ 0 & \frac{k_t}{k_{x_2}} & 0 & \dots & 0 \\ 0 & 0 & \frac{k_t}{k_{x_3}} & \dots & 0 \\ \vdots & & & \ddots & \\ 0 & 0 & 0 & \dots & \frac{k_t}{k_{x_N}} \end{bmatrix} \begin{bmatrix} \dot{x}_1 \\ \dot{x}_2 \\ \dot{x}_3 \\ \vdots \\ \dot{x}_N \end{bmatrix} = K_r \, \mathbf{f}\left(\mathbf{x}\left(t\right), \mathbf{u}\left(t\right), t\right)$$

4.4.1 Scaling Method

Good scaling practices typically scale the problem variables to be on the order of one. Bollino [15] suggests scaling the state, control, and time variables such that they vary between 0 and 1, while scaling the variable rates and the co-states to be on the same orders of magnitude ($\mathrm{O}(\epsilon)$).

Since the states, state rates, and co-states will have different magnitude ranges depending on the particular scenario examined, it is desired to have a scaling methodology that automatically scales the variables for a particular scenario. The objective is to scale all of the variables to be on the order of one and all of the dynamics to be on a similar order of magnitude. A general optimization problem can be formulated that seeks to satisfy these objectives subject to certain constraints. The variables for the scaling optimization problem are the individual scaling factors for time, states, controls.

$$\mathbf{y} = \begin{bmatrix} k_t \\ k_{x_1} \\ k_{x_2} \\ \vdots \\ k_{x_N} \\ k_{u_1} \\ \vdots \\ k_{u_N} \end{bmatrix}$$

Notice that the matrices K_x, K_r and K_u are expressed entirely of terms of the variables in the scaling optimization problem. The scaling optimization problem is given as follows:

$$\min \sum_{i=1}^{N_x} \left(K_r \dot{\mathbf{x}}_i - \epsilon \mathbf{e}\right)^2 + \sum_{i=1}^{N_x} K_x \left(\mathbf{x}_i - \mathbf{e}\right)^2 + \sum_{i=1}^{N_u} K_u \left(\mathbf{u}_i - \mathbf{e}\right)^2$$

$$s.t. \qquad A\mathbf{y} \leq \delta \mathbf{b}$$

$$\mathbf{y}_L \leq \mathbf{y} \leq \mathbf{y}_U$$

where

$$A = -\mathbf{I}_{\{N_y \times N_y\}}$$

$$\mathbf{b} = \begin{bmatrix} t & \mathbf{x} & \mathbf{u} \end{bmatrix}^T$$

δ = bound factor

ϵ = desired rates order of magnitude

$$\mathbf{e} = \begin{bmatrix} 1 & 1 & 1 & \ldots & 1 \end{bmatrix}^T$$

The cost function seeks to minimize the deviation of the scaled rates from some specified order of magnitude, ϵ, and the deviation of the scaled states and controls from one. The subscript i denotes the state, control, and rate vectors at a node time, t_i. The square of the deviation of these parameters at each nodal point is summed in the cost function.

The constraints in the problem, $A\mathbf{y} \leq \delta\mathbf{b}$, seek to constrain all scaled state, control, and time parameters at all nodal times to be less than a specified value, $\frac{1}{\delta}$. For example, if $\delta = 1$, the maximum scaled states, controls, and times cannot exceed 1 at any point in the trajectory. Thus, δ is a sensitivity parameter that relaxes the problem as it becomes smaller (e.g $\delta = 0.1$ constrains all values less than 10).

Lastly, the optimized variables, $\mathbf{y}$, are bounded by upper and lower bounds. The lower bounds, $\mathbf{y}_L$, of all the variables are set to zero so that the scaling factors do not change the sign of the states, controls, or time. The upper bounds, $\mathbf{y}_U$ are set such that the scaling factors do not reduce the scaled states, controls, or time to values that are too small. These bounds are specified as some constant, C, multiplied by the maximum values of the unscaled times, states, and controls.

$$\mathbf{y}_L = [0\,0\,0\,\ldots\,0]^T$$
$$\mathbf{y}_U = C\,[t_{max}\ x_{1_{max}}\ \ldots\ x_{n_{max}}\ u_{1_{max}}\ \ldots\ u_{n_{max}}]$$

The MATLAB function for constrained optimization, `fmincon`, is used to solve the scaling optimization problem presented above.

Although, the scaling method presented here does not constitute the "best" approach to scaling that will necessarily yield the most accurate and fastest solution, it does present a general method for quickly and consistently scaling a new problem according to certain metrics. As mentioned before, several metrics for scaling optimization problems have been suggested in the literature [6] [15], but no single approach has proven to be a universally optimal approach for all problems. The scaling metric used here attempts to consistently scale the problems such that the state and control variables are on the order of one and the rates are on the same order of magnitude, subject to maximum and minimum bounds on the scaled values. An illustrative example is given below for the scaled states and state rates during launch after running the scaling algorithm using values of $\delta = 0.001$, $\epsilon = 1$,

and $C = 10$.

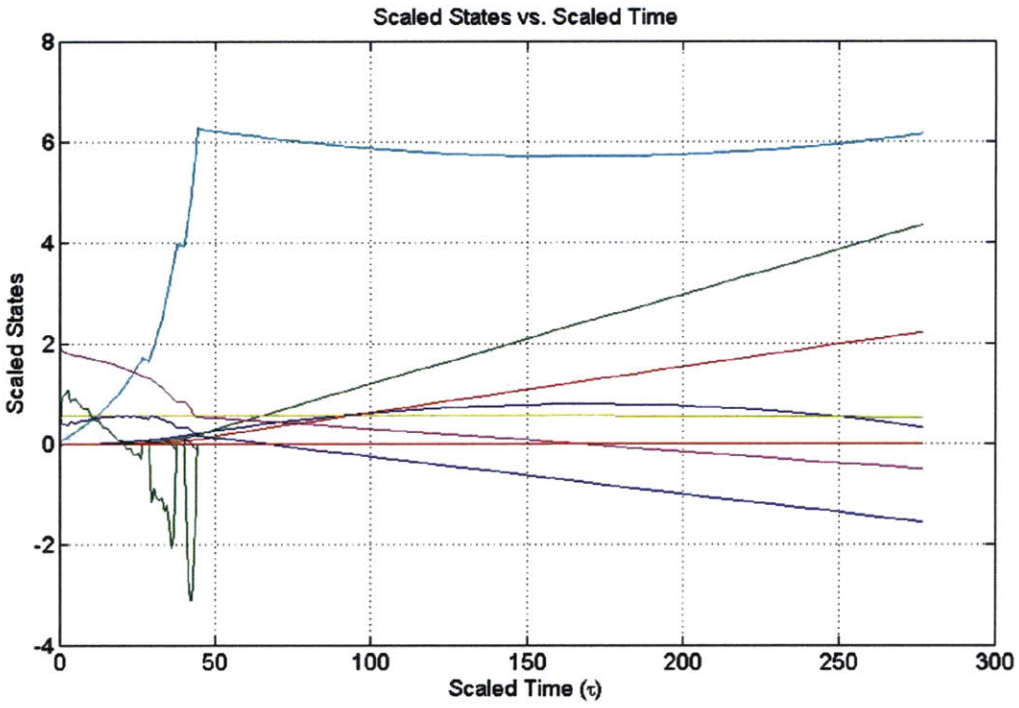

Figure 4-2: Scaled States Using Scaling Method

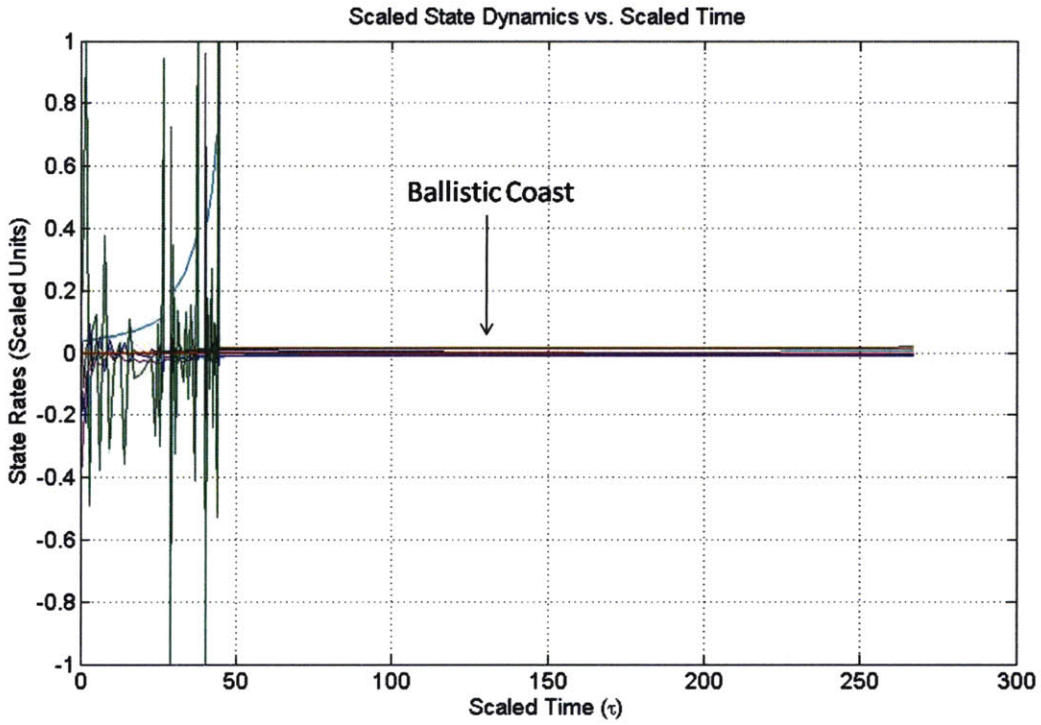

Figure 4-3: Scaled Rates Using Scaling Method

Another scaling metric commonly explored is scaling the problem co-state variables to be on the same order of magnitude as the state variables [6]. However, the current version of DIDO is unable to estimate the co-states for a problem containing knots. Since the problem studied in this thesis contains many knots, this metric was not fully explored in the work here. Future investigations into optimization scaling may consider using methods similar to the ones presented here to scale the co-states appropriately in the problem.

4.4.2 Segmented Scaling

Due to the significant variability of the states, controls, and dynamics over the different segments of the boost-through-reentry flight, it may be necessary to have separate scalings for separate segments. For example, the atmospheric forces experienced upon reentry will be more extreme than those experienced during launch since the reentry vehicle dives into the atmosphere traveling at approximately Mach 16 while the launch vehicle does not reach such speeds until it is well above the densest parts of the atmosphere. Therefore, separate scaling units are developed for the boost segment of flight and the reentry segment of flight. The only constraint is that the time scaling must be common to both segments, since the scaled time must be continuous over the entire trajectory.

The boundary between the boost scaled states and the reentry scaled states occurs at a knot located at the piercepoint location of 400,000 ft altitude. Let the time at an instant prior to the knot time be denoted as t_k^- and the time an instant after the knot time be denoted as t_k^+. The continuity constraints across this knot must account for the differences between the boost scaling (K_{x_1}) and the reentry scaling (K_{x_2}). In order to impose proper continuity constraints, the variables at t_k^+ are transformed from reentry scaled units to boost scaled units before being differenced with the t_k^- variables.

$$\overline{\mathbf{x}}\left(t_k^+\right) - K_{x_1} K_{x_2}^{-1} \overline{\mathbf{x}}\left(t_k^-\right) = \mathbf{0} \tag{4.18}$$

The scaling method presented in the previous section can now be performed with twice

as many variables, representing scaling factors for both the boost (K_{x_1}) and reentry (K_{x_2}) segments. The overall deviation of all the states and state rates from their desired orders of magnitude is reduced since the problem now scales the boost and reentry portions *independently*. An example of the segmented scaled states is given in Figure 4-4 for the boost-through-reentry flight.

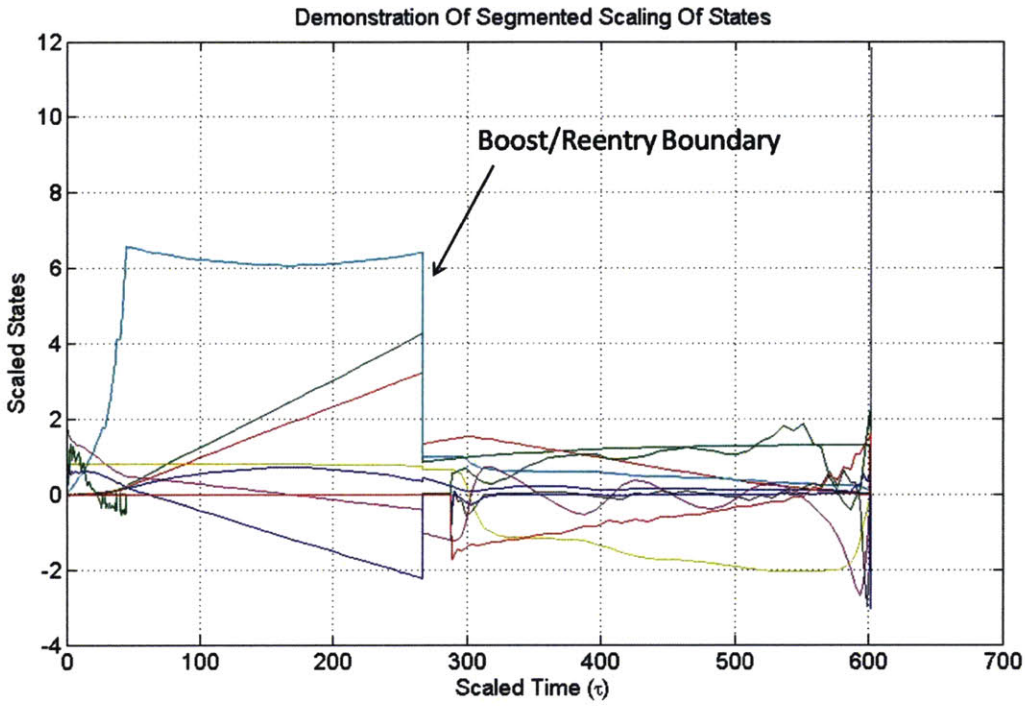

Figure 4-4: Scaled States Using Segmented Scaling

Although only two portions of the trajectory are scaled independently in this formulation, the use of independent scaling for *each* trajectory segment could prove to be even more efficient for future studies.

4.5 Summary

In this chapter, the framework for formulating an optimal control problem was presented. Both indirect and direct method concepts were introduced as solution methods for the optimal control problem. Due to the ability of direct methods to be flexible to a wide range of optimization problems and allow easy implementation of path constraints, direct

methods are chosen over indirect methods for this study. Problem formulation tools including event constraints, path constraints, and knotting conditions were presented and described in detail. A general scaling method was presented for scaling the optimization variables quickly and consistently according to a chosen metric. For the problem considered in this study, the boost and reentry segments of flight are scaled separately using segmented scaling. Now that the basic optimal control framework has been presented, chapters 5 and 6 will formulate optimal control problems for the launch problem and the reentry problem.

Chapter 5

The Boost Problem

This chapter initiates the discussion of boost-through-reentry trajectory optimization by examining the models incorporated for the boosting portion of flight and relating the boost end conditions to typical reentry initial conditions at the piercepoint reentry interface, located at 400,000 ft altitude.

The boost portion of the flight profile extends from first stage ignition through the final stage burnout and mass drop up until the piercepoint conditions are met that initiate reentry. This portion of flight consists of six segments, three of which include powered flight and three of which are coasting flight. Figure 5-1 illustrates the segments of flight associated with the boost problem. After each powered flight segment, the vehicle instantaneously drops the mass of the lowest stage and coasts for a period without thrusting until the next stage is ignited for another powered segment. After the third stage burns out, the vehicle coasts ballistically until reaching the piercepoint reentry interface at 400,000 ft altitude. The vehicle state at the piercepoint interface will define the initial conditions for the reentry portion of the flight profile.

5.1 Launch Vehicle

The reentry vehicle will be launched aboard a three-stage, intermediate-range ballistic missile (IRBM) with solid rocket engines. The launch vehicle must be sized appropriately to provide end conditions that are representative of typical reentry conditions for a vehicle

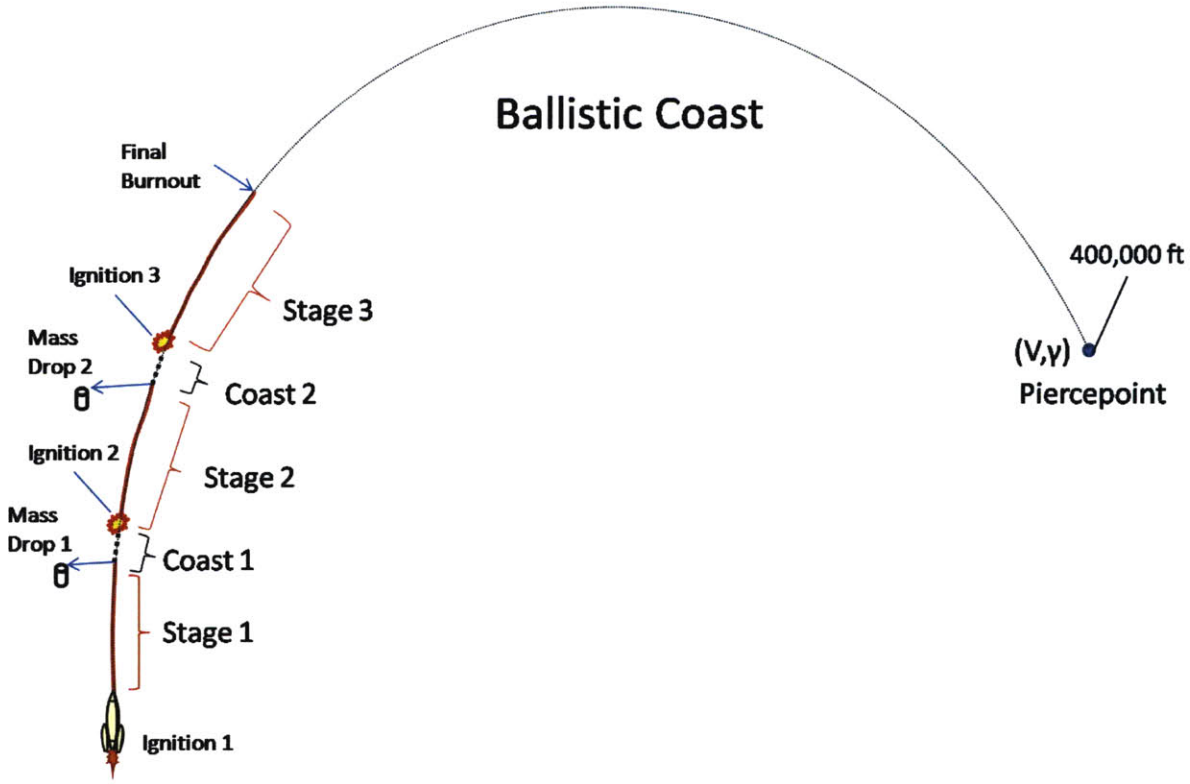

Figure 5-1: Flight Segments Of The Boost Portion Of Flight

of the size and shape mentioned in Chapter 1. For the scenario examined in this thesis, a final stage burnout velocity of approximately 16,000 feet per second after 90-100 seconds of powered flight is desired.

5.1.1 Mass Sizing

A common first-order approach to sizing a launch vehicle is to use the *rocket equation*, as given by [18].

$$\frac{m_f}{m_0} = \frac{m_0 - m_{prop}}{m_0} = e^{-\frac{\triangle V}{I_{sp}\, g_0}} \tag{5.1}$$

The rocket equation describes the *propellant mass*, m_{prop}, required to achieve an *increment of velocity*, $\triangle V$, with a rocket of *total mass*, m_0, and *specific impulse*, I_{sp}. The specific impulse is defined as the ratio of thrust, T, to the weight flow rate, $\dot{m}g$, and provides a measure of how efficient the rocket engine converts propellant into thrust. The

velocity increment decribed by this equation, $\triangle V$, describes the ideal velocity increase possible from the engine thrust in the absence of gravity and drag forces. In addition, g_0 represents the sea-level gravity acceleration, $9.81 m/s^2$.

The goal of this exercise is to calculate mass ratios for each stage of the launch vehicle that can achieve the desired burnout velocity. The rocket equation given above can be applied to each stage of the launch vehicle for these sizing calculations. At this point, it is convenient to define additional terms related to the mass ratios of each stage. The total mass of each stage, m_{stage_i}, will consist of propellant mass, m_{prop_i}, and dry mass, m_{dry_i}, which contains all structural masses excluding the propellant. Let β_i be equivalent to the *dry weight ratio of stage i* and μ_i equivalent to the ratio of initial mass at ith-stage ignition to the remaining mass at the i-th stage burnout before i-th stage separation. In addition, let m_{0_i} represent the remaining mass of the entire rocket stack at the beginning of the i-th stage. The stages of the launch vehicle are illustrated in Figure 5-2.

$$\beta_i = \frac{m_{dry_i}}{m_{stage_i}} = \frac{m_{dry_i}}{m_{dry_i} + m_{prop_i}} \tag{5.2}$$

$$\mu_i = \frac{m_{0_i}}{m_{0_i} - m_{prop_i}} = \frac{m_{0_{i+1}} + m_{stage_i}}{m_{0_{i+1}} + m_{dry_i}} = \frac{m_{0_{i+1}} + m_{stage_i}}{m_{0_{i+1}} + \beta_i m_{stage_i}} \tag{5.3}$$

The fundamental difference between these two terms is that β_i is an inherent property of the i-th stage that is limited by current technology while μ_i is a parameter that chooses the size of each stage. Therefore, μ_i is the parameter to be chosen to achieve the desired burnout velocity. Through algebraic manipulation, the rocket equation for each stage can be expressed in terms of μ_i, as given in [3].

$$\triangle V_i = Isp_i \, g_0 \, \ln \mu_i \tag{5.4}$$

Since the launch vehicle initially starts at rest in the Earth-relative frame, the desired burnout velocity is equivalent to the sum of velocity increments given by Equation 5.4 for each stage.

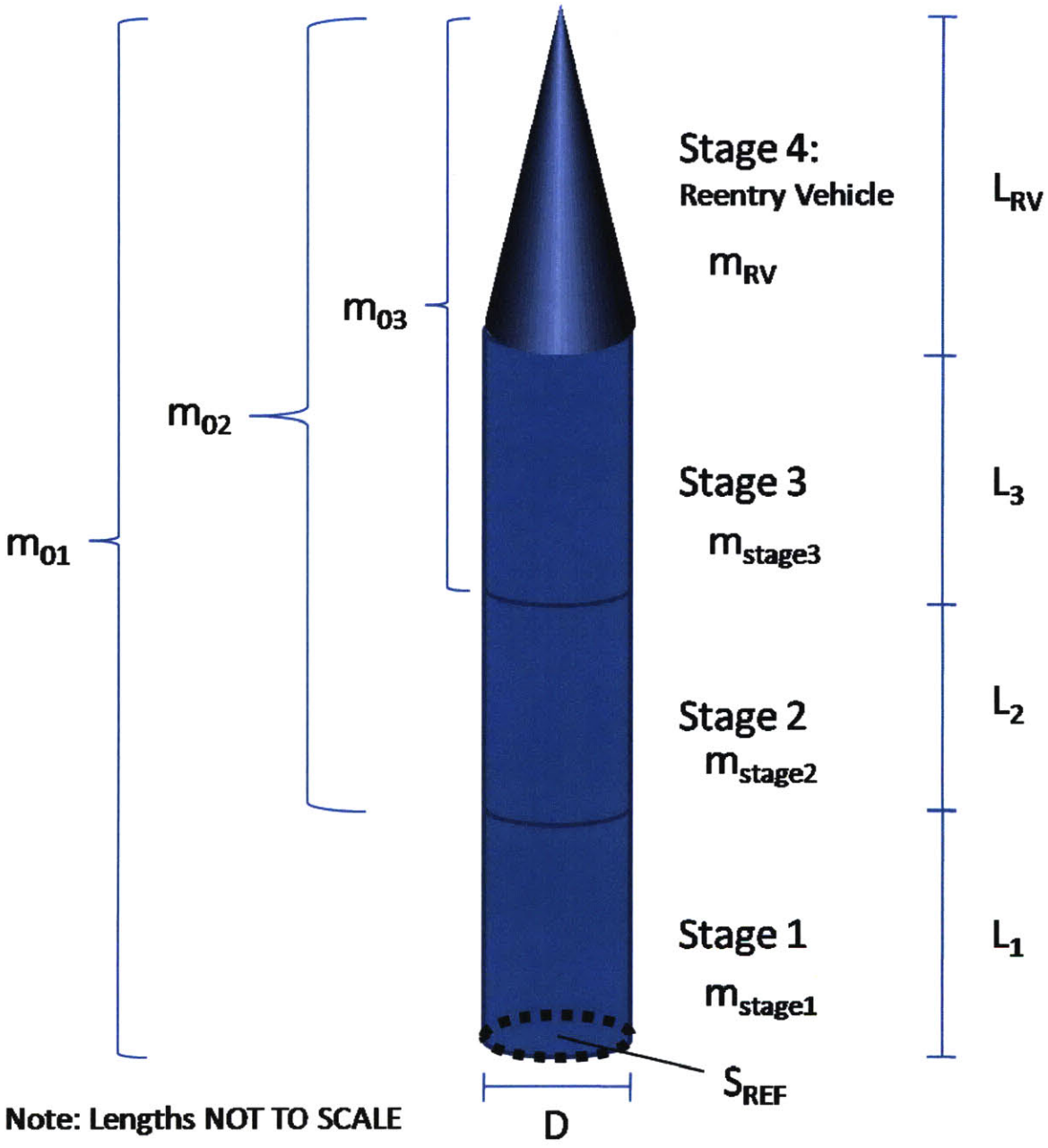

Figure 5-2: Illustration of Launch Vehicle Parameters

$$V_f = g_0 \sum_{i=1}^{3} Isp_i \ln \mu_i \tag{5.5}$$

Since the characteristic velocity specified in the rocket equation, V_f, neglects velocity loss due to gravity and drag, it is important to compensate for these losses in the sizing of the launch vehicle. Ashley [3] gives representative numbers for the three contributions to characteristic velocity composed of kinetic energy velocity increase, potential energy increase (gravity), and drag loss. The data suggests a ratio of 1.2:1 between the characteristic velocity increment and the actual kinetic energy velocity increment. Since the launch vehicle desires a burnout velocity of 16,000 feet per second, this value should be multiplied by a constant factor of 1.2 to account for effects due to gravity and drag.

$$V_f = 1.2 \times 16,000\, ft/s \equiv 1.2 \times 4876.8\, m/s = 5852.16\, m/s$$

Next, the performance numbers for the rocket stages must be specified. A list of representative solid rocket motors is given by [18], with performance values, such as I_{sp} and β_i given. Vacuum I_{sp} values for a solid rocket motor typically range from 280-300 seconds while the propellant weight of a solid rocket typically assumes about 85-90% of the total stage mass. Additionally, Sutton estimates that medium-sized solid rocket motors typically have propellant mass fractions between 0.8 and 0.91 [8]. For the sizing of this vehicle, a vacuum I_{sp} of 290 seconds will be assumed for each stage with a dry weight mass ratio, β_i, of 0.15 per stage.

Returning to the sizing of each stage, Equation 5.3 can be manipulated to form an expression relating the remaining rocket mass at each staging, m_{0_i}.

$$\begin{aligned} m_{0_{i+1}} &= \frac{m_{stage_i}(1-\beta_i\mu_i)}{\mu_i - 1} \\ m_{0_i} = m_{0_{i+1}} + m_{stage_i} &= \frac{m_{stage_i}\mu_i(1-\beta_i)}{\mu_i - 1} \\ \frac{m_{0_i}}{m_{0_{i+1}}} &= \frac{\mu_i(1-\beta_i)}{1-\beta_i\mu_i} \end{aligned} \tag{5.6}$$

Equation 5.6 allows for the mass of each stage stack to be easily reconstructed from μ_i. It should be remembered here that m_{stage_i} represents the total mass of the i-th stage while m_{0_i} represents the total mass of the i-th stack, which contains the i-th stage plus any additional stages above it.

The rocket equation can now be applied for sizing the launch vehicle with an assumed vacuum I_{sp} of 290 seconds for each stage and a β_i of 0.15. According to Ashley [3], if the Isp_i and β_i are assumed to be constant over all stages, the optimal μ_i for reaching V_f with minimum stack weight is invariant over all the stages. Therefore, Equation 5.5 reduces to

$$V_f = 3\, g_0\, I_{sp}\, \ln \mu \tag{5.7}$$

The mass fraction, μ, can then be solved by plugging in values for V_f, g_0, and I_{sp} defined previously.

$$\mu = e^{\frac{V_f}{3 g_0 I_{sp}}} = 1.985 \tag{5.8}$$

Now, using Equation 5.6, the mass of each stage can be sized appropriately beginning with the payload weight of 300 lbs (136.08 kg) assumed as the size of stage 4.

$$m_{0_3} = 136.08 \frac{1.985\,(1 - 0.15)}{1 - 0.15 * 1.985} = 326.9782\, kg$$

$$m_{0_2} = m_{0_3} \frac{1.985\,(1 - 0.15)}{1 - 0.15 * 1.985} = 785.6887\, kg$$

$$m_{0_1} = m_{0_2} \frac{1.985\,(1 - 0.15)}{1 - 0.15 * 1.985} = 1887.9144\, kg$$

The mass of each individual stage can be obtained by taking the difference of the total stack masses given above.

$$m_{stage1} = m_{0_1} - m_{0_2} = 1102.2256\,kg$$
$$m_{stage2} = m_{0_2} - m_{0_3} = 458.7106\,kg$$
$$m_{stage3} = m_{0_3} - m_{RV} = 190.9005\,kg$$
$$m_{RV} = 136.08\,kg$$

5.1.2 Propellant Burn Rates

The next consideration is to determine how long to burn each stage motor. For solid rocket motors, the internal fuel grain retains a constant surface area as the motor burns, creating a relatively constant mass flow rate and thrust [18]. Such a motor operates with a single start and burns until all propellant is used. Therefore, by choosing the motor burn time, the mass flow rate and the thrust are determined. As mentioned previously, the total powered flight time of these three stages will be a combined 90 seconds. The individual stage burn times will be proportioned such that the mass flow rates are relatively similar between stages, with the first stage burning a bit cooler than the second stage to avoid high dynamic pressure experienced at low altitudes. Thus, the burn times for stage 1, stage 2, and stage 3 in this problem are chosen as 60 seconds, 20 seconds, and 10 seconds, respectively. By fixing the burn times to these values and assuming a constant mass burn rate, the propellant burn rates for each stage are uniquely determined.

The mass burn rates can be computed by dividing the propellant of each stage by the burn times mentioned above, assuming constant burn rates.

$$m_{prop1} = m_{stage1} - 0.15 * m_{stage1} = 936.8918\,kg$$
$$m_{prop2} = m_{stage2} - 0.15 * m_{stage2} = 389.9040\,kg$$
$$m_{prop3} = m_{stage3} - 0.15 * m_{stage3} = 162.2654\,kg$$

$$\dot{m}_{prop1} = \frac{m_{prop1}}{60sec} = 15.61\,kg/sec$$
$$\dot{m}_{prop2} = \frac{m_{prop2}}{20sec} = 19.50\,kg/sec$$
$$\dot{m}_{prop3} = \frac{m_{prop3}}{10sec} = 16.23\,kg/sec$$

The mass of the launch vehicle will vary over time based upon these burn rates as well as the staging of the vehicle. A general expression can be given for the mass of the vehicle at a time t from launch during the i^{th} stage. Let m_{0_i} represent the mass of the vehicle at the start of the i^{th} stage and t_{0_i} represent the time when the i^{th} stage is ignited.

$$m(t) = m_{0_i} - \dot{m}_{prop_i}(t - t_{0_i}) \tag{5.9}$$

5.1.3 Thrust Force

The thrust force exerts an acceleration on the vehicle body that is proportional to the mass flow rate, $\dot{m}$, and the exit velocity of the propellant, v_e. As mentioned in Sutton [8], rocket engines produce a thrust that varies with altitude due to a difference in the nozzle exit pressure and the atmospheric pressure. As a rocket ascends to higher altitudes, the thrust and I_{sp} increase as the atmospheric pressure decreases. The difference in sea level thrust and vacuum thrust can amount to 10 to 30% of the overall thrust [8]. The equation for thrust in terms of exit velocity v_e, exit pressure, p_e, exit area, A_e, and atmospheric pressure, p_a is given as

$$T = \dot{m}\, v_e + (p_e - p_a)\, A_e \tag{5.10}$$

The I_{sp} for this vehicle was assumed to be 290 seconds in a vacuum. This represents the maximum efficiency the engine can obtain. Thus, the maximum thrust values for each stage are then obtained by multiplying the mass flow rates by the vacuum specific impulse, $I_{sp_{vac}}$, and sea-level gravity acceleration, g_0.

$$T_{stage1_{max}} = \dot{m}_{prop1}\, g_0\, I_{sp_{vac}} = 44423\, N$$
$$T_{stage2_{max}} = \dot{m}_{prop2}\, g_0\, I_{sp_{vac}} = 55462\, N$$
$$T_{stage3_{max}} = \dot{m}_{prop3}\, g_0\, I_{sp_{vac}} = 46163\, N$$

To model the 10 to 30% loss in overall thrust at lower altitudes due to atmospheric pressure, the following exponential model, with altitude specified in feet, is used to vary the I_{sp} from 260 sec (sea level) to 290 sec (vacuum), similar to a curve shown in Sutton

[8].

$$I_{sp} = 290 - 30\, e^{-\frac{alt}{12000}} \tag{5.11}$$

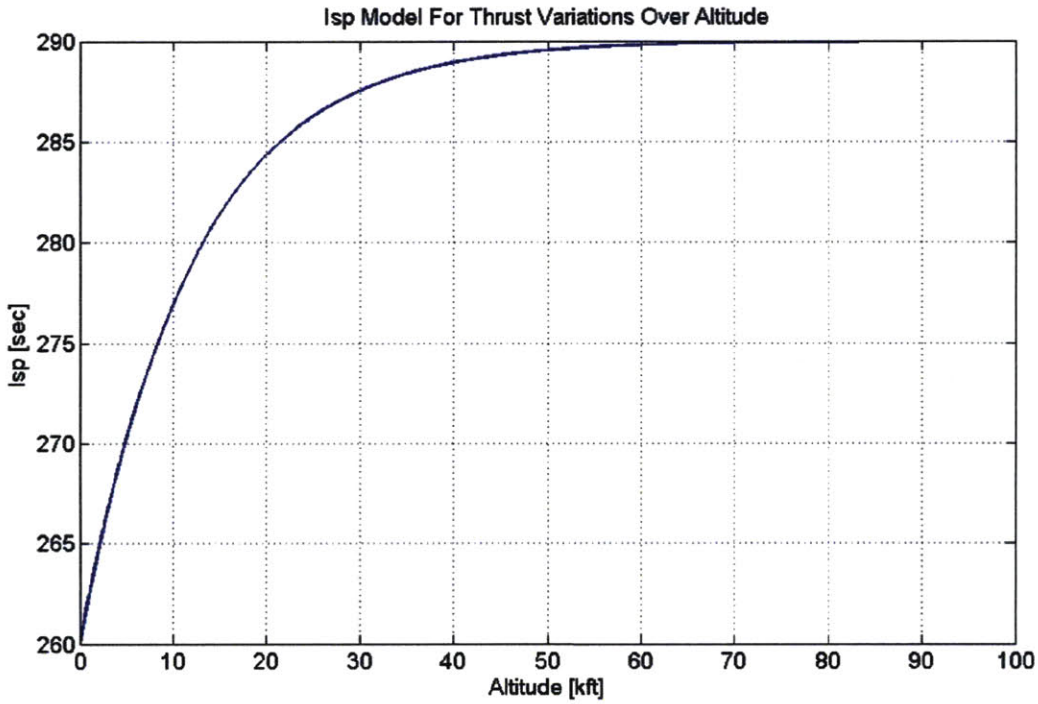

Figure 5-3: Isp Variation Over Altitude

Thus, the altitude varying thrust will be given by the mass flow rate of the engine and the altitude varying I_{sp}.

$$T = \dot{m}\, I_{sp}\, g_0 \tag{5.12}$$

5.1.4 Booster Length

The last consideration is to determine the length of each stage. As mentioned previously, the launch vehicle will have a uniform diameter of 21 inches and a circular cross area, as dictated by the mission requirements. This amounts to a cross section area, A_c, of $0.223\, m^2$. The length of each stage will be limited by the volume of the propellant. Using typical propellant density values for missile motors available in Sutton [8], the density,

ρ_{prop}, can be estimated to be $0.0635\,lbm/in^3$ $(1757\,kg/m^3)$. Sutton also estimates that the propellant grain typically accounts for 82 to 94% of the total motor mass [8]. For this vehicle, let it be assumed that the propellant accounts for 85% of the total mass for each stage. Using the known propellant mass for each stage as well as the cross sectional area, A_c, of the vehicle, the the required volume of each stage can be estimated. The expression for volume is then used to calculate the length of the propellant grain, L_{prop_i}, for each stage.

$$0.85\,V_{prop_i} = 0.85\,A_c L_{prop_i} = \frac{m_{prop_i}}{\rho_{prop_i}} \tag{5.13}$$

$$L_{prop_i} = \frac{m_{prop_i}}{0.85\rho_{prop_i}\,A_c} \tag{5.14}$$

The equation above solves for the required length of each stage for satisfying the propellant volume requirement. An additional factor must account for the exposed nozzle length of each stage. Let it be assumed that the exposed nozzle length represents 10% of the propellant length for each stage. Therefore, the total length of each stage can be calculated as follows.

$$\begin{aligned} L_i &= L_{prop_i} + L_{nozzle_i} \\ &= 1.1\,L_{prop_i} \end{aligned} \tag{5.15}$$

The calculated lengths are summarized in Table 5.1.

5.1.5 Summary

The table below summarizes the launch vehicle parameters for a launch vehicle designed to achieve 16,000 feet per second by final engine burnout.

	stage 1	stage 2	stage 3	payload	total
m_{prop} (kg)	936.8918	389.9040	162.2654	0.0	1489.0611
m_{dry} (kg)	165.3338	68.8066	28.6351	136.08	398.8532
m_{total} (kg)	1102.2256	458.7106	190.9005	136.08	1887.9144
$\dot{m}$ (kg/s)	15.61	19.50	16.23	N/A	N/A
T_{max} (N)	44423	55462	46163	N/A	N/A
Sea Level I_{sp} (s)	260	260	260	N/A	N/A
Vacuum I_{sp} (s)	290	290	290	N/A	N/A
$A_c\,(m^2)$	0.223	0.223	0.223	0.223	N/A
L (m)	3.088	1.285	0.535	1.450	6.358

Table 5.1: *Launch Vehicle Properties*

5.2 Environment Models

Environmental models are incorporated into the problem describing the variations and disturbances in the atmosphere as well as the non-sphericity of the Earth.

5.2.1 Ellipsoidal-Earth Model

An ellipsoidal-Earth model is used to model the Earth's shape as an oblate spheriod rather than as a simple sphere. Since the r, μ, and λ states defined in chapter 2 are defined relative to a spherical Earth (geocentric), they must be transformed to *geodetic* position coordinates, defined relative to an oblate Earth. The process involves first converting r, μ, and λ, as defined relative to a plane of reference, to geocentric longitude (η) and latitude (ζ) coordinates relative to the Equator (REF to ECEF). The geocentric radial distance and geocentric latitude are then transformed to geodetic altitude (distance above Earth's surface in direction perpendicular to surface), h, and geodetic latitude, κ, using the ellipsoidal-Earth model. These parameters will be used in the optimization algorithm to accurately specify initial and final altitude and latitude parameters that are relative to an oblate Earth. Computation of the atmospheric properties as a function of altitude

above the Earth's surface will also benefit from the increased accuracy of the ellipsoidal-Earth model.

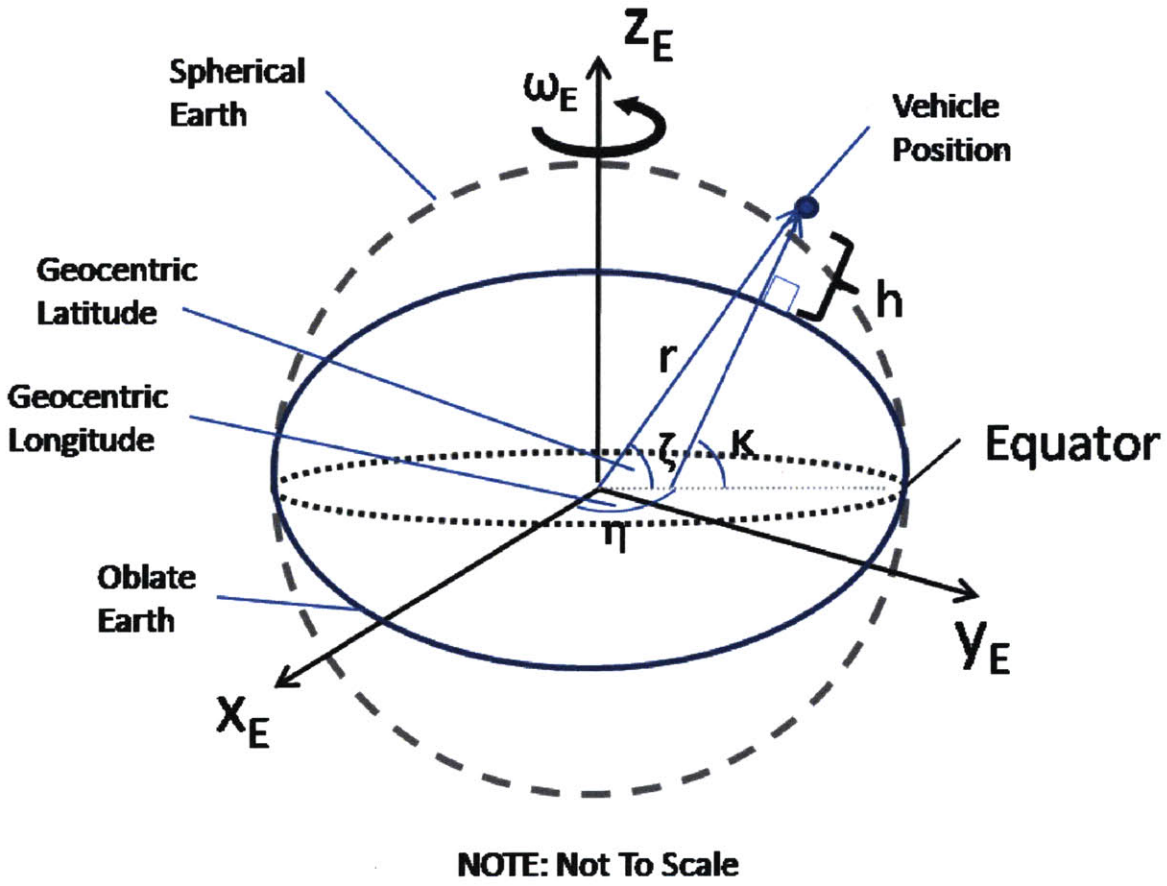

Figure 5-4: Oblate Earth Model With Geodetic Altitude, h, and Geodetic Latitude, κ

The ellipsoidal-Earth model is defined by a flatness coefficient, f, in terms of a semi-major axis, a, and a semi-minor axis, b. Additionally, as mentioned in the previous chapter, the Earth's surface is assumed to rotate about a constant axis of rotation with rotation rate, ω_E, and exert a gravitational force acting toward the Earth center with gravitational constant μ_G.

$$
\begin{aligned}
a &= 6,378,137\,m \\
b &= 6,356,752\,m \\
f &= \tfrac{a-b}{a} = 3.35281066474748 \times 10^{-3} \\
\omega_E &= 7.292115 \times 10^{-5}\,rad/sec \\
\mu_G &= 3.9860064 \times 10^{14}\,m^3/s^2
\end{aligned}
$$

5.2.2 Atmosphere Model

The density of the Earth's atmosphere is modeled using the Global Reference Atmospheric Model (GRAM-99) developed by Marshall Space Flight Center (MSFC). GRAM-99 is an atmospheric model that provides density, pressure, temperature, and wind data with complete global geographical variablility, complete altitude coverage from the surface to orbital altitudes, and complete seasonal and monthly variability [21]. In addition, GRAM-99 has the ability to simulate spatial and temporal perturbations in the atmospheric parameters related to turbulence, storms, gravity waves, and tides [21]. For the scenario examined in this study, an accurate model of atmospheric denisty is the most pressing need since all of the vehicle manuevering capability is dependent on aerodynamic control.

GRAM-99 was compiled into a MEX-file for easy and efficient function calls from the MATLAB interface. However, even with the efficient interface, GRAM-99 still takes approximately 10^{-2} seconds to return for each call. Since the optimization algorithm may perform thousands or tens of thousands iterations, this computation penalty is not acceptable for use in the optimization algorithm. In order to reduce computation time during each optimization iteration, the atmospheric density profile given by GRAM-99 is fit to an analytic function. Atmospheric density is commonly modeled as an exponential function of the altitude above the surface of the Earth, h, based on a fixed reference height, H, and the sea level density, ρ_0. For example, Undurti [1] models the atmospheric density as

$$
\rho(h) = \rho_0\, e^{\frac{-h}{H}}
$$

$$
\text{where} \quad H = 10000m, \rho_0 = 1.168\tfrac{kg}{m^3}
$$

A more accurate density fit can be obtained by choosing the exponential function coefficients using a least squares fit to the GRAM-99 density data.

$$\rho(h) = a_\rho e^{b_\rho h(t)+c_\rho} \tag{5.16}$$

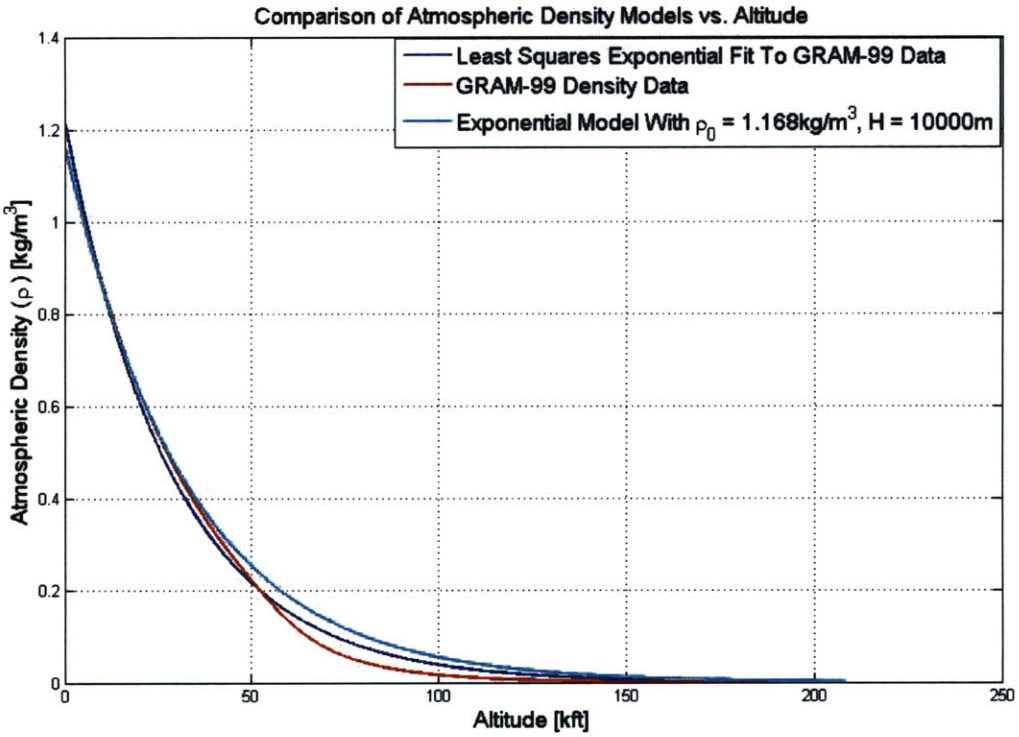

Figure 5-5: Comparison Of Atmospheric Density Models Versus Altitude

Notice that both exponential models significantly overestimate the density values in the region between 50,000 feet and 150,000 feet, where the reentry vehicle performs most of its maneuvering. The least-squares exponential fit is chosen to represent the atmospheric density in the optimization algorithm since it exhibits less error in this altitude range. Other higher-order analytical fits were considered for the atmospheric density, but few of these fits could approach $\rho = 0$ as $h \to \infty$ without becoming negative at some point. Since an exponential function has infinite smoothness and approaches zero while keeping ρ continually positive, it was chosen as the fitting function.

In order to incorporate slight variations in density based on latitude and longitude, the density function is automatically fit during each algorithm run to a unique GRAM-99

density profile generated from an initial guess trajectory (r, μ, λ).

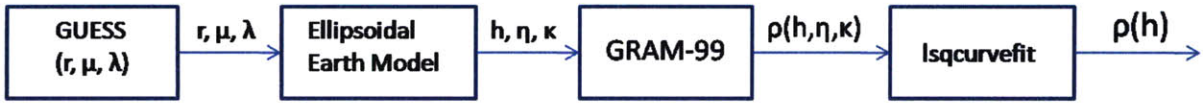

Figure 5-6: Algorithm Sequence For Automatic Density Curve Fit

Although the density is modeled as an exponential function of the altitude only, it is fit to data with a particular (η,κ) profile that is representative of the final trajectory.

The atmosphere is assumed to be rotating with the Earth's surface during the vehicle flight. Therefore, the dynamic pressure exerted on the vehicle during flight is a function of atmospheric density, ρ, and the Earth-relative velocity of the vehicle, V_E.

$$q = \frac{1}{2}\rho\,(h)\;V_E^2$$

5.3 Launch Vehicle Aerodynamics

The aerodynamics of a launch vehicle are typically defined in terms of an axial coefficient of force (C_X) acting along the body axis of symmetry and a normal coefficient of force (C_N) acting normal to the body axis of symmetry in the lift plane, as defined in section 2.6.1. These coefficients are defined as the axial (F_A) and normal (F_N) forces exerted on the vehicle normalized by the dynamic pressure, $q = \frac{1}{2}\rho V_E^2$, and reference area, S_{ref}. The center of pressure, C_P, specifies the location along the vehicle body where the resultant aerodynamic forces act. It is typically specified as a fraction of the total body length, L_{body}, along the body axis of symmetry, as measured positive from the body nose to the tail.

$$C_N = \frac{F_N}{qS_{ref}}$$

$$C_X = \frac{F_X}{qS} \tag{5.17}$$

$$C_P = \frac{X_{CP}}{q\,S_{ref}\,L_{body}} \tag{5.18}$$

The reference area for an axially symmetric (non-winged) vehicle is typically defined as some percentage of the maximum cross sectional area of the vehicle base. The choice for S_{ref} can be thought of as a parameter for determining the sensitivity of the vehicle motion to atmospheric forces. The reference area chosen for this problem is approximately one-third of the maximum cross-sectional area of the vehicle base, $S_{ref} = 0.075m^2$.

The normal and axial coefficients can be resolved into components representing the coefficient of lift (C_L) and the coefficient of drag (C_D) by using the angle of attack, α.

$$\begin{aligned} C_L &= -C_X \sin\alpha + C_N \cos\alpha \\ C_D &= C_X \cos\alpha + C_N \sin\alpha \end{aligned} \tag{5.19}$$

Drag is defined to be the component of force directly opposite the velocity vector. Therefore, the acceleration exerted by this force serves to solely reduce the velocity magnitude, but cannot change the direction of the vehicle motion. Lift represents the remainder of the force, which is constrained to remain in the lift plane, defined by the orientation of the body symmetric axis relative to the velocity vector. The component of the lift in the velocity vertical plane, $L\cos\sigma$, will change the flight path angle while the remaining component, $L\sin\sigma$ will change the heading angle. The lift and drag forces can be obtained from the coefficients above using atmospheric density (ρ), Earth-relative velocity, V_E, and the reference area, S_{ref}.

$$\begin{aligned} L &= \frac{1}{2}\rho(h)\, V^2 C_L(\alpha, M) S_{ref} \\ D &= \frac{1}{2}\rho(h)\, V^2 C_D(\alpha, M) S_{ref} \end{aligned}$$

In order to express the aerodynamic forces exerted on this vehicle, a set of axial and normal coefficients must be defined as functions of both Mach number (M) and angle of attack (α). Aerodynamic coefficient dependencies on Mach number and angle of attack are shown for the V-2 missile in Sutton [8] as well as for a variety of representative launch

vehicles in Ashley [3]. At least three distinctive features of the aerodynamic profiles are important to model for any vehicle crossing the transonic regime. First, the normal coefficients can be characterized by a sharp jump followed by a sharp drop in C_X in the transonic region (M $\approx$ 1-2). Second, the axial coefficients exhibit a linear increase in C_N with angle of attack for angles up to 15 degrees. Lastly, the center of pressure shifts towards the aft of the vehicle as it passes the transonic region. Similar trends can be observed in aerodynamic tables modeling a triconic reentry vehicle, used by Undurti for hypersonic reentry analysis [1].

It is desirable to develop a table of aerodynamic coefficients exhibiting the general features mentioned above, while having values to accurately represent the aerodynamic flow over a long, slender body representative of the launch vehicle. Therefore, Undurti's aerodynamic table is scaled to represent the typical launch vehicle aerodynamic coefficients observed in [3] and [8] while keeping intact the transonic and supersonic aerodynamic trends. The scaled table of coefficients are given on the next few pages along with plots representing the variations of the coefficients with Mach number and angle of attack.

Mach / α	0	1.0	5.0	10.0	15.0	30.0
0.0	0.2500	0.2500	0.2500	0.2500	0.2500	0.2500
0.5	0.2500	0.2500	0.2500	0.2500	0.2500	0.2500
0.8	0.3000	0.3000	0.3000	0.3000	0.3000	0.3000
1.0	0.4265	0.4265	0.4213	0.4048	0.3980	0.4360
1.2	0.4265	0.4265	0.4213	0.4048	0.3980	0.4360
1.5	0.4265	0.4265	0.4213	0.4048	0.3980	0.4360
2.0	0.4265	0.4265	0.4213	0.4048	0.3980	0.4360
3.0	0.3180	0.3180	0.3162	0.3116	0.3188	0.3878
4.0	0.2721	0.2721	0.2718	0.2724	0.2854	0.3878
5.0	0.2262	0.2262	0.2274	0.2332	0.2520	0.3878
8.0	0.1782	0.1782	0.1812	0.1937	0.2400	0.3878
10.0	0.1638	0.1638	0.1674	0.1821	0.2400	0.3878
12.5	0.1566	0.1566	0.1605	0.1764	0.2400	0.3878
15.0	0.1493	0.1493	0.1536	0.1707	0.2400	0.3878
20.0	0.1454	0.1454	0.1499	0.1684	0.2400	0.3878
25.0	0.1454	0.1454	0.1499	0.1684	0.2400	0.3878

Table 5.2: *The Axial Force Coefficient C_X As A Function Of Angle Of Attack And Mach Number.*

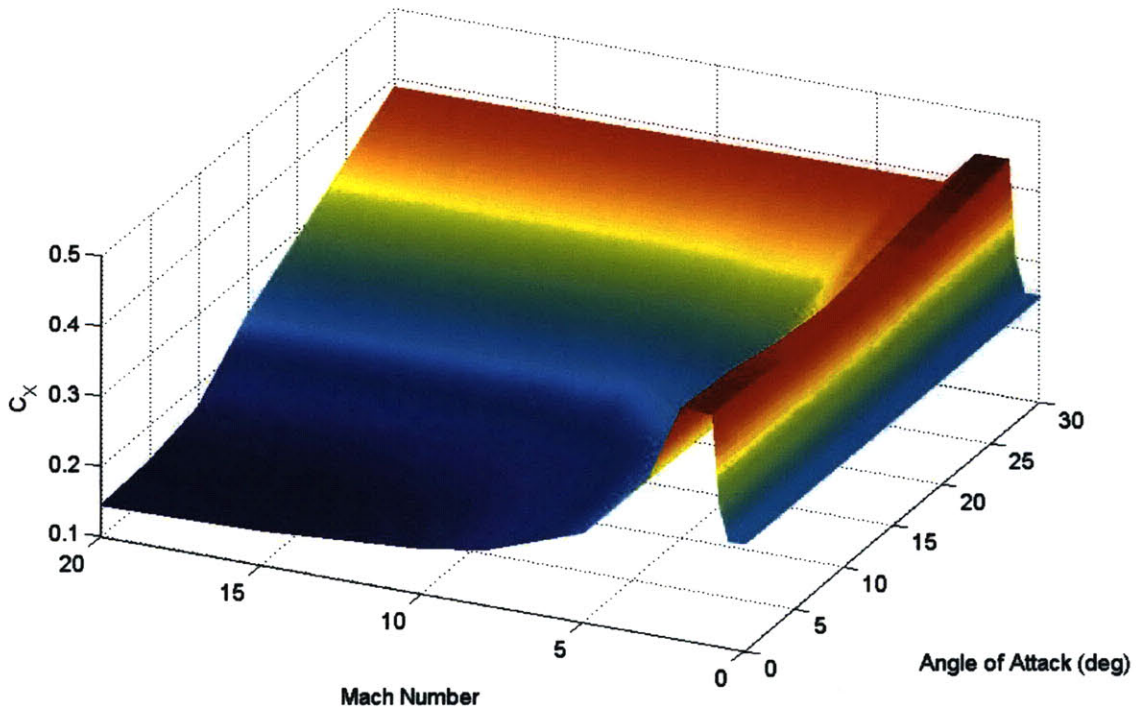

Figure 5-7: Axial Coefficient Of Force As A Function Of Mach Number And Angle Of Attack

Mach / α	0	1.0	5.0	10.0	15.0	30.0
0.0	0.0	0.0558	0.2855	0.5891	1.0	2.0733
0.5	0.0	0.0558	0.2855	0.5891	1.0	2.0733
0.8	0.0	0.0558	0.2855	0.5891	1.0	2.0733
1.0	0.0	0.0558	0.2855	0.5891	1.0	2.0733
1.2	0.0	0.0558	0.2855	0.5891	1.0	2.0733
1.5	0.0	0.0558	0.2855	0.5891	1.0	2.0733
2.0	0.0	0.0558	0.2855	0.5891	1.0	2.0733
3.0	0.0	0.0591	0.3007	0.6276	1.0	2.0733
4.0	0.0	0.0588	0.2970	0.6149	1.0	2.0733
5.0	0.0	0.0585	0.2933	0.6023	1.0	2.0733
8.0	0.0	0.0570	0.2831	0.5755	1.0	2.0733
10.0	0.0	0.0564	0.2793	0.5661	1.0	2.0733
12.5	0.0	0.0561	0.2767	0.6273	1.0	2.0733
15.0	0.0	0.0557	0.2742	0.5551	1.0	2.0733
20.0	0.0	0.0553	0.2720	0.5483	1.0	2.0733
25.0	0.0	0.0553	0.2720	0.5483	1.0	2.0733

Table 5.3: *The Normal Force Coefficient C_N As A Function Of Angle Of Attack And Mach Number*

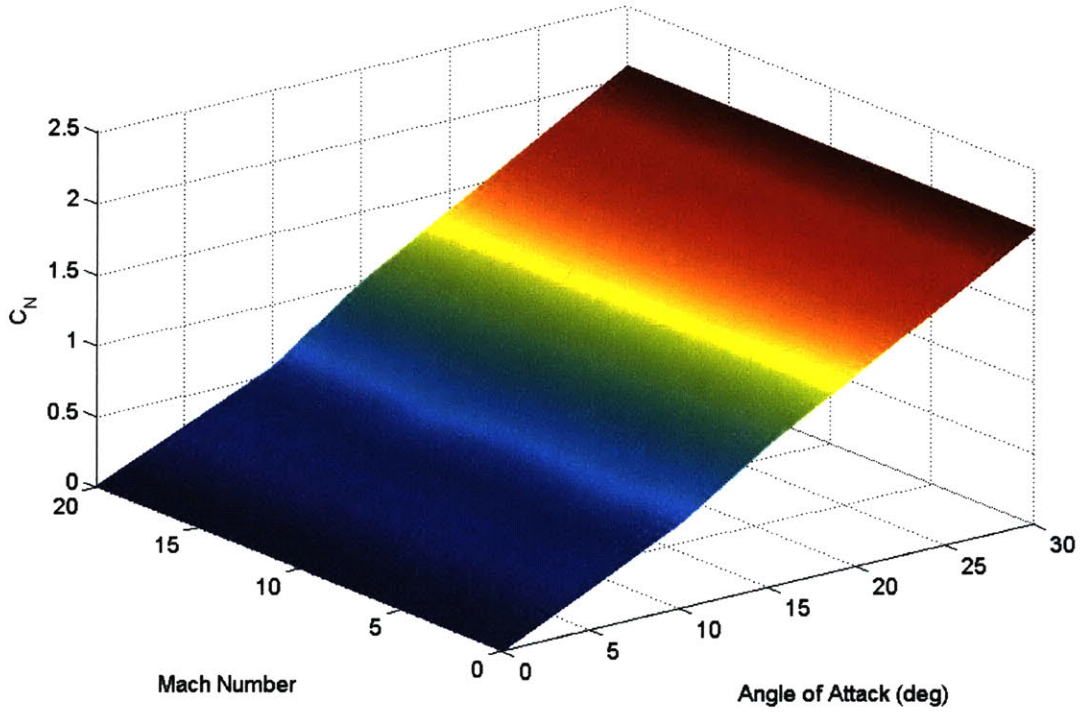

Figure 5-8: Normal Coefficient Of Force As A Function Of Mach Number And Angle Of Attack

Mach / α	0	1.0	5.0	10.0	15.0	30.0
0.0	0.5184	0.5184	0.5219	0.4866	0.5509	0.5920
0.5	0.5184	0.5184	0.5219	0.4866	0.5509	0.5920
0.8	0.5184	0.5184	0.5219	0.4866	0.5509	0.5920
1.0	0.5184	0.5184	0.5219	0.4866	0.5509	0.5920
1.2	0.5184	0.5184	0.5219	0.4866	0.5509	0.5920
1.5	0.5184	0.5184	0.5219	0.4866	0.5509	0.5920
2.0	0.5184	0.5184	0.5219	0.4866	0.5509	0.5920
3.0	0.5373	0.5373	0.5401	0.5479	0.5797	0.5920
4.0	0.5427	0.5427	0.5444	0.5518	0.5808	0.5920
5.0	0.5483	0.5483	0.5487	0.5559	0.5818	0.5920
8.0	0.5520	0.5520	0.5500	0.5563	0.5818	0.5920
10.0	0.5520	0.5520	0.5496	0.5559	0.5818	0.5920
12.5	0.5520	0.5520	0.5490	0.5557	0.5818	0.5920
15.0	0.5518	0.5518	0.5483	0.5550	0.5818	0.5920
20.0	0.5518	0.5518	0.5477	0.5537	0.5818	0.5920
25.0	0.5518	0.5518	0.5477	0.5537	0.5818	0.5920

Table 5.4: *The Center Of Pressure C_P As A Function Of Angle Of Attack And Mach Number Expressed As A Percentage Of Vehicle Length*

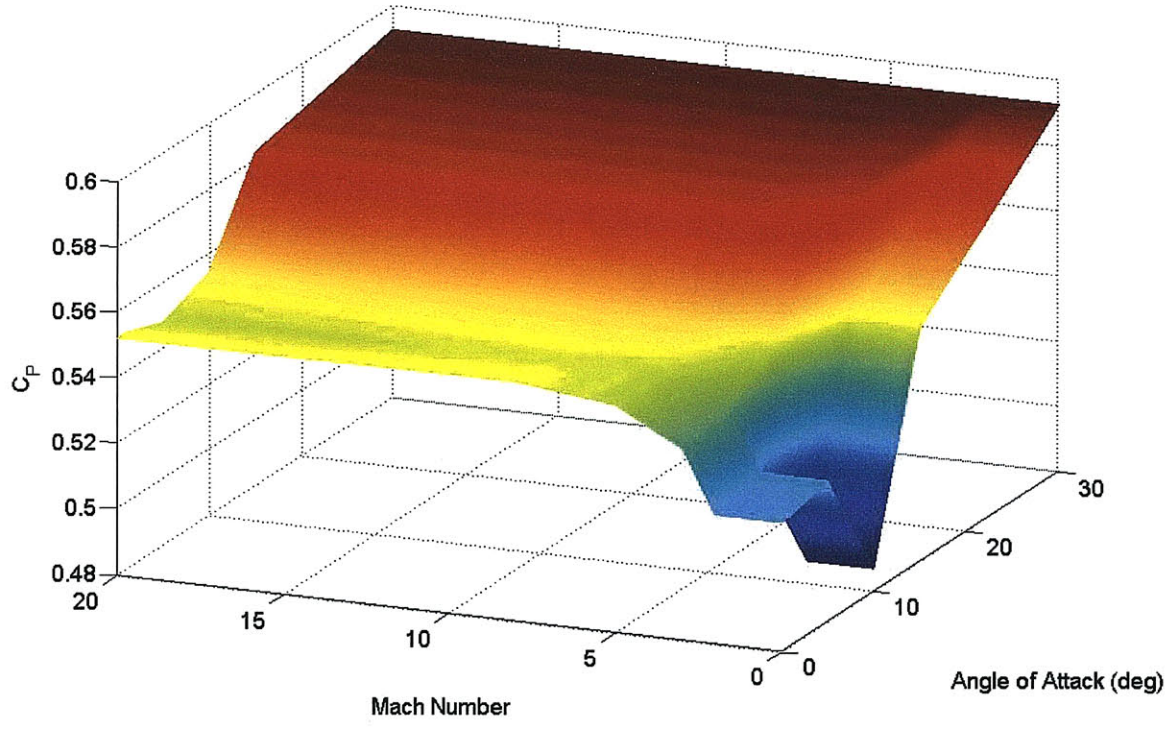

Figure 5-9: The Normalized Center Of Pressure As A Function Of Angle Of Attack And Mach Number

Using a table lookup can add significant computation time to an optimization algorithm, since the lookup operation must be performed multiple times for each iteration. The data may also be nonsmooth, creating some difficulties in calculating the finite difference approximations to the gradients. Therefore, C_X, C_N, and C_P can be approximated by analytic functions in order to speed up the computation time. The choice of functions must be such that the distinctive features of the aerodynamics remain intact. The analytic function for C_X is chosen such that a jump in the value of C_X is observed in the transonic (M≈1) region followed by an exponential decay to a steady state value as Mach number (M) increases. In addition, it models an increase in C_X as α increases in the supersonic region. The analytic function for C_N will be a linear function of α since there is little variation in C_N as Mach number increases. Lastly, C_P will be modeled using a heaviside function to represent the sharp increase in center of pressure across the transonic region (M≈1). For the analytic functions below, α is specified in degrees.

$$C_X = a_X + \frac{b_X}{1 + e^{-c_X((M-1)-d_X)}} e^{-e_X(M-1)} + \left(\frac{\alpha}{5}\right) \log \frac{1 + (\alpha\, M)}{10000} \tag{5.20}$$

$$C_N = a_N \alpha \tag{5.21}$$

$$C_P = \frac{a_P}{1 + e^{-M+b_P}} + c_P \tag{5.22}$$

The values for a_X, b_X, c_X, d_X, e_X, a_N, a_P, b_P, and c_P are chosen using a least squares fit to the tabular data. Comparisons between tabular data and analytic functions are shown in Figures 5-10, 5-11, and 5-12.

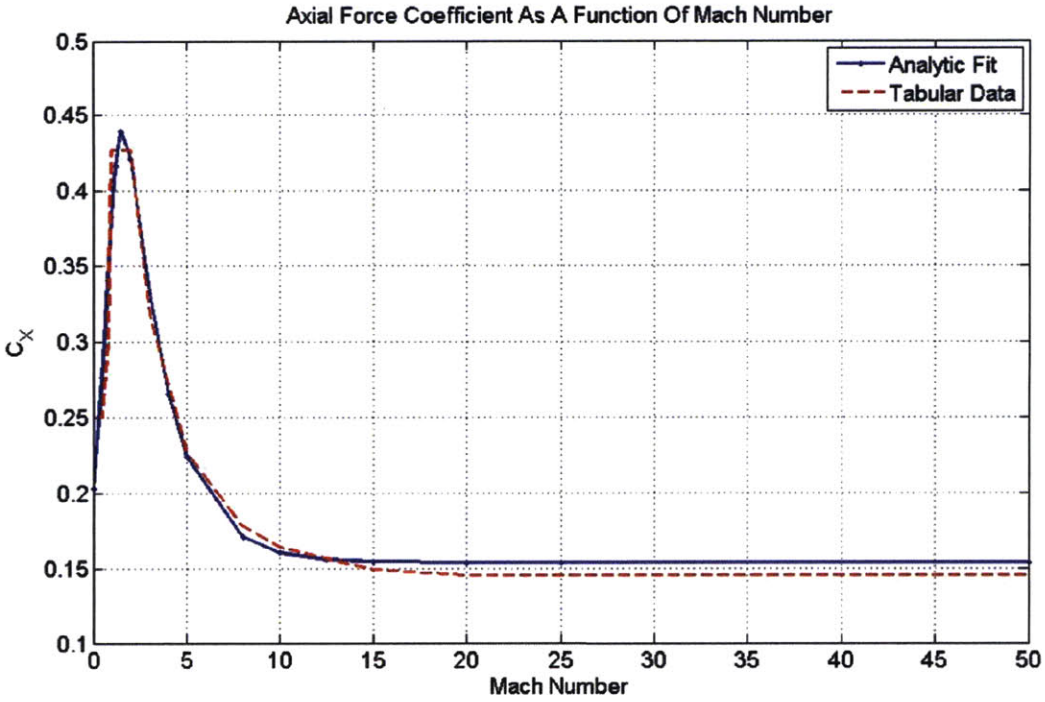

Figure 5-10: The Angle of Attack-Averaged Curve Fit To The Axial Coefficient Of Force Plotted Versus Mach Number

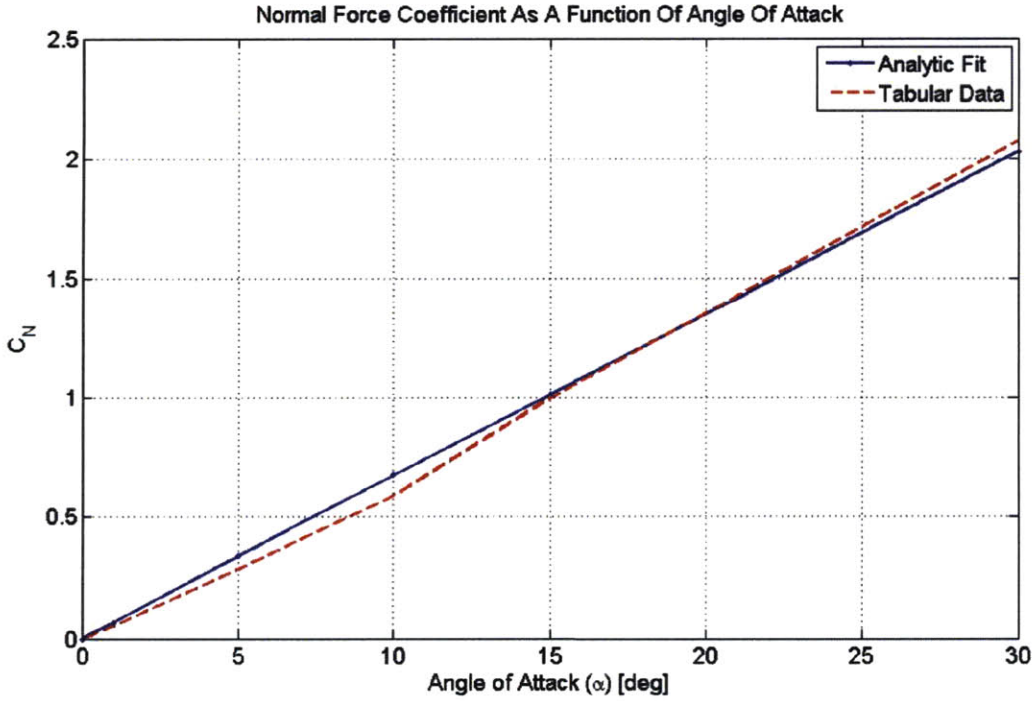

Figure 5-11: The Mach Number-Averaged Curve Fit For Normal Coefficient Of Force Plotted Versus Angle Of Attack

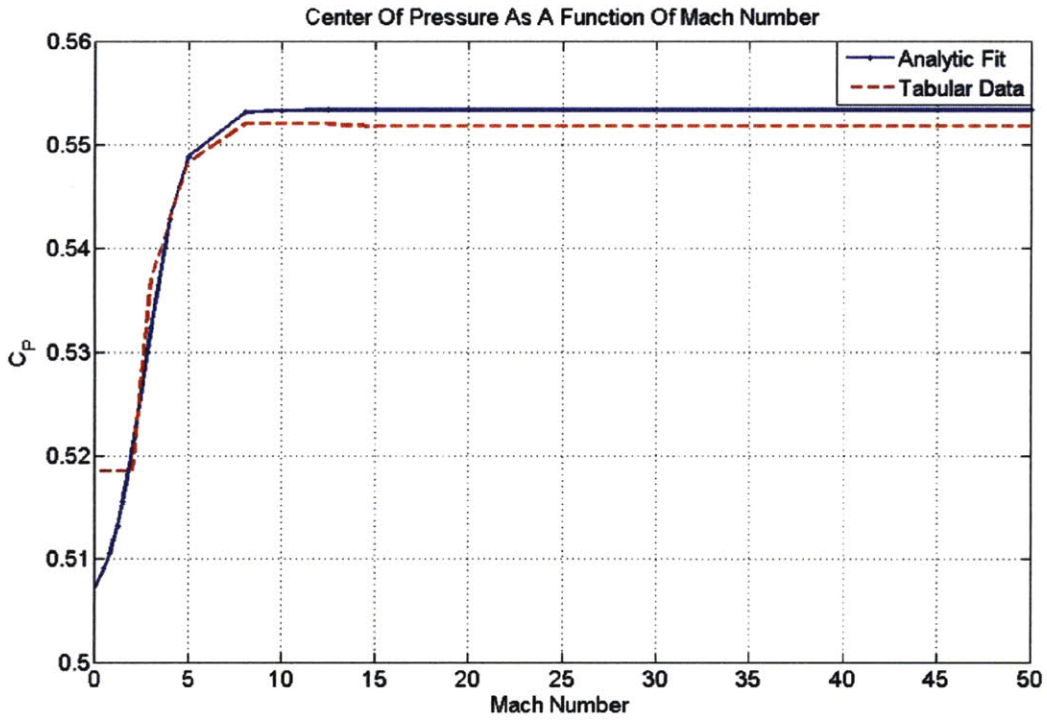

Figure 5-12: The Angle of Attack-Averaged Curve Fit For Center Of Pressure Plotted Versus Mach Number

5.4 Launch Vehicle Attitude Control

The launch vehicle exhibits two types of control to appropriately shape the trajectory and target the proper reentry interface conditions. The primary method of control is Thrust-Vector Control (TVC), in which the rocket engine is gimballed about nose axis of the vehicle body in order to direct moments that control the attitude. The secondary control is an attitude control system (ACS) with small thrusters that serve to stabilize the vehicle attitude during the coasting phases when the TVC control is inactive. The TVC control will be specified in terms of the gimbal angles while the ACS will be specified as moments about the vehicle's center of mass.

5.4.1 Thrust Vector Control

The TVC system diverts part of the engine thrust normal to the vehicle nose axis in order to create a moment about the body center of mass with the length from the center of mass to the engine nozzle serving as the moment arm. Let the component of thrust normal to the nose axis be denoted as $\mathbf{T_N}$ and the component of thrust acting along the nose axis be denoted as $\mathbf{T_A}$. $\mathbf{T_N}$ creates a moment about the vehicle center of mass while $\mathbf{T_A}$ accelerates the translational motion of the center of mass, as discussed in chapter 3. The direction of the total thrust, $\mathbf{T}$, relative to the nose axis will be described by the gimbal angles β and ξ. The angle β will denote the thrust angular offset from the nose axis in the plane of motion, while ξ will represent the out of plane offset of the thrust vector.

The thrust vector can be expressed as components along the body frame axes in terms of the gimbal angles as follows.

$$T_{x_B} = T\cos\beta\cos\xi \tag{5.23}$$

$$T_{y_B} = T\cos\beta\sin\xi \tag{5.24}$$

$$T_{z_B} = T\sin\beta \tag{5.25}$$

where

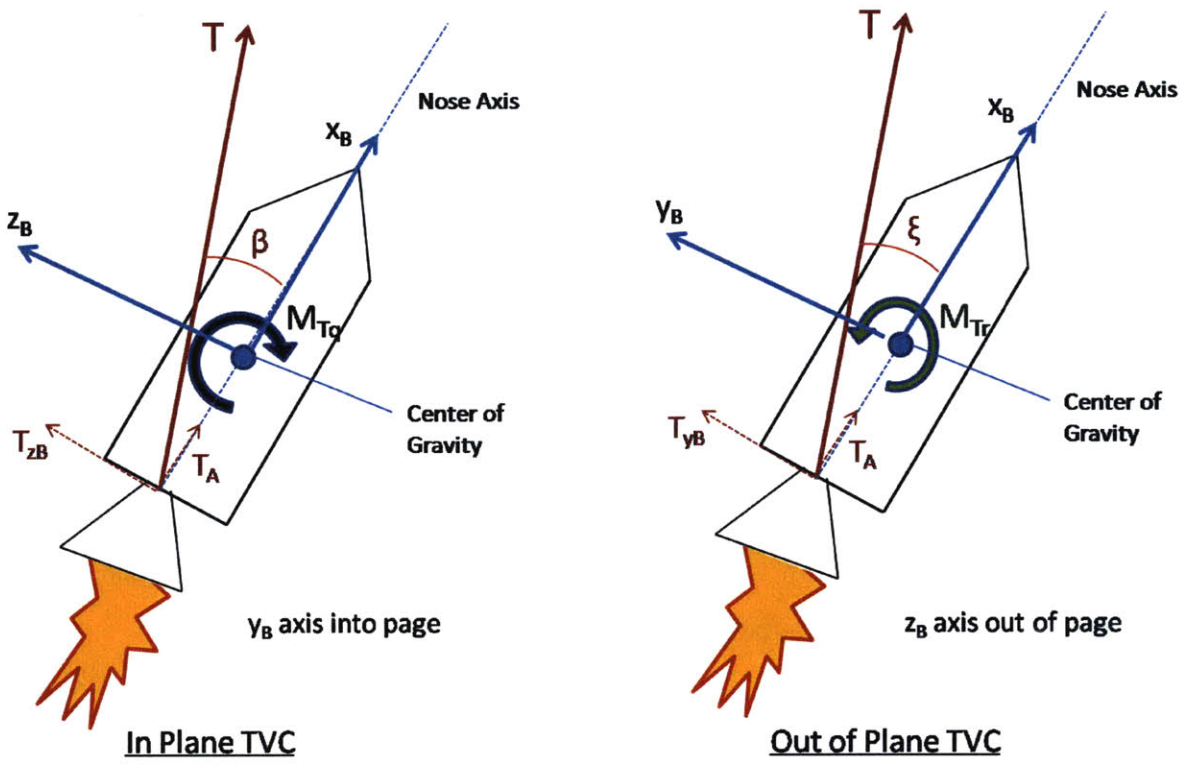

Figure 5-13: In Plane and Out of Plane Thrust Vectoring Control

$$|\mathbf{T_A}| = \quad T_{x_B}$$
$$|\mathbf{T_N}| = \sqrt{T_{y_B}^2 + T_{z_B}^2}$$

As mentioned above, T_{x_B} will provide acceleration to the vehicle, while T_{y_B} and T_{z_B} will create moments about the vehicle center of mass. The pitch and yaw control moments (M_{T_q}, M_{T_r}) exerted by the TVC about the y_B and z_B axes can be expressed in terms of the thrust components as well as the vehicle center of mass and length. The center of mass is assumed to be equivalent to the center of gravity (CG) in this formulation. Let CG represent the vehicle *center of gravity* as a percentage of the total body length, measured from the nose toward the aft of the vehicle, and L represent the total length of the launch vehicle stack at each stage. For this vehicle, the center of gravity (CG) is chosen as a constant value of 0.5086.

$$\mathbf{M_{Tq}} = T_{z_B} (1 - CG) L \tag{5.26}$$

$$\mathbf{M_{Tr}} = -T_{y_B} (1 - CG) L \tag{5.27}$$

The moments about the center of mass from the TVC, $\mathbf{M_{Tq}}$ and $\mathbf{M_{Tr}}$, are *defined to be positive* about the body axes y_B and z_B. Notice that a positive β gimbal angle creates a positive moment in the pitch direction (about y_B), while a positive ξ gimbal angle creates a negative moment in the yaw direction (about z_B). In other words, a positive β angle will increase the body pitch rate (q_{body}), forcing the nose downward, while a positive ξ angle will decrease the body yaw rate (r_{body}), forcing the nose in a direction to the right, as seen from the z_B axis, and reducing the heading angle (ψ).

5.4.2 Attitude Control System

The attitude control system (ACS) consists of small thrusters oriented normal to the body nose axis that are used to stabilize the body attitude during the coast (unpowered) portions of the boost flight. The ACS exerts the appropriate moments about the vehicle center of mass to keep the nose pitch angle, θ, and nose yaw angle, ϕ, constant during the coast phases. The pitch and yaw moments exerted by the ACS about the y_B and z_B axes are defined as M_{C_q} and M_{C_r}, respectively. These torques are only used for control during the unpowered segments of flight.

5.4.3 Aerodynamic Torques

The vehicle control discussed above will be counteracting aerodynamic torques exerted on the vehicle from the aerodymamic forces acting at the vehicle center of pressure. The offset of the center of pressure from the center of mass is referred to as the *static margin.*

$$L_{SM} = (C_P - CG) L \tag{5.28}$$

The normal aerodynamic force, F_N, will exert a moment about the vehicle center

of mass with a moment arm of L_{SM}. The vehicle is a stable system since the center of pressure is always farther aft than the center of mass ($L_{SM} > 0$) and the applied aerodynamic moment (M_A) will always rotate the vehicle in a direction toward zero angle of attack.

$$M_A = F_N \, L_{SM} = \frac{1}{2} \rho \, V_E^2 \, S_{ref} \, C_N \, L_{SM} \tag{5.29}$$

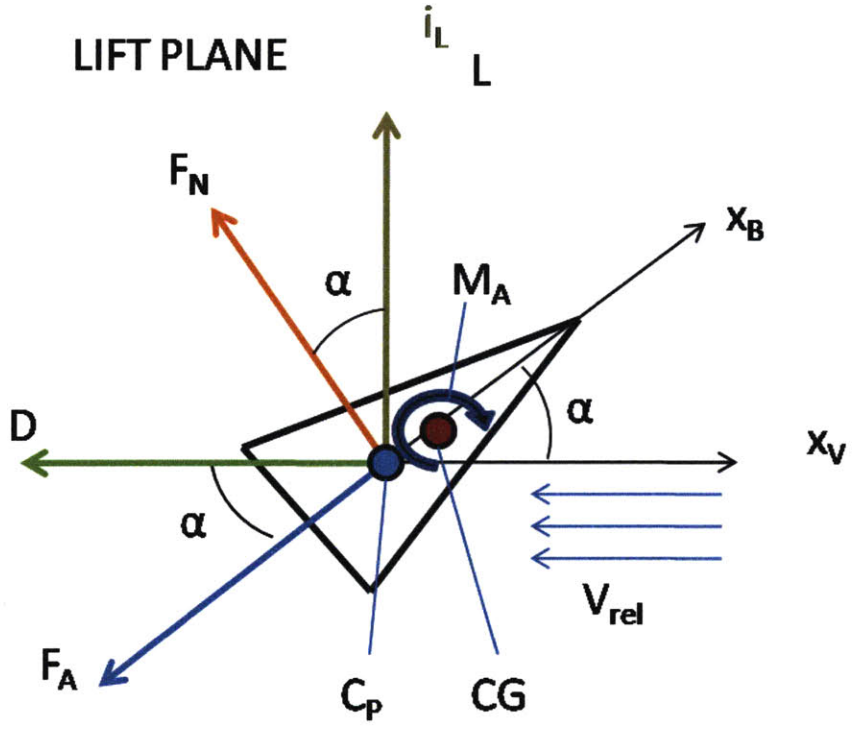

Figure 5-14: External Aerodynamic Torque

Since F_N acts in the lift plane, the total aerodynamic moment M_A also acts in the lift plane and can be expressed in components along the body axes using the lift bank angle, σ. Let the component along the y_B axis be denoted as M_{A_q} and the component along the z_B axis be denoted as M_{A_r}.

$$\mathbf{M_{A_q}} = M_A \cos\sigma \tag{5.30}$$

$$\mathbf{M_{A_r}} = -M_A \sin\sigma \tag{5.31}$$

The negative sign on $\mathbf{M_{A_r}}$ occurs because σ is defined as a positive angle when the vehicle is turning to increase its heading (i.e. turning left), and the restoring aerodynamic moment at this attitude has a negative component along $\mathbf{z_B}$.

5.4.4 Launch Vehicle Control Summary

The sum of external moments exerted on the vehicle during the boost flight can be summed along the y_B and z_B axes to obtain expressions for the total torques used in the rotational equations of motion.

$$\sum \tau_{y_B} = T_{z_B} (1 - CG) L + M_{C_q} + M_A \cos\sigma \tag{5.32}$$

$$\sum \tau_{z_B} = -T_{y_B} (1 - CG) L + M_{C_r} - M_A \sin\sigma \tag{5.33}$$

Note that the first and second terms on the right side act on the vehicle during separate segments and will never exert moments on the vehicle simultaneously.

5.5 Launch Optimal Control Problem Formulation

The launch portion of flight will be formulated as an optimal control problem in terms of path, event, state bound, and control bound constraints as well as a series of knots for segmenting the trajectory. The launch trajectory problem will be formulated such that the vehicle remains in the same inertial plane of motion for the entirety of the launch flight, the angle of attack is stabilized to zero during the coasting segments, and the states remain continuous over the entire trajectory.

5.5.1 Initial Conditions

The initial conditions for a launch vehicle problem typically involve a vehicle located on the surface of the Earth at a given latitude and longitude that is at rest relative to the rotating Earth and fixed upright on a launch pad. These initial conditions are difficult to describe in terms of the state vector, $\mathbf{x}$, formulated in this problem since the flight path

angle, γ, and velocity heading angle, ψ, are undefined when velocity is equal to zero. In addition, singularities exist in the equations of motion when $V_E = 0$ or $\gamma = 90$ degrees. Therefore, initial conditions are obtained by propagating values very close to the singular values out to a reasonable distance away from the singularities. The initial conditions used in this problem are as follows.

$$
\begin{aligned}
r_I &= \mathbf{f}\left(h_I, \lambda_I\right), \quad \text{where } h_I = 100 ft \\
\mu_I &= 0\, deg \\
\lambda_I &= 0\, deg \\
V_{E_I} &= 90\, ft/sec \\
\gamma_I &= 70\, deg \\
\psi_I &= \text{open} \\
q_{body_I} &= \text{open} \\
r_{body_I} &= \text{open} \\
\theta_I &= 0\, deg \\
\phi_I &= 0\, deg
\end{aligned}
$$

The initial conditions of the vehicle are at an altitude of 100 feet above the surface of the Earth at a velocity of 90 feet per second and a flight path angle of 70 degrees. In order to properly define the initial value for the radial distance, r_I, the initial geodetic altitude, h_I, is transformed to the geocentric radial distance using the ellipsoidal-Earth model and λ_I. Since the relative longitude, μ, and relative latitude, λ, can always be defined relative to the launch point, the initial values of μ and λ can be fixed to zero for all cases. The initial heading angle will be determined by the particular scenario examined in each case, while the body rates will be determined by the optimizer.

5.5.2 Knots

As mentioned in chapter 3, the trajectory is split up into separate segments with knots located at the boundaries of the segments. The inclusion of knots into the problem allows for placement of dynamic, path, event, state, and control constraints that may only act

over a portion of the trajectory. For the boost problem, seven knots are used to separate the boosting and coasting portions of flight. Five of these knots are *interior knots*, which lie along the trajectory between the initial time, t_0, and the final time t_f. The other two knots are *boundary knots*, which lie at t_0 and t_f to specify initial and end conditions.

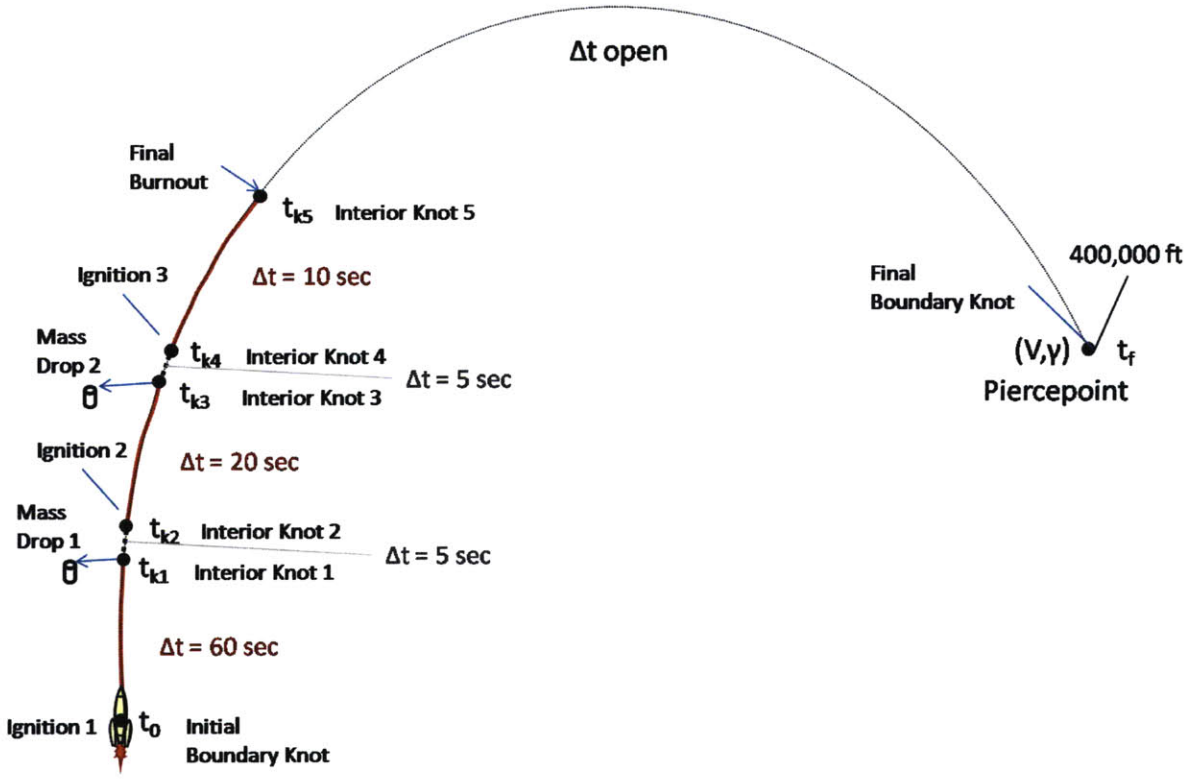

Figure 5-15: Knot Locations Along Launch Trajectory

For the launch trajectory, all interior knots times, t_{k_i}, will be fixed to predetermined times while the final boundary knots at time t_f will be allowed to vary. Bounds are set on the time of the final knot to ensure that it is not placed before any of the five interior knots. The boost segment times are fixed to 60 seconds, 20 seconds, and 10 seconds, respectively, as given in section 5.1.2, while the coasting segments between burns are fixed to 5 seconds each. The final ballistic coast segment has an open time interval that will stretch from the final burnout point until the vehicle reaches the piercepoint altitude.

5.5.3 State Bounds

The following state bounds are adopted to reasonably limit the vehicle motion as well as avoid potential singularities.

$$
\begin{array}{rcccl}
R_E - 60,000\,ft & \leq & r & \leq & R_E + 50,000,000\,ft \\
-1\,deg & \leq & \mu & \leq & 180\,deg \\
-1\,deg & \leq & \lambda & \leq & 89\,deg \\
10\,ft/sec & \leq & V_E & \leq & 500,000\,ft/sec \\
-89\,deg & \leq & \gamma & \leq & 89\,deg \\
-180\,deg & \leq & \psi & \leq & 180\,deg \\
-10\,deg/sec & \leq & q_{body} & \leq & 10\,deg/sec \\
-10\,deg/sec & \leq & r_{body} & \leq & 10\,deg/sec \\
-30\,deg & \leq & \theta & \leq & 30\,deg \\
0\,deg & \leq & \phi & \leq & 0\,deg
\end{array}
$$

The radial distance, r, is given a lower bound that allows values slightly less than the Earth mean radius, R_E, due to the oblateness of the Earth. The upper bound on r is made large enough that it cannot physically limit any feasible trajectories. The relative longitude, μ, is bounded on the lower end by -1 degrees to limit the optimization search to trajectories that head in a direction of increasing longitude, while the upper bound is 180 degrees. Similarly, the lower bound of -1 degrees on relative latitude is imposed to limit the search space, while an upper bound of 89 degrees is imposed to avoid a singularity at $\lambda = 90\,deg$. The Earth-relative velocity, V_E, is bounded to be positive at all times, with the lower bound at $10\,ft/sec$ to avoid a singularity when $V_E = 0$ and the upper bound set large enough that it cannot physically limit any feasible trajectories. The flight path angle, γ, is bounded to be within ± 89 degrees in order to avoid singularities at $\gamma = \pm 90$ degrees. The heading angle, ψ, is allowed to be open to all values $\pm$ 180 degrees to allow a full range of motion for turning the vehicle in various directions. The body rates, q_{body} and r_{body}, are limited to $\pm\,10\,deg/sec$, while the nose pitch angle, θ, is limited to $\pm$ 30 degrees. The nose yaw angle, ϕ, is constrained to zero in order to keep the vehicle

traveling in the same plane of motion throughout the boost trajectory. In order to satisfy this constraint, the optimizer will choose the lateral thrust vector control angle, ξ, and the ACS yaw control M_{C_r}, such that the thrust torque balances any out of plane motion.

5.5.4 Control Bounds

The controls are bounded based upon the limitations of the control systems on the launch vehicle.

$$\begin{aligned} -10\,deg \leq\ & \beta & \leq\ & 10\,deg \\ -10\,deg \leq\ & \xi & \leq\ & 10\,deg \\ -1\,\text{N-m} \leq\ & M_{C_q} & \leq\ & 1\,\text{N-m} \\ -1\,\text{N-m} \leq\ & M_{C_r} & \leq\ & 1\,\text{N-m} \end{aligned}$$

The thrust vector control system has the capability to gimbal the engine nozzle a maximum of 10 degrees in both the pitch direction and the yaw direction. Likewise, the small ACS thrusters used to stabilize the vehicle during the coasting segments can exert a maximum torque of 1 Newton-meter (N-m) in both the pitch direction and the yaw direction.

5.5.5 Event Constraints

Event constraints are enforced at the knot locations to dictate continuity of the states and also specify state values that are desired at the knot locations.

$$
\begin{aligned}
\mathbf{x}\left(t_{k_i}^{+}\right) - \mathbf{x}\left(t_{k_i}^{-}\right) &= \mathbf{0} \qquad \forall i = 1, \ldots, K \\
h\left(t_f\right) - 400{,}000\, ft &= 0 \\
-1\, deg \leq \gamma\left(t_f\right) &\leq -89\, deg \\
\theta\left(t_{k_1}^{-}\right) &= 0 \\
\theta\left(t_{k_2}^{+}\right) &= 0 \\
\theta\left(t_{k_3}^{-}\right) &= 0 \\
\theta\left(t_{k_4}^{+}\right) &= 0 \\
\theta\left(t_{k_5}^{-}\right) &= 0
\end{aligned}
$$

The first set of event constraints specify that the states must be continuous across all of the interior knots. The second and third event constraints dictate conditions that must be met at piercepoint. The piercepoint must occur at 400,000 feet above the surface of the Earth and the flight path angle, γ, must have a negative value less than -1 degree to ensure that the piercepoint occurs when the vehicle is re-entering the atmosphere and not when it is exiting the atmosphere. The remainder of the events specify constraints on the nose pitch angle (θ) at the boundaries between the trajectory segments. Since ϕ is constrained to zero for the entirety of the launch flight, θ is equivalent to the aerodynamic angle of attack, α, during the launch flight, as given by Equation 2.6. In order to eliminate potential instabilities that may occur during engine ignition or burnout if the vehicle is at a high angle of attack, θ is constrained to be zero at these boundaries.

5.5.6 Path Constraints

Path constraints are enforced on the trajectory nodal points between the knots in order to specify special limits on the states and controls during particular segments of flight.

$$
\begin{aligned}
0 \leq\ & h(t) && \leq 5,000,000 ft && \forall t \\
& \beta(t) && = 0 && \forall t_{k_1} \leq t \leq t_{k_2},\ t_{k_3} \leq t \leq t_{k_4},\ t_{k_5} \leq t \leq t_f \\
& \xi(t) && = 0 && \forall t_{k_1} \leq t \leq t_{k_2},\ t_{k_3} \leq t \leq t_{k_4},\ t_{k_5} \leq t \leq t_f \\
& M_{C_q}(t) && = 0 && \forall t_0 \leq t \leq t_{k_1},\ t_{k_2} \leq t \leq t_{k_3},\ t_{k_4} \leq t \leq t_{k_5} \\
& M_{C_r}(t) && = 0 && \forall t_0 \leq t \leq t_{k_1},\ t_{k_2} \leq t \leq t_{k_3},\ t_{k_4} \leq t \leq t_{k_5} \\
& \theta(t) && = 0 && \forall t_{k_1} \leq t \leq t_{k_2},\ t_{k_3} \leq t \leq t_{k_4},\ t_{k_5} \leq t \leq t_f
\end{aligned}
$$

The first path constraint dictates that the altitude of the vehicle above the surface of the Earth (ellipsoidal model) must remain positive over the entire flight. This must be imposed by a path constraint since the altitude is not a state variable. The following four path constraints dictate the segments of the trajectory in which certain controls are inactive. The thrust vectoring controls (β, ξ) are inactive during the coasting periods, while the attitude control system is inactive during the thrusting segments. The limitation of the thrust vectoring control (TVC) angles during coasting is especially important since β and ξ have no controllability of the vehicle when the thrust is equal to zero. Without fixing these controls to zero during the coasts, the optimization algorithm would detect the objective function to be invariant with respect to a variation in the TVC controls during coast and would not be able to converge on a unique solution for the TVC control profile during the coasting flight.

The final path constraint dictates that the nose pitch angle, and therefore angle of attack, is stabilized to zero over each of the coasting periods. The reasons for imposing this constraint involve both stability and controllability. For stability reasons, the angle of attack is set to zero because the attitude control system (ACS) is only designed with enough control authority to stabilize the vehicle, not to maneuver the vehicle. As the angle of attack increases, the aerodynamic forces increase in magnitude, leading to more intense aerodynamic moments exerted on the vehicle body which require a powerful control system to counteract. In order to avoid high frequency attitude motion, the event constraints mentioned in the previous section specify that the TVC system must drive the angle of attack to zero prior to each stage burnout and the path constraint here specifies that the

ACS control will stabilize the angle of attack to zero for the entire length of each coast. The angle of attack is also stabilized to zero for controllability purposes. As the vehicle ascends to higher altitudes, the atmospheric density exponentially decreases, leading to a substantial decrease in dynamic pressure exerted on the vehicle by the relative wind. As the dynamic pressure descreases, so does the ability to generate lift for manuevering the vehicle. As the vehicle ascends higher, the sensitivity of the vehicle trajectory to changes in the vehicle attitude approaches zero. This can create ill-conditioned sensitivity matrices in the optimization algorithm, leading to incorrect or infeasible solutions. Therefore, the angle of attack is stabilized to a constant value of zero during the ballistic coast to piercepoint to avoid controllability issues.

5.6 Launch Vehicle Capabilities

Now that the launch vehicle has been formulated, the full capabilties of the vehicle will be examined.

5.6.1 Initial Guess

The DIDO solver used in this study requires an initial guess for the state, control, and time variables to initialize the optimization algorithm. It is recommended, but not required, that the initial guess represents a dynamically feasible trajectory that obeys the state dynamics throughout the trajectory [6]. An initial guess is obtained for the boost problem by starting with the initial conditions presented in section 5.5.1 and integrating the vehicle dynamics equations developed in chapter 3 with all controls set to zero. Since the vehicle is a stable system ($SM > 0$), it is expected that propagation of the initial conditions with zero control will provide a reasonable guess. The initial heading angle, ψ, is initially set to be traveling along the Equator ($\psi = 0$), while q_{body} and r_{body} are also initially set to zero. The guess altitude profile plotted versus relative longitude (downrange) is given in Figure 5-16.

The guess trajectory travels 30.5 degrees downrange and peaks at an altitude of 2000 kilofeet with no applied attitude control. Since the initial heading was 0 degrees, the

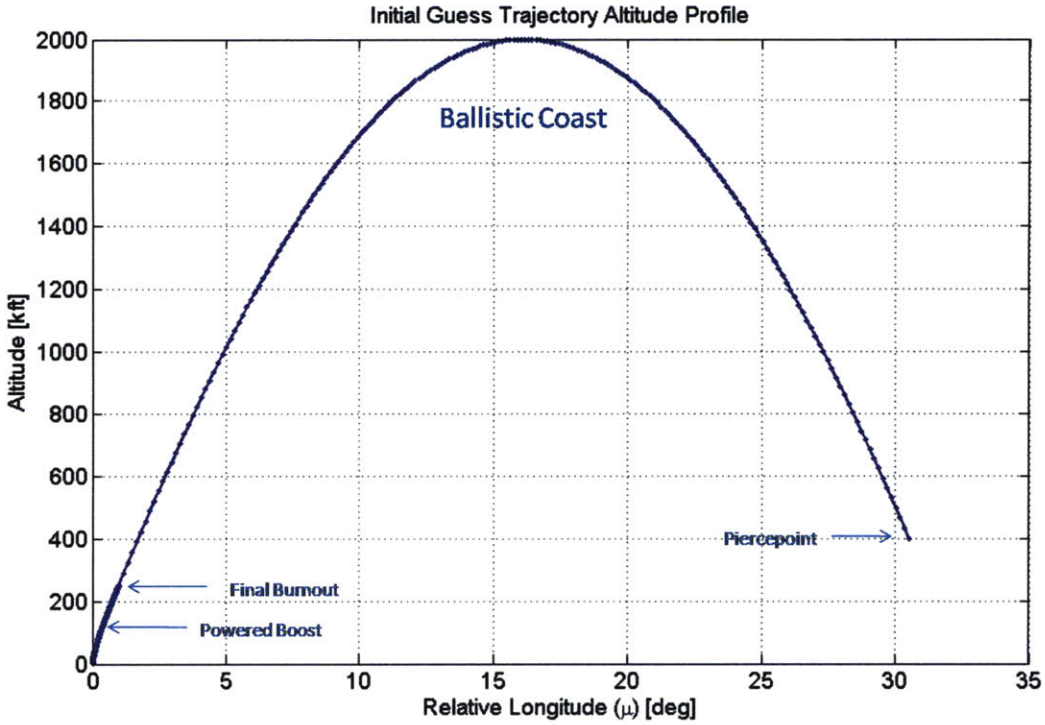

Figure 5-16: Altitude Versus Relative Longitude For Guess Trajectory

vehicle does not travel out of plane and the relative longitude (λ) and heading (ψ) are equal to zero for the duration of the flight. As designed in section 5.1, the vehicle achieves a velocity of approximately 16,000 feet per second upon the final engine burnout, as shown in Figure 5-17.

Each of the coasting and powered segments of flight can be easily identified in Figure 5-17. After final burnout, the vehicle ascends until gravity is able to turn the velocity vector downward, then descends and gains velocity as it approaches the piercepoint.

The flight path angle, γ, begins at 70 degrees and initially begins to drop due to gravitational acceleration and a low initial speed. However, the reduction in flight path angle creates a positive angle of attack, which decelerates the flight path angle drop using a torque created by the thrust force acting along the nose axis. This positive angle of attack is short-lived, as stabilizing aerodynamic torques drive the angle of attack toward zero, as seen in Figure 5-19.

The final stage burnout is shown to occur when γ is approximately 30 degrees. From

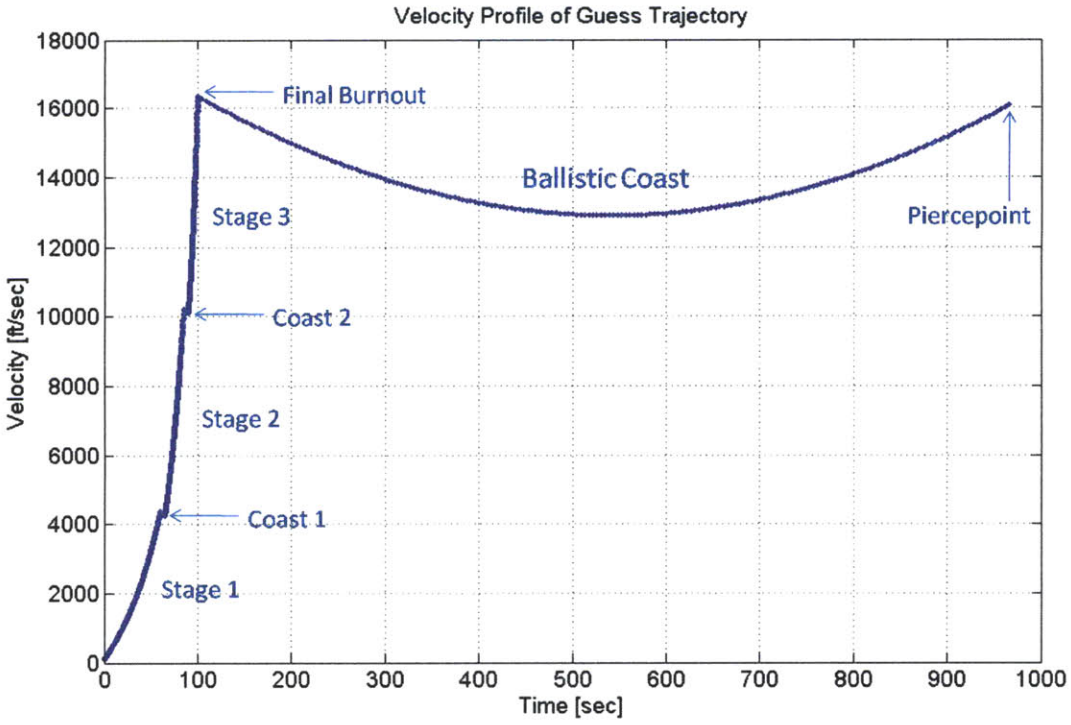

Figure 5-17: Earth-Relative Velocity Versus Time For Guess Trajectory

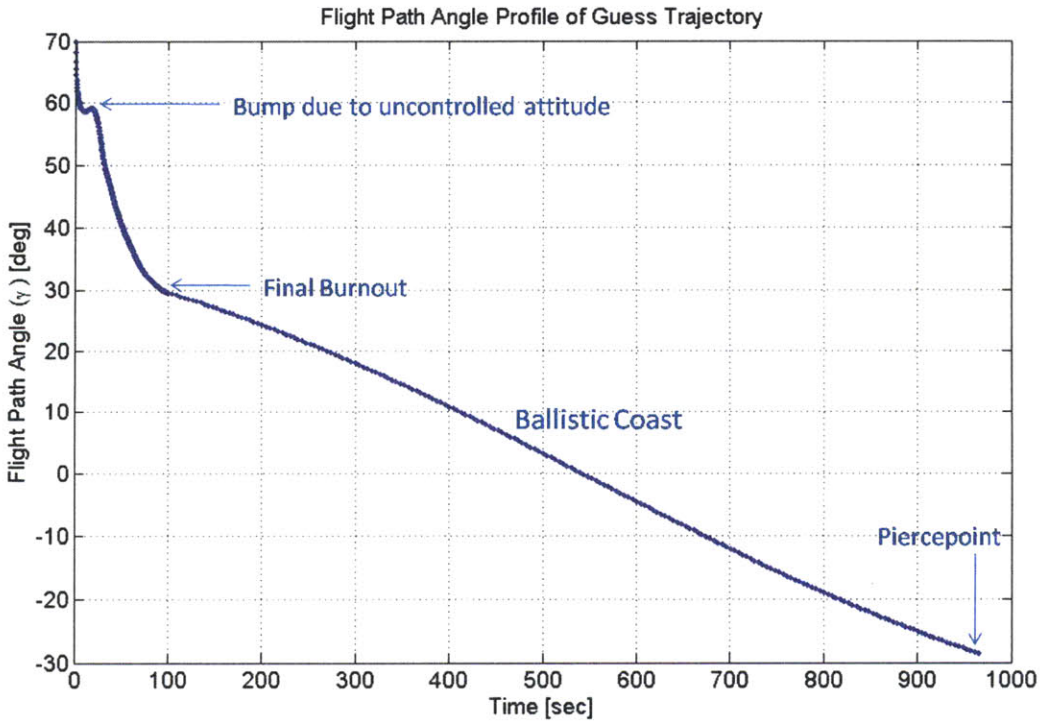

Figure 5-18: Flight Path Angle Versus Time For The Guess Trajectory

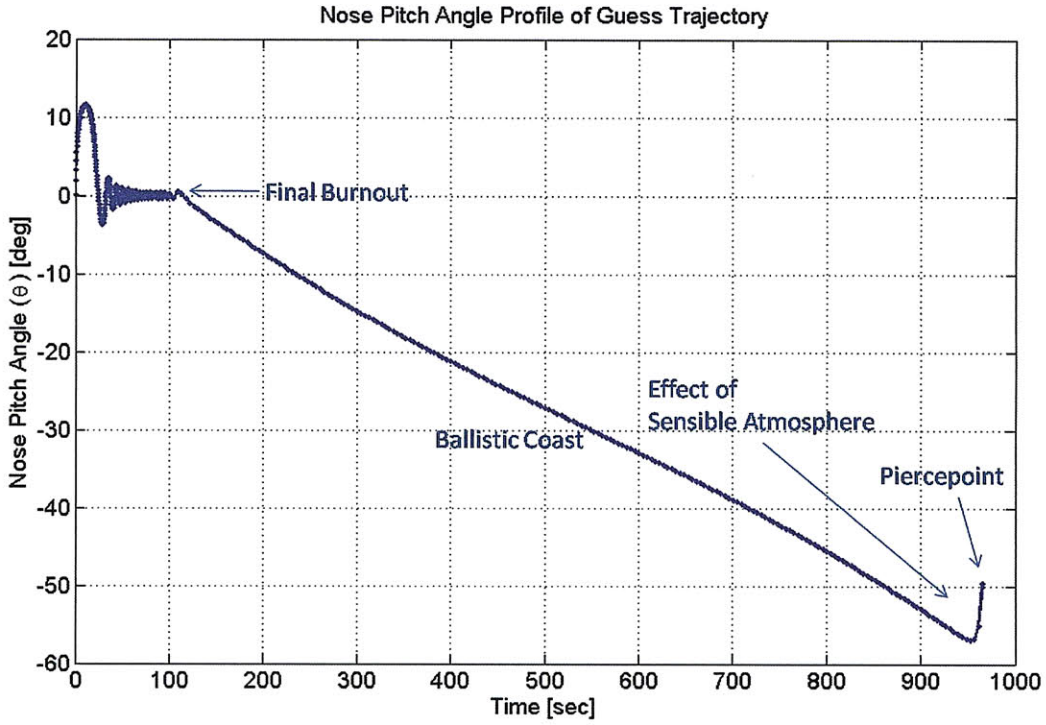

Figure 5-19: Nose Pitch Angle Profile For Guess Trajectory

this point, gravity turns the flight path angle negative until the vehicle reaches the piercepoint altitude. Notice that the flight path angles at piercepoint and final burnout are nearly symmetric about $\gamma = 0$.

The nose pitch angle, θ, oscillates about $\theta = 0$ due to the stabilizing aerodynamic moments exerted on the vehicle. The change in the amplitude and frequency of the oscillations can be explained by variation of the applied aerodynamic moments over time. The dynamic pressure exerted on the vehicle body increases with the square of velocity, increasing the aerodynamic moments significantly. However, as the vehicle ascends to higher altitudes, the exponential decay of atmospheric density eventually reduces the dynamic pressure to zero.

Additionally, as the vehicle gains speed, the center of pressure, C_P, moves toward the aft of the vehicle, increasing the static margin and, therefore, the stability of the vehicle. All of these factors contribute to the observed attitude dynamics of the vehicle with no applied controls. It can be seen in Figure 5-19 that the oscillations reduce in magnitude,

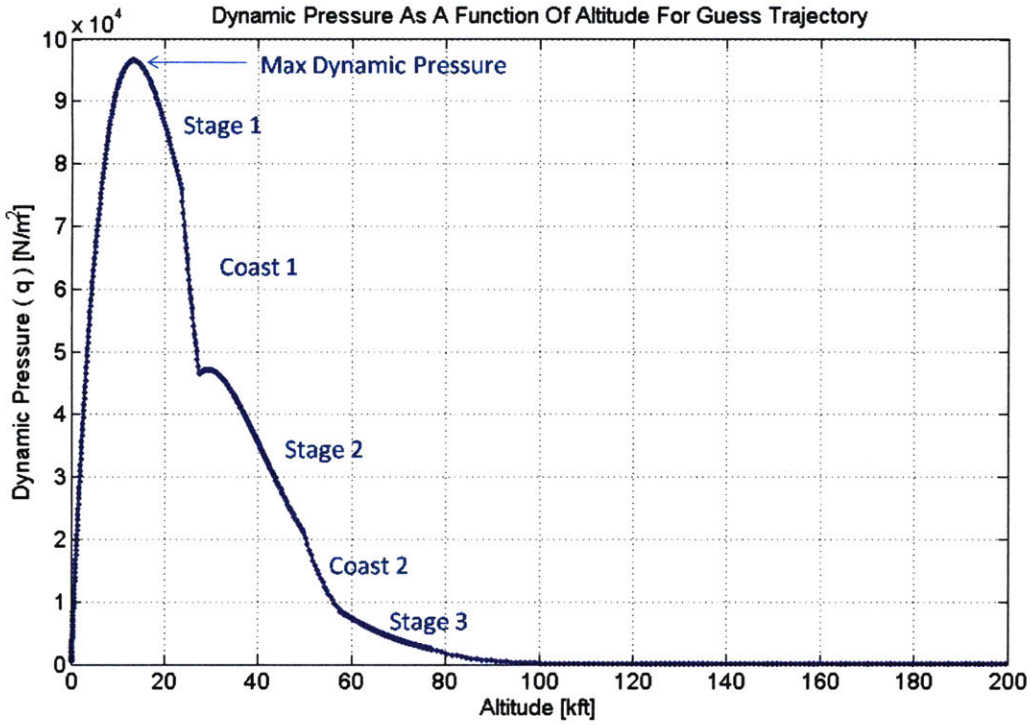

Figure 5-20: Dynamic Pressure As A Function Of Altitude For The Guess Trajectory

but increase in frequency as the vehicle gains altitude and velocity.

It can be observed that as the vehicle leaves the atmosphere, it loses stability since the stabilizing aerodynamic moments approach zero. This results in the body pitch rate leveling out to a constant value as the vehicle heads into space. The attitude control system (ACS) described in section 5.4 is used to stabilize the vehicle attitude during this portion of flight.

These dynamically feasible states are input into the DIDO solver as a guess to solve for optimal trajectories.

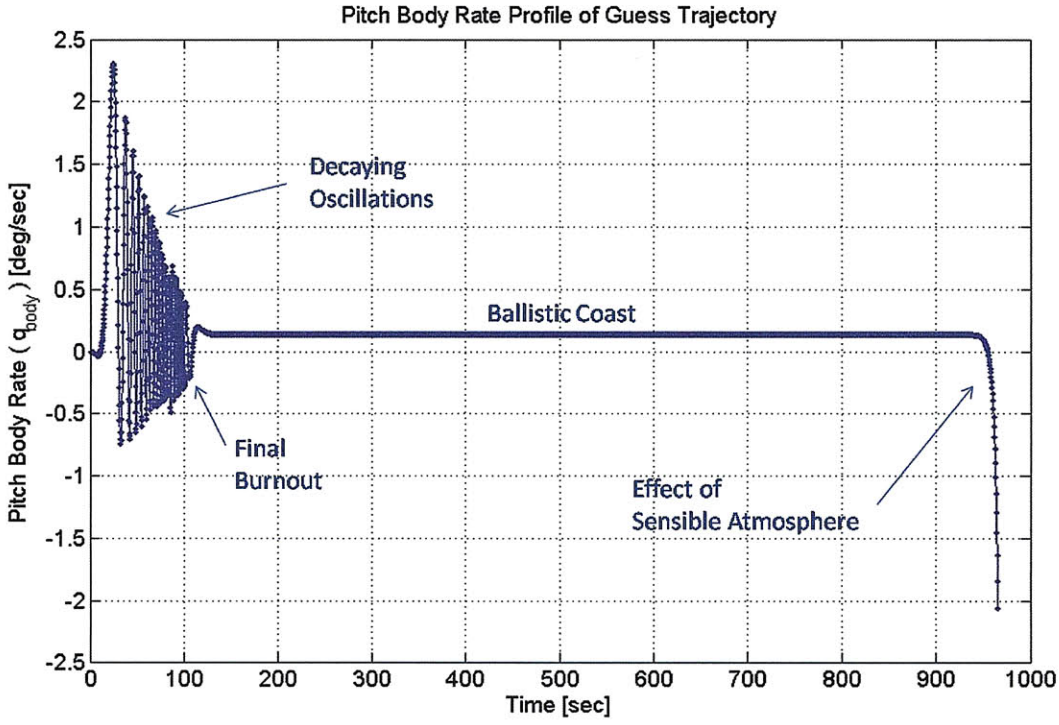

Figure 5-21: Body Pitch Rate Versus Time For Guess Trajectory

5.6.2 Maximum Piercepoint Range Case

The first capability of the launch vehicle to be examined is the maximum range piercepoint that can be reached. This problem enforces the dynamic, event, and path constraints formulated in the previous sections and applies the following cost function.

$$J = -\mu\left(t_f\right)$$

The launch vehicle is able to enhance its range capability by using optimal thrust vectoring controls to control the vehicle attitude during the boosting segments of flight. The attitude control system stabilizes the attitude during the coasting segments and thus has no influence on the optimal motions of the vehicle. The maximum range capability for the launch vehicle is approximately 31.5 degrees downrange, as can be observed in Figure 5-22.

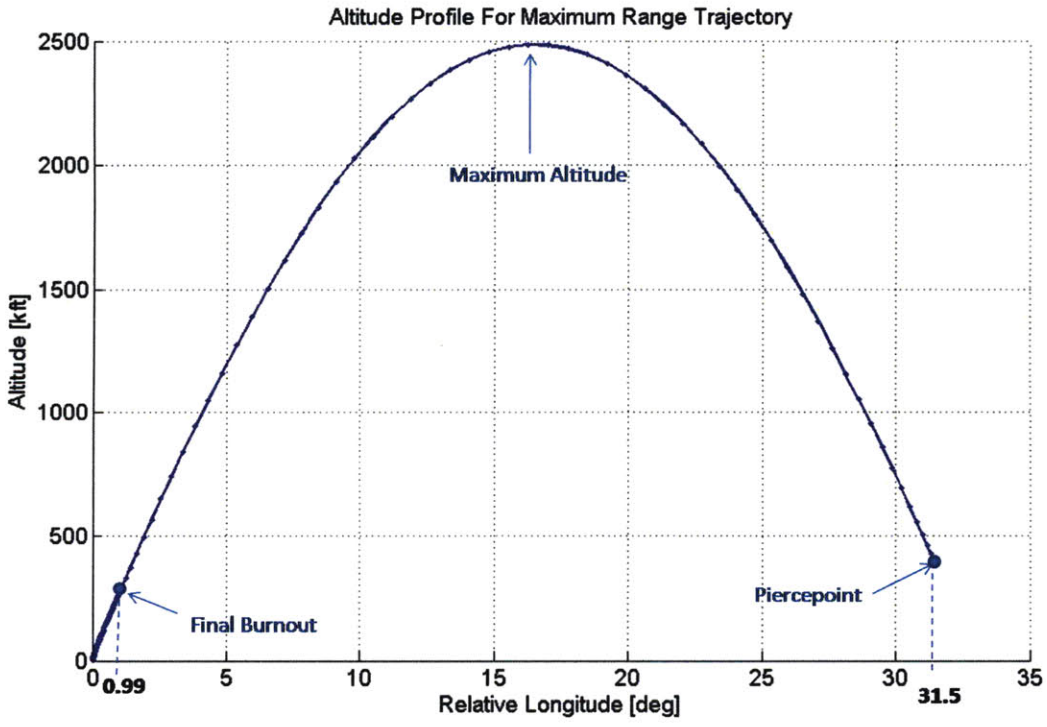

Figure 5-22: Maximum Range Boost Trajectory

The final stage burnout occurs at an altitude of 265,400 feet and a relative longitude

of 0.99 degrees downrange from the launch point with a velocity magnitude of 16,337 feet per second and a flight path angle of 34.4 degrees. From this point, the vehicle glides ballistically with angle of attack stabilized to zero until it reenters at the piercepoint altitude of 400,000 feet. The conditions upon reentry at piercepoint are as follows:

$$\begin{aligned} t_f &= 1072\,sec \\ h(t_f) &= 400,000\,ft \\ \mu(t_f) &= 31.5\,deg \\ V_E(t_f) &= 16,077 ft/sec \\ \gamma(t_f) &= -33.7\,deg \end{aligned}$$

The results here show that the maximum range can be attained by reaching the final burnout location with a flight path angle of approximately 34 degrees. Since the flight path angle profile is nearly symmetric about $\gamma = 0$ during the ballistic coast, this corresponds to an optimal reentry flight path angle of -33.7 degrees at piercepoint. The value for γ at the final burnout represents an optimal balance between vertical velocity and downrange velocity. Higher values of γ at burnout will result in higher maximum altitudes but reduced piercepoint ranges, while lower values of γ will have lower maximum altitudes and hit piercepoint uprange of the maximum range piercepoint. In Figure 5-23, it can be observed that the vehicle optimally manuevers during the boost segments to target $\gamma = 34.4\,deg$ at the final burnout. For comparison, the suboptimal guess trajectory illustrated in Figure 5-18 reaches final burnout with $\gamma \approx 29\,deg$.

The flight path angle profile is influenced by the nose pitch angle variation over time. Figure 5-24 shows the nose pitch angle profile for the maximum range trajectory. The optimal pitch angle profile during the boosting segments involves entirely positive pitch angles. By choosing positive pitch angles during the boost, the vehicle slows the reduction in γ caused by gravity and targets a higher γ at final burnout than in the guess trajectory. This nose pitch angle profile is optimally chosen to target an optimal γ of 34.4 degrees at final burnout. The maximum altitude is shown to increase from about $2000\,kft$ in the guess trajectory to approximately $2500\,kft$ for the maximum range trajectory.

The motion of the nose pitch angle is a function of the body pitch rate as well as the

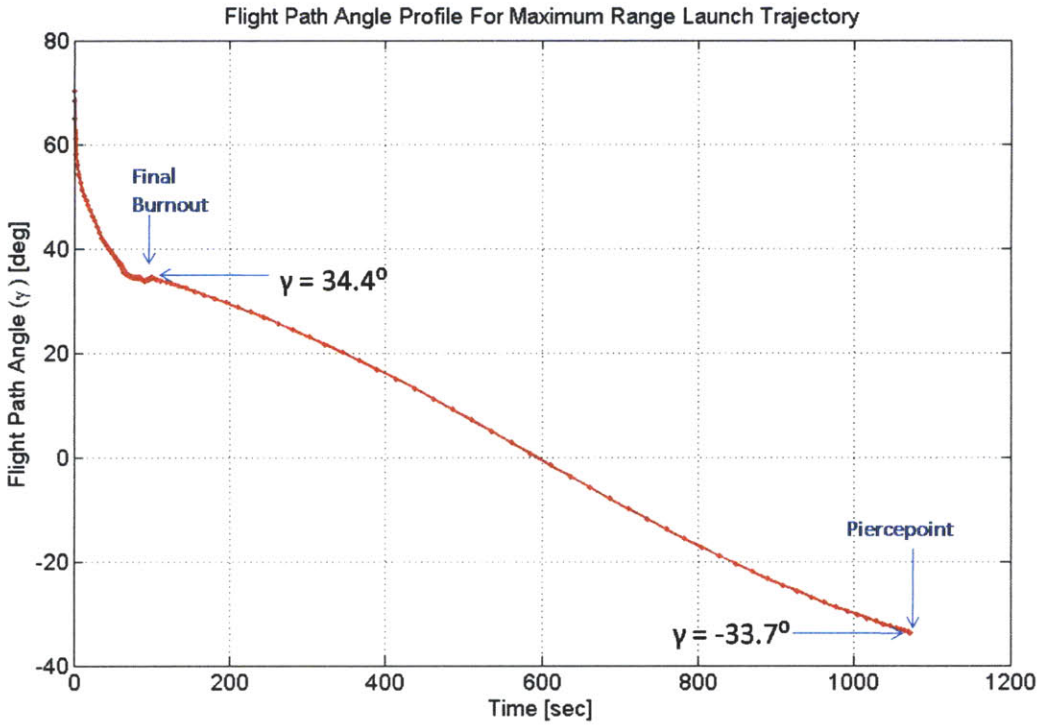

Figure 5-23: Flight Path Angle Profile For Maximum Range Launch Trajectory

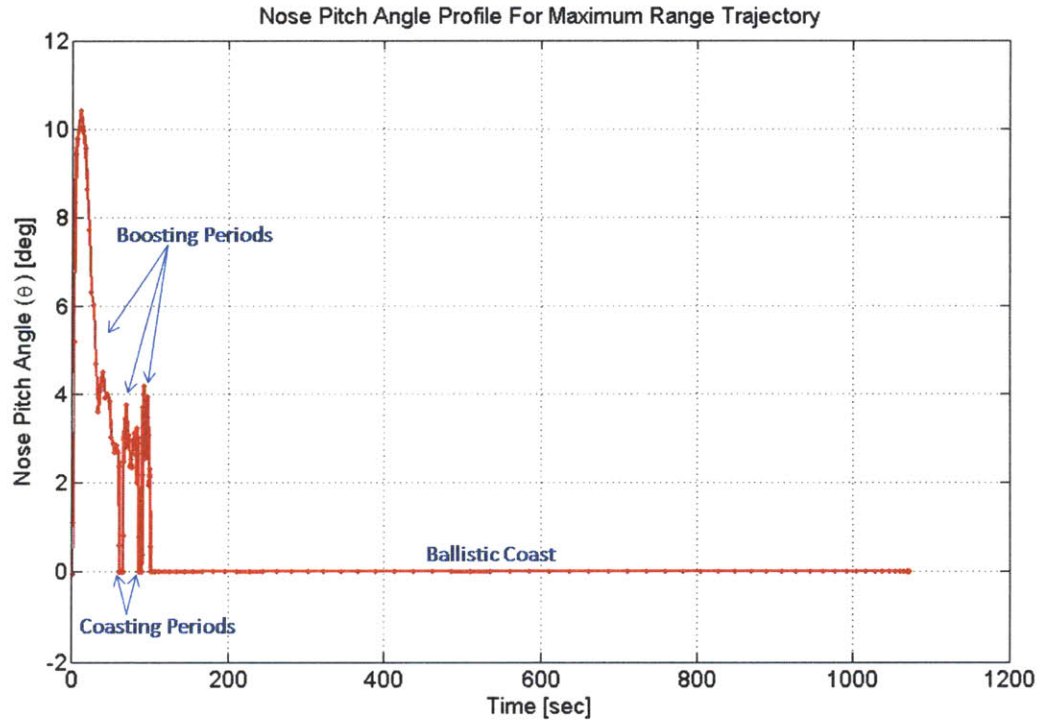

Figure 5-24: Nose Pitch Angle Profile For Maximum Range Launch Trajectory

motion of the velocity vector over time. The body pitch rate is shown in Figure 5-25. The pitch rate profile is no longer a damped oscillation, as in the guess trajectory, but is instead controlled by the TVC and ACS control systems. Recall from the definitions in chapter 3 that a positive pitch rate directs the vehicle nose downward while a negative pitch rate directs the nose upward. The rates remain small for the boosting phases of flight in order to keep the nose pitch angle relatively constant. At the boundaries between the boosting segments and coasting segments, large impulsive jumps in the pitch rate occur in order to satisfy the zero angle of attack constraints for each stage ignition and burnout. The pitch rate during the ballistic coast is a small, non-zero value that rotates the vehicle nose such that it remains coincident with the velocity vector.

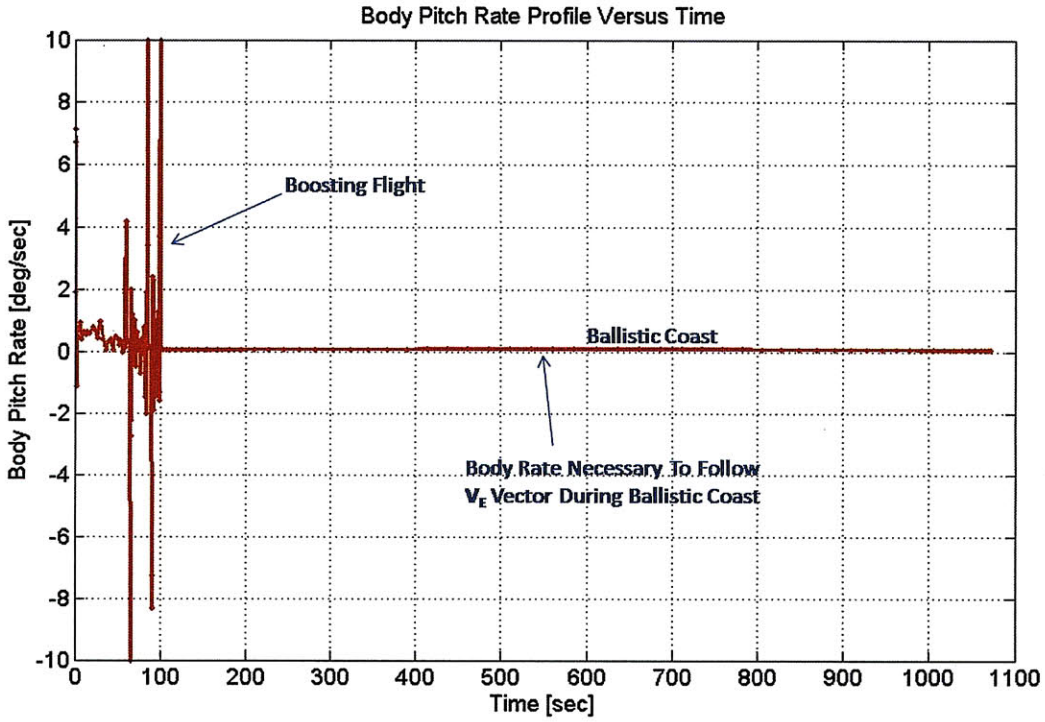

Figure 5-25: Body Pitch Rate Profile For Maximum Range Trajectory

The pitch rate is directly influenced by pitch controls from the TVC and ACS systems as well as from aerodynamic torques applied about the vehicle center of mass. In Figure 5-26, the TVC control is described in terms of the engine gimbal angle and the ACS control is described in terms of the applied torque magnitude. The controls are relatively smooth

except for impulsive controls at the boost-coast boundaries that are used to quickly drive the angle of attack to zero. The ACS control requires very small torques to stabilize the vehicle during the coast periods. The largest ACS control is on the order of magnitude of 10^{-2} N-m for the first coast since the dynamic pressure is higher during this portion of the flight. The stabilizing moments for the second coast and the ballistic coast are even smaller on the order of 10^{-4} N-m since the counteracting aerodynamic torques are near zero during these periods.

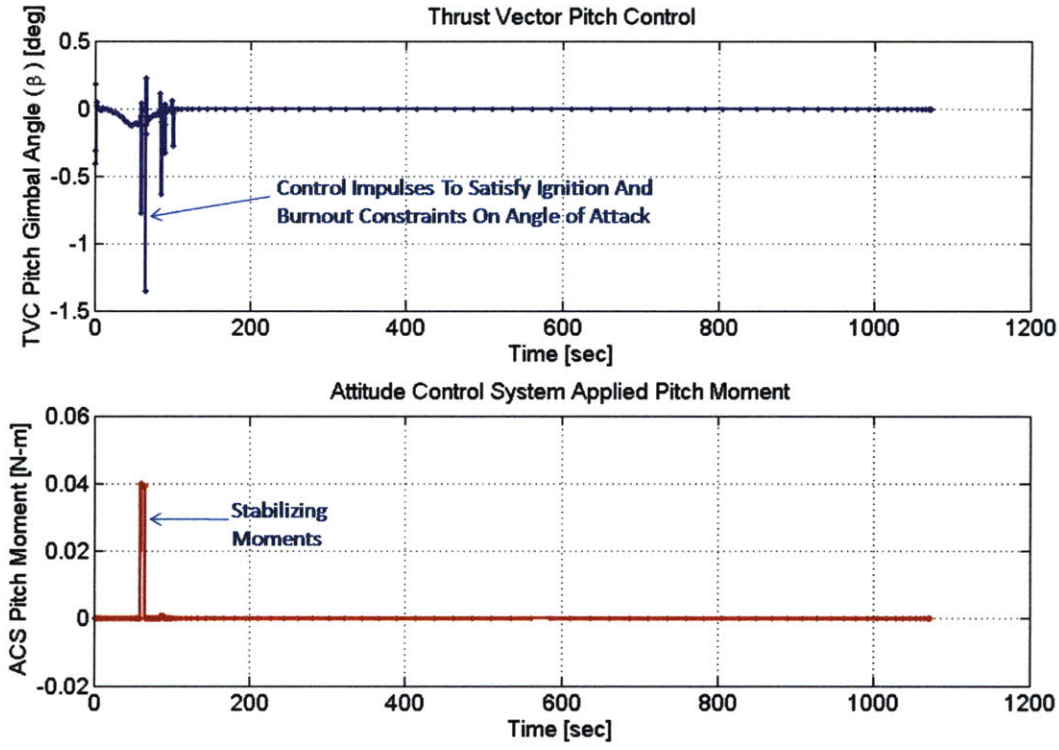

Figure 5-26: Pitch Controls For Maximum Range Launch Trajectory

5.7 Minimum Piercepoint Range Case

Another limiting capability of the launch vehicle to be examined is the minimum achievable piercepoint range. The minimum piercepoint range case seeks to find the minimum downrange piercepoint location that can be reached by the launch vehicle. Launch trajectories with very steep final burnout and reentry conditions ($|\gamma| > 80\,\text{deg}$) are not considered in this study since these trajectories reenter with flight path angles that are far too steep for the boost-through-reentry problem. The performance index for this problem is the relative longitude of the piercepoint location.

$$J = \mu\left(t_f\right)$$

Figure 5-27 gives the minimum piercepoint range solution for the launch trajectory. The trajectory can be characterized by an initial steep ascent to gain altitude, followed by a rapid pitch-over maneuver toward the horizontal that achieves a shallow reentry at piercepoint.

The final burnout occurs at an altitude of 216,300 feet and a relative longitude of 0.68 degrees with a burnout velocity of 14,072 feet per second and a flight path angle of 11.2 degrees. The final burnout for the minimum range case occurs at a lower altitude and closer to the launch point than the final burnout for the maximum range case. In addition, the final burnout velocity has a much lower magnitude and a much lower flight path angle for the minimum range case. The final burnout state results in a piercepoint reentry location at a relative longitude of 6.1 degrees downrange with a velocity of 13,638 feet per second and a flight path angle of -1 degrees. The maximum altitude reached during the flight is 401,400 feet, just slightly above the piercepoint reentry altitude. The flight path angle profile is no longer symmetric over the ballistic coast due to the large difference between final burnout altitude and piercepoint altitude as well as the low maximum altitude.

Figure 5-28 shows the flight path angle profile of the minimum range launch trajectory. The most interesting feature of the flight path angle profile is the series of oscillations that occur during the first 50 seconds of flight. The flight path oscillates at very high values

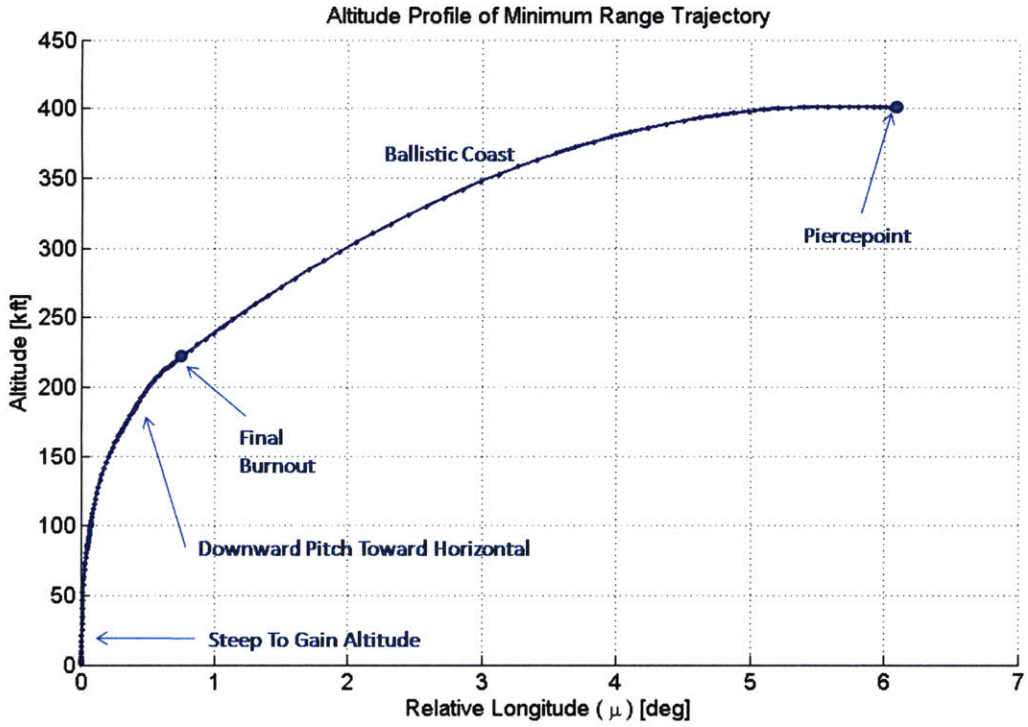

Figure 5-27: Minimum Range Launch Trajectory

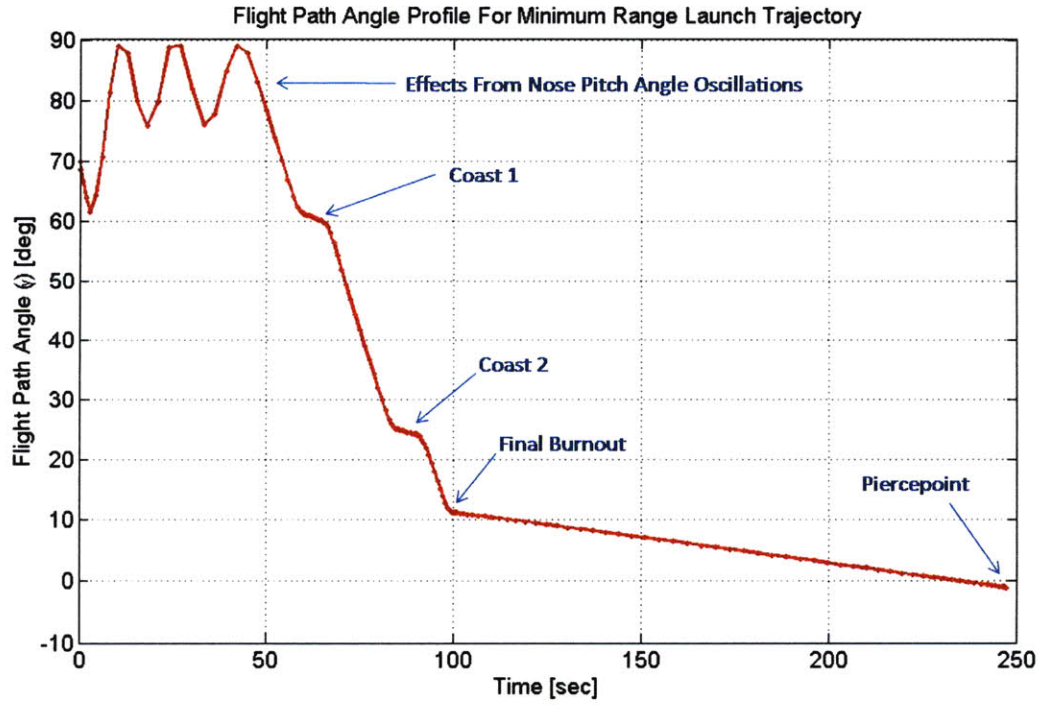

Figure 5-28: Flight Path Angle Profile For Minimum Range Launch Trajectory

between 75 degrees and the maximum allowable value of 89 degrees in order to gain sufficient altitude while at the same time performing energy wasting maneuvers. After the oscillations, the flight path angle makes a rapid descent in order to quickly turn the motion of the vehicle toward the horizontal for a shallow final burnout condition.

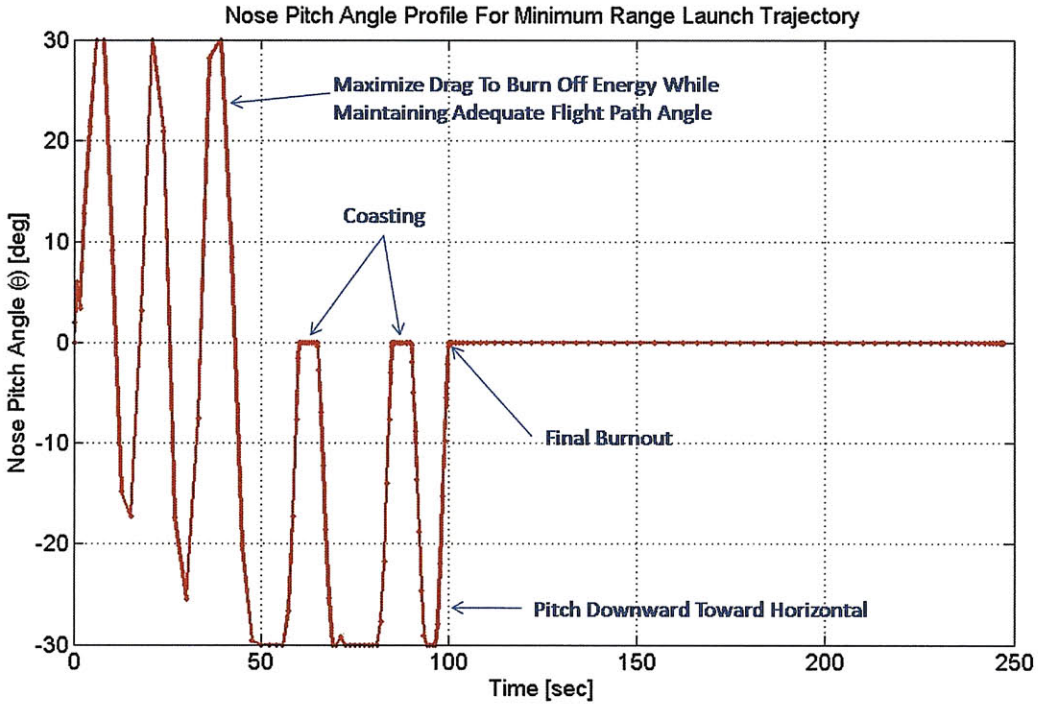

Figure 5-29: Nose Pitch Angle Profile For Minimum Range Launch Trajectory

Figure 5-29 gives the nose pitch angle (θ) profile over time, which is equivalent to the angle of attack (α) profile since the nose yaw angle (ϕ) is constrained to zero during the launch flight. The pitch angle profile gives additional insight into the energy wasting maneuvers as well as the rapid reduction in flight path angle. Figure 5-29 shows that the pitch angle oscillates between its maximum and minimum values ($\pm 30\,deg$) during the first 50 seconds of flight. The purpose of hitting these angle of attack limits is to exert a maximum amount of the normal aerodynamic force along the drag direction, since this force increases significantly with angle of attack. This maximizes the vehicle energy loss due to drag in order to reduce the amount of vehicle velocity at burnout, which in turn reduces the piercepoint range. The reason for the oscillation between the bounds is to prevent the flight path angle from violating its maximum limit of 89 degrees. Thus, the

vehicle must control the proper flight path angle while at the same time controlling the velocity magnitude through control of the drag force exerted on the vehicle. Once the vehicle has reached a sufficient altitude, the flight path angle begins to drop very rapidly. The limit on how fast the flight path angle can drop is enforced by the minimum allowable nose pitch angle (-30 degrees). Notice in Figure 5-29 that the pitch angle remains at the minimum limit of -30 degrees from 50 seconds into the flight until final burnout, with the exception of the coasting phases. This choice of the pitch angle serves the dual purpose of driving the flight path angle down while also burning off the maximum possible velocity with drag. The drag profile is shown in Figure 5-30 as a function of time. Since drag is directly proportional to dynamic pressure, the maximum drag profile exhibits a curve similar to the dynamic pressure curve.

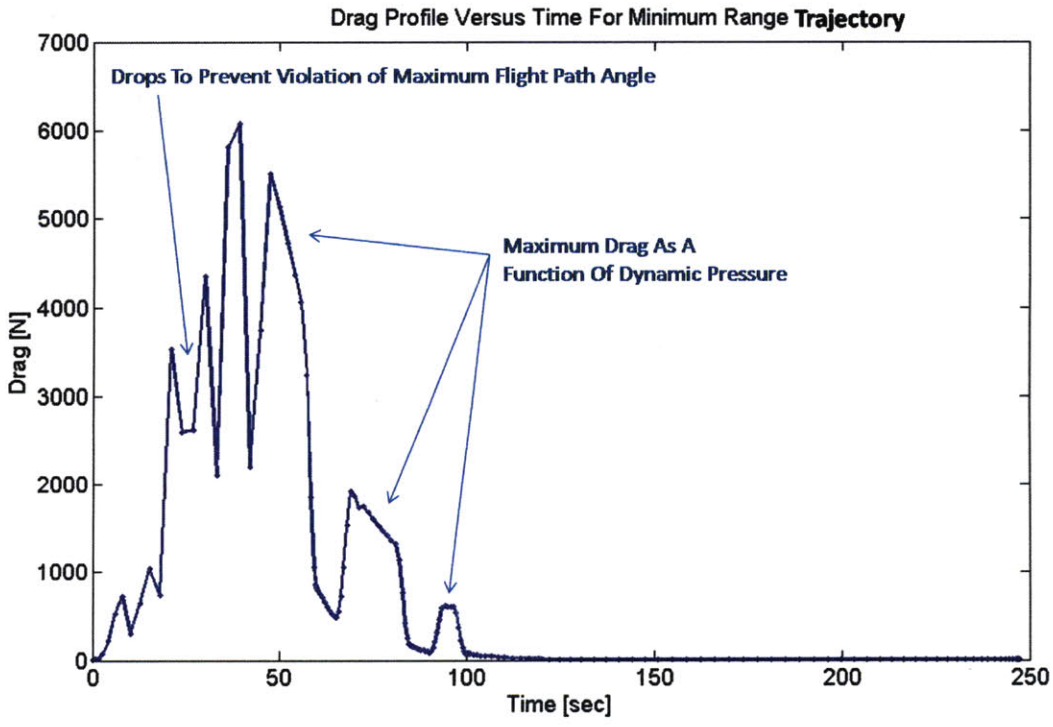

Figure 5-30: Drag Profile For Minimum Range Launch Trajectory

5.8 Summary

In this chapter, a three-stage launch vehicle model was developed to boost a maneuvering reentry vehicle to suborbital altitudes with a maximum velocity of approximately 16,000 feet per second. The launch vehicle controls its attitude during the boosting phases with thrust vectoring control (TVC) and during the coasting phases using a stabilizing attitude control system (ACS). Analysis of the limiting capabilities of the vehicle has shown that the launch vehicle has the capability to deliver a payload a maximum downrange piercepoint distance of 31.5 degrees and a minimum uprange piercepoint distance of 6.1 degrees.

Chapter 6

The Reentry Problem

The portion of the vehicle flight profile extending from the piercepoint location at 400,000 ft altitude to arrival at the target is considered the reentry flight. Unlike the boost flight, the reentry portion of flight is entirely unpowered and consists of a vehicle with constant mass and length maneuvering to a final target state using aerodynamic controls. The vehicle passes through the piercepoint location at hypersonic speeds ($M \approx 16$) and slows to supersonic speeds by the time the target is reached ($M \approx 1.5$).

The reentry flight is partitioned into two segments. The first segment extends from an altitude of 400,000 ft to an altitude of 200,000 ft, while the second segment covers the vehicle flight from the 200,000 ft altitude to the target location.

The vehicle will not exhibit any maneuvering capabilities during the first segment of the reentry flight due to the lack of substantial dynamic pressure available for flap control. Instead, the attitude control system (ACS) used for the ballistic exo-atmospheric coast will continue to fix the vehicle angle of attack to zero using small control torques until 200,000 ft altitude is reached. At that point, the vehicle will begin to use aerodynamic flaps to control the nose attitude of the vehicle relative to the velocity vector. The second segment of the reentry flight may exhibit one or more *skips*, in which the vehicle regains altitude in order to extend its range capability.

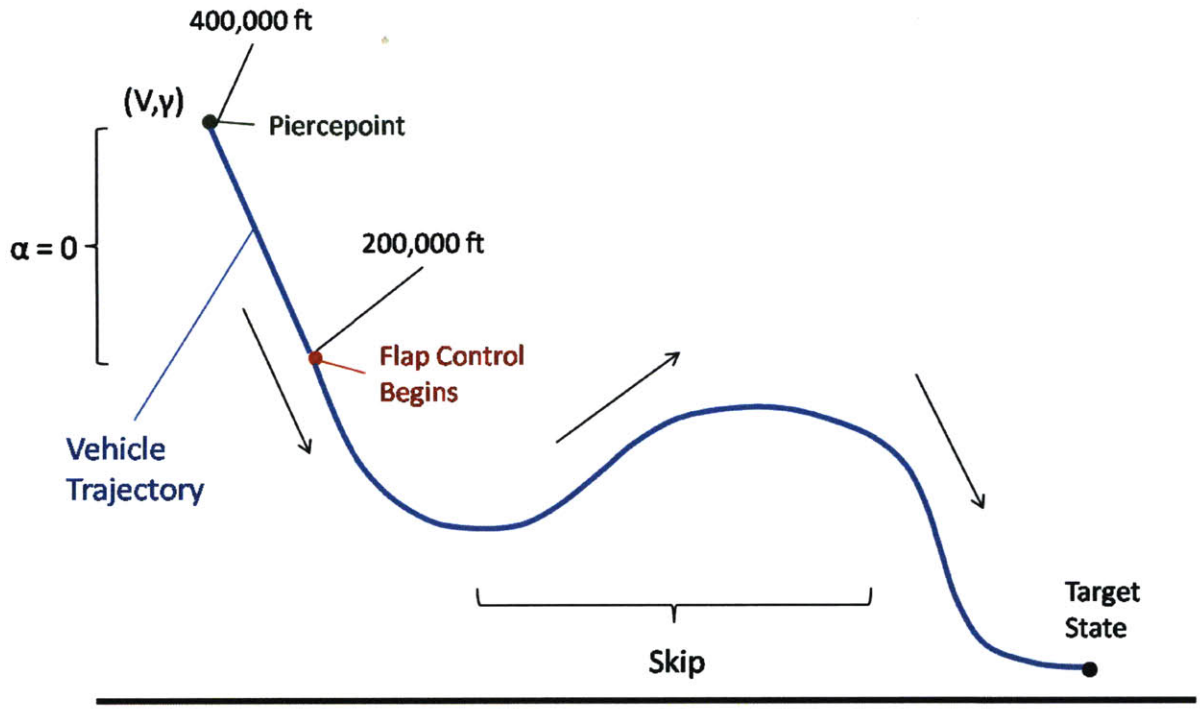

Figure 6-1: Reentry Flight Profile

6.1 Reentry Vehicle Aerodynamics

During the reentry phase of flight, aerodynamic forces are exerted on the vehicle body by dynamic pressure from the relative wind. The reentry vehicle aerodynamics will be specified by axial and normal coefficients of force as functions of Mach number and angle of attack, as was done for the launch vehicle. However, the aerodynamic characteristics of the reentry vehicle are much simpler than that of the launch vehicle since the reeentry vehicle does not pass through the transonic region (M $\approx$ 1). Therefore, the highly nonlinear aerodynamic effects modeled for the launch vehicle are not necessary here.

Aerodynamic tabular data for a manuevering reentry vehicle exhibiting a lift-to-drag ratio of approximately two (L/D $\approx$ 2) is used to create analytic functional fits to the coefficient data [1]. The simplified analytic functions approximate the coefficient of normal force, C_N, as a function of angle of attack (α) only and the coefficient of axial force, C_X, as a function of Mach Number (M) only. C_N is fit as a linear function of angle of attack (α) while C_X is fit as an exponential function of Mach Number (M).

[1] M. Bottkol, *Maneuvering RV Simulation*, Internal Draper Memo

$$C_N = a_N \alpha \tag{6.1}$$

$$C_X = a_X \, e^{-b_X (M - c_X)} + d_X \tag{6.2}$$

The coefficients a_N, a_X, b_X, c_X, and d_X are determined using a least squares curve fit. The simplified aerodynamic coefficients are plotted in Figures 6-2 and 6-3.

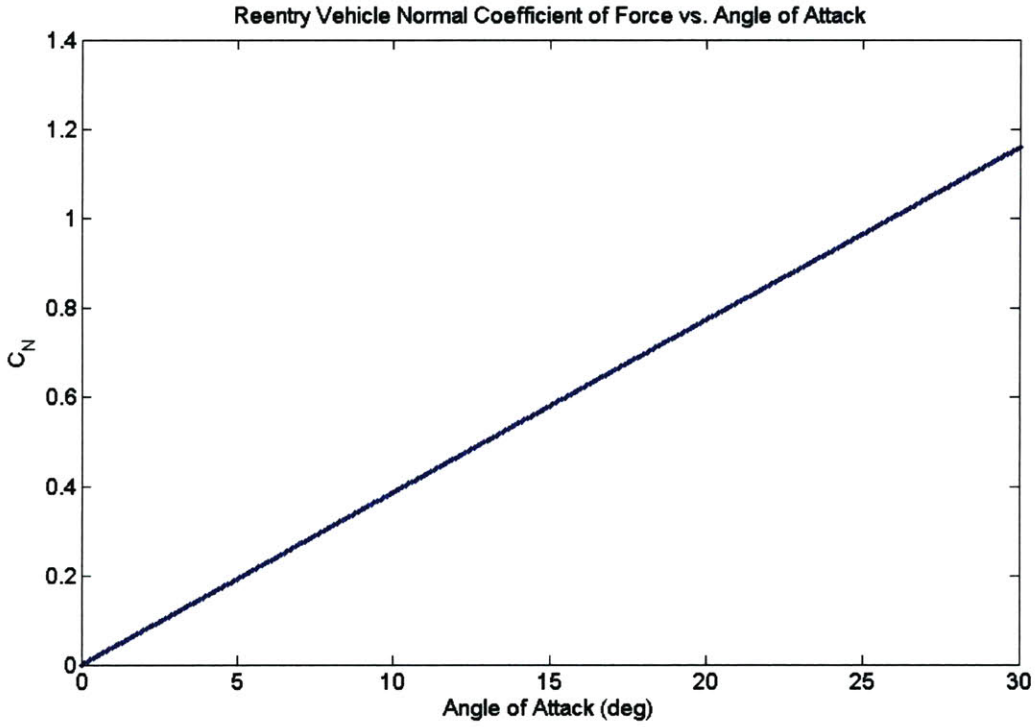

Figure 6-2: Reentry C_N as a Function of Angle of Attack

The center of pressure (C_P) model used for the reentry vehicle remains the same as was used for the launch vehicle, as described in section 5.3.

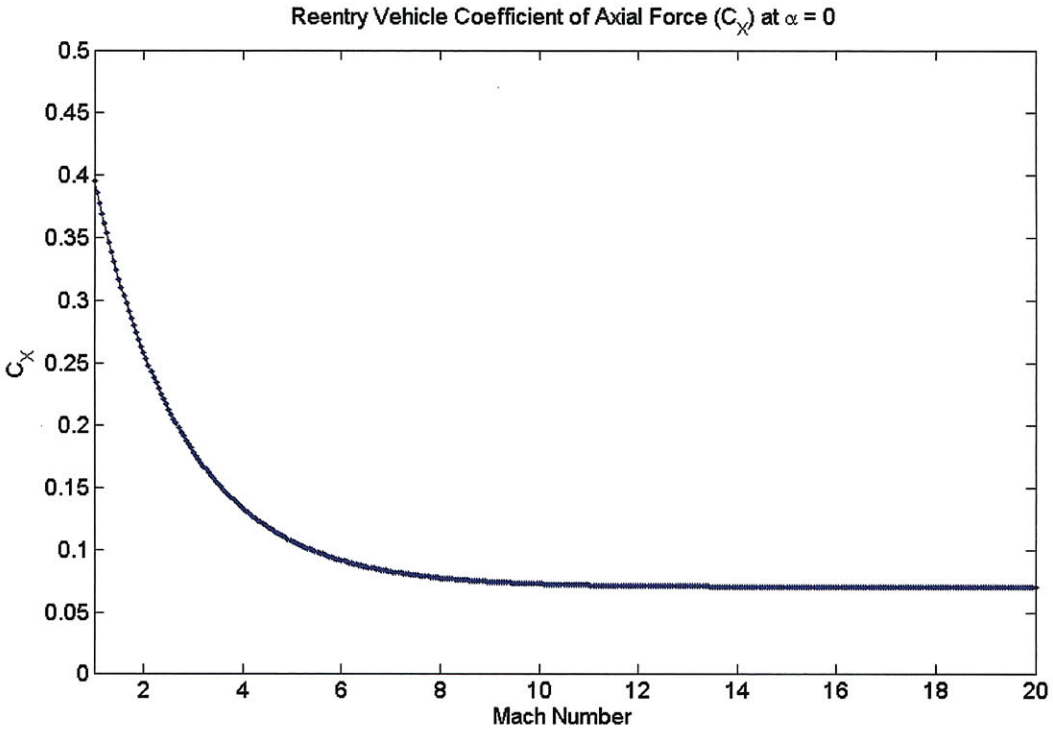

Figure 6-3: Reentry Vehicle C_X as a Function of Mach Number (M)

6.2 Reentry Vehicle Control

During reentry, a set of aerodynamic flaps located at the vehicle base are used to control the nose attitude. The flaps exert pitch and yaw moments (M_q, M_r) on the vehicle by actuation of the flap deflection angles. These control moments are used to counteract aerodynamic moments exerted on the vehicle in an effort to control the vehicle. Figure 6-4 illustrates the location of the flaps on the body and the directions of the resultant moments, M_q and M_r.

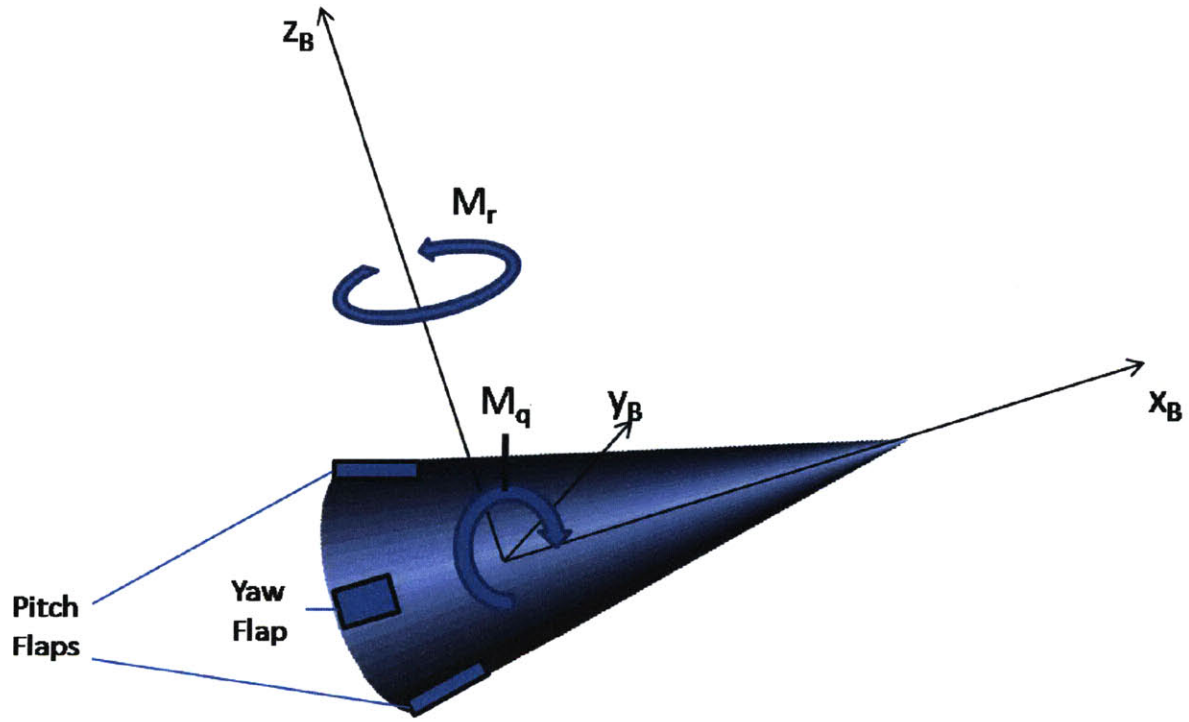

Figure 6-4: Reentry Vehicle Control Flaps

The aerodynamic moments exerted on the vehicle during reentry are given by the same general expressions governing the aerodynamic torques during launch, given in Equation 5.29. The only difference in the moment calculation here is the use of the reentry vehicle normal force coefficients, C_N, which exhibit higher L/D characteristics than the launch vehicle coefficients.

$$
\begin{aligned}
M_A = F_N\, L_{SM} &= \tfrac{1}{2}\rho\, V_E^2\, S_{ref}\, C_N\, L_{SM} \\
M_{A_y B} &= M_A \cos\sigma \\
M_{A_z B} &= -M_A \sin\sigma
\end{aligned}
$$

The pitch flaps exert a control torque, M_q, along the y_B axis, while the yaw flaps exert a control torque, M_r, along the z_B axis. The resultant angular motion of the vehicle body is determined by the sum of the external torques along the pitch and yaw axes, given as

$$\sum \tau_{y_B} = M_q + M_A \cos\sigma \tag{6.3}$$

$$\sum \tau_{z_B} = M_r - M_A \sin\sigma \tag{6.4}$$

Although the flap control can be specified as a deflection angle, δ, it will instead be specified as a moment exerted about the vehicle center of mass in this formulation. In order to adequately describe the control capabilities of the flaps, reasonable bounds must be placed upon the torque control indicating the maximum control authority of the flaps. The torque exerted by an aerodynamic flap can be expressed in terms of dynamic pressure, $q = \frac{1}{2}\rho V_E^2$, a reference area, S_{ref}, a mean aerodynamic chord, $\bar{c}$, and a nondimensional moment coefficient, C_m.

$$(M_q)_{max} = \frac{1}{2}\rho\,(h)\; V_E^2\, S_{ref}\, \bar{c}\, \left(C_{m_q}\right)_{max} \tag{6.5}$$

$$(M_r)_{max} = \frac{1}{2}\rho\,(h)\; V_E^2\, S_{ref}\, \bar{c}\, \left(C_{m_r}\right)_{max} \tag{6.6}$$

The vehicle reference area used in the reentry flight is equivalent to the area used for the launch vehicle aerodynamics, $S_{ref} = 0.075m^2$. For vehicles with no primary lifting surface, $\bar{c}$ is often replaced by body length or maximum diameter [3]. For this vehicle, $\bar{c}$ is chosen as vehicle length, $\bar{c} = 1.43\,m$. The flaps are assumed to have identical control authority in the pitch and yaw directions, so $\left(C_{m_q}\right)_{max}$ and $\left(C_{m_r}\right)_{max}$ will be

equal to one another. In addition, it is assumed that the flaps have an equal ability to exert both positive and negative torques (i.e. $\left(C_{m_q}\right)_{max} = \left(C_{m_q}\right)_{min}$). The moment coefficient is chosen to be on the same order of magnitude as the maximum flap moment coefficients used by Bollino in his investigation of the X-33 manuevering capabilties [15], $\left(C_{m_q}\right)_{max} = (C_{m_r})_{max} = 0.05$. Therefore, the optimizer will choose values for the pitch and yaw control torques within these bounds that optimally control the vehicle attitude and, consequently, maneuverability.

6.3 Problem Formulation

The reentry portion of flight will now be formulated as an optimal control problem in terms of path, event, state bound, and control bound constraints as well as a knot for segmenting the trajectory. The initial conditions for the reentry problem will be dependent upon the end conditions of a particular launch trajectory. In general, the initial conditions will always occur at the piercepoint altitude of 400,000 feet with θ_I and ϕ_I set to zero to be consisitent with the attitude constraints imposed in the launch problem.

6.3.1 The Submunitions Deployment Mission

The reentry problem will be solving for a trajectory that meets sufficient end conditions to complete a *submunitions deployment mission.* The submunitions deployment mission involves dispensing a payload from the vehicle at level flight conditions. The mission may or may not require the payload to be dispensed while traveling along a particular heading. For this mission, it is assumed that the vehicle must be traveling along the plane of reference defined by the launch point and target point when dispensing the payload. The submunitions deployment mission considered in this study must reach end conditions of $h_f = 3\,km$, $\mu_f = 30\,deg$, $\lambda_f = 0\,deg$, $V_{E_f} = 1300\,ft/sec$, $\gamma_f = 0\,deg$, $\psi_f = 0\,deg$, $\theta_f = 0\,deg$, and $\phi_f = 0\,deg$.

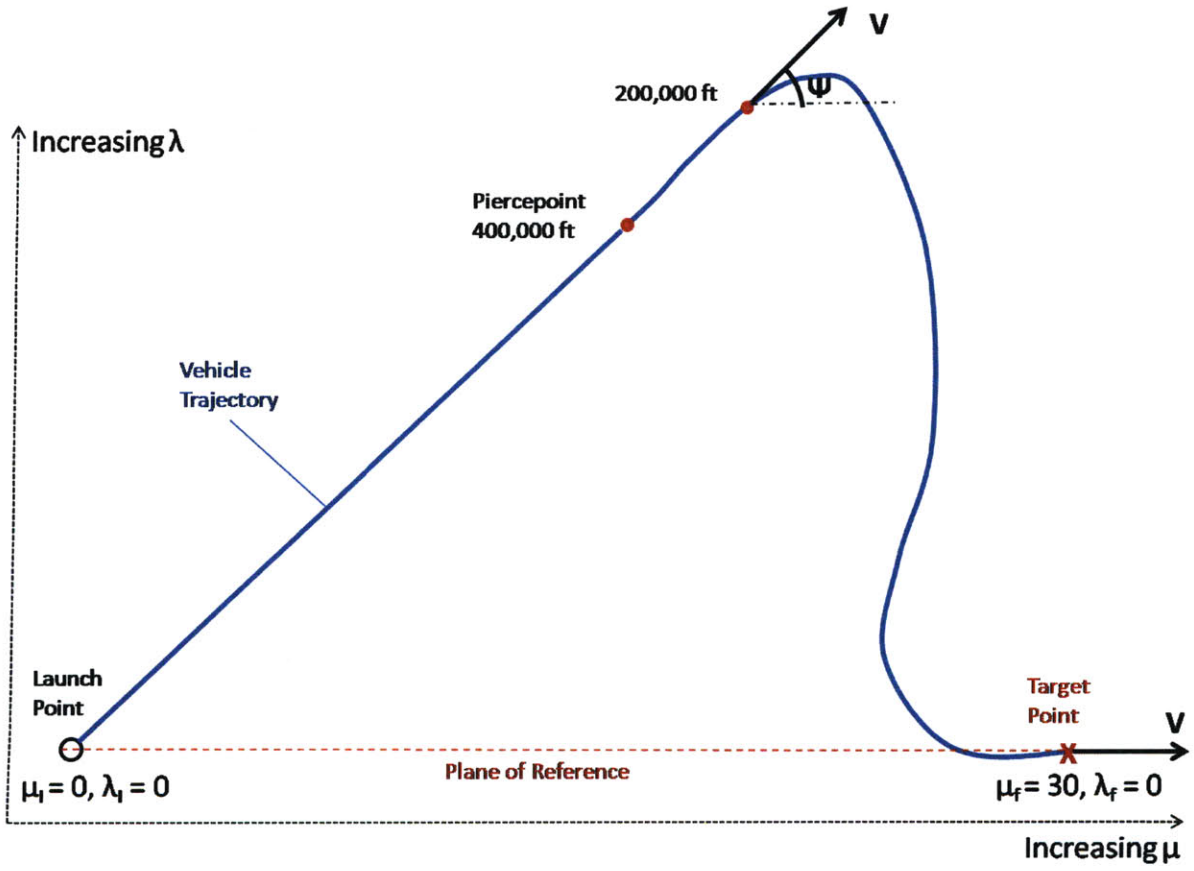

Figure 6-5: Submunitions Profile In Terms Of Relative Longitude And Relative Latitude

6.3.2 Knots

One interior knot is used in the reentry problem to enforce attitude constraints at altitudes above 200,000 feet and also to prevent the vehicle from skipping out of the atmosphere. Boundary knots are also located at the reentry initial time (piercepoint) and the end time of the trajectory (t_{end}). In order to be consistent with the notation from the launch problem, the time at piercepoint will be referred to as t_{k_6} and the knot located at 200,000 feet will be referred to as t_{k_7}. The boundary knot at the end of the trajectory will occur at time t_{end}.

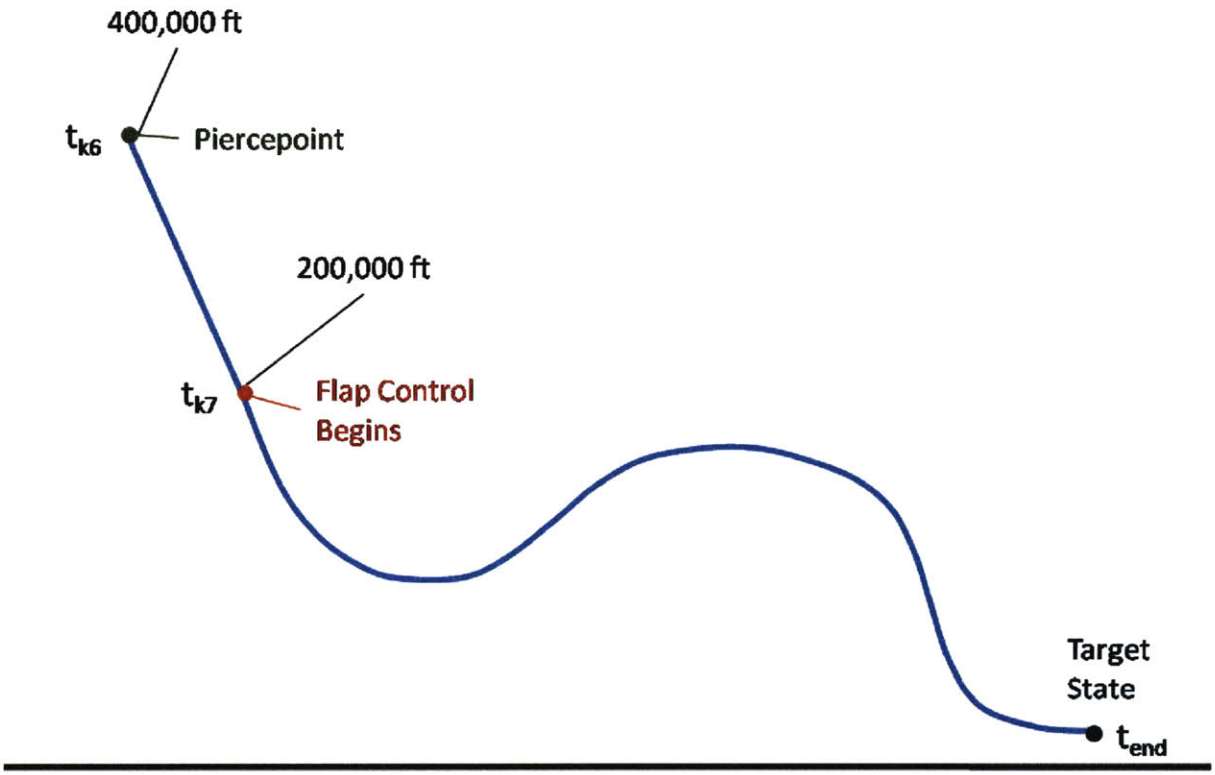

Figure 6-6: Knots Locations For The Reentry Problem

Unlike the launch problem knots, the interior knot as well as the final boundary knot in the reentry problem are free to vary. While the initial knot at t_{k_6} is fixed to a piercepoint location and time determined by the launch end conditions, the interior knot at 200,000 feet and the final knot do not have fixed times or bounds. However, it is important to restrict the open knots such that the optimization algorithm does not choose overlapping knots (i.e. knot 8 placed before knot 7). This issue will be dealt with

using event constraints.

6.3.3 State Bounds

The following state bounds are adopted to reasonably limit the vehicle motion as well as avoid potential singularities.

$$
\begin{array}{rcccr}
R_E - 60,000\,ft & \leq & r & \leq & R_E + 500,000\,ft \\
-1\,deg & \leq & \mu & \leq & 180\,deg \\
-1\,deg & \leq & \lambda & \leq & 89\,deg \\
10\,ft/sec & \leq & V_E & \leq & 500,000\,ft/sec \\
-89\,deg & \leq & \gamma & \leq & 89\,deg \\
-180\,deg & \leq & \psi & \leq & 180\,deg \\
-20\,deg/sec & \leq & q_{body} & \leq & 20\,deg/sec \\
-20\,deg/sec & \leq & r_{body} & \leq & 20\,deg/sec \\
-30\,deg & \leq & \theta & \leq & 30\,deg \\
-30\,deg & \leq & \phi & \leq & 30\,deg
\end{array}
$$

The state bounds imposed during reentry are very similar to the state bounds used in the launch problem. The only differences are a lower limit on the maximum radial distance, relaxation of the $\phi = 0$ constraint, and widened bounds on the maximum and minimum body rates. The maximum radial distance is lowered to 500,000 feet above the Earth mean radius, R_E, since the entire reentry trajectory must remain below an altitude of 400,000 feet. The lowering of the maximum bound reduces the potential search space of the optimization algorithm. The bounds for the nose yaw angle (ϕ) are expanded to ± 30 degrees since the reentry vehicle has significant out-of-plane maneuvering capability that is equivalent to its in-plane maneuvering capability. The bounds on the body pitch rate, q_{body}, and the body yaw rate, r_{body}, are expanded to $\pm 20\,deg/sec$ since the reentry vehicle is much smaller and more agile than the launch vehicle.

6.3.4 Control Bounds

The controls are bounded based upon the limitations of the reentry vehicle control mechanisms. These include both limits on the attitude control applied moments and on the flap control applied moments.

$$
\begin{aligned}
-1\text{ N-m} \leq M_{C_q} &\leq 1\text{ N-m} \\
-1\text{ N-m} \leq M_{C_r} &\leq 1\text{ N-m} \\
-\infty \leq M_q &\leq \infty \\
-\infty \leq M_r &\leq \infty
\end{aligned}
$$

The limits on the attitude control are equivalent to the limits used in the launch problem while limits on the flap control moments are specified by path constraints since the limits vary over the course of the trajectory.

6.3.5 Event Constraints

The event constraints for the reentry problem include continuity conditions as well as specification of conditions at the interior knot and the final knot.

$$
\begin{aligned}
\mathbf{x}\left(t_{k_7}^{+}\right) - \mathbf{x}\left(t_{k_7}^{-}\right) &= \mathbf{0} \\
h\left(t_{k_6}\right) - 400000ft &= 0 \\
h\left(t_{k_7}\right) - 200000ft &= 0 \\
-89deg \leq \gamma\left(t_{k_6}\right) &\leq -1deg \\
-89deg \leq \gamma\left(t_{k_7}\right) &\leq -1deg \\
t_{k_7} - t_{k_6} &> 0 \\
t_{end} - t_{k_7} &> 0 \\
h\left(t_{end}\right) - 3000m &= 0
\end{aligned}
$$

The piercepoint knot is constrained to be at an altitude of 400,000 feet with a reentry flight path angle between -1 degrees and -89 degrees. Similarly, the interior knot must be located at 200,000 feet with a reentry flight path angle between -1 degrees and -89 degrees. The time constraints dictate the necessary order of the knot times such that the

knots do not overlap. The last event constraint dictates that the final trajectory point ends at an altitude of 3 km to satisfy the submunitions mission.

6.3.6 Path Constraints

The path constraints dictate special bounds on the states and/or controls that only act over a particular segment of the trajectory. Path constraints will be imposed to constrain the angle of attack to zero at high altitudes, prevent skipping out of the atmosphere, prevent impact with the ground, and enforce bounds on the maximum control authority of the flaps. Due to the high velocity at which the vehicle reenters the atmosphere, it is also important to include physical constraints on the maximum heat loading and g-loading of the vehicle to ensure vehicle safety.

State Path Constraints

Path constraints are imposed on the θ and ϕ states, as well as the altitude above the surface of the Earth, h.

$$\begin{aligned}
0\,deg \leq \theta(t) \leq \quad & 0\,deg & \forall t_{k_6} \leq t \leq t_{k_7} \\
0\,deg \leq \phi(t) \leq \quad & 0\,deg & \forall t_{k_6} \leq t \leq t_{k_7} \\
0\,ft \leq h(t) \leq & 200,000\,ft & \forall t_{k_7} \leq t \leq t_{end}
\end{aligned}$$

The first two state path constraints constrain the attitude angles θ and ϕ to zero during the first segment of reentry flight from 400,000 feet to 200,000 feet. This constraint is necessary due to a lack of flap controllability at altitudes above 200,000 feet due to very low dynamic pressure. Attempting to control the vehicle with flaps during this segment of flight would lead to an incorrect or inaccurate optimization search since the sensitivity of the vehicle trajectory to flap control would be very low at these altitudes and very high at low altitudes, creating ill-conditioned sensitivity matrices.

The third constraint ensures that the altitude of the vehicle above the Earth's surface remains between 0 and 200,000 feet during the second segment of the reentry flight. The lower bound ensures that the vehicle does not impact the ground while the upper bound

ensures that the vehicle remains within a region with adequate controllability.

Flap Control Path Constraints

As mentioned in the control bounds section, the bounds on the flap controls are enforced by path constraints since they vary over the course of the reentry flight.

$$-\frac{(M_q)_{max}}{0.5\rho V_E^2} \leq \frac{M_q}{0.5\rho V_E^2} \leq \frac{(M_q)_{max}}{0.5\rho V_E^2}$$
$$-\frac{(M_r)_{max}}{0.5\rho V_E^2} \leq \frac{M_r}{0.5\rho V_E^2} \leq \frac{(M_r)_{max}}{0.5\rho V_E^2}$$

The maximum moments that can be generated by the pitch and yaw flaps are given in Equation 6.6. Notice that these limits are a linear function of the dynamic pressure ($q = \frac{1}{2}\rho(h)\ V_E^2$) acting against the vehicle body during flight, which varies over time. Since the control bounds must be fixed values, a path constraint is imposed on the maximum moment divided by the dynamic pressure. In this manner, the flap control can be thought of as a linear function of q, $M_q = Kq$, where the coefficient $K = S_{ref}\,\bar{c}\,C_{m_q}$, is limited by a maximum value of $\left(C_{m_q}\right)_{max} = 0.05$. Given a certain amount of dynamic pressure, the flaps can convert at most a maximum percentage of the dynamic pressure to a control moment.

Heating Path Constraints

The reentry vehicle cannot sustain an indefinite amount of heating. The heat load experienced by the vehicle will be limited by a maximum stagnation point heating rate, $\dot{Q}_{max}$. The stagnation point heating rate of a vehicle is given by Chapman's Equation [22].

$$\dot{Q} = K\left(\frac{\rho(h)}{\rho_0}\right)^{0.5}\left(\frac{V_E}{V_c}\right)^{3.15} BTU/ft^2/s \tag{6.7}$$

where

$$K = 17600\,BTU/ft^2/s$$

In the Equation 6.8, $\rho(h)$ represents the atmospheric density as a function of altitude,

ρ_0 represents the sea level density, V_E is the Earth-relative velocity of the vehicle, and V_c is the speed required to maintain a circular orbit at zero altitude ($7.9km/sec$). The maximum stagnation point heating rate is $1800BTU/ft^2/s$ for this vehicle.

$$0 \leq K\left(\frac{\rho(h)}{\rho_0}\right)^{0.5}\left(\frac{V_E}{V_c}\right)^{3.15} \leq 1800BTU/ft^2/s \tag{6.8}$$

G-Loading Path Constraints

The reentry vehicle also has structural limits that can only sustain limited accelerations. The acceleration limits are often specified in terms of multiples of the sea-level gravity acceleration, $g_0 = 9.81m/s^2$, referred to as gs. The maximum gs allowable for this reentry vehicle is $60gs$. A structural safety margin is introduced by limiting this value to $55gs$. For the reentry vehicle, the g-loading acceleration is computed as the total acceleration from aerodynamic forces, $a = \sqrt{L^2 + D^2}/m$.

$$0 \leq \frac{\sqrt{L^2 + D^2}}{m} \leq 55g_0 \tag{6.9}$$

Path Constraints Summary

The total path constraints used in the reentry problem are summarized below.

$$\begin{array}{ccccc}
0\,deg & \leq & \theta(t) & \leq & 0\,deg \qquad \forall t_{k_6} \leq t \leq t_{k_7} \\
0\,deg & \leq & \phi(t) & \leq & 0\,deg \qquad \forall t_{k_6} \leq t \leq t_{k_7} \\
0\,ft & \leq & h(t) & \leq & 200,000\,ft \qquad \forall t_{k_7} \leq t \leq t_{end} \\
-\frac{(M_q)_{max}}{0.5\rho V_E^2} & \leq & \frac{M_q}{0.5\rho V_E^2} & \leq & \frac{(M_q)_{max}}{0.5\rho V_E^2} \\
-\frac{(M_r)_{max}}{0.5\rho V_E^2} & \leq & \frac{M_r}{0.5\rho V_E^2} & \leq & \frac{(M_r)_{max}}{0.5\rho V_E^2} \\
0 & \leq K\left(\frac{\rho(h)}{\rho_0}\right)^{0.5}\left(\frac{V_E}{V_c}\right)^{3.15} & & \leq 1800\,BTU/ft^2/s & \\
0 & \leq & \frac{\sqrt{L^2+D^2}}{m} & \leq & 55g_0
\end{array}$$

6.4 Reentry Vehicle Capabilities

The capabilities of the reentry vehicle formulated in the previous sections will be briefly examined here. The cases here will use the end conditions from the maximum range

launch trajectory, examined in section 5.6.2, as initial conditions for the reentry problem.

6.4.1 Ballistic Reentry

Figure 6-7 shows the ballistic trajectory from the piercepoint conditions of $V_E = 16,077\, ft/sec$ and $\gamma = -33.7\, deg$ to the final altitude of 3 kilometers. The vehicle travels just over 1.5 degrees downrange and reaches the final altitude at non-level flight conditions.

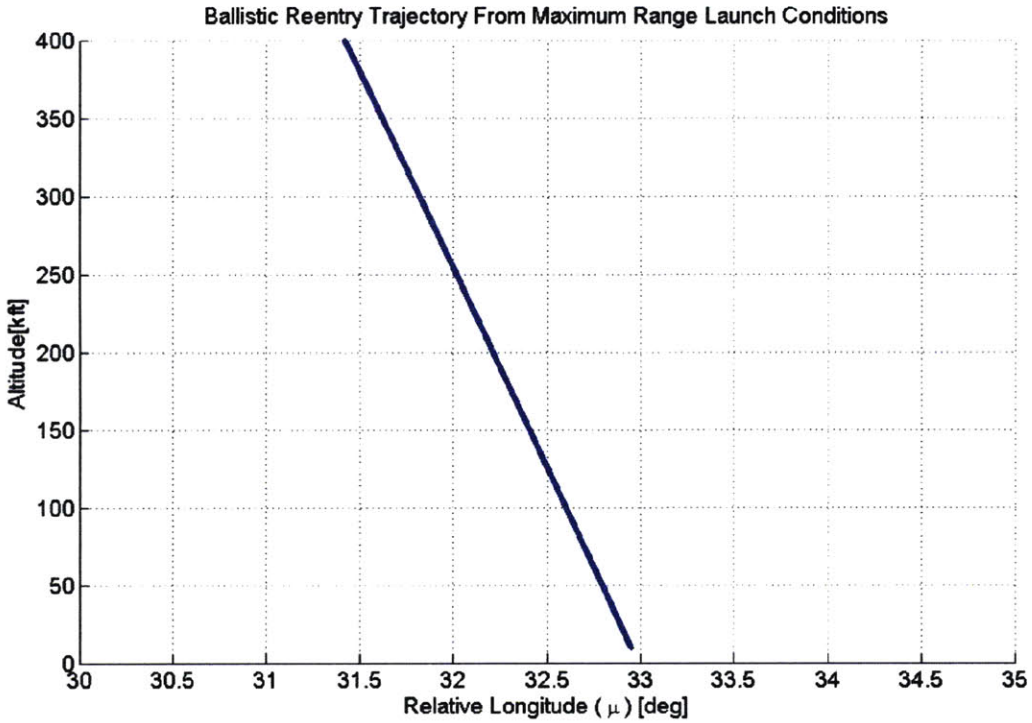

Figure 6-7: Ballistic Reentry Trajectory

Figure 6-8 shows the nose pitch angle profile for the ballistic reentry trajectory. The vehicle attitude exhibits the properties of a stable system, with the nose pitch angle profile appearing as a damped oscillation that reduces in magnitude and increases in frequency as the vehicle descends into the atmosphere.

Figure 6-9 gives the velocity and flight path angle profiles for the ballistic reentry trajectory. The velocity initially increases due to gravity, but decreases due to drag upon hitting the atmosphere. Despite the decrease in velocity due to drag, the vehicle is still traveling at a velocity slightly less than 13,000 feet per second with a flight path angle

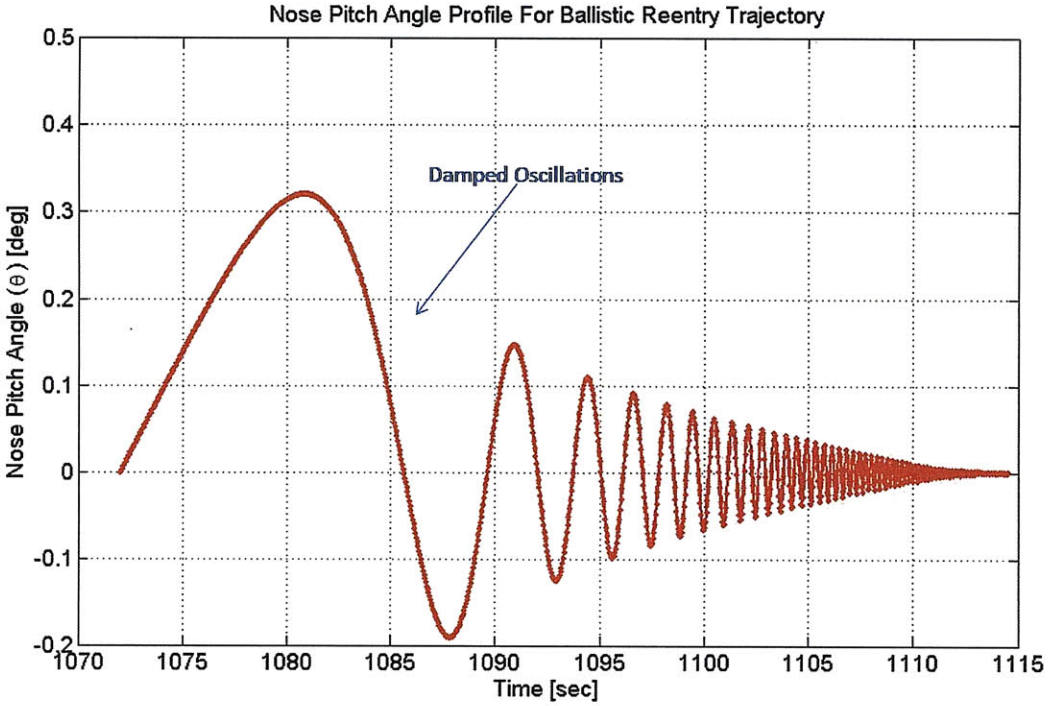

Figure 6-8: Nose Pitch Angle Profile For Ballistic Reentry Trajectory

approaching -36 degrees when the final altitude of 3 kilometers is reached. Thus, maneuvering is required to reach the intended terminal states for the submunitions deployment mission.

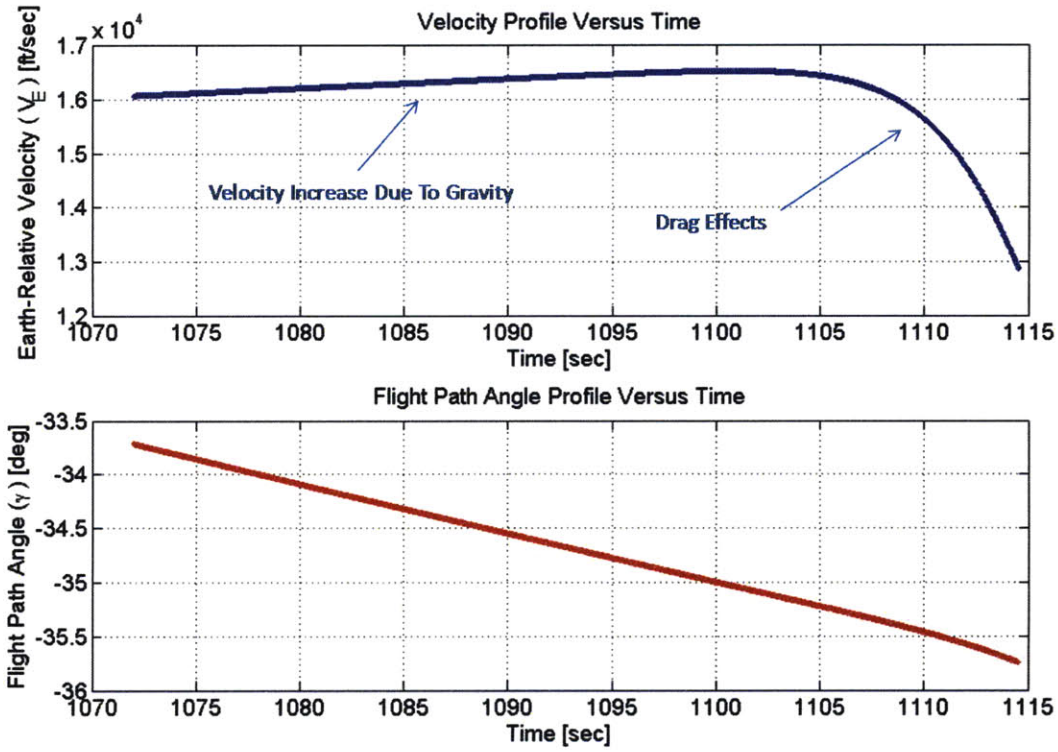

Figure 6-9: Velocity And Flight Path Angle Profiles For The Ballistic Reentry Trajectory

6.4.2 Maximum And Minimum Downrange

In order to determine the maneuvering limitations of the vehicle for satisfying the submunitions mission, reentry trajectories are considered which maximize and minimize the downrange distance of the end state. The performance index used for the maximum range case is $J = -\mu\left(t_{end}\right)$ and the performance index used for the minimum range case is $J = \mu\left(t_{end}\right)$. The resulting optimal trajectories are shown in Figure 6-10 along with the ballistic trajectory for comparison. The maximum range trajectory reaches a total downrange distance (μ) of 44.9 degrees in a total boost-through-reentry time of 1768 seconds while the minimum range trajectory ends up at 34.3 degrees in a time of 1272 seconds. Notice that the minimum range trajectory must perform one skip to burn off enough velocity to meet the terminal conditions, while the maximum range trajectory performs three skips to extend the maximum range. Additionally, the maximum range trajectory skips up to the maximum altitude of 200,000 feet during the first skip to maximize downrange distance while the minimum range trajectory remains lower in the atmosphere to reach the terminal state at a minimum range.

The velocity profile of the minimum range trajectory is shown in Figure 6-11 while the velocity profile of the maximum range trajectory is shown in Figure 6-12. The minimum range trajectory is shown to decrease in velocity from approximately 16,000 feet per second to 4,000 feet per second during the first skip. The remainder of the velocity is expended during the final dive and maneuver to reach the target condition of 1,300 feet per second. The maximum range trajectory, in contrast, only reduces to approximately 9,000 feet per second after the first skip and retains enough energy to perform two additional shallower skips before expending the remaining velocity during a final dive to the target altitude.

The reason for the large differences in velocity expenditure for the two cases can be explained by examining the attitude profile of both cases. Figure 6-13 gives the nose pitch angle (θ) profile for the minimum range reentry trajectory and Figure 6-14 gives the nose pitch angle profile for the maximum range reentry trajectory. Notice that the nose pitch angle for the minimum range trajectory is near the bounds of ± 30 degrees for a majority of the flight. This attitude maximize the drag force exerted on the vehicle, leading to the

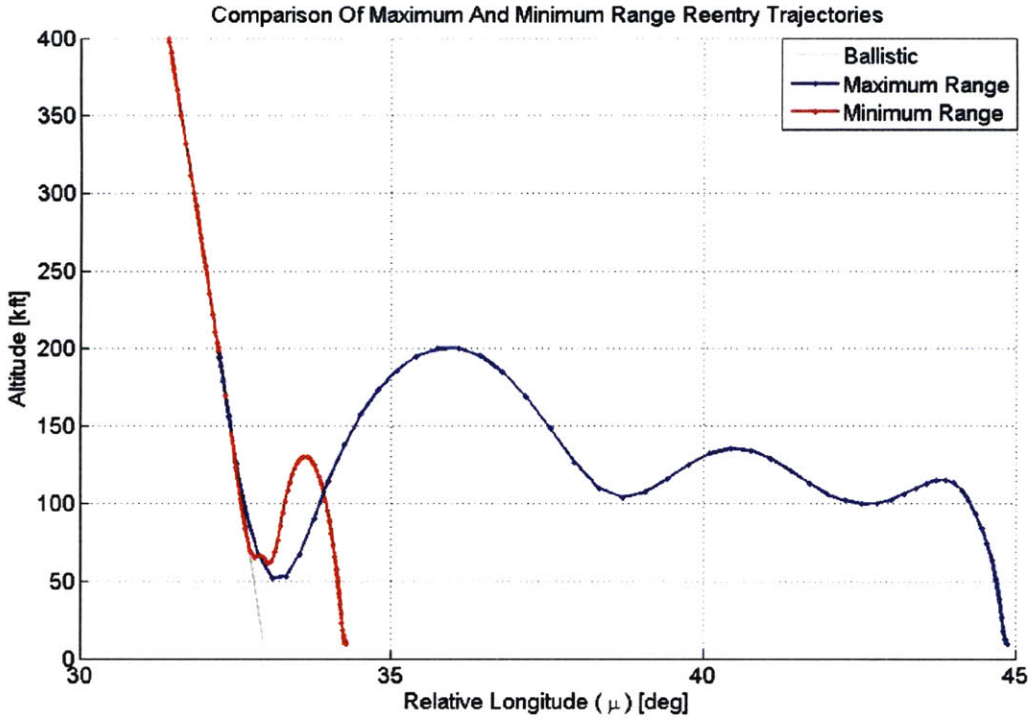

Figure 6-10: Comparison Of Maximum And Minimum Downrange Reentry Trajectories

maximum expenditure of velocity and, therefore, minimizing the range. The phenomenon seen at approximately 1120 seconds into the flight is an attempt by the vehicle to remain at low altitudes, where dynamic pressure is high, while still maximizing the drag. Since a positive nose pitch angle not only generates a large amount of drag, but also rapidly increases the flight path angle, the vehicle must temporarily maneuver to a negative flight path angle to avoid an increase in altitude. The nose pitch angle for the maximum range trajectory, in contrast, only approaches the bounds during the initial skip to prevent the vehicle from dipping too deep into the atmosphere. In addition, the vehicle must begin pitching down early enough to avoid violating the maximum altitude limit of 200,000 feet. From that point, the nose pitch angle avoids the bounds in order to avoid high drag and conserve enough energy to complete three skips.

The optimal pitch flap controls along with their upper and lower bounds are given for the minimum range reentry trajectory in Figure 6-15 and the maximum range trajectory in Figure 6-16. The pitch control profile for the minimum range trajectory spends a

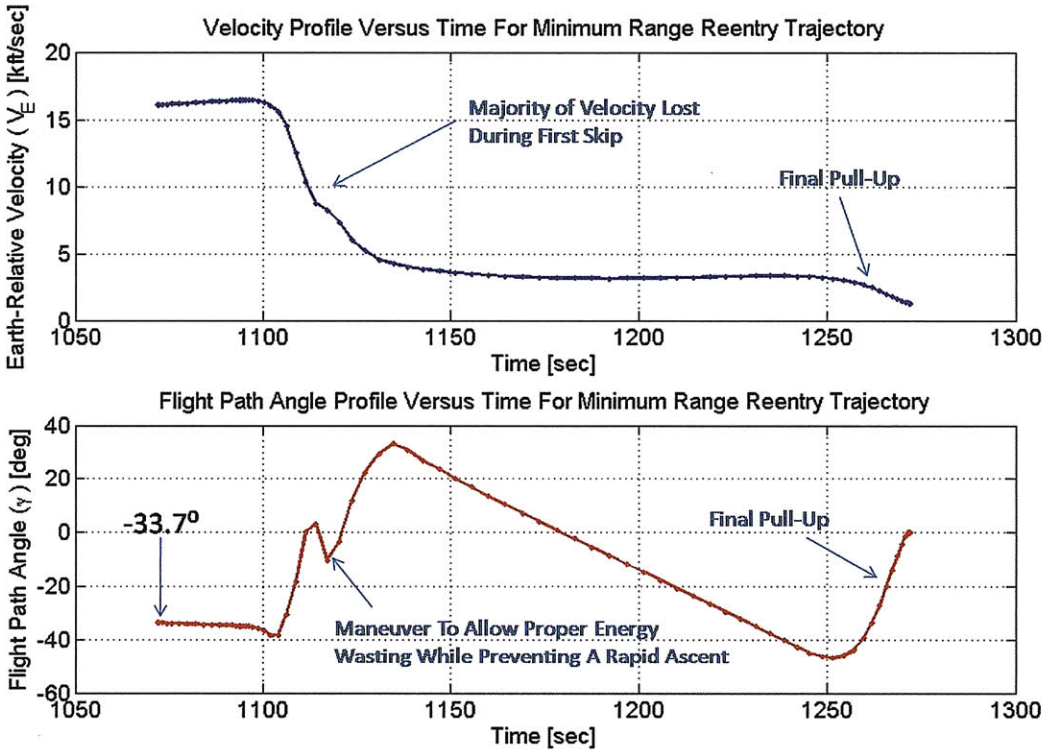

Figure 6-11: Velocity And Flight Path Angle Profiles For Minimum Range Reentry Trajectory

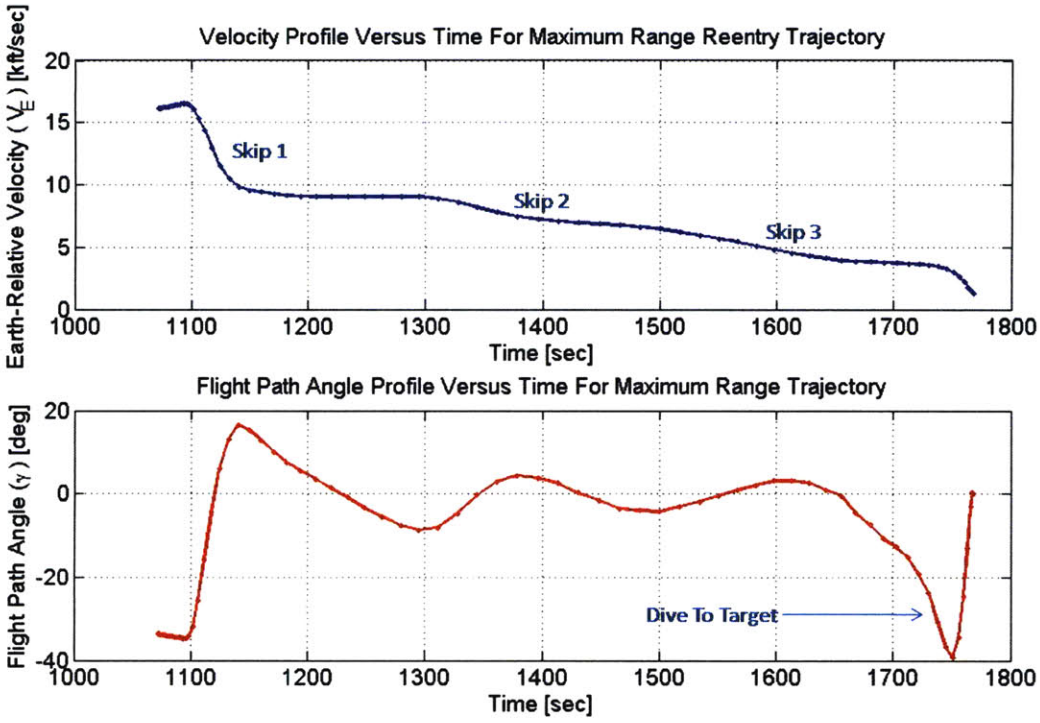

Figure 6-12: Velocity And Flight Path Angle Profiles For Maximum Range Reentry Trajectory

majority of its time along the maximum and minimum control bounds due to the extreme maneuvers described above while the pitch control for the maximum range trajectory only encounters the control bound during the first pitch up maneuver for the first skip. Notice that the control authority is extremely limited during the high altitude skips due to a lack of dynamic pressure. Future investigations into this work may consider a bound on minimum dynamic pressure for controllability purpose, or simply reduce the maximum altitude to a lower value.

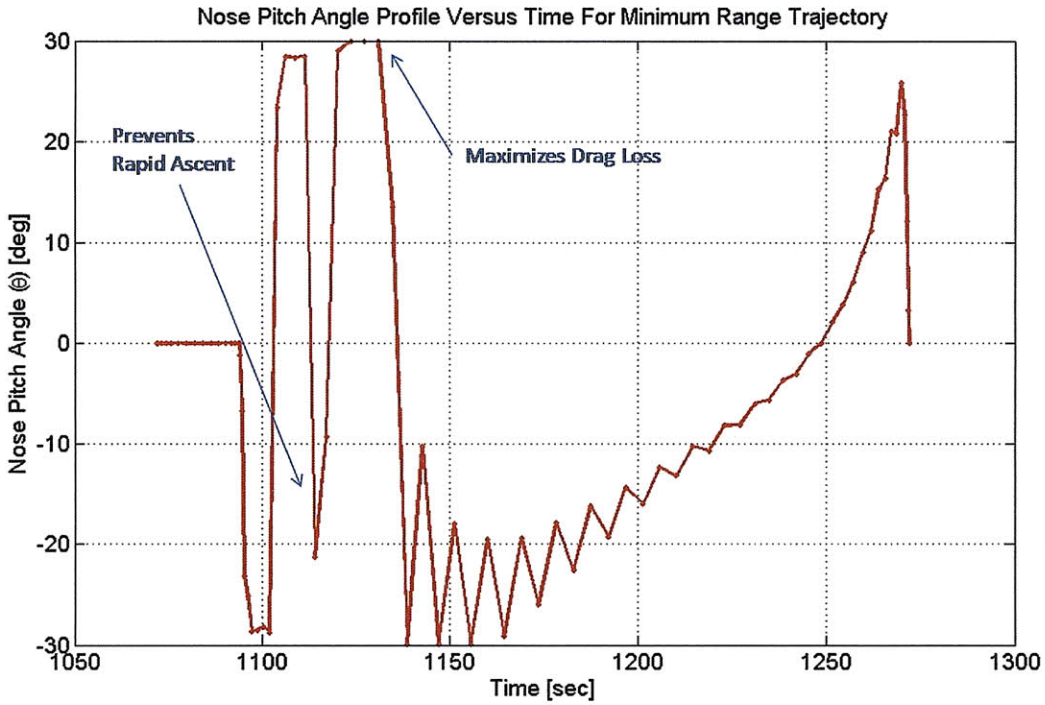

Figure 6-13: Nose Pitch Angle Profile Versus Time For Minimum Range Reentry Trajectory

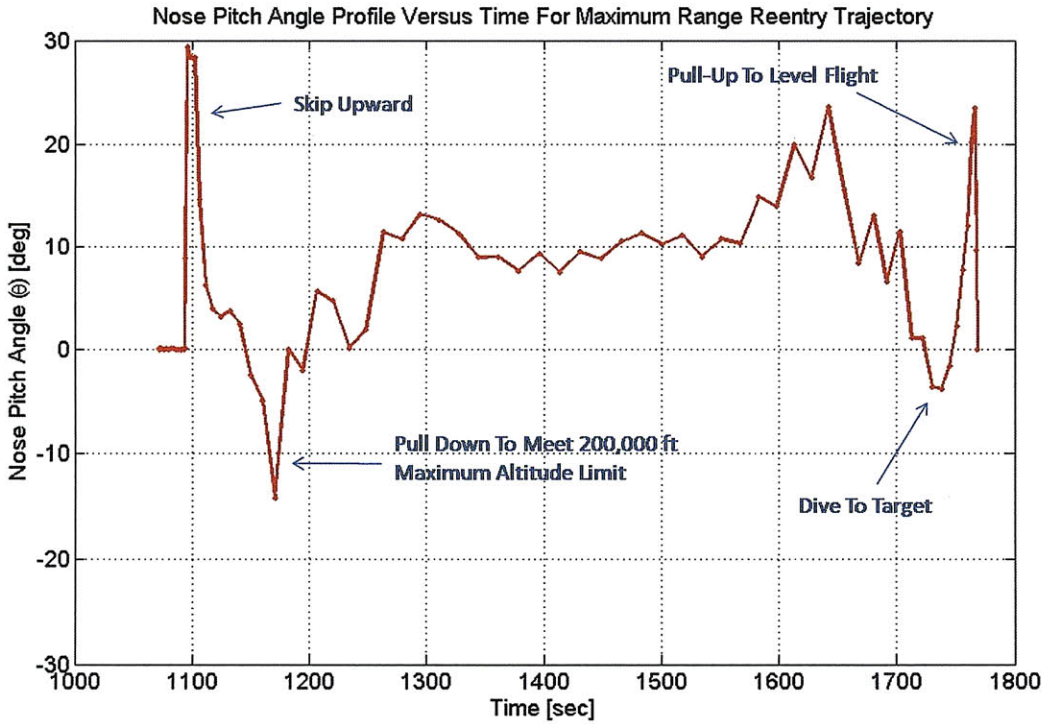

Figure 6-14: Nose Pitch Angle Profile For Maximum Range Reentry Trajectory

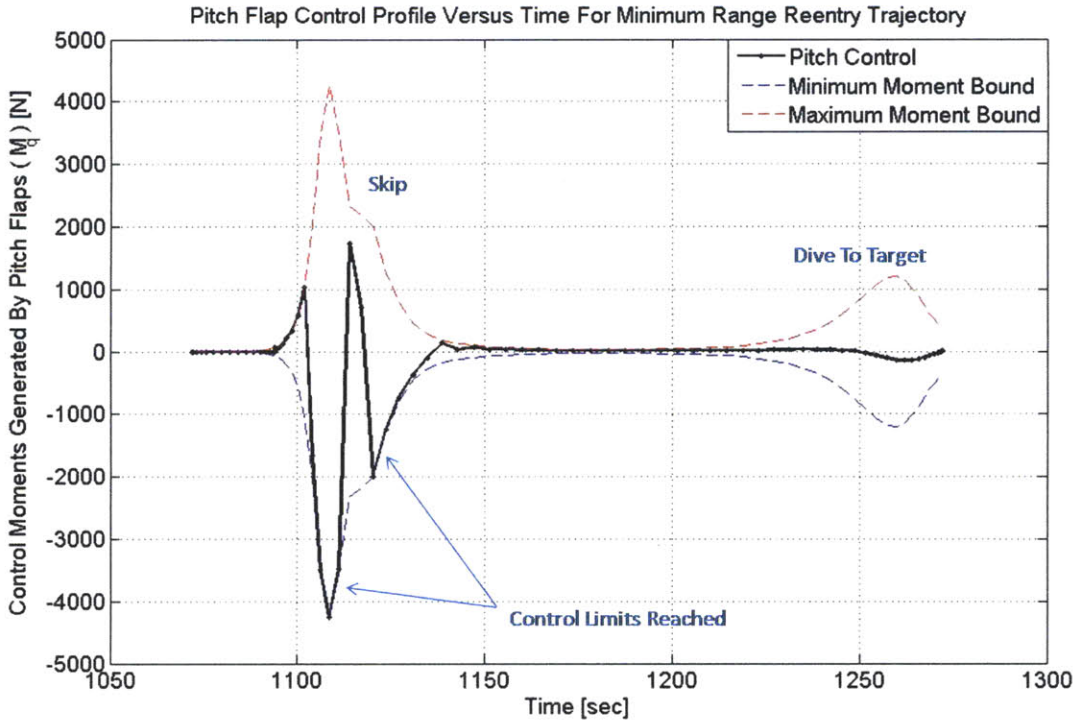

Figure 6-15: Optimal Pitch Flap Control For The Minimum Range Reentry Trajectory

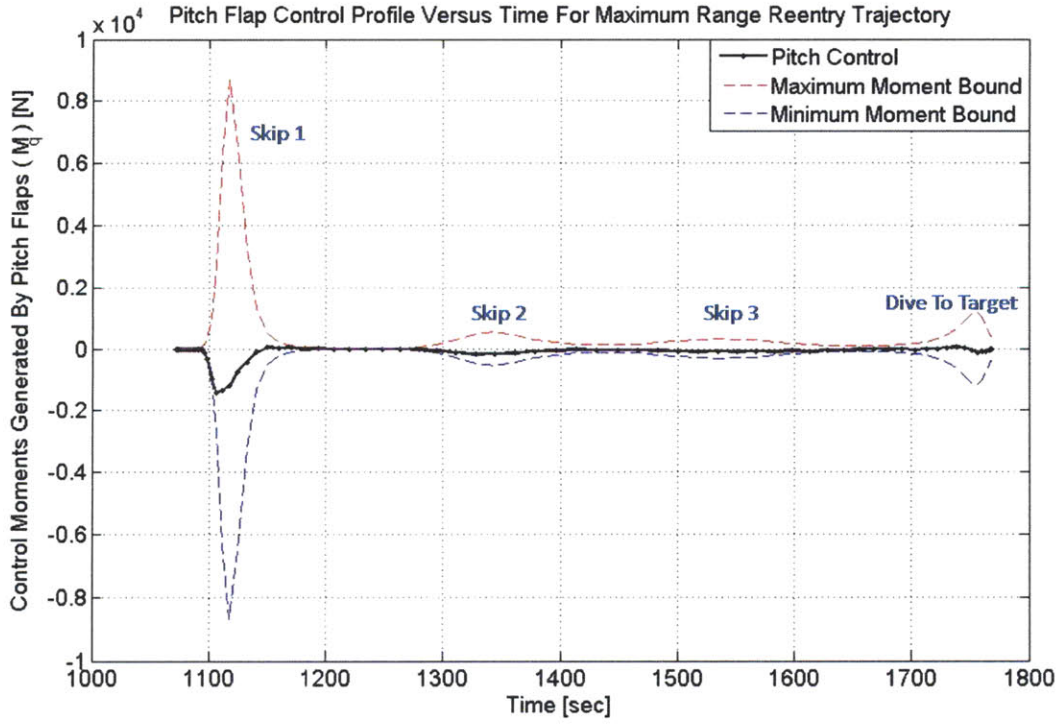

Figure 6-16: Optimal Pitch Flap Control For The Maximum Range Reentry Trajectory

6.4.3 Maximum Crossrange

The maximum crossrange reentry trajectory will be examined to investigate the crossrange maneuvering capabilities of the reentry vehicle. The maximum crossrange case maximizes the final latitude position of the vehicle upon reaching the target and the performance index used is $J = \lambda(t_{end})$. Figure 6-17 shows the maximum crossrange trajectory in comparison with the minimum and maximum downrange trajectories. The vehicle reaches a final relative latitude (λ) of 9.3 degrees at a relative longitude (μ) of 39.7 degrees, which is about halfway between the minimum relative longitude and maximum relative longitude. The total boost-through-reentry flight time is 1740 seconds. The maximum crossrange trajectory also performs a total of three skips, exhibiting similar characteristics to the maximum downrange trajectory.

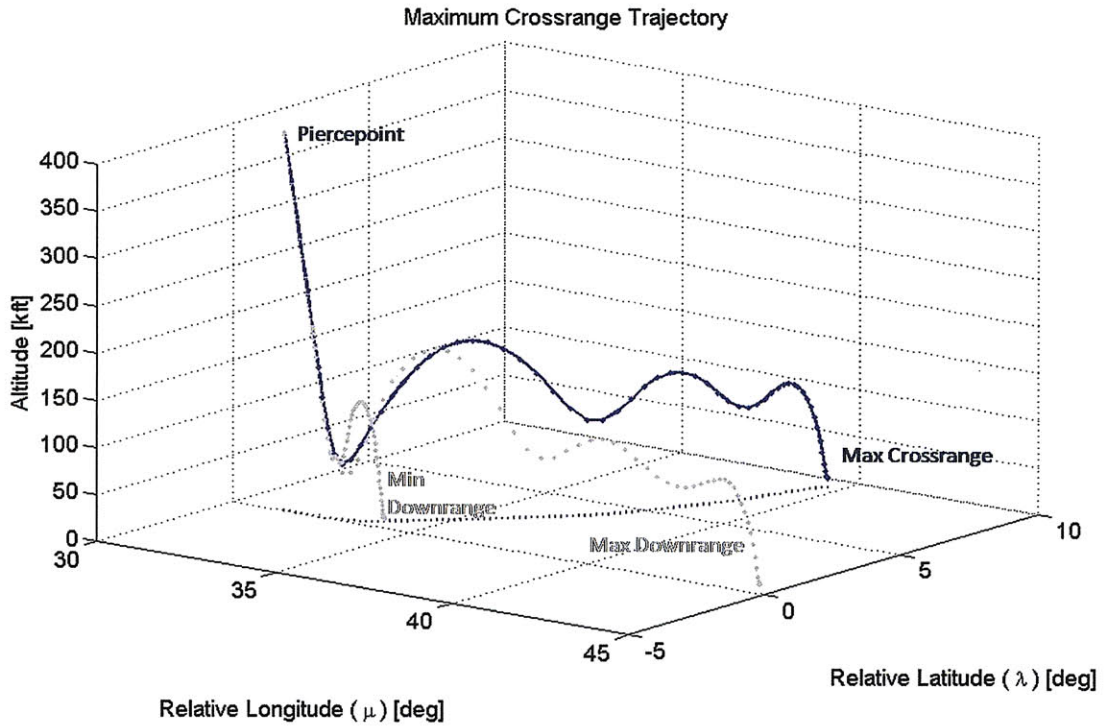

Figure 6-17: Maximum Crossrange Reentry Trajectory

Figure 6-18 gives the pitch and yaw flap controls for the maximum crossrange reentry trajectory. Notice that the yaw control is generally lower in magnitude than the pitch control. This is because the pitch control is more vital to keeping the skipping features of the trajectory intact. While the yaw control turns the vehicle toward the crossrange

direction, it is the pitch control that enables skipping to enhance the range capability and reach maximum latitude values. The pitch and yaw controls must be balanced since the nose pitch and yaw angles both contribute to the angle of attack, and higher angles of attack result in higher drag and more immediate energy loss.

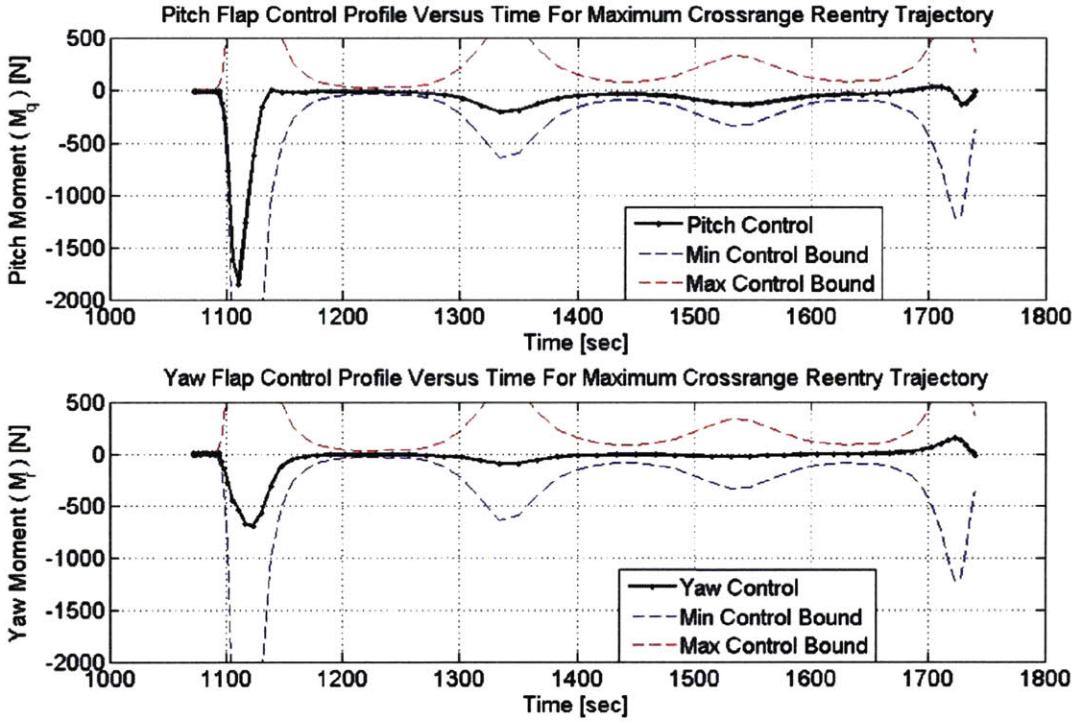

Figure 6-18: Pitch And Yaw Flap Controls For Maximum Crossrange Reentry Trajectory

Figure 6-19 gives the heading angle profile for the maximum crossrange reentry trajectory. The heading angle profile indicates a set of three left turns to increase the heading angle and one final right turn to turn back toward the target. The first three turns correspond to the trajectory skips, while the final turn corresponds to the final altitude dive toward the target altitude of 3 kilometers. The turns occur during each dip into the atmosphere since the vehicle control authority is proportional to the dynamic pressure exerted on the vehicle. More will be discussed on this topic in the next chapter.

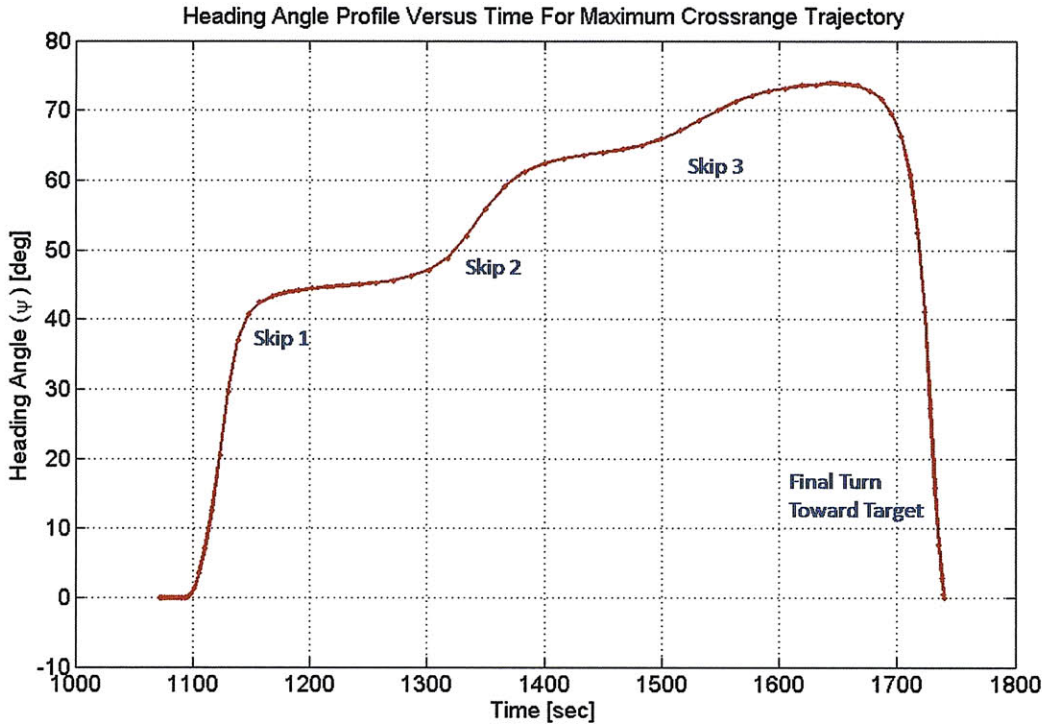

Figure 6-19: Heading Angle Profile For Maximum Crossrange Trajectory

6.5 Summary

In this chapter, a maneuvering reentry vehicle model was formulated for achieving the submunitions mission by maneuvering from a given piercepoint location at 400,000 feet to a target location. The vehicle uses a set of pitch and yaw flaps to control the vehicle attitude below an altitude of 200,000 feet and manuevers according to a skid-to-steer approach. The control authority of the flaps is directly proportional to the dynamic pressure exerted on the vehicle body, resulting in more aggressive maneuvering at lower altitudes. The limiting maneuvering capabilities of the vehicle are investigated by examining the maximum downrange, minimum downrange, and maximum crossrange target locations that can be reached from a fixed piercepoint. The maximum downrange and maximum crossrange trajectories exhibit a series of three skips to extend the maximum range of the vehicle, while the minimum downrange trajectory performs one low-altitude skip to expend extra energy. Now that the boost and reentry problems have been investigated individually, the boost-through-reentry problem will be considered as a unified optimal

control problem for the purpose of examining trajectory planning metrics.

[This page intentionally left blank.]

Chapter 7

The Aimpoint Map

In this chapter, a set of potential trajectory planning tools will be demonstrated for the submunitions mission formulated in the previous chapters. The primary tool, called the Aimpoint Map, will illustrate the set of all possible locations where the launch vehicle can be aimed while still satisfying the mission requirements. The Aimpoint Map can provide the mission planner with a set of potential aiming choices in order to satisfy certain flyover constraints, such as sovereign airspace avoidance or proper booster disposal. In order to provide additional valuable information to the mission planner, several properties of the Aimpoint Map and its associated trajectories will be examined using boost-through-reentry trajectory optimization. In addition to the Aimpoint Map, concepts such as the Launch Footprint, the Reverse Reentry Footprint, and the Piercepoint V-Gamma Map will be demonstrated as useful tools for trajectory planning.

The boost-through-reentry problem will be formulated by combining the bounds and constraints of the launch problem with the bounds and constraints of the reentry problem, as formulated in chapters 5 and 6. The piercepoint will serve as an interface between the two models. The final boundary knot in the launch problem and the initial boundary knot in the reentry problem are combined into one interior knot at the piercepoint time, t_{k_6}. Since the launch problem and reentry problem may use different scaling units, an additional event constraint is required to ensure continuity of the states across the piercepoint. Let K_{x_1} represent the launch problem state scaling matrix and K_{x_2} represent the reentry problem state scaling matrix. In order to ensure continuity across the t_{k_6} knot, it

is necessary that

$$\overline{\mathbf{x}}\left(t_{k_6}^{+}\right) - K_{x_1}\, K_{x_2}^{-1} \overline{\mathbf{x}}\left(t_{k_6}^{-}\right) = \mathbf{0}$$

Several interesting properties of the Aimpoint Map will be investigated in the following sections.

7.1 Aimpoint Boundaries

The characteristics of the Aimpoint Map boundaries are of prime interest since they provide valuable information about the limiting capabilities of both the launch and reentry vehicles. The aimpoint boundaries can provide useful information to the mission planner, such as the maximum heading angle relative to the target direction that the launch vehicle can be aimed such that it can still reliably reach the target. The aimpoint boundaries are broken down into three categories for analysis: the corner point boundary, the maximum boundary, and the minimum boundary. Each boundary will be analyzed in detail to fully explain the limiting factors in each case.

7.1.1 Corner Point Case

The first step in computing the boundary points of the Aimpoint Map is to compute the *corner point trajectory.* The corner point represents the aimpoint boundary point that lies on a Great Circle with the maximum inclination, ζ, relative to the plane of reference containing the launch location and target location. A Great Circle is defined as a plane passing through the center of the Earth and intersecting a 360 degree slice of the surface, as shown in Figure 7-1.

The corner point is computed by finding the feasible piercepoint $(r\left(t_{k_6}\right), \mu\left(t_{k_6}\right), \lambda\left(t_{k_6}\right))$ with the maximum ζ. The optimal control problem should seek to maximize ζ as a function of the piercepoint relative latitude and longitude states. Since the launch trajectory is constrained to remain in plane ($\phi = 0$), the corner point also represents the maximum heading angle (ψ) allowable at piercepoint such that the vehicle can maneuver back to the

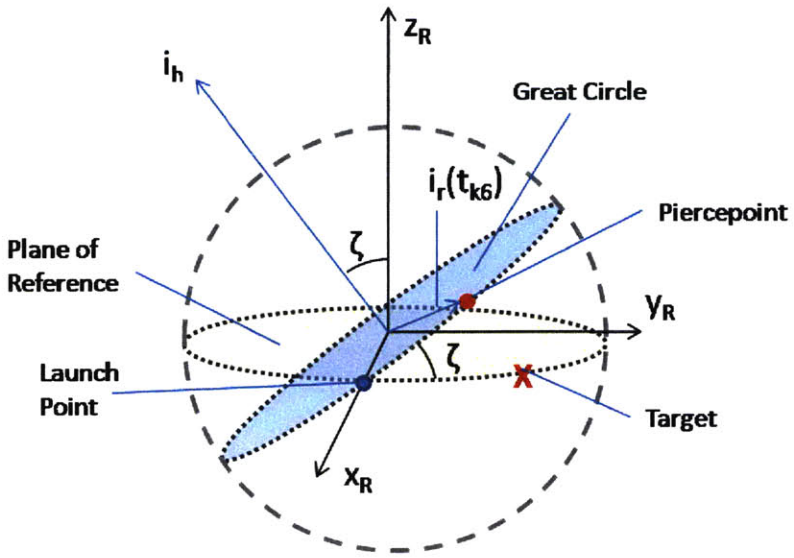

Figure 7-1: Illustration Of Geometry Used To Computed Corner Point Trajectory

target. In order to obtain an expression for the performance index, general expressions for the piercepoint position unit vector, $\hat{\mathbf{i}}_r\left(t_{k_6}\right)$, and the unit normal to the piercepoint plane, $\hat{\mathbf{i}}_h$, are computed.

$$\begin{aligned} \hat{\mathbf{i}}_r &= \cos\lambda\cos\mu\hat{\mathbf{x}}_{\mathbf{R}} + \cos\lambda\sin\mu\hat{\mathbf{y}}_{\mathbf{R}} + \sin\lambda\hat{\mathbf{z}}_{\mathbf{R}} \\ \hat{\mathbf{i}}_{r_0} &= \hat{\mathbf{x}}_{\mathbf{R}} \\ \hat{\mathbf{i}}_h = \frac{\hat{\mathbf{i}}_{r_0}\times\hat{\mathbf{i}}_r}{|\hat{\mathbf{i}}_{r_0}\times\hat{\mathbf{i}}_r|} &= \frac{-\sin\lambda\hat{\mathbf{y}}_{\mathbf{R}}+\cos\lambda\sin\mu\hat{\mathbf{z}}_{\mathbf{R}}}{\sqrt{\sin^2\lambda+\cos^2\lambda\sin^2\mu}} \end{aligned}$$

In order to incline the piercepoint plane as much as possible relative to the plane of reference, the $\hat{\mathbf{y}}_{\mathbf{R}}$ component of $\hat{\mathbf{i}}_h$ should be made as negative as possible. Therefore, the performance index for the corner point problem is given as the $\hat{\mathbf{y}}_{\mathbf{R}}$ component of the unit normal to the piercepoint plane.

$$J = \frac{-\sin\lambda\left(t_{k_6}\right)}{\sqrt{\sin^2\lambda\left(t_{k_6}\right)+\cos^2\lambda\left(t_{k_6}\right)\sin^2\mu\left(t_{k_6}\right)}}$$

The boost-through-reentry trajectory for the Aimpoint Map corner point reaches a piercepoint at 7.4 degrees relative longitude and 4.7 degrees relative latitude, resulting in

a maximum ζ of 32.44 degrees. The corner point trajectory is shown below.

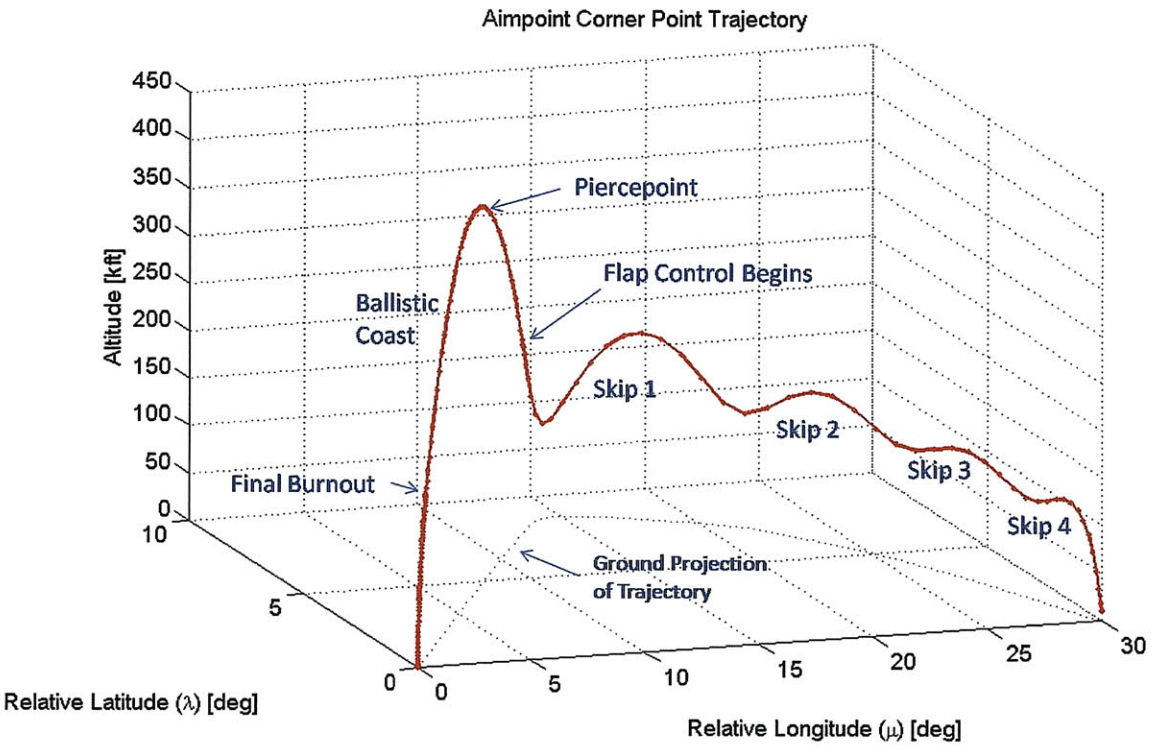

Figure 7-2: Corner Point Trajectory of Aimpoint Map

The corner point trajectory reaches the piercepoint at the shallowest possible reentry flight path angle (-1 deg) and exhibits four skips while manuevering to the target. The total flight time from launch to mission completion is 1313 seconds. After reaching piercepoint, the reentry vehicle must travel much farther crossrange since it cannot begin maneuvering until it reaches an altitude of 200,000 feet. Once the vehicle begins applying flap control at 200,000 feet, it must decide how to manuever back to the target. The skips represent an optimal choice for maneuvering because they minimize velocity loss due to atmospheric drag by repeatedly lofting up to higher altitudes. However, the vehicle also has less control authority at higher altitudes, representing a limited turning capability for the vehicle at high altitudes. There is a fundamental tradeoff between energy management and control authority during the reentry flight. With every skip, the vehicle must balance how much to turn versus how much velocity to conserve for range extension. This decision essentially involves choosing how far to dive into the atmosphere. A deep dive

will provide high controllability for a large turn, but will burn off a great deal of velocity while a shallow dive will burn off minimal velocity but only allow a small turn.

It is especially important for the vehicle to make a large turn during the first skip in the corner point trajectory since the heading angle is very large for this case and not turning on the first skip could send the vehicle another 2 or 3 degrees crossrange (relative latitude) before the vehicle is able to turn back toward the target. The corner point case represents the maximum inclined direction that the launch vehicle can be aimed toward while still having enough energy and control authority to reach the target. By examining the latitude-longitude profile of the trajectory as well as the altitude-longitude profile, it can be observed that the vehicle turns the greatest amount during the first skip, which also happens to be the deepest skip.

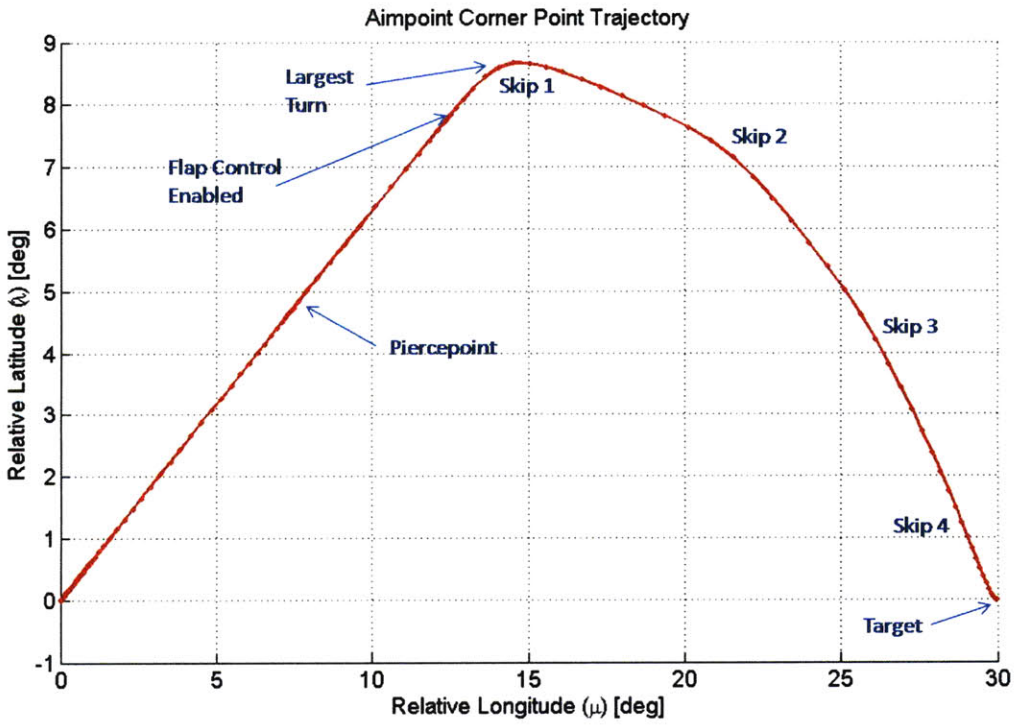

Figure 7-3: Top-View of Corner Point Trajectory

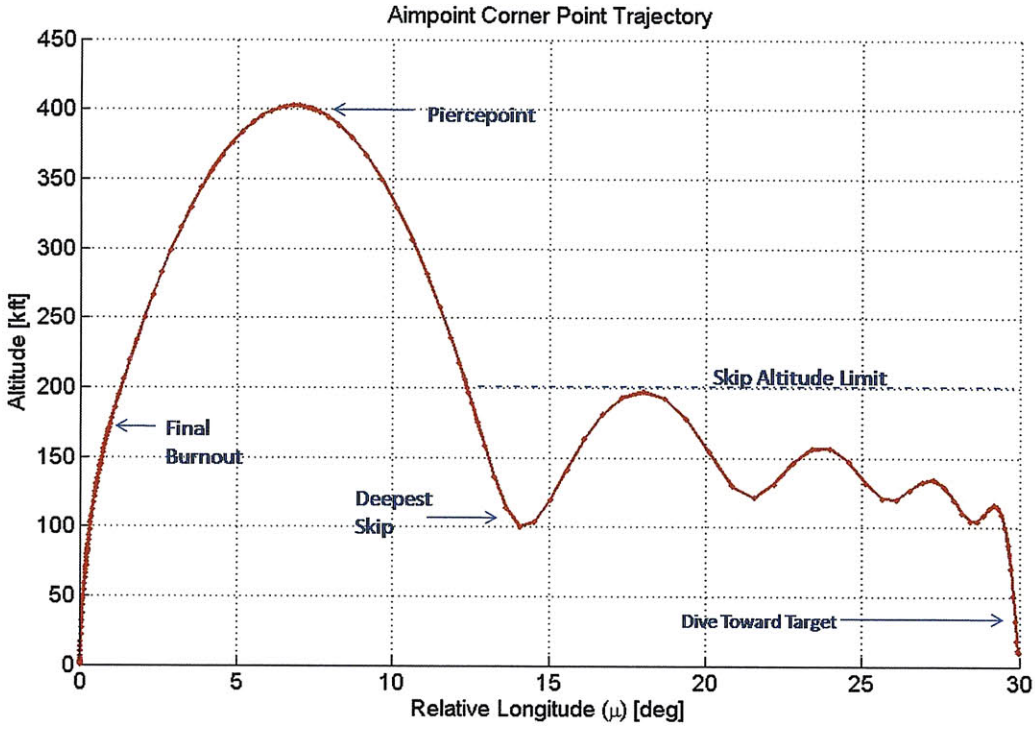

Figure 7-4: Side-View of Corner Point Trajectory

Velocity Profile

The velocity profile of the corner point trajectory clearly illustrates the energy management issues facing the reentry vehicle. The reentry vehicle faces a hard constraint of 1300 ft/sec on the terminal velocity and must budget the use of the 16000 ft/sec reentry velocity such that all end conditions can be met. The turning of the vehicle heading angle to direct the vehicle toward the target is one use of the energy budget. Another use of the budget that requires a large amount of energy is the final dive toward the target. As the vehicle dives toward the target, it encounters a dense atmosphere and sheds off a large amount of energy due to increased drag. The final dive must be initiated with enough spare energy to ensure that the vehicle will be travelling at 1300 ft/sec after the dive is completed. As can be observed in Figure 7-5, the vehicle initiates the final dive towards the target with a velocity of approximately 4000 ft/sec and reaches 1300 ft/sec by the time it pulls up to level flight at 3 km altitude.

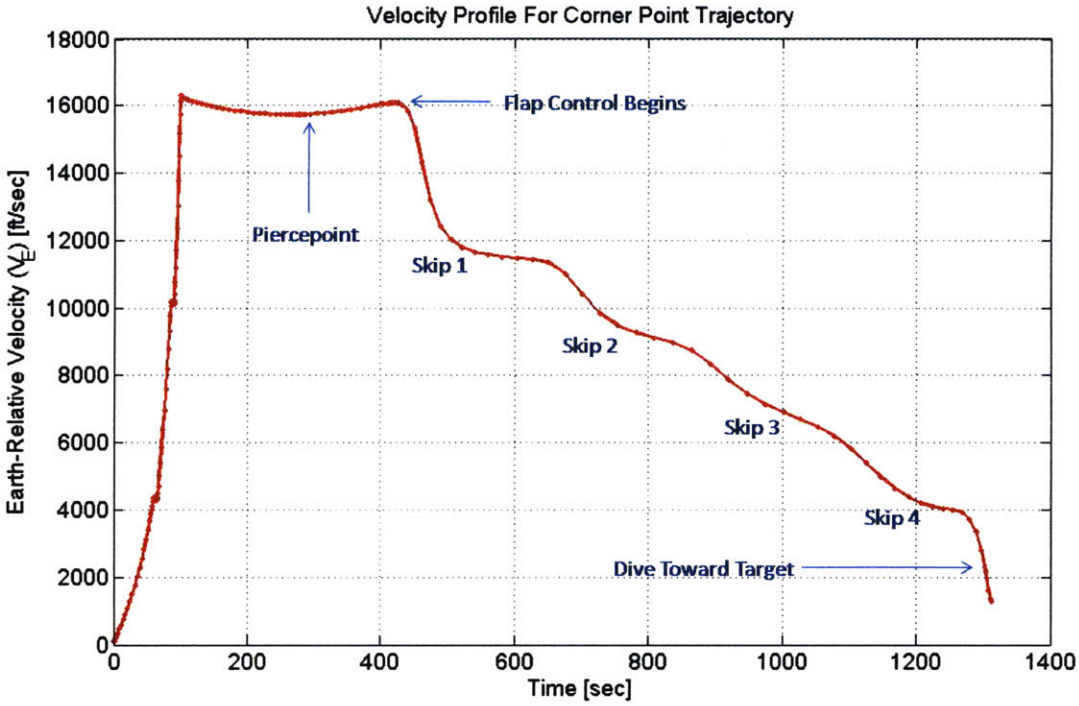

Figure 7-5: Velocity Profile Of Corner Point Trajectory

Flight Path Angle Profile

The flight path angle profile can give insight into the skipping characteristics, as well as the final dive and pull-up to reach the target state. The flight path angle profile for the corner point case is given by Figure 7-6. During the first 100 seconds, the launch vehicle maneuvers to target a final burnout γ of approximately 10 degrees. The flight path angle is turned by gravity during the ballistic coast and reaches piercepoint at a γ of only -1 degree, the shallowest possible flight path angle allowed by the event constraint at t_{k_6}. From this point, the flight path angle continues to drop under gravity until the flap controls are enabled at 200,000 ft and the vehicle begins to pitch upward. The flight path angle oscillates about $\gamma = 0$ as the vehicle performs four skips, then dives deep into the atmosphere to reach the target altitude of $3\,km$ and pulls up to level flight.

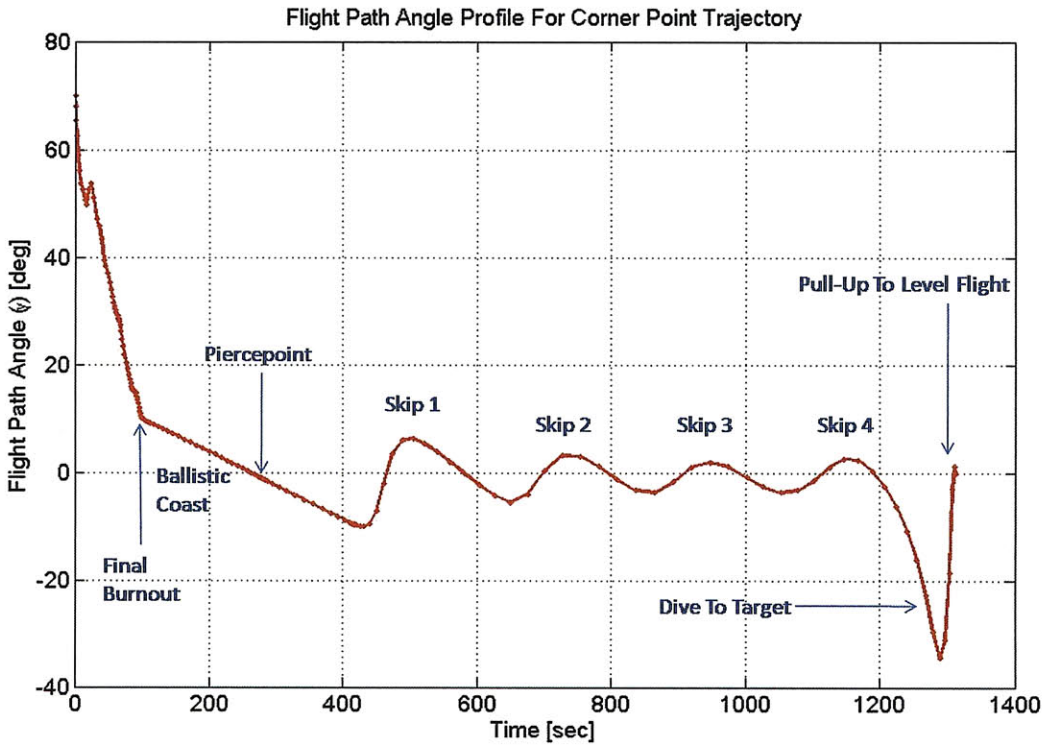

Figure 7-6: Flight Path Angle Profile For Corner Point Trajectory

Heading Angle Profile

Insight into the turning characteristics of the vehicle can be obtained by examining the heading angle profile for the corner point trajectory. Figure 7-7 gives the heading angle profile. It can be observed that the vehicle heading remains relatively constant during the launch portion of the trajectory due to the restriction that $\phi = 0$ over this segment. The heading angle will vary slightly during this period due to the rotation of the Earth and the rotation of the local level frame as the vehicle ascends to higher latitudes. The vehicle cannot constrain the heading to be constant during the launch because the vehicle motion is governed by inertial forces and will remain in an inertial plane of motion while the Earth rotates below it. The vehicle cannot manuever to stay in a rotating plane of motion because it has zero controllability during the ballistic coast and must travel in an inertial plane of motion.

It can be observed that soon after the flap control is enabled, the vehicle makes a large turn towards the right. Three additional turns of reducing magnitude corresponding to the skips turn the vehicle further to the right until a sharp left turn at the end returns the vehicle heading to the plane of reference ($\psi = 0$). While the first turn associated with the first skip is the largest right turn, the final left turn associated with the dive toward the target represents an even larger turn. The reason for this is that the vehicle is trying to balance energy conservation with turning authority during the first skip, but is required to dive all the way down to the terminal altitude of $3\,km$ during the last dive. Therefore, energy management is not a consideration for the final turn since a fixed amount of energy is required to satisfy the end conditions. The required deep dive at the end of the trajectory provides plenty of control authority to make a sharp left turn prior to reaching the target.

Attitude Angle Profile

Further insight into the skipping and turning characteristics can be obtained by examining the profile of the attitude angles over time. The attitude angle profile is given by Figure 7-8. During launch, the nose pitch angle is used to shape the flight path angle profile in

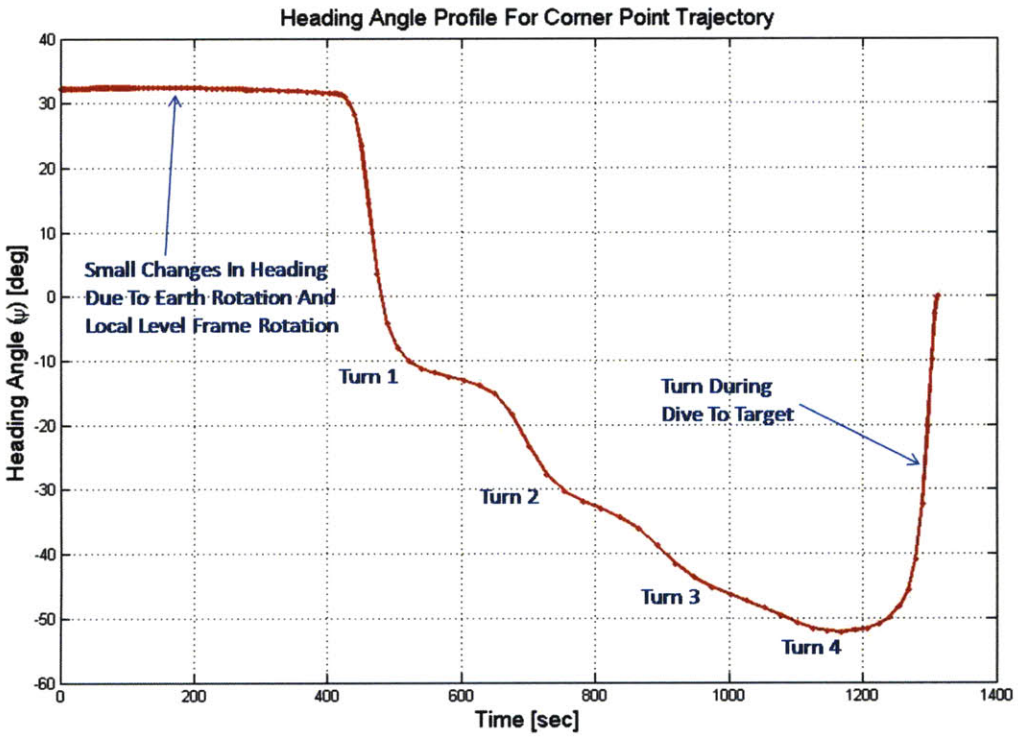

Figure 7-7: Heading Angle Profile For Corner Point Trajectory

order to target an appropriate γ at final burnout to achieve optimal reentry conditions. The pitch angle is initially positive to raise the flight path angle up to ensure the vehicle reaches an adequate altitude before pitching over to the side. A bump in the flight path angle profile can be observed at approximately 20 seconds due to the positive pitch angles observed here. Once the vehicle has been guided to an adequate altitude, the pitch angle takes a negative value to turn the vehicle towards the horizontal and target a shallow reentry. Note that this is very similar to the launch profile seen for the minimum range launch trajectory in section 5.7.

Once the flap control is enabled upon reentry, the nose pitch angle is quickly commanded to a positive value, where it remains until the final dive to the target near the end of the trajectory. The positive pitch angle allows the vehicle to perform its skipping maneuvers by continually generating a positive lift force. As the vehicle skips upward, the magnitude of the lift force decays due to a loss of dynamic pressure and gravity turns the flight path downward for another dip into the atmosphere. As the vehicle decends into the atmosphere, the lift force grows to a sufficient value to overcome gravity and allow another skip. Since a higher nose pitch angle will generate more lift upward in proportion to dynamic pressure, the choice of the pitch angle determines how far into the atmosphere the vehicle will dip prior to each skip. Again, the choice of the pitch angle represents a balance between energy management and turning capability. A larger pitch angle will enable a shallower skip while a smaller pitch angle will enable a deeper skip into the atmosphere for more turning authority. It can be observed in Figure 7-8 that the pitch angle for the first skip is approximately 5 degrees, allowing a deep dip into the atmosphere for a large turn, while the later skips exhibit pitch angles of 10 degrees of higher, indicating shallower dips and smaller turns. The final dive toward the target conditions exhibits a slightly negative pitch angle to quickly lose altitude, followed by a sharp increase to pull up the flight path angle to level flight conditions.

The nose yaw angle (ϕ) is fixed to zero for the launch and ballistic coast segments of flight to ensure planar motion. Once the flap control is enabled, the nose yaw angle is commanded to a value of approximately -10 degrees to begin turning the vehicle toward the right by reducing the heading angle. The nose yaw angle remains negative until it

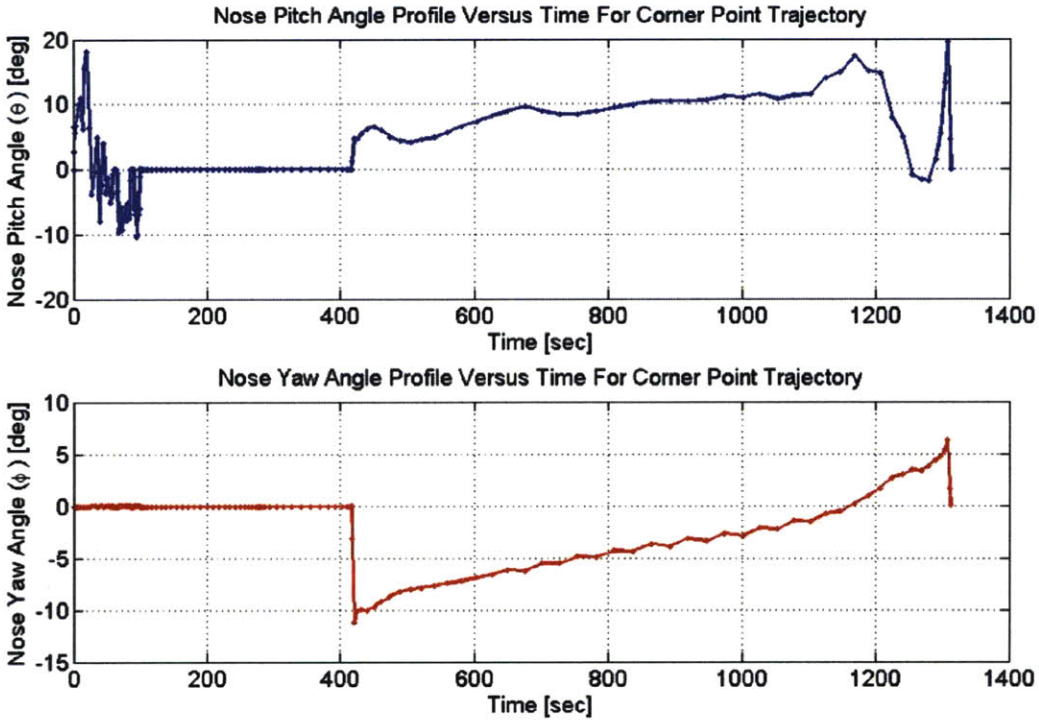

Figure 7-8: Nose Attitude Profile For Corner Point Trajectory

approaches a value of 5 degrees during the final dive toward the target to enable a left turn back to $\psi = 0$.

Optimal Controls

The motion described in the previous sections is entirely enabled by an optimal choice of the TVC, ACS, and flap controls. All three types of control include control capability in both the pitch and yaw channels. The thrust vector pitch control (β) is initially negative immediately after the first ignition in order to keep the nose pitched upward and drive toward higher altitudes. However, β soon takes on positive values to drive the nose downward and turn the vehicle towards the horizontal for a shallow reentry. The ACS pitch control (M_{C_q}) exerts positive moments about the $\mathbf{y}_B$ axis during the coasting period to constrain the nose pitch angle to zero. Since the flight path angle is dropping during the coasting periods, M_{C_q} must be positive to drive the vehicle nose downward to follow the motion of the velocity vector. It can be observed that only very small

moments are required to maintain this stability. The pitch flap control is proportional to the amount of dynamic pressure exerted on the vehicle. It can be observed that the primary pitching control occurs at discrete locations associated with each skip. The pitch flap exerts negative moments about the $\hat{\mathbf{y}}_\mathbf{B}$ axis to drive the nose upward and enable a skip. The control authority degrades significantly during the periods between each skip due to the vehicle ascent to high altitudes. The flap control pitches downward for the first time (positive moment) during the final dive to the target, followed by a quick command of a negative moment to pull up the nose attitude to level flight. The pull-up maneuver requires a larger moment than the diving maneuver because gravity assists the diving maneuver while the pull-up maneuver must counteract gravity.

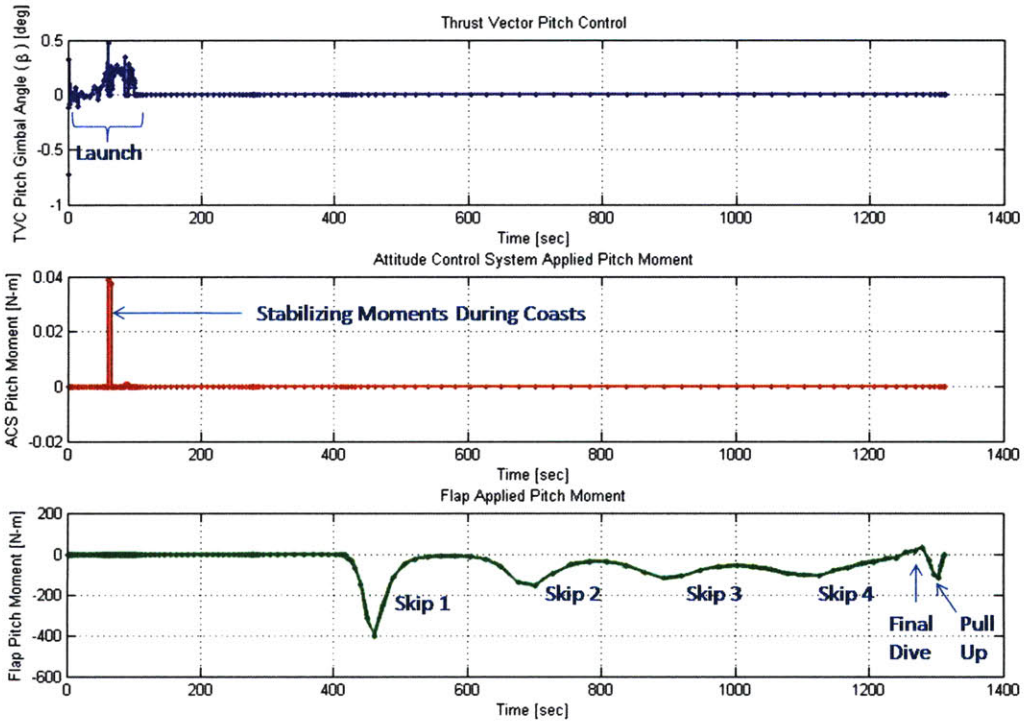

Figure 7-9: Pitch Control Profile For Corner Point Trajectory

The optimal yaw controls have similar characteristics to the pitch controls. The ACS yaw control applies small negative moments to stabilize the vehicle attitude to zero angle-of-attack during the coasting periods while the yaw flap control exerts a series of negative moments proportional to the dynamic pressure. The negative yaw moments turn the

vehicle toward the right and decrease the vehicle heading angle. As mentioned previously, the primary turning moments occur at discrete locations associated with the skips. For this trajectory, most of the turning moment is applied during the first skip while the turning moments during the remaining skips are substantially lower in magnitude. A positive yaw moment is applied at the end of the trajectory to enable a right turn to meet the end condition $\psi = 0$.

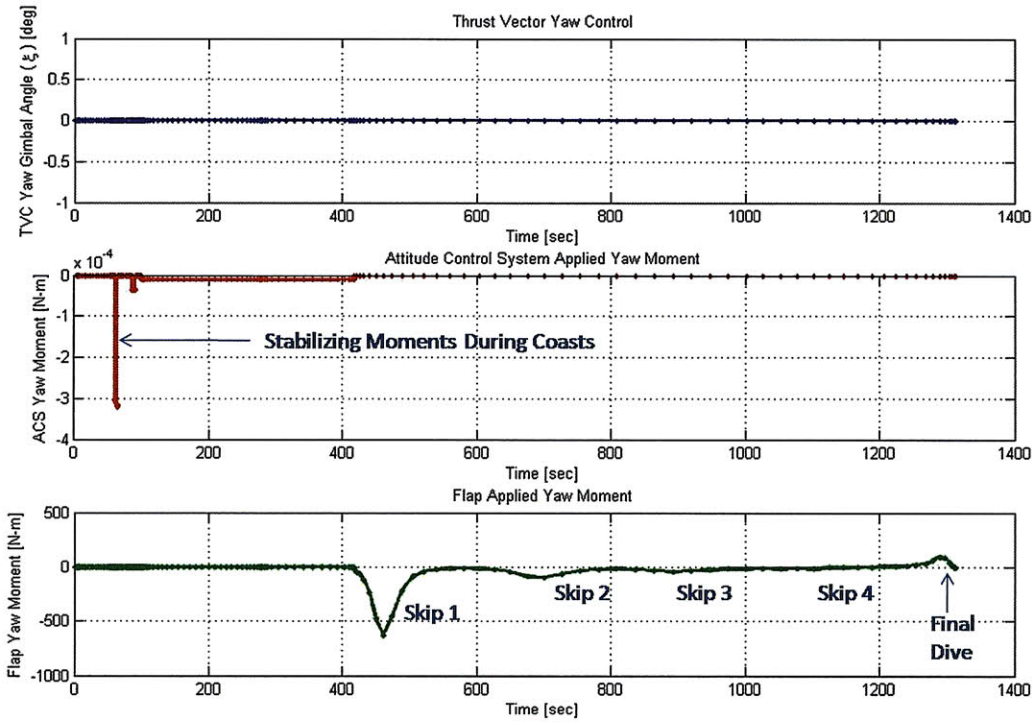

Figure 7-10: Yaw Control Profile For Corner Point Trajectory

7.2 Aimpoint Minimum and Maximum Piercepoint Cases

Once the corner point is established, additional boundary points on the Aimpoint Map can be computed by sweeping out intermediate planes between the corner point plane and the plane of reference. Since the corner point plane was inclined with a ζ of approximately 32 degrees relative to the plane of reference, the remaining boundary points are

computed by sequentially solving for maximum and minimum range trajectories that lie along planes with a ζ between 32 degrees and 0 degrees. In order to accomplish this, a series of maximum range and minimum range optimization problems are solved with the initial heading angle ($\psi(t_0)$) for each case fixed to a value between 32 degrees and 0 degrees. A looping algorithm is implemented that solves all minimum and maximum cases sequentially starting at $\psi(t_0) = 30$ degrees and sweeping out over 2 degree decrements to $\psi(t_0) = 0$ degrees. Since ϕ is constrained to zero, this amounts to sweeping out intermediate piercepoint planes that lie between the corner point piercepoint plane and the plane of reference, as illustrated in Figure 7-11. The Aimpoint Map is assumed to be symmetric about the plane of reference since the reentry vehicle has equal control authority for right and left turns.

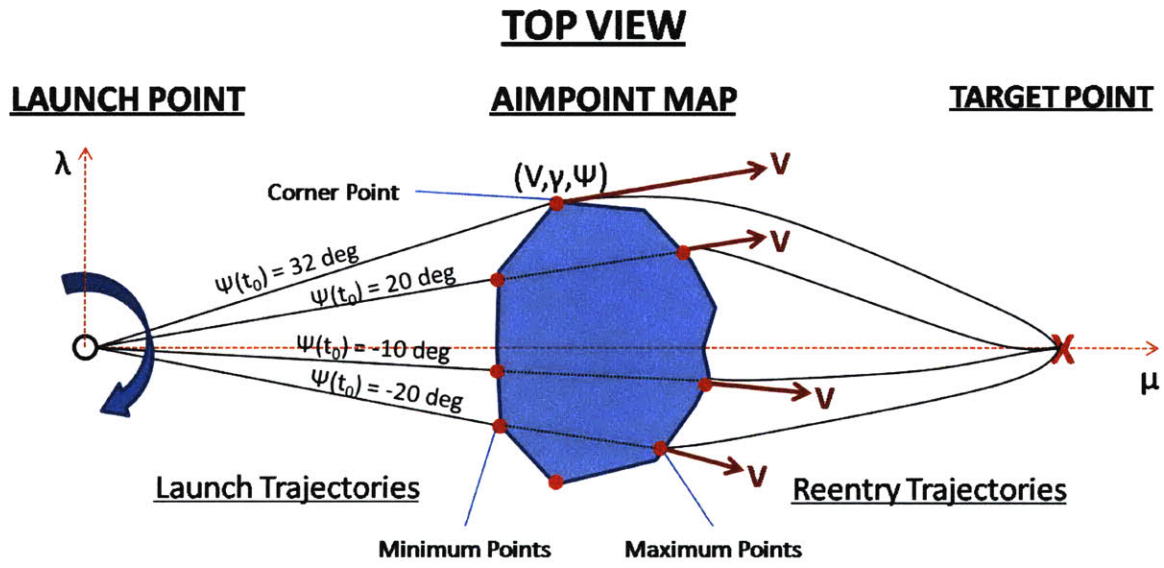

Figure 7-11: Concept For Sweeping Across The Aimpoint Map To Compute Minimum And Maximum Boundaries

The initial guess for kickstarting the algorithm is the corner point case. From that point, the minimum range problem is solved first for each choice of $\psi(t_0)$, followed by the maximum range problem. The cost function for the minimum range problem is $J = \mu(t_{k_6})$ while the cost function for the maximum range problem is $J = -\mu(t_{k_6})$. The most recent minimum range solution is used as a guess for the corresponding maximum range problem as well as for the next minimum range problem with a new choice of $\psi(t_0)$. The Aimpoint

Map boundaries for the submunitions mission with a target at 30 degrees downrange and 0 degrees crossrange are shown below.

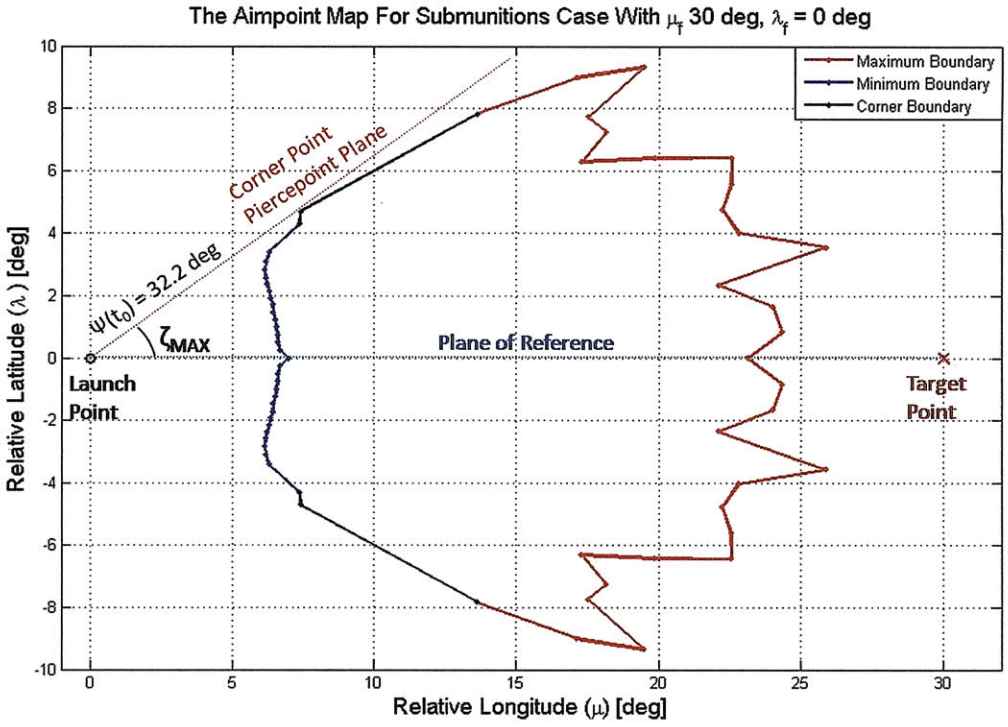

Figure 7-12: The Aimpoint Map For The Submunitions Mission

The boundaries of the Aimpoint Map are composed of minimum and maximum range piercepoint locations as well as a corner point boundary where the maximum and minimum bounds come together. The Aimpoint Map resembles a maple leaf, with smooth, well-defined minimum and corner boundaries and less well-defined boundaries along the maximum edge. The corner point boundary was examined in detail in the previous section. Now the minimum and maximum Aimpoint Map boundaries will be examined in detail.

Minimum Boundary Points

The minimum boundary of the Aimpoint Map lies entirely between 6 and 8 degrees relative longitude and exhibits a smooth, uniform shape. The minimum range trajectories which pass through the minimum boundary points are examined to infer characteristics

of the aimpoint minimum boundary. The minimum range trajectories corresponding to $\psi(t_0) = 0\,deg$, $\psi(t_0) = 10\,deg$, $\psi(t_0) = 20\,deg$, $\psi(t_0) = 32.2\,deg$ (Corner Point) are plotted along the Aimpoint Map boundary in Figures 7-13 and 7-14.

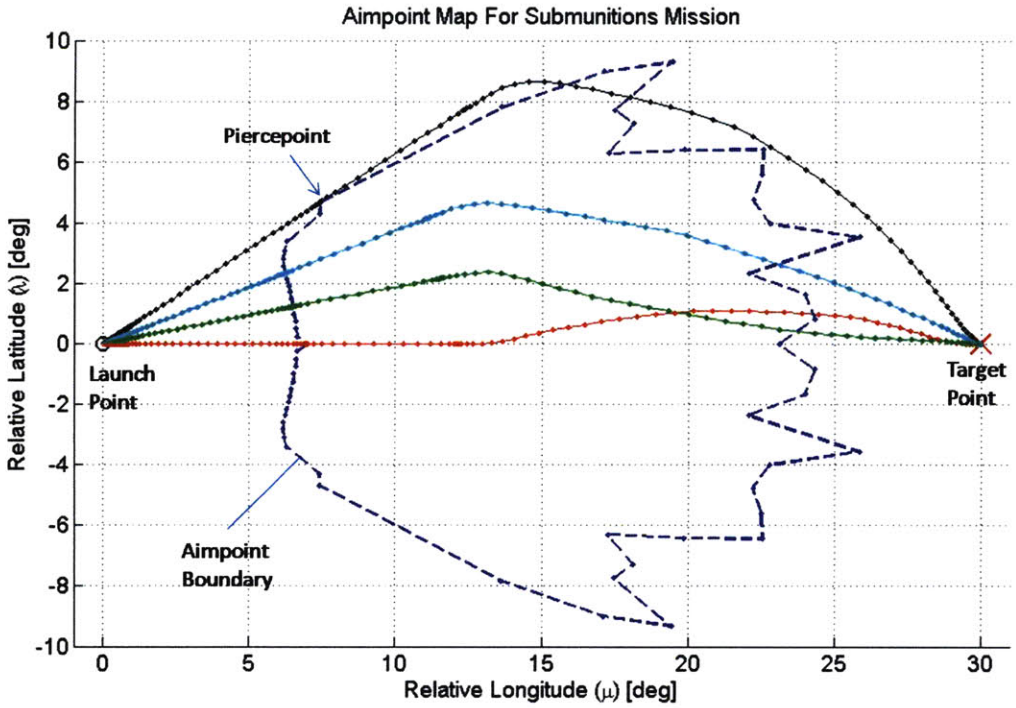

Figure 7-13: Top-View Of Minimum Boundary Trajectories

Notice that the minimum range trajectories have similar characteristics to the corner point trajectory. All minimum range trajectories pitch over towards the horizontal considerably before the final burnout, allowing a shallow reentry at piercepoint. This profile also resembles the minimum range launch trajectory computed in section 5.7, which reached piercepoint with $\gamma = -1\,deg$ and $\mu = 6.1\,deg$. The flight path angle profiles of the minimum boundary trajectories, corner point trajectory, and minimum range launch trajectory are compared in Figure 7-15.

All five trajectories maneuver such that they reenter with the maximum possible flight path angle (-1 deg) at piercepoint. This suggests that the minimum aimpoint boundary is defined by trajectories with the shallowest allowable reentry conditions. The shallowest reentry conditions can result in the minimum aimpoint boundary because the piercepoint-to-target range is maximized by allowing for the best possible energy conservation during

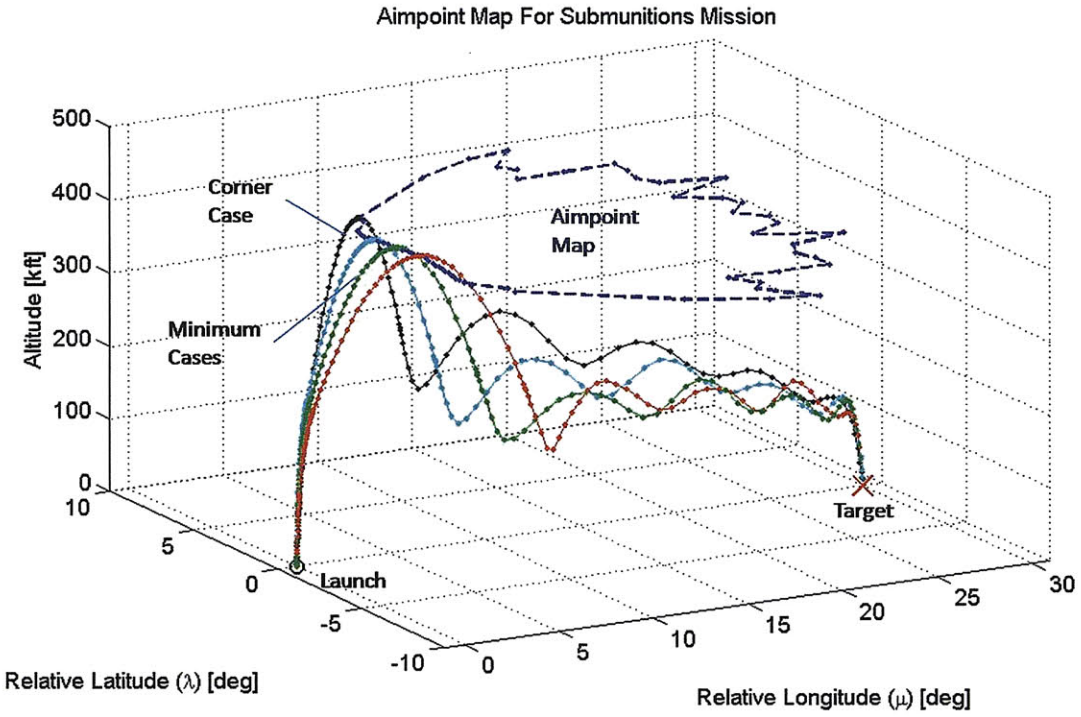

Figure 7-14: Aimpoint Minimum Boundary Trajectories

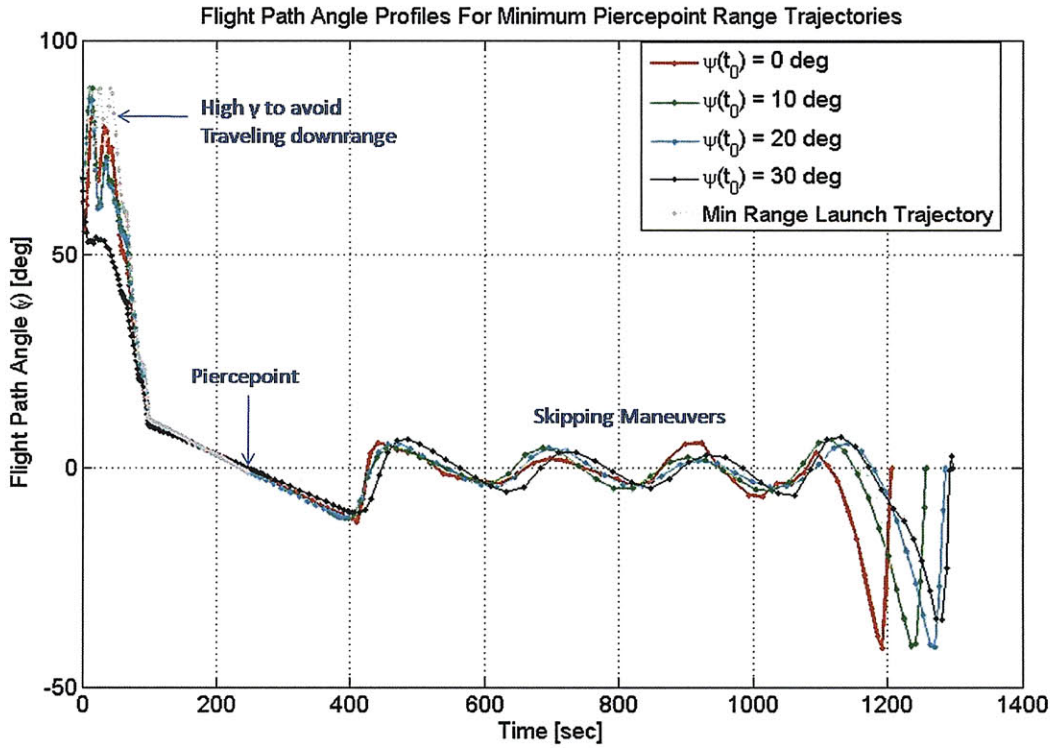

Figure 7-15: Flight Path Angle Profile For Minimum Aimpoint Boundary Trajectories

the reentry flight. By reentering with the shallowest allowable γ, the reentry vehicle loses a minimal amount of energy during the first reentry skip and retains a maximum amount of energy for range extension.

Another characteristic of the minimum boundary trajectories is that they all use a total of four skips during reentry to reach the target location. This suggests that the region in which the minimum boundary lies (6 to 8 degrees longitude) can be characterized as a *four skip region.* That is, the reentry vehicle must maneuver with four skips to reach the target from any piercepoint in this region. This suggests that the minimum aimpoint boundary is also characterized by an energy limitation of four reentry skips. The total energy budget of approximately $16,000\, ft/sec$ for reaching the target will be over the limit if a fifth skip is added to the reentry profile.

Maximum Boundary Points

The maximum aimpoint boundary defines the maximum range along a given heading (ψ) where a reentry vehicle can hit piercepoint and still reach the terminal conditions at the target point. The maximum boundary represents limitations enforced by both minimum energy bounds as well as the vehicle turning capability. The vehicle turning capability represents a limiting factor for the maximum aimpoint boundaries because the vehicle reenters at piercepoints with heading angles that are directing the vehicle away from the target. Unlike the minimum and corner aimpoint boundary piercepoints, these piercepoints are much further downrange and/or crossrange from the launch point and require sharper turns to maneuver back to the target.

The vehicle turning authority must be balanced with energy management to ensure the the vehicle can reach the terminal conditions. Since the flap controls of the reentry vehicle are directly proportional to dynamic pressure, the vehicle must descend to low altitudes with high velocities to ensure a large turning capability. However, since drag is also directly proportional to dynamic pressure, increasing the turning authority consequently reduces the vehicle velocity, thereby reducing the range of the vehicle. In addition, large turns require large angles of attack, which also increase the drag force. Therefore, the vehicle's ability to turn must be balanced appropriately with its range capability. Figure

7-16 illustrates a sample of the maximum boundary trajectories.

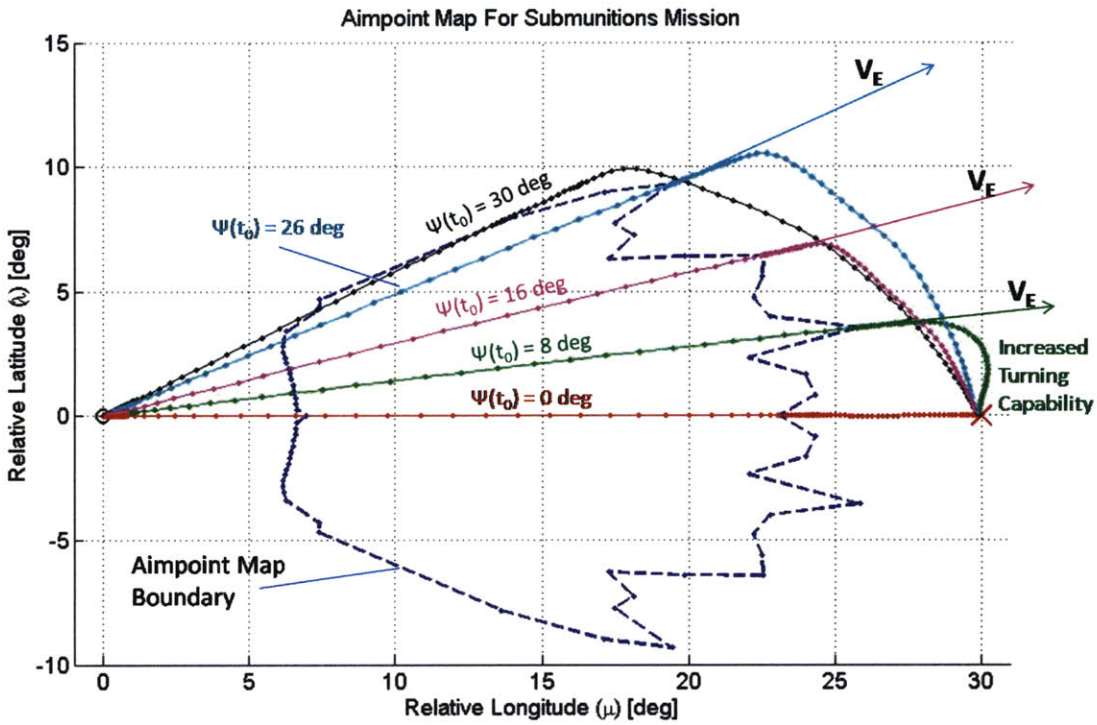

Figure 7-16: Top View Of Maximum Piercepoint Range Trajectories

Figure 7-16 provides a good depiction of the turning requirements for each piercepoint along the maximum boundary. Notice that the trajectory with $\psi(t_0) = 8\,deg$ is capable of turning the greatest amount since it does not require a large range capability to reach the target, resulting in a piercepoint over 25 degrees downrange of the launch point. The piercepoints associated with $\psi(t_0) = 16\,deg$, $26\,deg$, and $30\,deg$, however, cannot extend as far because of the inability of the vehicle to perform sharp turns while properly managing energy. In fact, the piercepoints located crossrange of the target perform turns with a number of skips that increases as the piercepoint is moved further crossrange.

Figure 7-17 illustrates the vehicle's method of maneuvering to the target from various piercepoints along the maximum aimpoint boundary. It is important to note that the vehicle maneuvers with fewer skips as the piercepoint is moved closer to the plane of reference. The piercepoints can be categorized based upon the number of skips used to maneuver to the target. A one-skip region, two-skip region, three-skip region, and four-

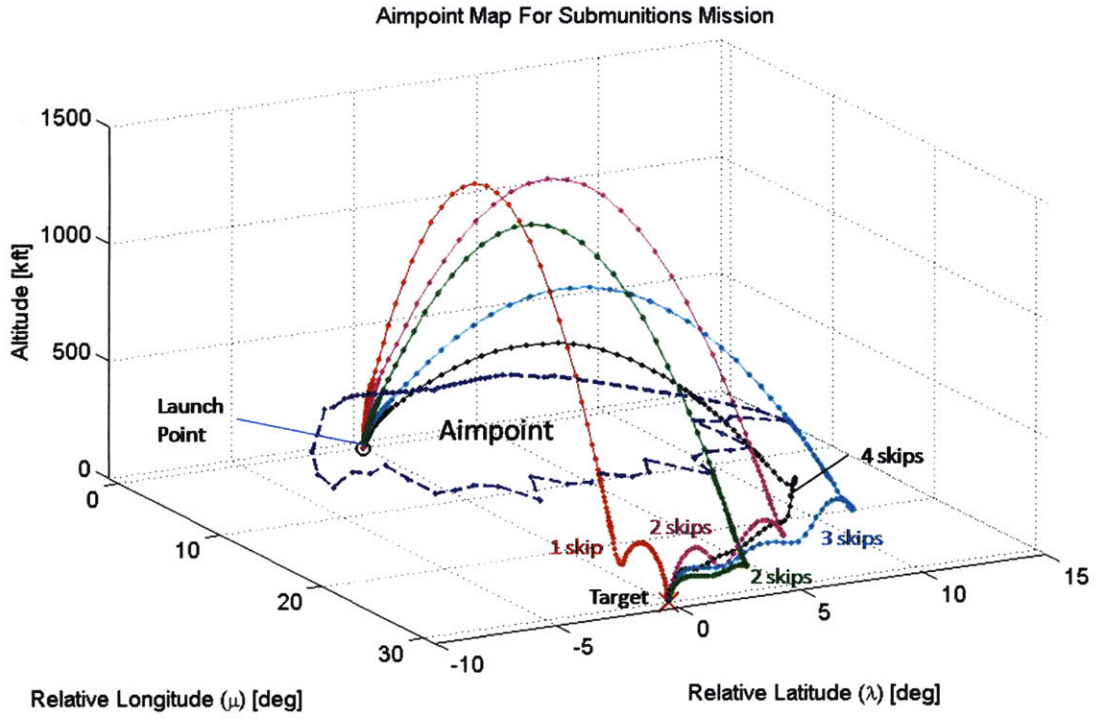

Figure 7-17: Maximum Boundary Trajectories

skip region can be defined to indicate the number of skips required for a given aimpoint. The one-skip region represents the region closest to the target, while the four-skip region represents the minimum and corner boundaries of the aimpoint. The regions are defined here at the aimpoint boundaries, but further investigation is required to segment the aimpoint interior into distinct skip regions.

The jagged shape of the maximum aimpoint boundary may be attributed to interesting phenomena occuring at the boundaries of the skip regions as well as complexities associated with phasing the skips correctly. This subject warrants further investigation in future studies.

7.3 Launch Footprint

The launch problem can be revisited by examining the state conditions that can be reached at various piercepoints within the Aimpoint Map. Since at a given piercepoint location the position variables (r, μ, λ) are fixed and the attitude variables (q_{body}, r_{body}, θ, ϕ) are

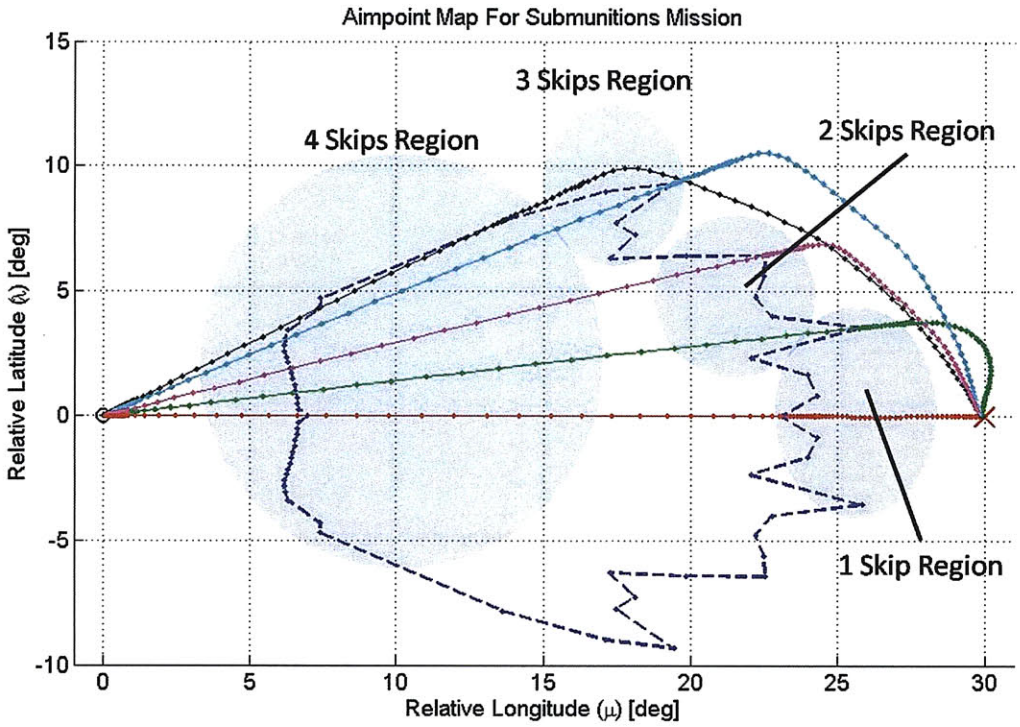

Figure 7-18: Illustration of Skip Regions Along Aimpoint Boundaries

uniquely determined by the constraint that the angle of attack must be zero at piercepoint, the remaining state variables to consider are the velocity states (V_E, γ, ψ). The heading angle (ψ) is nearly unique at piercepoint due to the constraint that $\phi = 0$ during launch. Therefore, only secondary effects due to the Earth sphericity and rotation affect the heading angle during launch. For this study, analysis of the effects of slight variations in heading angle are not considered. An analysis will be performed to evaluate the set of *launch footprints* of V_E and γ states that can be reached at each fixed piercepoint in the Aimpoint Map.

The launch footprint is computed by first solving for the steepest (γ_{min}) and shallowest (γ_{max}) reentry conditions that can be reached at a piercepoint. For this analysis, the final Earth-relative velocity (V_E) is free to vary in order to obtain the absolute steepest and shallowest reentry profiles possible over all possible reentry velocities. The performance index used for the steepest descent problem is given as

$$J = \gamma\left(t_{k_6}\right)$$

For a piercepoint located in the Aimpoint Map at $\mu\left(t_{k_6}\right) = 15\,deg$ and $\lambda\left(t_{k_6}\right) = 4\,deg$, the minimum achievable flight path angle at piercepoint is -67.8 degrees. The flight path angle for this case is shown in Figure 7-19.

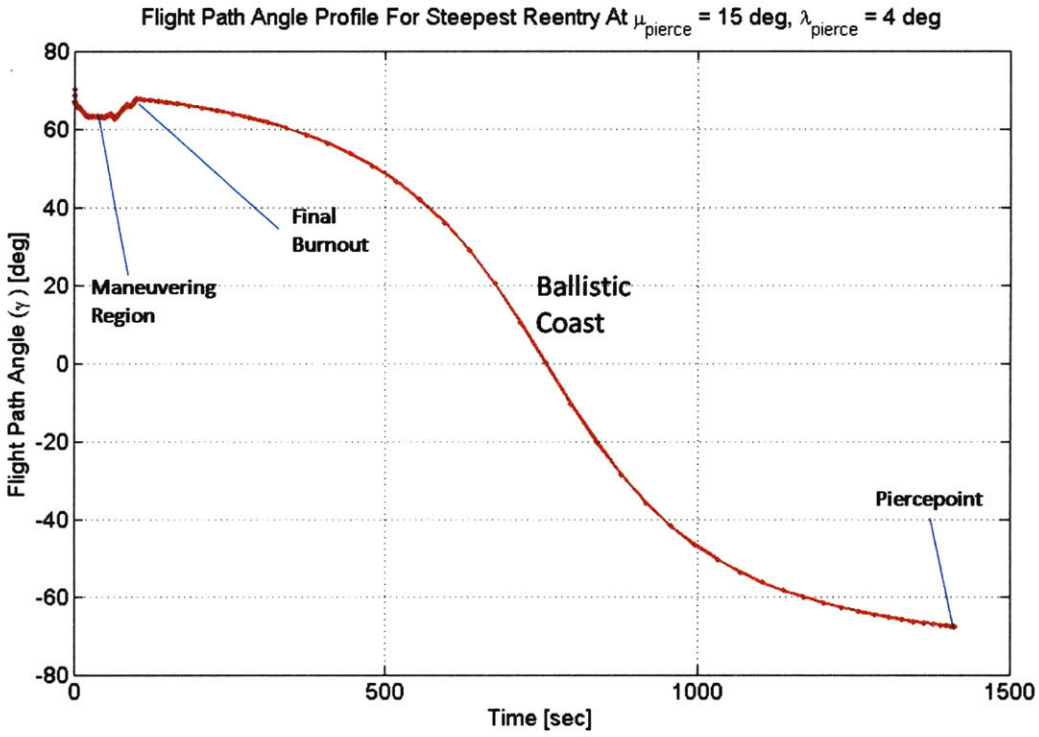

Figure 7-19: Flight Path Angle Profile For Minimum γ Trajectory With $\mu_{pierce} = 15$ deg, $\lambda_{pierce} = 4$ deg

Notice that the vehicle maneuvers during the launch to maintain the flight path angle at approximately 65 degrees for a majority of the powered flight until the final burnout, when the flight path angle rises to approximately 70 degrees. The vehicle is manuevering such that it can hit a particular final burnout location (r,μ,λ) with a certain (V_E, γ) pair. Maintaining the flight path angle at 65 degrees allows the vehicle to reach a particular location at final burnout while also ensuring that altitude is gained quickly to mimimize drag loss. Thus, reaching certain conditions at piercepoint essentially involves targeting specific conditions at final burnout.

Similarly, for the shallowest descent problem the performance index is given as

$$J = -\gamma\left(t_{k_6}\right)$$

For a piercepoint located in the Aimpoint Map at 15 degrees relative longitude and 4 degrees relative latitude, the maximum achievable flight path angle is approximately -8 degrees. The flight path angle profile is shown in Figure 7-20 for the shallowest launch trajectory. The profile for this case differs considerable from the steepest launch trajectory. The flight path angle drops off very quickly to allow the vehicle to pitch toward the horizontal and target a γ at final burnout of approximately 13 degrees. In addition, the quick dropoff of the flight path angle allows the launch trajectory to target a final burnout location that is much farther downrange from the target than the final burnout location for the steepest launch trajectory.

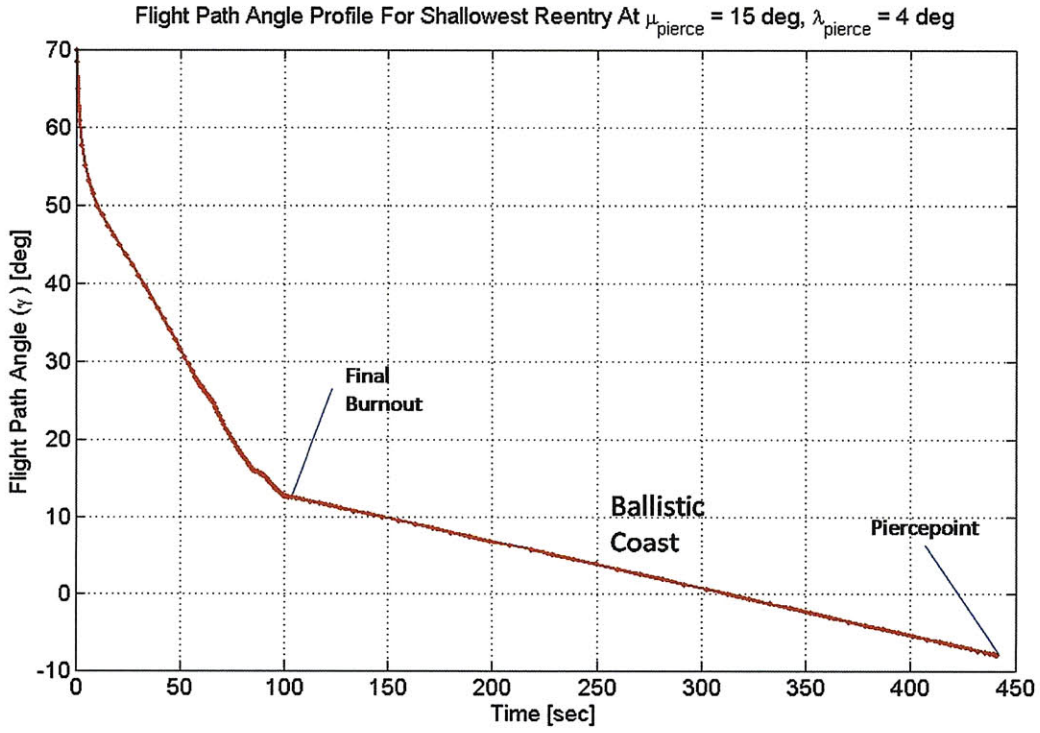

Figure 7-20: Flight Path Angle For Shallowest Launch Trajectory For $\mu_{pierce} = 15$ deg, $\lambda_{pierce} = 4$ deg

The altitude profiles for the steepest and shallowest launch trajectories can be compared to evaluate the differences in conditions at the final burnout as well as the piercepoint conditions. Figure 7-21 illustrates the steepest and shallowest reentry conditions possible at the piercepoint located as $\mu = 15$ degrees and $\lambda = 4$ degrees. The final burnout for the steepest case occurs at an altitude of slightly over 400,000 feet at a location less

than one degree downrange of the launch point. From this burnout point, a large velocity with a high flight path angle is needed to reach the specified piercepoint location. If the velocity is inclined any shallower at this point, the trajectory will overshoot the piercepoint and if the velocity is inclined any steeper, the vehicle will fall short of the piercepoint. From this point, a high velocity is needed with a low flight path angle to reach the piercepoint location. If the velocity magnitude or the flight path angle are any lower, the vehicle will undershoot the piercepoint location and may not even cross 400,000 feet. The final burnout location for the shallowest case, in contrast, occurs much farther downrange at a much lower altitude. The farther downrange the burnout location is located, the lower the maximum altitude of the ballistic coast will be needed to reach the piercepoint.

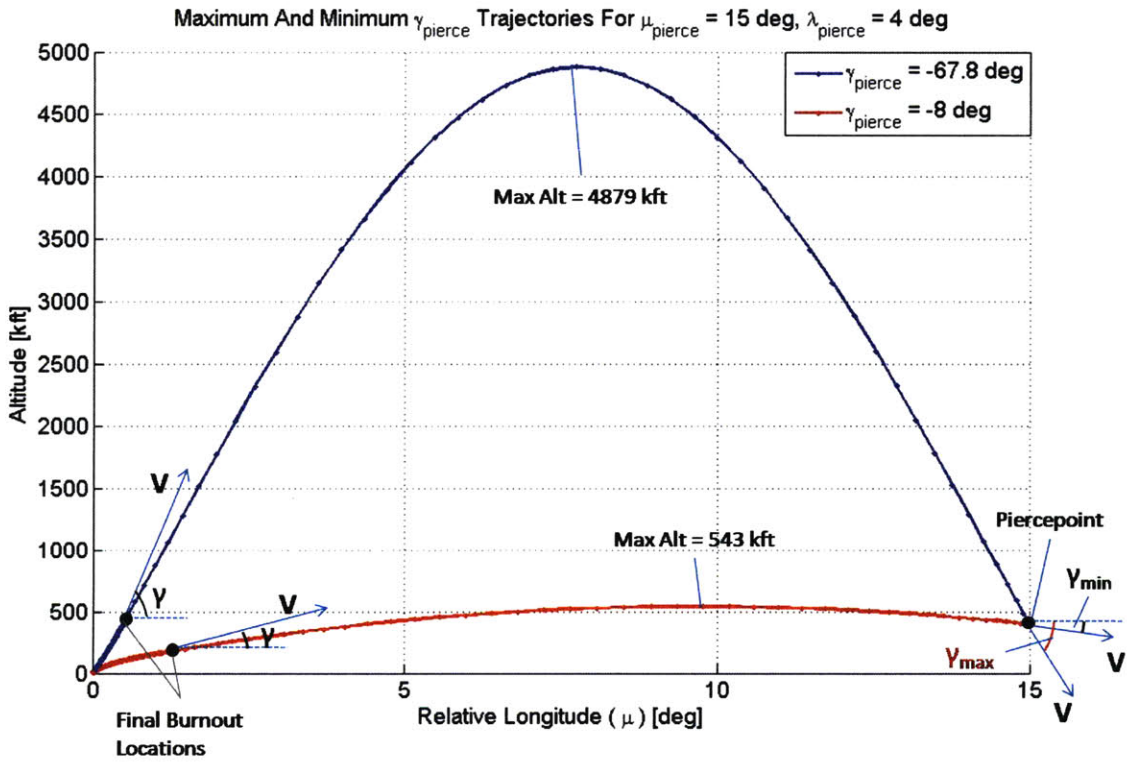

Figure 7-21: Steepest And Shallowest Launch Trajectories For $\mu_{pierce} = 15$ deg, $\lambda_{pierce} = 4$ deg

Once the maximum and minimum flight path angles achievable at the piercepoint are computed, maximum and minimum velocities achievable for each gamma within the range of $(\gamma_{max} - \gamma_{min})$ are computed. The algorithm used in this study splits the interval of

between γ_{max} and γ_{min} into 15 equally spaced points and sequentially solves for minimum and maximum velocities starting at γ_{max} and moving at equal intervals toward γ_{min}. The performance index used in the minimum velocity problem with $\gamma\left(t_{k_6}\right)$ fixed to a particular flight path angle between γ_{max} and γ_{min} is given as

$$J = V_E^2\left(t_{k_6}\right)$$

Likewise, the performance index for the maximum velocity problem is given as

$$J = -V_E^2\left(t_{k_6}\right)$$

The local launch footprint for the piercepoint at $\mu = 15$ degrees and $\lambda = 4$ degrees is shown in Figure 7-22.

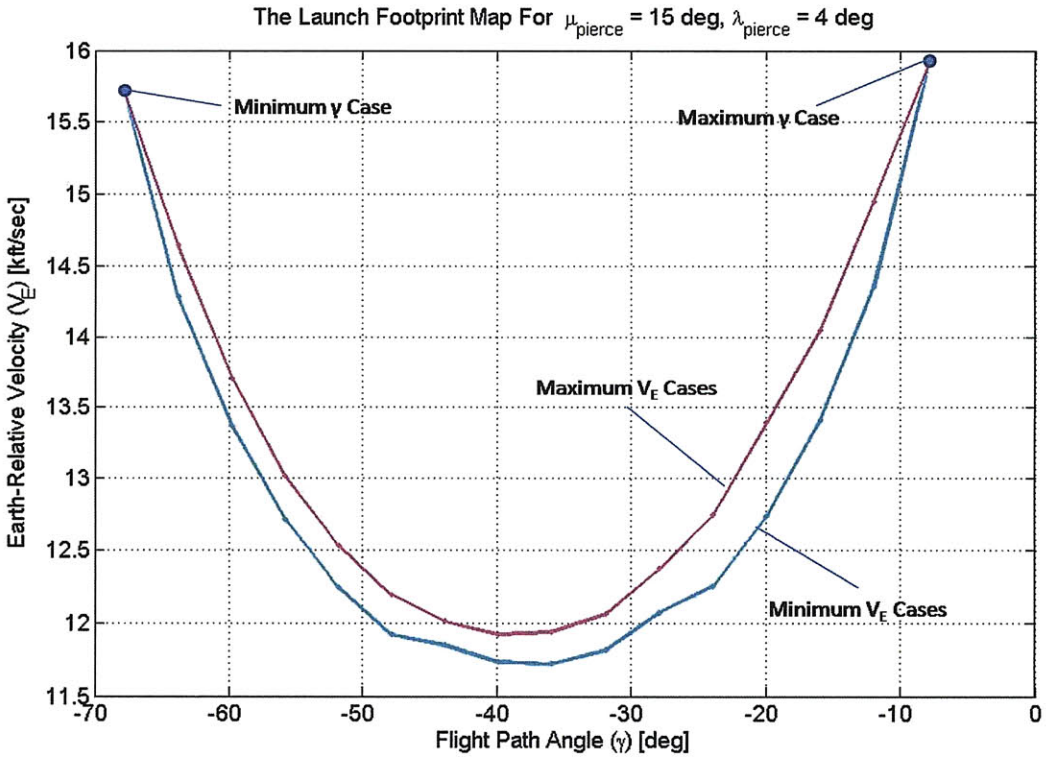

Figure 7-22: Launch Foorprint For $\mu_{pierce} = 15$ deg, $\lambda_{pierce} = 4$ deg

The launch footprint for a given piercepoint resembles a crescent shape with closed

ends and a positive, bounded area between the maximum and minimum velocities associated with each $\gamma(t_{k_6})$. The minimum and maximum flight path angle cases occur at the edges of the launch footprint. The minimum and maximum flight path angle cases can be reached with velocities on the order of 16,000 feet per second while the cases associated with intermediate values of $\gamma(t_{k_6})$ require lower velocities to reach the piercepoint location.

It should be noted that for each of the intermediate $\gamma(t_{k_6})$ values in the Launch Footprint, there is not a unique piercepoint velocity that can be obtained. Instead, the maneuverability of the launch vehicle enables different final burnout locations to be reached with different velocity conditions, resulting in multiple reentry velocities for a single reentry flight path angle. Figure 7-23 illustrates the differences in the minimum and maximum velocity trajectories that intersect a piercepoint at $\mu = 15$ degrees and $\lambda = 4$ degrees with a reentry flight path angle of γ = -31.9 degrees. The minimum velocity trajectory remains in the lower atmosphere for a longer period of time and reaches a final burnout location that is much lower in altitude further downrange than the maximum velocity trajectory. Due to increased exposure to drag, the minimum velocity trajectory reaches final burnout at a lower velocity and lower altitude than the maximum velocity case, resulting in a lower velocity at the piercepoint. As $\gamma(t_{k_6})$ approaches its limiting values, γ_{max} and γ_{min}, the difference in minimum and maximum velocity reduces to zero and converges on a unique piercepoint velocity.

7.3.1 Launch Footprint Trends

For trajectory planning purposes, it is important to examine the variations in launch footprints when moving from one aimpoint location to another aimpoint location. For the launch problem, the most important metric to examine is the variation of the launch footprint with increasing range across the Aimpoint Map. Three distinct piercepoint locations in the Aimpoint Map are chosen to demonstrate the variation in the launch footprint for trajectories launched with an initial heading of 4 degrees ($\psi(t_0) = 4\,deg$). The piercepoint locations within the Aimpoint Map are shown in Figure 7-24. One piercepoint is chosen at the Aimpoint Map minimum boundary, another is chosen at the maximum aimpoint

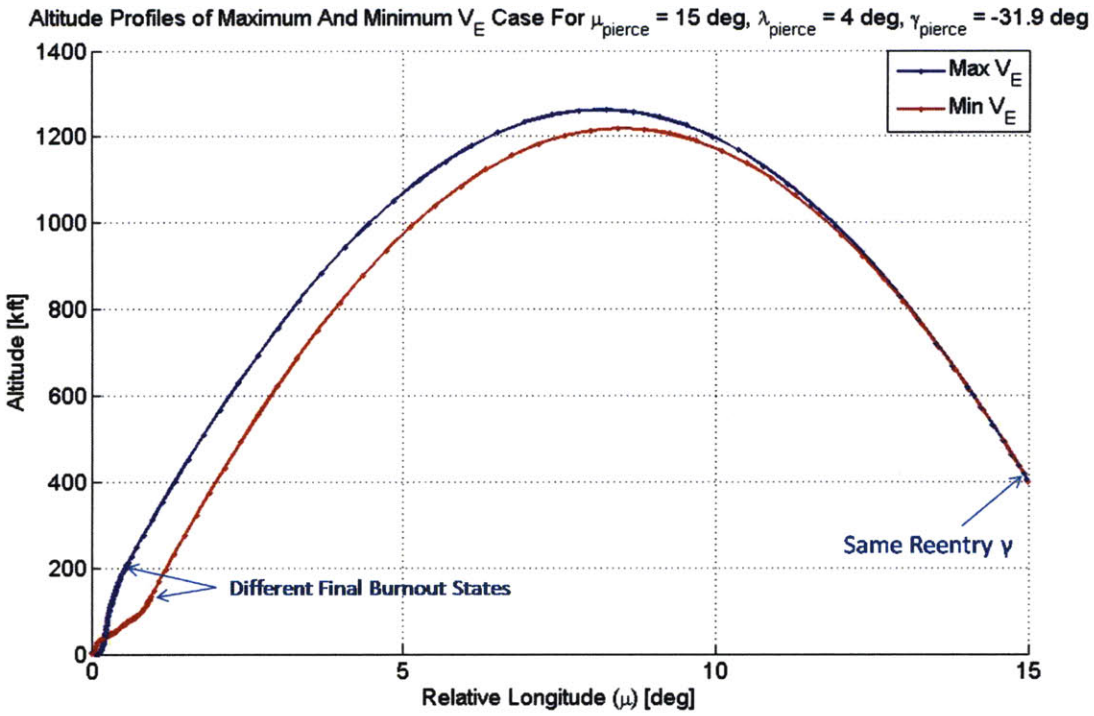

Figure 7-23: Maximum And Minimum Velocity Trajectories For μ_{pierce} = 15 deg, λ_{pierce} = 4 deg, γ_{pierce} = -31.9 deg

boundary, and the third aimpoint is chosen about mid-distance between the minimum and maximum piercepoints for the $\psi(t_0) = 4\,deg$ case. In addition, the local launch footprint for the maximum range case examined in section 5.6.2 is included to demonstrate an extreme case.

Figure 7-25 depicts launch footprints for the chosen points within the Aimpoint Map. The launch footprints are observed to reduce in area and increase in velocity as the range from launch point increases. The corners of the launch footprints shrink inward towards the median flight path angle and the differences between maximum and minimum velocities decreases. The ability of the launch vehicle to target various (V_E,γ) pairs at piercepoint is diminished as the range from launch point increases.

The launch footprints increase in velocity as the range from launch point increases because the vehicle must reduce its energy loss during the boost phase in order to increase range. For the minimum range trajectories, the vehicle seeks to maximize drag in order to burn off as much energy as possible, while the vehicle must minimize drag loss to reach

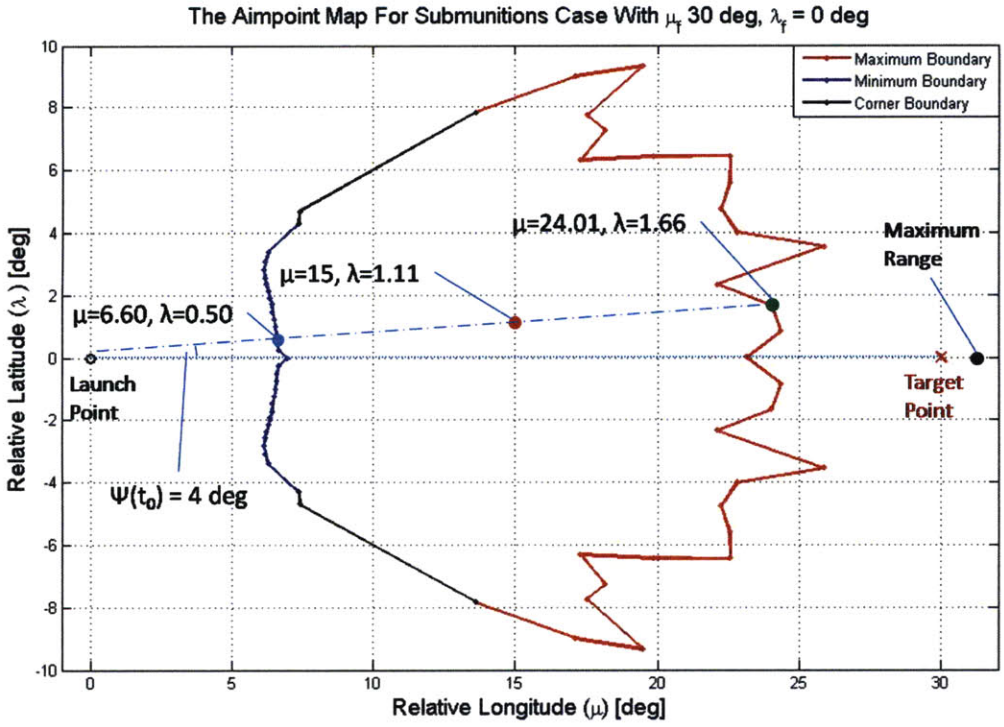

Figure 7-24: Piercepoint Locations At Various Ranges For $\psi(t_0) = 4$ deg

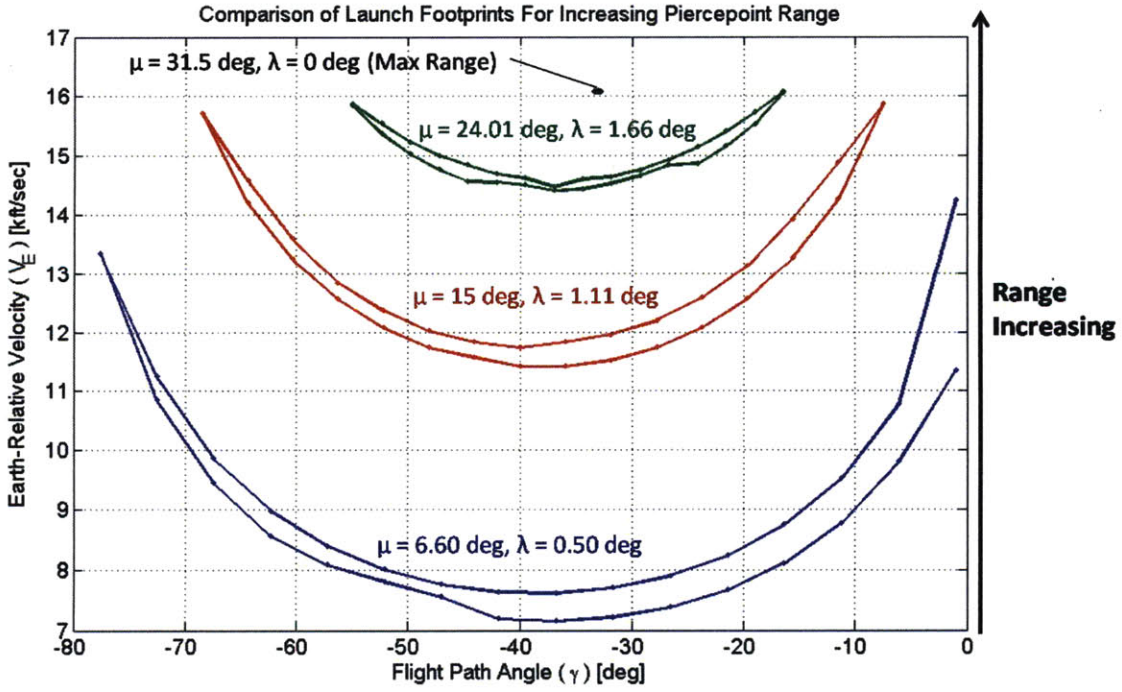

Figure 7-25: Launch Footprints For Various Piercepoints Within The Aimpoint Map

the maximum range piercepoints. Therefore, launch trajectories with greater range allow reentry with greater velocities.

7.4 Reverse Reentry Footprint

The capabilities of the reentry vehicle departing a given piercepoint in the Aimpoint Map can be compared to the launch capability to reach that piercepoint by computing a *reverse footprint.* Instead of considering the final conditions that a reentry vehicle can reach, the reverse footprint considers the set of initial conditions the can enable the vehicle to reach a particular final condition. For the problem at hand, we wish to consider the space of all possible $V - \gamma$ pairs at a fixed piercepoint location that can enable the vehicle to reach the submunitions mission final conditions.

The reverse reentry footprint is computed in similar fashion to the computation of the launch footprint in the previous section. First, the maximum and minimum flight path angles ($\gamma(t_{k_6})$) are computed with $V_E(t_{k_6})$ free to take on any feasible value. Next, a series of optimization problems are solved with each case fixing $\gamma(t_{k_6})$ to a particular value between γ_{min} and γ_{max}. For each case with $\gamma(t_{k_6})$ fixed, the maximum and minimum piercepoint velocities are computed. The algorithm begins with γ_{min} and increases $\gamma(t_{k_6})$ at equal intervals until γ_{max} is reaches. The resulting profile of minimum and maximum $V_E(t_{k_6})$ for each value of $\gamma(t_{k_6})$ make up the reentry reverse footprint.

The reverse footprint for the piercepoint location of $\mu = 15$ degrees and $\lambda = 4$ degrees is given in Figure 7-27. The reentry reverse footprint exhibits a conical shape with the minimum and maximum boundaries converging to a point at the minimum flight path angle case. The minimum boundary of the footprint is enforced by minimum energy constraints for reaching the target from the piercepoint. As the flight path angle becomes steeper, this bound increases because more energy will be lost during the first skip, requiring a higher amount of energy for reaching the target. The upper bound of the footprint is enforced by maximum heat rate and g-load constraints as well as an overshoot constraint. This bound decreases as the flight path angle becomes steeper because the vehicle will be plunging deeper into the atmosphere with higher velocities, resulting in very high dy-

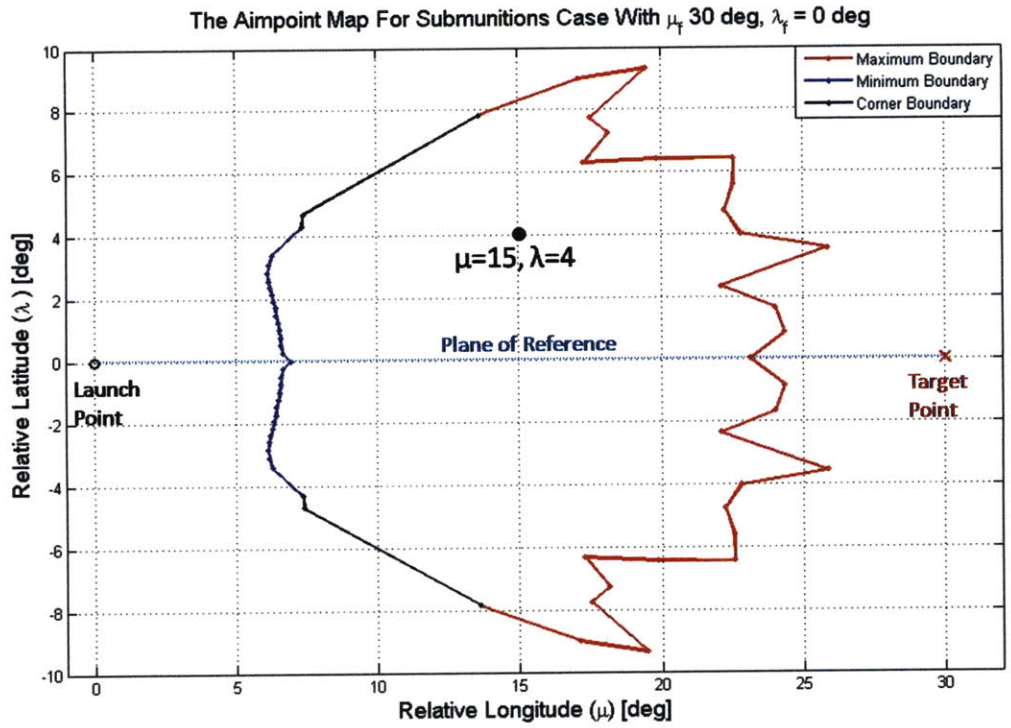

Figure 7-26: Piercepoint Located In The Aimpoint Map At $\mu = 15$ deg, $\lambda = 4$ deg

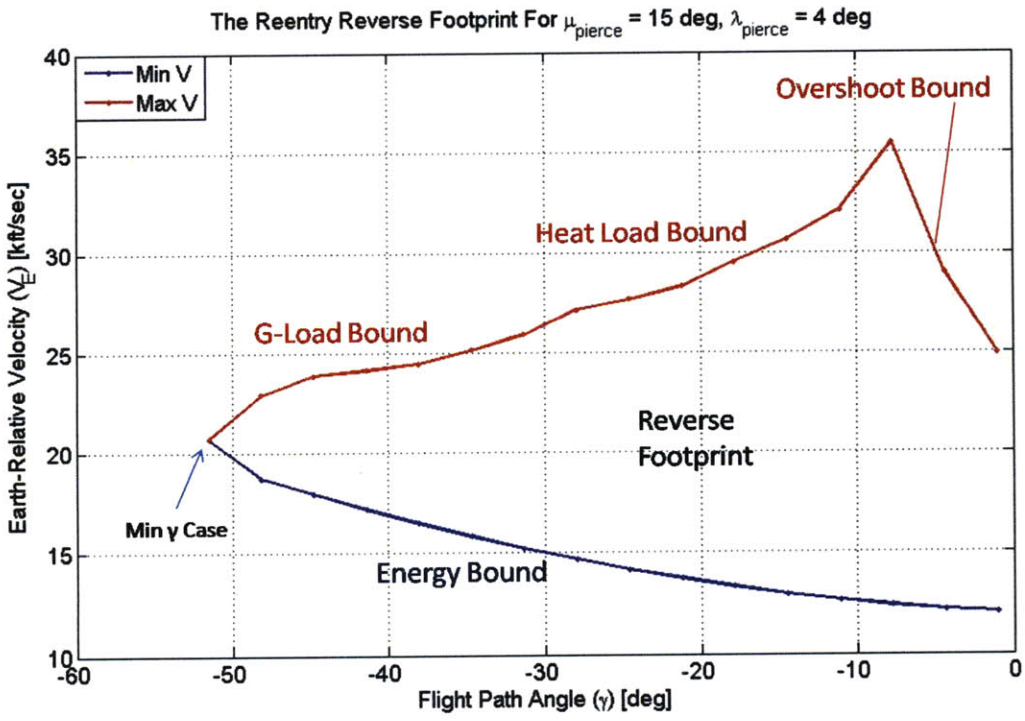

Figure 7-27: The Reverse Footprint For $\mu_{pierce} = 15$ deg, $\lambda_{pierce} = 4$ deg

namic pressures which are proportional to the heating rate and structural g-loads. The g-load and heating rate constraints are both active at steep flight path angles because the vehicle must perform a sharp pull-up maneuver with high dynamic pressure to enable a skip, while only the heating rate constraints are active at shallower flight path angles since the vehicle is not required to pull-up as sharply. The upper bound also decreases as the flight path angle approaches very shallow values, since the vehicle will overshoot the target if the velocity is too high.

7.4.1 Reverse Footprint Trends

For trajectory planning purposes, it is important to examine the variation of the reverse footprint over various piercepoints within the Aimpoint Map. Reverse footprints will be compared for interior piercepoints, minimum boundary piercepoints, and maximum boundary piercepoints. Figure 7-28 illustrates the locations of the chosen interior piercepoints within the Aimpoint Map. One piercepoint is located along the plane of reference ($\mu = 19\,deg$, $\lambda = 0\,deg$) while the other piercepoint ($\mu = 15\,deg$, $\lambda = 4\,deg$) is located in the upper half of the Aimpoint Map at a location nearly equidistant from the aimpoint boundaries and the plane of reference.

Figure 7-29 shows the reverse footprints for the interior piercepoints. The piercepoint that is located closer to the target point ($\mu = 19\,deg$,$\lambda = 0\,deg$) has a steeper minimum flight path angle (γ_{min}) than the piercepoint farther from the target ($\mu = 15\,deg$,$\lambda = 4\,deg$). As the range from the piercepoint to the target increases, the left corner of the reverse footprint will shrink inward to shallower γ_{min} values. The movement of this minimum point is largely due to a rise in the minimum energy bound, which bounds the lower edge of the reverse footprint. As the piercepoints move farther away from the target and have a larger piercepoint heading angle, they require a higher amount of energy to manuever to the target, thus raising the lower bound. In contrast, the reverse footprint upper bounds enforced by heating and g-loading limits are relatively invariant to changes in the piercepoint location. At very shallow flight path angles, however, the vehicle has the danger of gliding past the target if it reenters with too much velocity. Thus, the upper bound drops significantly as the flight path angle approaches the upper limit of -1 degrees.

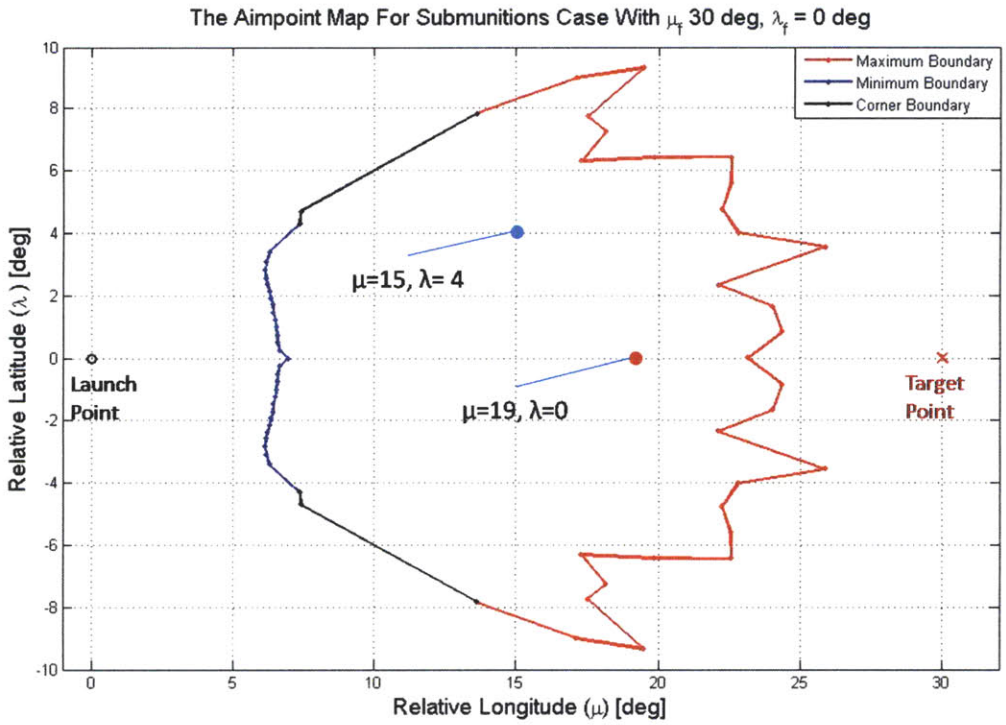

Figure 7-28: Interior Piercepoints Chosen For Comparison Of Reverse Footprints

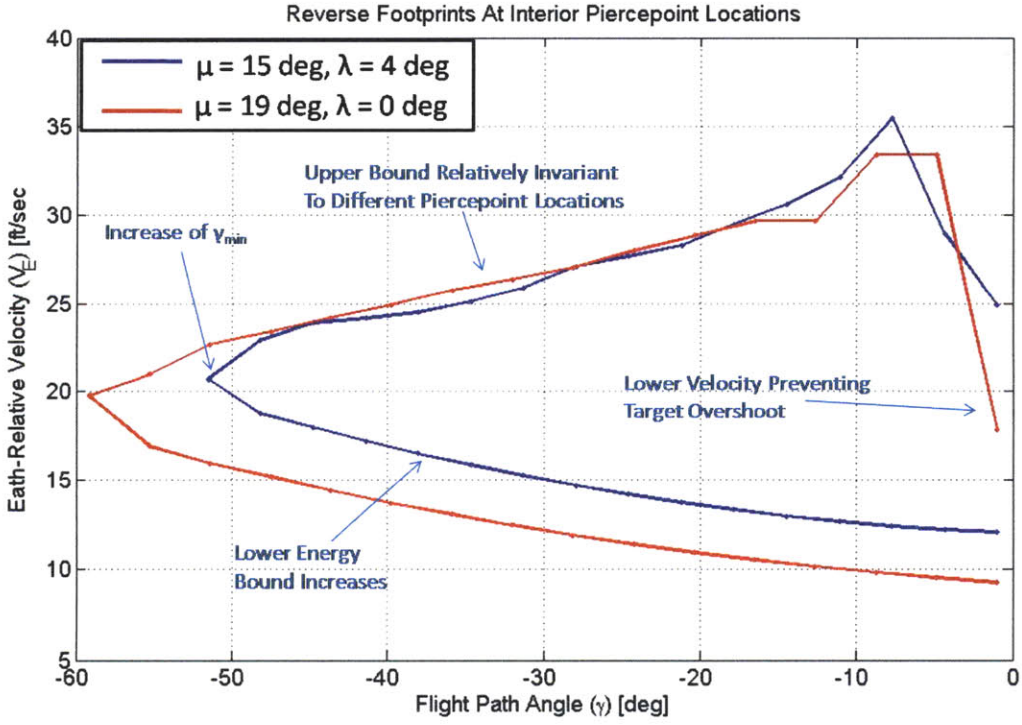

Figure 7-29: Reverse Footprints For Interior Piercepoints

The upper bound drop is greater in magnitude for piercepoints closer to the target, since they have a greater chance of overshooting the target. Figure 7-30 shows the maximum velocity reentry trajectory for a flight path angle of -1 degrees that originates from the piercepoint at $\mu_{pierce} = 19\,deg$ and $\lambda_{pierce} = 0\,deg$.

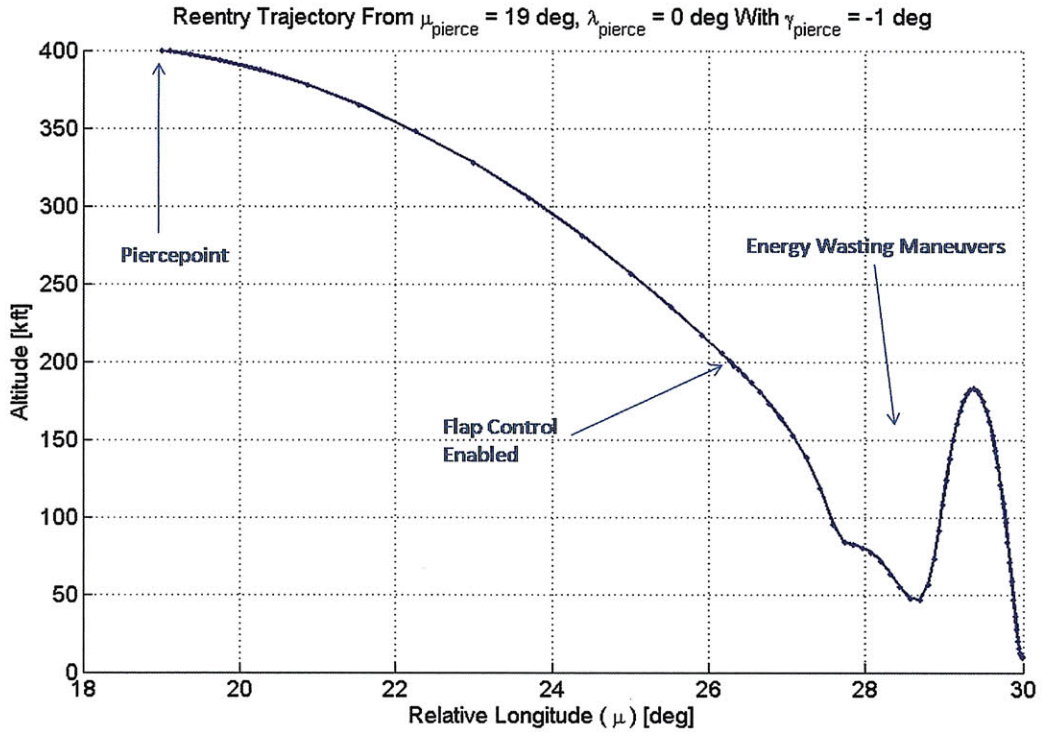

Figure 7-30: Shallow Reentry Trajectory From $\mu_{pierce} = 19$ deg, $\lambda_{pierce} = 0$ deg

This trajectory reenters with a maximum velocity of 17,797 feet per second, which is significantly lower than the maximum velocities of 33,000 feet per second observed when the flight path angle on the order of -10 degrees. Due to the shallowness of the reentry conditions for this trajectory, the vehicle travels more than 7 degrees downrange before it passes 200,000 feet and can begin manuevering to the target. Once manuvering begins, the vehicle is within 4 degrees uprange of the target and has limited space to burn off sufficient energy to meet the 1300 ft/sec end condition. Therefore, due to target overshoot and energy wasting considerations, the upper bound on the reverse footprint significantly reduces as shallow flight path angles are approached.

In similar fashion, reverse footprints can be compared for piercepoints located along the

maximum boundary of the Aimpoint Map. Aimpoint locations are chosen that correspond to trajectories with initial heading angles of 2 degrees, 4 degrees, 8 degrees, and 26 degrees. These piercepoints are illustrated in Figure 7-31.

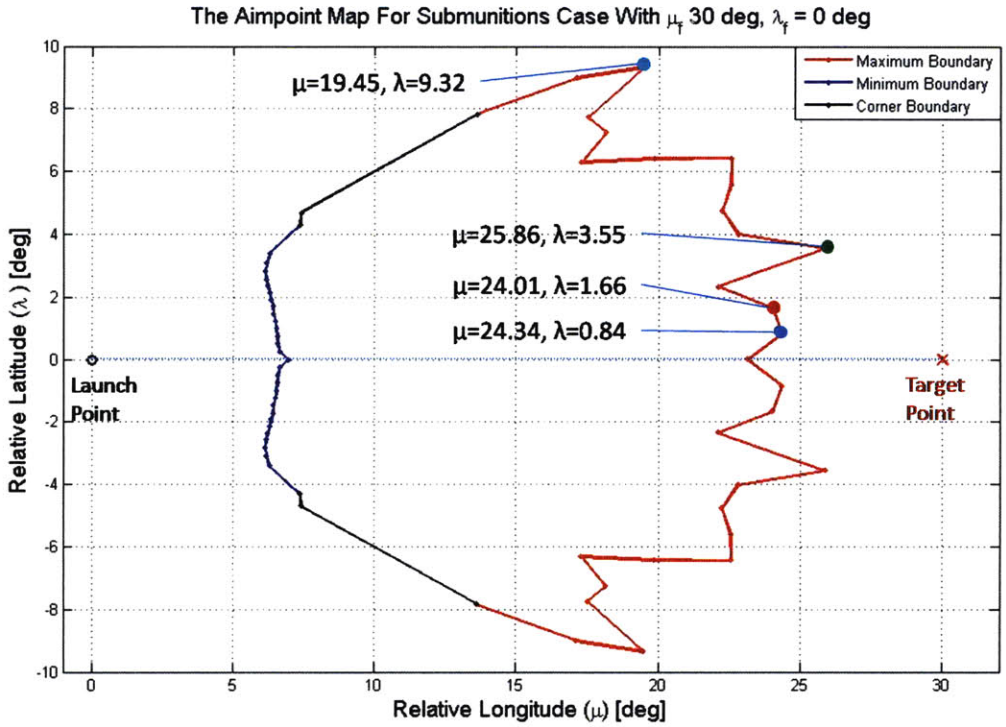

Figure 7-31: Piercepoints Located Along The Maximum Aimpoint Boundary

The corresponding reverse footprints are given by Figure 7-32. It can again be observed that the lower bound on the reverse footprint moves upward while the upper bounds stay relatively constant as the piercepoint moves further away from the target. Therefore, the bound on the steepest flight path angle moves to shallower values as the piercepoint moves away from the target. The reverse footprint corresponding to $\mu_{pierce} = 24.34\,deg$ and $\lambda_{pierce} = 0.84\,deg$ shows a decrease in the upper bound for flight path angles greater that -15 degrees. This can be explained by the same phenomenon seen in Figure 7-30, where the maximum velocity is limited by target overshoot and energy management concerns. As the piercepoint moves further from the target, it is observed that higher maximum velocities are achievable at these shallow flight path angles. Lastly, the minimum bound is observed to curve upward as the flight path angles approach γ_{max} for the two piercepoints

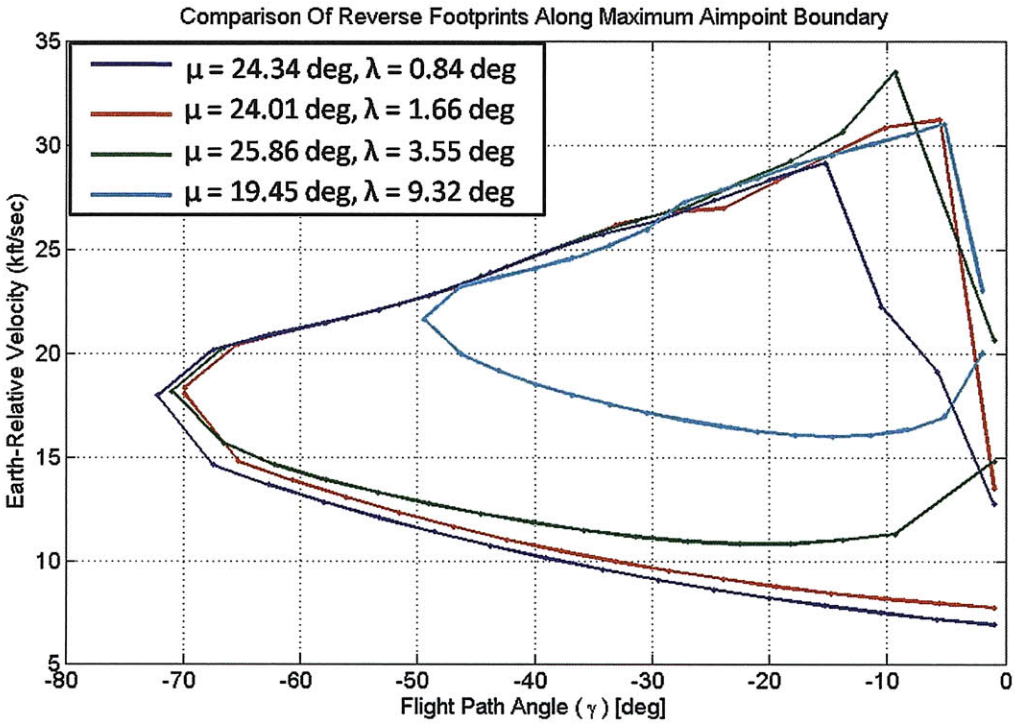

Figure 7-32: Reverse Footprints For Piercepoints Along The Maximum Aimpoint Boundary

furthest from the target. As the piercepoint moves further from the target, the minimum velocity for shallow flight path angles rises since the vehicle cannot turn as sharply when reentering at very shallow angles and requires more energy to reach the target.

Finally, a set of piercepoints spanning the length of the Aimpoint Map with be examined to determine variations in the reverse footprint maps across the Aimpoint Map. The points chosen for this analysis are the same points used in the launch footprint analysis, shown in Figure 7-24. The set of piercepoints represent potential aimpoints for the mission planner to use for a mission launched with an initial heading of 4 degrees. The reverse footprints correpsonding to these three piercepoint locations are given in Figure 7-33.

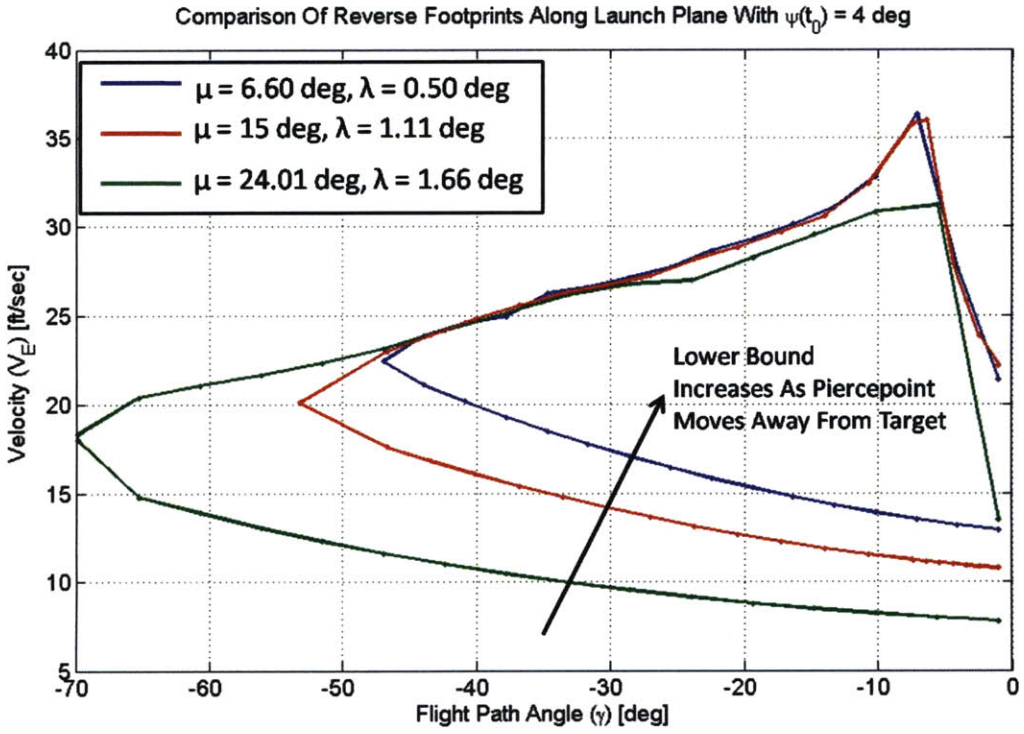

Figure 7-33: Reverse Footprints For Trajectories With $\psi(t_0) = 4$ deg

By choosing a piercepoint closer to the target, the mission planner has a much greater range of options for reentry (V_E,γ) conditions. However, as discussed in section 7.3.1, the launch footprint decreases in area as the piercepoint is moved closer to the target and further from the launch point. Thus, a mission planner will be expected to balance the size of the launch footprint with the size of the reentry footprint to ensure mission robustness.

Now that the launch footprint and reentry footprint concepts have been established,

the *Piercepoint V-Gamma Map* will combine the launch footprints and reentry footprints for demonstration of a potential trajectory planning capability.

7.5 Piercepoint V-Gamma Map

The Piercepoint $V - \gamma$ Map combines the Launch Footprint and Reentry Reverse Footprint concepts to evaluate the robustness of a boost-through-reentry trajectory that passes through a given piercepoint. The launch forward footprint is superimposed onto the reentry reverse footprint in order to determine feasible V-γ pairs for the boost-through-reentry problem of reaching a *fixed target* from a *fixed launch point* on a trajectory which passes through a *fixed piercepoint.* Several cases are presented below to depict the Piercepoint V-γ Map at representative piercepoints within the Aimpoint Map.

7.5.1 Minimum Point Case

The first case represents a piercepoint on the minimum boundary of the Aimpoint Map at $\mu_{pierce} = 6.60\,deg$ and $\lambda_{pierce} = 0.5\,deg$. Since the piercepoint is close to the launch point and far from the target point, the launch footprint appears large and wide while the reverse reentry footprint is reduced in size. The only overlap of feasible (V_E,γ) pairs that occurs is near $\gamma = -1deg$ and $V_E \approx 14000\,ft/sec$. The piercepoint conditions for the boost-through-reentry trajectory corresponding to this piercepoint location lie within this feasible space at $V_E = 14,238 ft/sec$ and $\gamma = -1deg$. Ignoring small numerical inaccuracies, this suggests that a unique (V_E,γ) exists for piercepoints along the aimpoint boundary. Therefore, for trajectory planning purposes, the aimpoint boundaries should be avoided.

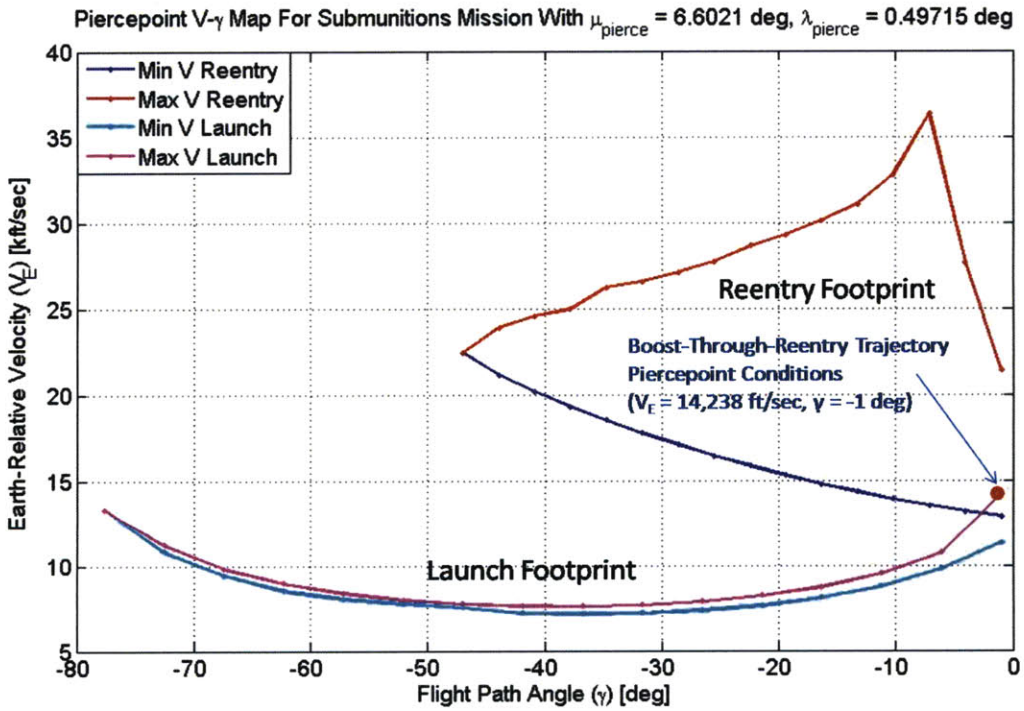

Figure 7-34: Piercepoint V-γ Map For Minimum Aimpoint Boundary Piercepoint Corresponding To $\psi(t_0) = 4$ deg

7.5.2 Corner Point Case

Figure 7-35 depicts the Piercepoint $V-\gamma$ Map for the corner piercepoint location. The piercepoint conditions for the corner point trajectory represent the only overlapping $V-\gamma$ conditions at $V_E = 15,731 ft/sec$ and $\gamma = -1.07 deg$. Therefore, the corner point can only satisfy all terminal and path constraints with this unique V-γ pair.

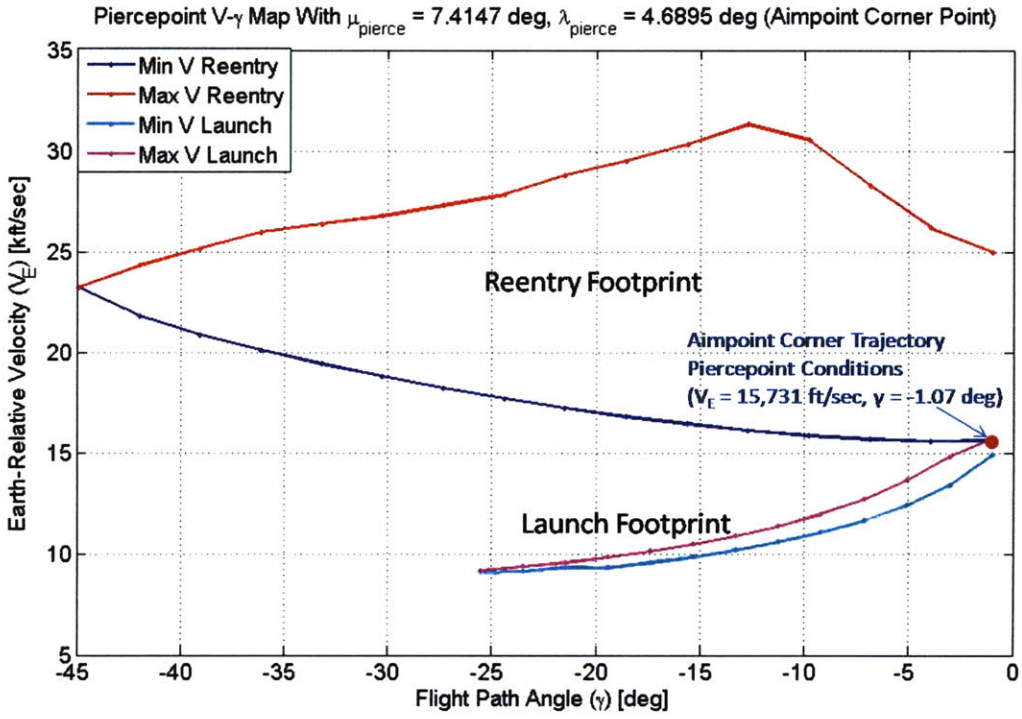

Figure 7-35: The Piercepoint V-γ Map For The Corner Point Trajectory

7.5.3 Maximum Point Case

Figure 7-36 depicts the Piercepoint $V-\gamma$ Map for a piercepoint located on the maximum aimpoint boundary at $\mu_{pierce} = 19.45\,deg$ and $\lambda_{pierce} = 9.32\,deg$. Again, it can be shown that a unique $V-\gamma$ pair exists for a piercepoint located on the aimpoint boundary. The unique $V-\gamma$ pair is equivalent to the $V-\gamma$ conditions of $V_E = 16,035 ft/sec$ and $\gamma = -14.04 deg$ solved for at piercepoint for the corresponding boost-through-reentry trajectory. Notice that the vehicle is required to hit piercepoint at faster and steeper conditions for points along the maximum aimpoint boundary. The vehicle must reenter with a steeper flight path angle due to launch limitations and must reetry with a faster velocity due to reentry energy requirements.

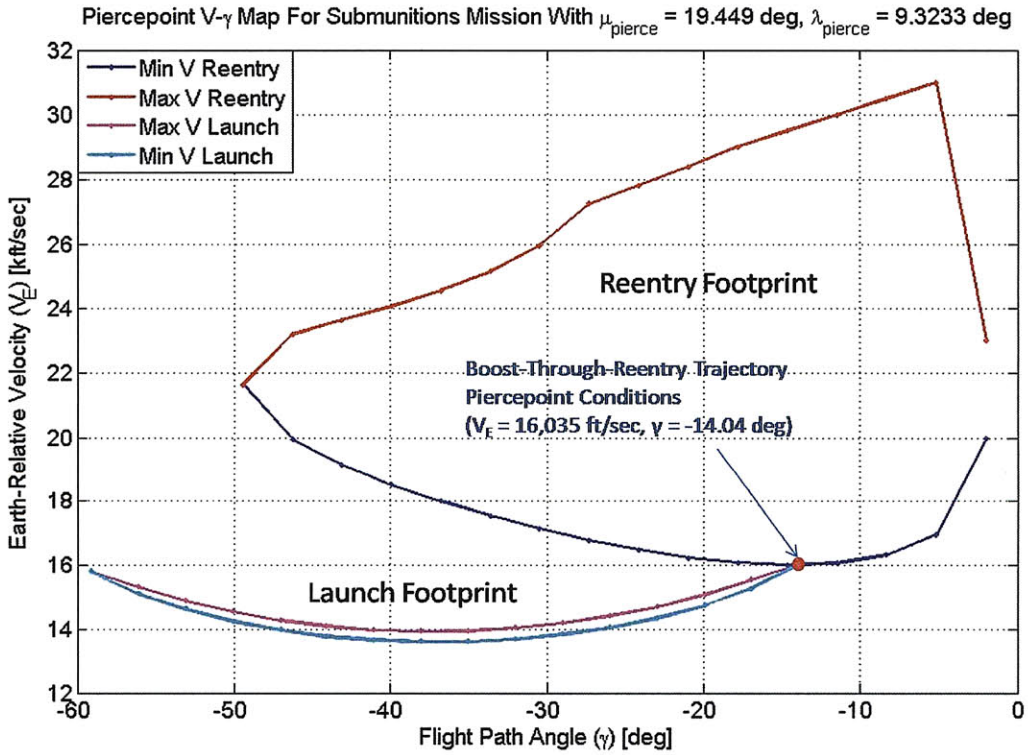

Figure 7-36: Piercepoint V-γ Map For Maximum Aimpoint Boundary Corresponding To $\psi(t_0) = 26$ deg

7.5.4 Interior Point Cases

It has been demonstrated with the previous boundary cases that only one unique $V - \gamma$ pair exists for each aimpoint on the aimpoint boundary. $V - \gamma$ Manifolds for aimpoint interior points will be now be examined that are representative of typical piercepoints the mission planner may consider before choosing a boost-through-reentry trajectory. Two cases are investigated for the piercepoints located at ($\mu_{pierce} = 15\,deg, \lambda_{pierce} = 4\,deg$) and ($\mu_{pierce} = 19\,deg, \lambda_{pierce} = 0\,deg$)

Case 1: $\mu_{pierce} = 15$ **deg,** $\lambda_{pierce} = 4$ **deg**

Figure 7-37 illustrates the Piercepoint $V - \gamma$ Map for Case 1 and demonstrates that multiple $V - \gamma$ pairs are possible for this piercepoint choice. In particular, flight path angles ranging from -8 degrees to -20 degrees are possible with velocities that range from 15,900 feet per second to 13,200 feet per second. Notice that only shallow flight path angles are allowed at this piercepoint due to minimum energy constraints associated with the large distance away from the target.

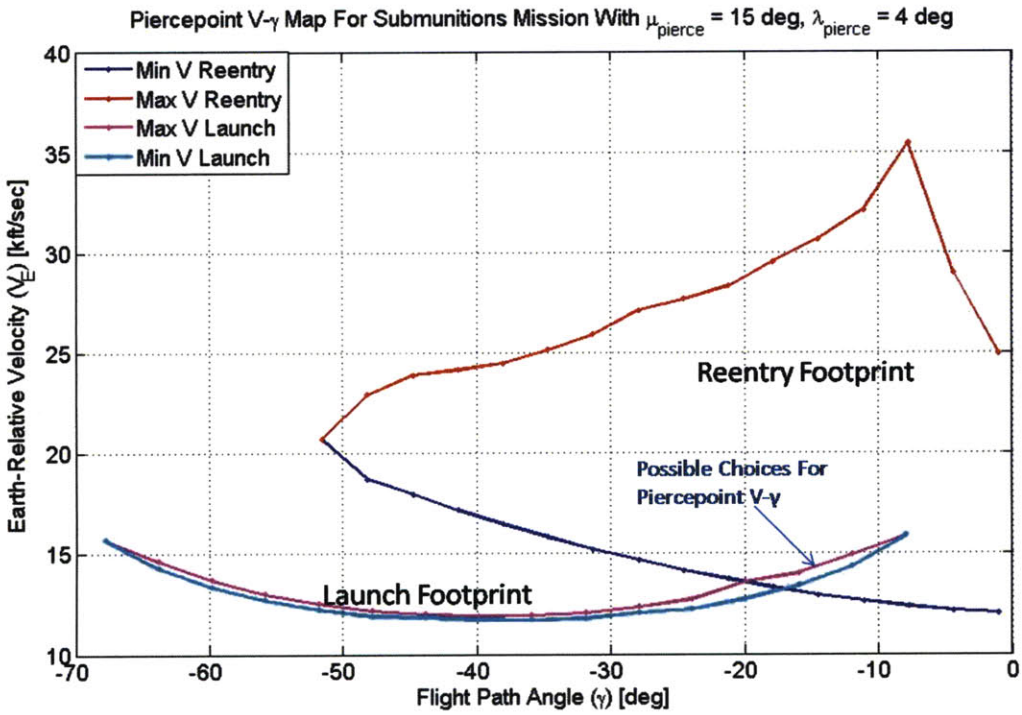

Figure 7-37: Piercepoint V-γ Map For $\mu_{pierce} = 15$ deg, $\lambda_{pierce} = 4$ deg

Case 2: $\mu_{pierce} = 19$ **deg,** $\lambda_{pierce} = 0$ **deg**

Figure 7-38 illustrates the Piercepoint $V - \gamma$ Map for Case 2 and shows that a greater number of feasible $V - \gamma$ pairs exist for piercepoints closer to the target. In particular, flight path angles ranging from -11.2 degrees to -36.8 degrees are possible with velocities that range from 15,980 feet per second to 12,900 feet per second. Steeper flight path angles are allowed at this piercepoint since the piercepoint is closer to the target and the minimum energy constraint is relaxed. However, since the piercepoint is further away from the launch point, the launch footprint is smaller and therefore the ability for shallow reentry shinks.

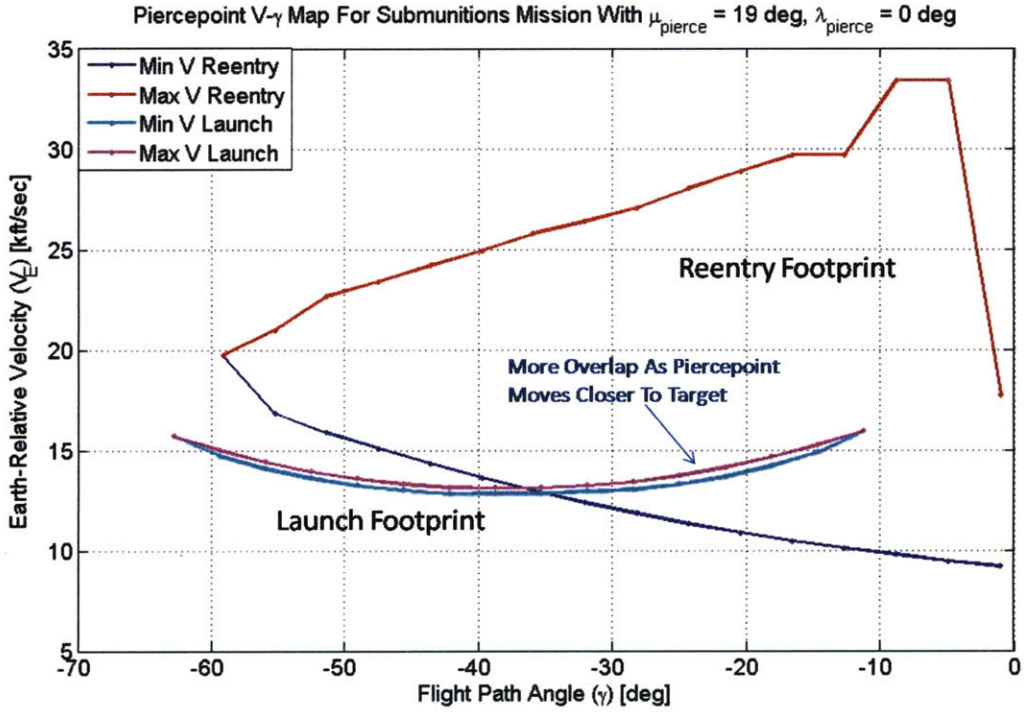

Figure 7-38: Piercepoint V-γ Map For $\mu_{pierce} = 19$ deg, $\lambda_{pierce} = 0$ deg

7.6 Summary

In this chapter, several trajectory planning metrics were investigated using boost-through-reentry trajectory optimization. The Aimpoint Map, a set of latitude (λ) and longitude (μ) points at an altitude of 400,000 feet through which a boost-through-reentry trajectory satisfying all mission constraints can be flown, is computed by first optimizing the offset of the piercepoint location from the plane of reference. Once this corner point is calculated, a series of optimizations sweep out the maximum and minimum boundaries of the Aimpoint Map between the corner point and the plane of reference. In order to evaluate the robustness of piercepoints within the Aimpoint Map boundaries, launch footprints and reverse reentry footprints are computed for several representative piercepoints. By taking the intersection of the launch footprint and the reverse reentry footprint for a given piercepoint, the Piercepoint V-γ Map can provide the mission planner some insight into the robustness of a particular piercepoint. It was demonstrated that piercepoints along the Aimpoint boundary typically have a single, unique V-γ pair that satisfies a boost-through-reentry trajectory, indicating a lack of robustness to potential uncertainties. However, Piercepoint V-γ Maps computed for piercepoints located on the interior of the Aimpoint Map provided many more V-γ options for the mission planner when choosing a boost-through-reentry trajectory.

Chapter 8

Conclusions

In this work, the optimal maneuvering capabilities of a launch vehicle and a reentry vehicle were investigated for application to a long range, rapid response mission. A unified 6-DOF dynamics model was developed to accurately model the motion of both the launch and reentry vehicle in both endo and exo-atmospheric flight. Detailed vehicle models were also developed for a solid rocket launch vehicle using thrust vector control and a manuevering reentry vehicle using flap control that met the specifications of the boost-through-reentry mission. Optimal control and nonlinear programming techniques were employed to solve a range of optimization problems related to the maximum and minimum maneuvering capabilities of the launch and reentry vehicles.

The fundamental motivation behind this study was to explore the space of potential aimpoint locations for a highly maneuverable reentry vehicle with a lift-to-drag ratio of approximately two. The capability now exists to aim a launch vehicle in a direction significantly away from the target while still satisfying all mission objectives. This capability is crucial for satisfying certain flyover constraints, including avoidance of hostile airspaces and residential areas. The vehicle formulated in this study was able to acquire the target while being aimed with initial headings offset up to 32 degrees relative to the target direction. This resulted in aimpoint locations as much as 620 miles crossrange of the target location. An Aimpoint Map was formulated to depict the space of all possible aimpoints for the boost-through-reentry problem. While the minimum and corner boundaries of the Aimpoint Map were limited by energy constraints, the maximum boundaries are limited

by the turning capability of the vehicle and the number of skips it can endure without exceeding the energy limit. In particular, since the control authority of the vehicle as well as the energy loss of the vehicle due to drag are directly proportional to dynamic pressure, the vehicle must carefully choose how deep to dive into the atmosphere during each skip. The trajectories along the maximum edge use anywhere from one to four skips to reach the target. The uneven edges at the maximum boundary suggest that the phasing of the skips may play a factor in the location of maximum piercepoint range locations.

In order to help the mission planner quickly decipher the characteristics of various points in the Aimpoint Map, the concept of a Piercepoint V-Gamma Map was demonstrated by the calculation of launch footprints and reverse reentry footprints. By superimposing the launch and reverse reentry footprints, the Piercepoint V-Gamma Map provides a metric for determining the robustness of a chosen piercepoint. It was shown that the piercepoints located on the Aimpoint Map boundaries may only have a single V-γ pair that is common to both the launch footprint and the reverse reentry footprint. Piercepoints examined in the interior of the Aimpoint Map contained many more feasible V-γ pairs for the boost-through-reentry problem.

The mission planner must choose a piercepoint that satisfies necessary flyover constraints while ensuring robustness of the trajectory. The launch footprint was shown to shrink in size as the piercepoint is moved away from the launch point while the reentry footprint was shown to shrink as the piercepoint is moved away from the target point. Since increasing the crossrange distance of the piercepoint increases the distance from both the launch point and the target, the mission planner must balance the need to satisfy flyover constraints and the need to choose a trajectory with sufficient robustness.

Additional specific conclusions of this study include:

- The Aimpoint Maximum Boundaries Are Limited By The Vehicle Turning Capability As Well As By Energy Constraints
- The Aimpoint Minimum Boundaries Are Limited By Energy And The Maximum Piercepoint Flight Path Angle ($\gamma_{max}\left(t_{k_6}\right)$)
- The Aimpoint Corner Point Is Limited By Energy

- The Launch Vehicle Targets A Particular Piercepoint By Maneuvering To A Final Burnout Location With A Particular Velocity And Flight Path Angle
- The Launch Vehicle Can Shed Off Energy By Manuevering For Extended Periods At Low Altitudes
- For A Fixed Piercepoint Location With A Fixed Flight Path Angle ($\gamma(t_{k_6})$), $V_{max}(t_{k_6})$ and $V_{min}(t_{k_6})$ Can Differ Due To The Ability Of The Launch Vehicle To Manuever To Different Burnout Locations
- The Reentry Reverse Footprint Is Limited By Energy, Heating, G-Loading, And Overshoot Constraints
- Proper Parameter Scaling Is Crucial For Highly Nonlinear Optimization Problems
- Controllability During Reentry Is A Function Of Altitude

8.1 Future Work

In this study, the concepts of an Aimpoint Map and a Piercepoint V-Gamma Map were developed for trajectory planning purposes as applied to the boost-through-reentry problem. Future work to be done on this subject includes analysis of the effects of navigational and environmental uncertainties on the Aimpoint Map, further investigation of automated scaling techniques for a wide range of problems, and additional analysis of the skipping abilities at piercepoints within the Aimpoint Map. The tool developed in this study should serve as a starting point for further investigation of the Aimpoint Map properties.

[This page intentionally left blank.]

Bibliography

[1] A. Undurti, *Optimal Trajectories for Maneuvering Reentry Vehicles*, Masters Thesis, MIT Department of Aeronautics and Astronautics, May 2007.

[2] H. Ikawa, "A Unified Three-Dimensional Trajectory Simulation Methodology," J. Guidance, Control, and Dynamics, vol. 9, no. 6, pp. 650-656. Nov.-Dec. 1986.

[3] H. Ashley, *Engineering Analysis of Flight Vehicles.* New York: Dover Publications, 1992

[4] G. M. Siouris, *Missile Guidance and Control Systems.* New York: Springer, 2004.

[5] N. X. Vinh, *Optimal Trajectories in Atmospheric Flight.* Elsevier Scientific Publishing Company, 1981.

[6] I. M. Ross, *Users Manual for DIDO (Ver. PR 1β): A MATLAB Application Package for Solving Optimal Control Problems*, Naval Postgraduate School Technical Report 04-01.0, February 2004.

[7] J. Betts, Survey of Numerical Methods for Trajectory Optimization, J. Guidance, Control and Dynamics, vol. 21, no. 2, pp. 193-207, Mar. 1998.

[8] G. P. Sutton, O. Biblarz, *Rocket Propulsion Elements.* New York: John Wiley & Sons, 2001.

[9] T. B. Cochran, W. M. Arkin, M. M. Hoenig, *Nuclear Weapons Databook Vol. 1: U.S. Nuclear Forces and Capabilities.* Ballinger Publishing Company, 1984.

[10] R. T. Reichert, *Homing Performance Comparison of Selected Airframe Configurations Using Skid-To-Turn and Bank-To-Turn Steering Policies.* NASA Contractor Report 3420, 1981.

[11] Sarah Bairstow, *Reentry Guidance with Extended Range Capability for low L/D Spacecraft*, Masters Thesis, MIT Department of Aeronautics and Astronautics, February 2006.

[12] K. A. Clarke, *Performance Optimization Study of a Common Aero Vehicle using a Legendre Pseudospectral Method*, Masters Thesis, MIT Department of Aeronautics and Astronautics, May 2003.

[13] G. Richie, *The Common Aero Vehicle: Space Delivery System of the Future.* AIAA Space Technology Conference and Exposition, 28-30 Sept. 1999, Albuquerque, NM.

[14] K. P. Bollino, I. M. Ross, D. B. Doman, *Six-Degree-Of-Freedom Trajectory Optimization For Reusable Launch Vehicle Footprint Determination.* AAS/AIAA Astrodynamics Specialist Conference, 19-23 August 2007, Mackinac Island, MI.

[15] K. P. Bollino, *High-Fidelity Real-Time Trajectory Optimization For Reusable Launch Vehicles*, Dissertation, Naval Postgraduate School, Monterey, CA, Dec. 2006.

[16] R. T. Bibeau, *Trajectory Optimization For A Fixed-Trim Reentry Vehicle Using Direct Collocation and Nonlinear Programming*, AIAA Guidance, Navigation, and Control Conference and Exhibit , 14-17 August 2000, Denver, CO.

[17] R. T. Bibeau, *Trajectory Optimization For A Fixed-Trim Reentry Vehicle Using Direct Collocation With Nonlinear Programming*, Masters Thesis, MIT Department of Aeronautics and Astronautics, May 1999.

[18] W. J. Larson, J. R. Wertz, eds. *Space Mission Analysis and Design.* 3rd Ed. Microcosm Press, 1999.

[19] W. Kang, Q. Gong, I. M. Ross, *Convergence of Pseudospectral Methods for a Class of Discontinuous-Control Nonlinear Optimal Control Problems.* Proc. IEEE Conference on Decision and Control and European Control Conference, 2005

[20] D. Bertsimas, J. N. Tsitsiklis, *Introduction to Linear Optimization.* Belmont, MA: Athena Scientific, 1997.

[21] C. G. Justus, D. L. Johnson, *The NASA/MSFC Global Reference Atmospheric Model - 1999 Version.* NASA Technical Report 209630, 1999.

[22] D. R. Chapman, *An Approximate Analytical Method for Studying Entry into Planetary Atmospheres.* NASA Technical Report R-11, 1958.